

CHARACTERIZATION OF EXOPLANETS AND STELLAR SYSTEMS WITH NEW
ROBOTS

Carl Andrew Ziegler

A dissertation submitted to the faculty at the University of North Carolina at Chapel Hill
in partial fulfillment of the requirements for the degree of Doctor of Philosophy in the
Department of Physics and Astronomy.

Chapel Hill
2018

Approved by:

Nicholas M. Law

J. Christopher Clemens

Fabian Heitsch

Amy Oldenburg

Daniel E. Reichart

© 2018
Carl Andrew Ziegler
ALL RIGHTS RESERVED

ABSTRACT

**Carl Andrew Ziegler: CHARACTERIZATION OF EXOPLANETS AND
STELLAR SYSTEMS WITH NEW ROBOTS.**
(Under the direction of Nicholas M. Law.)

Large astronomical surveys find thousands of interesting transient events, such as exoplanets. Beyond detection, these surveys are limited in their ability to study the properties of these discoveries. In particular, a common problem with wide-field surveys is because they observe huge swaths of the sky, their resolution is often quite coarse, leading to source confusion and photometric contamination. In this dissertation, I discuss the use of robotic, high-resolution instruments to confirm and characterize exoplanets and also better understand the demographics of stellar populations. These surveys are only feasible with autonomous instruments due to the order-of-magnitude increase in observational time efficiency gained with automation.

I present first the design and construction of Robo-SOAR, a moderate-order NGS-AO system in development for the SOAR telescope. With robotic software adapted from Robo-AO, Robo-SOAR will be capable of observing hundreds of targets a night. With an innovative, low-cost dual knife-edge WFS, similar in concept to a pyramid WFS but with reduced chromatic aberrations, Robo-SOAR can reach the diffraction limit on brighter targets.

I then discuss the observations of 348 cool subdwarf stars with Robo-AO, a pilot study for future kilo-target surveys. Cool subdwarfs are remnants of the first population of stars formed in the Milky Way. I find that approximately 12% of cool subdwarfs have binary companions, a multiplicity fraction three times lower than similar dwarf stars. The disparity between the two populations may be evidence of the different environments in which they formed. The lack of companions to cool subdwarfs suggests they may have formed in less dense regions, or over their long lifetimes may have had more disruptive encounters with

other stars and the Galactic tide. It is also possible that they are galactic interlopers, and formed in small, less-dense galaxies that merged with the Milky Way. We show that the disparity between cool subdwarf and red dwarf multiplicity is consistent with this scenario.

I report the results of the Robo-AO survey of every planetary candidate discovered with *Kepler* to search for previously unknown nearby stars. These stars contaminate the exquisite photometry of *Kepler* and can either dilute the transit signal from a real planet, resulting in underestimated radii estimates, or be the source of an astrophysical false positive transit signal. More than half of the over 4000 *Kepler* planetary candidates have only been observed with Robo-AO. We find 610 stars within 4" of a planetary candidate host star, and correct the derived radii estimates of the more than 800 planets within these systems. On average, we find that the planetary radii increase by a factor of approximately 1.59 in systems with a detected nearby star. We quantify the probability of association for over 150 multiple systems hosting planets using multi-band photometry. In particular, we examine five planetary candidate host stars with four nearby stars detected by Robo-AO and quantify the probability they are high-order planet-hosting systems.

Lastly, I use the results of the Robo-AO *Kepler* survey to search for evidence of the impact multiple star systems have on planets. The presence of a companion star is believed to have a significant impact on the properties of planetary systems. I find that hot Jupiters are more likely than any other planet to be found in a binary star system. This suggests that stellar companions drive orbital migration of giant planets. I also find that single and multiple-transiting planet systems are equally likely to be found in a binary. I find that KOIs from later data releases are less likely to have a nearby star than systems from earlier data releases, possibly a result of the automation of the *Kepler* vetting pipeline. I find that KOIs follow trends observed in field stars with respect to the relationship between stellar multiplicity and stellar effective temperature and metallicity.

In addition to the work described in this dissertation, I have contributed to additional studies on the highly inflated hot Jupiter, KELT-8b (Fulton et al., 2015); on the eclipsing

binary HII 2407 in the Pleiades (David et al., 2015); on the small terrestrial planet K2-26 (Schlieder et al., 2016); on the probability of association of nearby stars to 104 planetary candidates (Atkinson et al., 2017); on confirmation of 104 exoplanets (Crossfield et al., 2016); on an ultra-short period planet (Adams et al., 2017); on nearby stars to astroseismic gold standard stars (Schonhut-Stasik et al., 2017); on the performance of laser-only AO for faint planet candidates (Howard et al., 2018); and on 66 binary systems in the nearby clusters (Hillenbrand et al., 2018).

ACKNOWLEDGMENTS

The work presented here was only possible due to the support of a great many people. My gratitude extends to far more people than listed here—there are simply too many people who deserve thanks.

I am thankful for the guidance of my advisor, Nick Law. In addition to providing the resources and opportunities for me to succeed, he always had an open door to talk about anything and share his knowledge and wisdom. His enthusiasm for astronomy has instilled in me a drive to always continue asking questions and seeking answers.

I am thankful for the assistance and camaraderie provided by my lab mates: Octavi Fors, Jeff Ratzloff, Ward Howard, Hank Corbett, Phil Wulfken. They all provided to a warm and friendly work environment with many illuminating discussions.

I thank my committee, Nick, Chris Clemens, Fabian Heitsch, Amy Oldenburg, and Dan Reichart, for their advice and time.

Much of the work presented here was performed with Robo-AO. I am thankful to Nick, Christoph Baranec, and Reed Riddle for constructing this unique instrument, without which much of this work would not be possible. I am thankful to the staff at Palomar Observatory and Kitt Peak Observatory for their work. I am thankful to Dmitry Duev, Maïssa Salama, Rebecca Jensen-Clem, and Dani Atkinson for their work in operating and upgrading Robo-AO. I also thank Christoph for hosting me during Keck observations and taking me to the most spicy food in Hawai’i.

I am thankful for the financial support provided by the NASA Exoplanets Research Program, grant #NNX 15AC91G and the NSF CAREER AST-155175 grant. I also thank the citizens of North Carolina for supporting me as a Teaching Assistant for one year and through the North Carolina Space Grant in the summer of 2017.

I am thankful to friends in the department for their support and encouragement. Particularly, I thank members of the Carolina United soccer team for a weekly distraction from research.

I thank my family for their assistance and support during my graduate years. I appreciate their willingness to visit North Carolina on many occasions, as well as support me from afar. I thank my parents for fostering my curiosity and encouraging me to follow my passion. I thank my siblings for always keeping me grounded. I thank my in-laws, for their unending support and curiosity about what I do. I thank Caroline for always being able to make me smile.

Lastly, I thank my wonderful wife Kristina, without whose love and support this would not be possible. From spending weekends alone because I was doing homework to getting up before sunrise with Caroline each morning so that I could be rested for each day, you have given so much to allow me to pursue my dream. You have always been my greatest champion and you motivate me every day to do my best. Thank you.

TABLE OF CONTENTS

LIST OF FIGURES	xvi
LIST OF TABLES	xvii
LIST OF ABBREVIATIONS AND SYMBOLS	xviii
1 INTRODUCTION	1
1.1 Automated Adaptive Optics	2
1.1.1 Adaptive Optics	2
1.1.2 Robo-AO	10
1.2 Exoplanet Confirmation and Characterization	13
1.2.1 Detection Techniques	16
1.2.2 Transit Method	22
1.2.3 <i>Kepler</i> Telescope	25
1.2.4 Photometric Contamination	27
1.2.5 The Need For High-resolution Follow-up Observations	28
1.3 Overview of Contents	41
1.3.1 Other Research	41
2 ROBO-SOAR: SOUTHERN ROBOTIC NGS-AO	44
2.1 System Capabilities	44
2.2 Optical Design	45
2.2.1 Software Design	47
2.3 Dual Knife-edge WFS	48

2.3.1	Wavefront Sensor Prototype	52
2.4	Conclusions	53
3	THE ROBO-AO COOL SUBDWARF SURVEY	54
3.1	Cool Subdwarfs	54
3.1.1	Stellar Multiplicity	55
3.1.2	Cool Subdwarf Multiplicity	57
3.2	Survey Targets and Observations	59
3.2.1	Sample Selection	59
3.2.2	Observations	61
3.3	Data Reduction and Analysis	63
3.3.1	Robo-AO Imaging	63
3.3.2	Previously Detected Binaries	68
3.3.3	Goodman Spectroscopy	69
3.3.4	Candidate Companion Follow-ups	71
3.4	Discoveries	72
3.4.1	Probability of Association	74
3.4.2	Photometric Parallaxes	75
3.5	Discussion	76
3.5.1	Comparison to Main-Sequence Dwarfs	76
3.5.2	Binarity and Metallicity	77
3.6	Conclusions	80
4	THE ROBO-AO KEPLER SURVEY	81
4.1	Survey Targets and Observations	83
4.1.1	Observations	83
4.2	Data Reduction	87

4.2.1	Imaging Pipeline	87
4.2.2	Target Verification	87
4.2.3	PSF Subtraction	88
4.2.4	Companion Detection	89
4.2.5	Imaging Performance Metrics	91
4.2.6	Nearby Star Properties	92
4.3	Discoveries	93
4.3.1	Comparison to Other Surveys	94
4.3.2	Multiplicity and Other Surveys	97
4.4	Stellar Multiplicity and <i>Kepler</i> Planet Candidates	99
4.4.1	Stellar Multiplicity and KOI Number	99
4.4.2	Stellar Multiplicity and Multiple-planet Systems	101
4.4.3	Stellar Multiplicity and Close-in Planets	102
4.5	Conclusion	107
5	CUMULATIVE STATISTICS AND CORRECTED PLANETARY RADII FROM THE ROBO-AO KEPLER SURVEY	108
5.1	Cumulative Survey Targets and Observations	108
5.1.1	Observations	108
5.2	Data Reduction	110
5.3	Discoveries and analysis	111
5.3.1	Robo-AO KOI Survey Cumulative Statistics	111
5.3.2	Implications for <i>Kepler</i> Planet Candidates	113
5.3.3	Rocky, Habitable Zone Candidates	119
5.3.4	High-order KOI multiples	120
5.4	Conclusions	133

6 STELLAR BINARITY AND PLANETARY SYSTEMS	134
6.1 Observations	134
6.2 Stellar Characterization	135
6.2.1 Photometric Analysis	135
6.2.2 Galactic Stellar Model Simulations	138
6.2.3 Expected Giant Star Contamination	139
6.2.4 Galactic Latitude and Stellar Density	141
6.3 Stellar Binarity and Planetary Systems	142
6.4 Conclusions	152
7 CONCLUSIONS & OUTLOOK	155
7.1 Robo-SOAR	155
7.2 Cool Subdwarf Multiplicity	156
7.3 Robo-AO KOI Survey	156
7.4 Future Outlook	157
7.4.1 Rapid TESS follow-ups	157
7.4.2 Planetary host star identification	158
7.4.3 Lucky imaging	159
7.5 Final Thoughts	159
Appendix A Properties of Detected Nearby Stars to Cool Subdwarfs . . .	161
Appendix B Properties of Detected Nearby Stars to KOIs	164
Appendix C Keck-AO Observations of <i>Kepler</i> Planetary Candidates . . .	178
Appendix D Updated <i>Kepler</i> Planetary Candidate Radii	182
Appendix E Characterization of Multi-band Imaged KOI Systems	201

Appendix F Cutouts of KOIs with Nearby Stars Observed with Robo-AO	207
BIBLIOGRAPHY	228

LIST OF FIGURES

1.1	Illustration of atmospheric turbulence	3
1.2	Example of atmospheric seeing	4
1.3	Schematic of AO system	5
1.4	Schematic of a Shack-Hartmann WFS	7
1.5	Schematic of a Pyramid WFS	8
1.6	LBT pyramid	10
1.7	Overhead times of LGS-AO on Keck	11
1.8	Robo-AO mounted in Palomar	12
1.9	Schematic of Robo-AO	14
1.10	Robo-AO observations at Palomar	14
1.11	Cumulative exoplanet discoveries	16
1.12	Properties of detected exoplanets	17
1.13	Example of the radial velocity method	18
1.14	Example of the directly imaged planet	20
1.15	Example of planet detected with microlensing	21
1.16	Illustration of the transit method	23
1.17	Observed transit of WASP-25b	24
1.18	The <i>Kepler</i> telescope	25
1.19	<i>Kepler</i> rocky habitable zone planets	26
1.20	<i>Kepler</i> resolution compared to Robo-AO	27
1.21	Follow-up scenarios for KOIs	28
1.22	Illustration of dilution of transit depth due to a nearby star	30
1.23	Correction to planetary radius	31
1.24	Mass-radius plot of exoplanets	33
1.25	False positive KOI scenarios	35

1.26	Odd-even false positive test	36
1.27	Centroid false positive test	37
1.28	Secondary eclipse false positive test	38
1.29	Ephemeris matching false positive test	40
2.1	Simulated planets discovered by TESS	45
2.2	Performance simulations of Robo-SOAR	46
2.3	Robo-SOAR schematic of major components	46
2.4	Robo-SOAR optomechanical design	49
2.5	Rendering of dual knife-edge WFS	50
2.6	Prototype dual knife-edge wavefront sensor	52
2.7	Robo-SOAR testbed	53
3.1	Cool Subdwarfs HR diagram	56
3.2	Dwarf multiplicity as a function of stellar mass	57
3.3	Reduced proper motion diagram of rNLTT	59
3.4	Properties of observed cool subdwarfs	60
3.5	Example of PSF subtraction on cool subdwarfs	64
3.6	Example of cool subdwarf spectra	66
3.7	Keck-AO image of cool subdwarf confirming Robo-AO detection	70
3.8	Comparison of companions to M-dwarfs and subdwarfs	71
3.9	Properties of Keck confirmed subdwarf companions	72
3.10	Cutouts of close subdwarf companions	73
3.11	Binary fraction of cool subdwarfs as a function of color	74
3.12	Comparison of companion contrasts between M-dwarfs and subdwarfs	76
3.13	Comparison of separations of companions to M-dwarfs and subdwarfs	78
4.1	Properties of KOIs observed in the Robo-AO KOI survey	83
4.2	On-sky positions of targeted KOIs	86
4.3	PSF subtraction example	90

4.4	Cutouts of observations of KOIs with Keck	95
4.5	Cutouts of observations of KOIs with Gemini North	97
4.6	Multiplicity fraction as a function of KOI number	100
4.7	Nearby star fraction as a function of effective temperature	101
4.8	Nearby star fraction of single and multiple planet systems	103
4.9	Nearby star fraction of KOIs as a function of period and size	104
4.10	Nearby star fraction of likely bound KOIs as a function of period and size	105
4.11	Multiplicity fraction of four planetary populations	105
4.12	Likely bound multiplicity fraction of four planetary populations	106
4.13	Multiplicity fraction as a function of orbital semi-major axis	107
5.1	Properties of KOIs observed with Robo-AO	109
5.2	LP600 passband	111
5.3	Properties of detected nearby stars to KOIs	112
5.4	KOI nearby star fraction as a function of separation	115
5.5	Keck-AO imaging of KOI-3214	125
5.6	Archival images of KOI-3214	125
5.7	Keck-AO imaging of KOI-3463	127
5.8	Archival images of KOI-3463	127
5.9	Keck-AO imaging of KOI-4495	129
5.10	Archival images of KOI-4495	130
5.11	Keck-AO imaging of KOI-5327	131
5.12	Archival images of KOI-5327	131
5.13	Keck-AO imaging of KOI-6800	132
5.14	Archival images of KOI-6800	133
6.1	Observational evidence for KOI association	137
6.2	Simulated Robo-AO KOI survey	139
6.3	Probability of association density map	140

6.4	Observed stellar densities in <i>Kepler</i> field	142
6.5	Location on the sky of KOIs with nearby stars	143
6.6	Nearby star fraction as a function of KOI number	145
6.7	Nearby star fraction as a function of Teff	146
6.8	Nearby star fraction as a function of Teff (CKS)	146
6.9	Nearby star fraction of single and multi-planet systems	148
6.10	Nearby star fraction as a function of planet size and period	151
6.11	Nearby star fraction and stellar metallicity	153
7.1	Simulated planets discovered by TESS	157
7.2	Example of lucky imaging	159
7.3	Publications by LGS-AO system	160
C.1	Cutouts of KOIs with nearby stars observed with Keck-AO	180
C.2	Cutouts of KOIs with nearby stars observed with Keck-AO	181
F.1	Cutouts of KOIs with nearby stars observed with Robo-AO	208
F.2	Cutouts of KOIs with nearby stars observed with Robo-AO	209
F.3	Cutouts of KOIs with nearby stars observed with Robo-AO	210
F.4	Cutouts of KOIs with nearby stars observed with Robo-AO	211
F.5	Cutouts of KOIs with nearby stars observed with Robo-AO	212
F.6	Cutouts of KOIs with nearby stars observed with Robo-AO	213
F.7	Cutouts of KOIs with nearby stars observed with Robo-AO	214
F.8	Cutouts of KOIs with nearby stars observed with Robo-AO	215
F.9	Cutouts of KOIs with nearby stars observed with Robo-AO	216
F.10	Cutouts of KOIs with nearby stars observed with Robo-AO	217

LIST OF TABLES

3.1	The specifications of the Robo-AO subdwarf survey	62
3.2	Full SOAR Spectroscopic Observation List	67
3.3	Keck-AO Cool Subdwarf Observations	69
4.1	The specifications of the Robo-AO KOI survey	85
4.2	Full Keck-AO Observation List	94
4.3	Full Gemini Observation List	95
5.1	The specifications of the Robo-AO KOI survey	110
5.2	Robo-AO KOI Survey Cumulative Nearby Star Fraction Rates	114
5.3	Nearby Star Fraction Rates By Planet Candidate Type	114
5.4	Planetary Candidates Likely Not Rocky Due to Nearby Stars	117
5.5	High-order multiple KOIs resolved using Keck-AO	122
5.6	Photometric distance estimates of high-order multiple KOIs	123
5.7	Corrected radii of planetary candidates in potential high-order multiple systems	124
A.1	Multiple subdwarf systems resolved using Robo-AO	162
B.1	Measured properties of detected nearby stars to KOIs	164
C.1	Keck-AO KOI Observation List and Detected Companions	178
D.1	Updated <i>Kepler</i> Planetary Candidate Radii	182
E.1	Photometric parallax estimates of KOIs and nearby stars	202

LIST OF ABBREVIATIONS AND SYMBOLS

AO	Adaptive Optics
CCD	Charge-coupled Device
CKS	California <i>Kepler</i> Survey
DM	Deformable Mirror
DSS	Digital Sky Survey
FWHM	Full Width Half Max
KOI	<i>Kepler</i> Input Catalog
KOI	<i>Kepler</i> Object of Interest
LGS-AO	Laser Guidestar Adaptive Optics
$\log g$	log of the surface gravity (cm s^{-2})
NGS-AO	Natural Guidestar Adaptive Optics
NIR	Near Infrared
NLTT	New Luyten Two-Tenths catalog
OAP	Off-Axis Parabolic mirror
PM	Proper Motion
PRF	Pixel Response Function
PSF	Point Spread Function
PWFS	Pyramid Wavefront Sensor
RPM	Reduced Proper Motion
SDSS	Sloan Digital Sky Survey
SED	Spectral Energy Distribution
T_{eff}	Effective Temperature
UKIDSS	UKIRT Infared Deep Sky Survey
UKIRT	United Kingdom Infrared Telescope
WFS	Wavefront Sensor

CHAPTER 1: INTRODUCTION

Space, it says, is big. Really big. You just wont believe how vastly, hugely, mindbogglingly big it is. I mean, you may think its a long way down the road to the chemists, but thats just peanuts to space.

— *The Hitchhiker’s Guide to the Galaxy*

In the last decade, astronomy has entered an era of large surveys and big data. The emergence of inexpensive detectors and robotic telescopes have contributed to the advent of wide-field surveys in both space and on the ground that deliver a plethora of discoveries. Some of these surveys, such as the Evryscope (Law et al., 2015), observe tens of millions of stars continuously throughout a night. They are able to detect a single star brighten or dim over the span of a few minutes. Others, such as *Kepler*, are adept at observing fewer stars but with high photometric precision, searching for a periodic signal consistent with an exoplanet.

To understand the discoveries of these surveys often requires further follow-up observations and careful analysis. In particular, high-resolution imaging is needed to identify the source of the signal and characterize the source. These observations are required to confirm and characterize the thousands of exoplanet candidates discovered with *Kepler*, as hundreds of unknown nearby stars can be found within 1” of the host star, undetectable without correction for atmospheric turbulence. Planets in these systems are much larger than previously estimated due to this contamination, and many systems host no planets at all, with the detected signal emanating from some other astrophysical phenomena.

The sheer number of observations necessary to validate these planets dwarfs the observing resources available on conventional systems. We must turn to new, innovative instruments and methods to perform these studies.

This thesis presents the use of robotic adaptive optics to study exoplanets and stellar populations. The unparalleled efficiency provided by automated instruments are proving themselves vital in the current era of astronomy. I used the robotic instrument, Robo-AO, to provide the high-resolution images needed to understand the properties of thousands of planetary candidates. I also present a study into the multiplicity of cool subdwarfs, remnants of the first stars formed in the galaxy. I also present the design and construction of a new robotic instrument, Robo-SOAR, an NGS-AO system to be mounted on the SOAR telescope.

In this introduction, I first describe the design of adaptive optics and the Robo-AO system. I conclude with an overview of the state of the exoplanet field, the *Kepler* spacecraft, and the role of ground-based follow-up observations.

1.1 Automated Adaptive Optics

1.1.1 Adaptive Optics

Atmospheric Seeing

Adaptive optics (AO) is a method to remove wavefront aberrations in light from astrophysical sources caused by turbulent inhomogeneities in the Earth's atmosphere, as illustrated in Figure 1.1. These turbulent layers have different temperatures and wind velocities, leading to slightly different indices of refraction. An incoming plane wave will be distorted as it moves through these different regions in the atmosphere. The turbulence in the atmosphere is usually characterized by a measure of the atmospheric correlation length, the Fried parameter (Fried, 1967), or r_0 .

The resulting corrugated wavefronts turns images of point sources, such as stars, into speckle patterns that vary on the order of a 100 times a second. Long exposures of these speckle patterns result in a blurred disc (see Figure 1.2). The full angular width of this disc at half maximum (FWHM) is the atmospheric seeing and is equal to λ/r_0 , where λ is the wavelength of light. The Fried parameter is wavelength dependent ($r_0 \propto \lambda^{6/5}$), and thus the

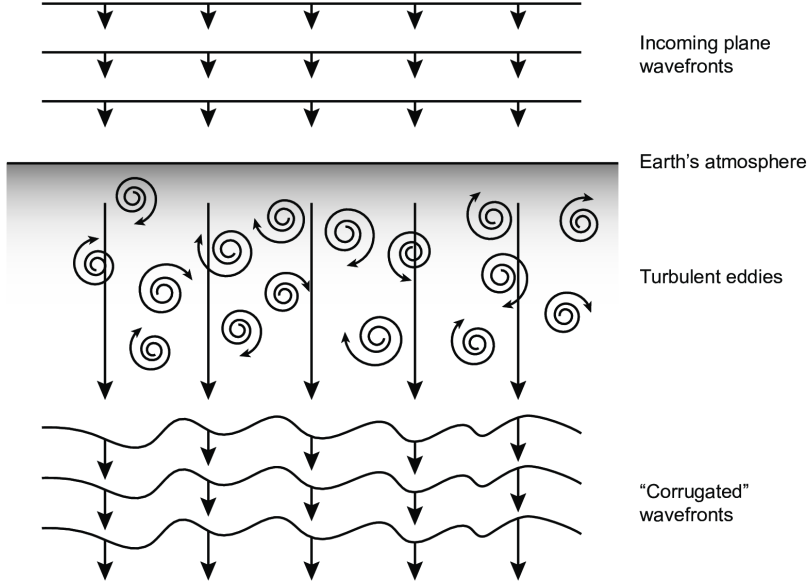


Figure 1.1: In this illustration, light from an astrophysical object consisting of initially plane wavefronts is perturbed when entering the atmosphere by turbulent layers, resulting in corrugated wavefronts at the ground. [Image courtesy of D. Buscher]

seeing disk scales with $\lambda^{-1/5}$, i.e. seeing improves at longer wavelengths.

At excellent observing sites, seeing is typically on the order of an arcsecond. Consequently, while large telescopes have theoretically sub-arcsecond resolution limited only by diffraction, they will in practice have a resolution equal to the atmospheric seeing. A survey of exoplanet candidate hosts with seeing-limited resolution would not detect the majority of previously unknown nearby stars contaminating the photometry.

Basic Design

To correct these wavefront distortions, light from the telescope can be fed through an adaptive optics system before being imaged. A basic schematic of an AO system is shown in Figure 1.3. The aberrated wavefronts enter as a focused beam from the telescope. An off-axis parabolic mirror (OAP) collimates the light and directs it towards a deformable mirror (DM) located conjugate to the telescope pupil. The DM uses actuators to adjust the shape of the mirror to correct high-order phase distortions in the incoming wavefront. A

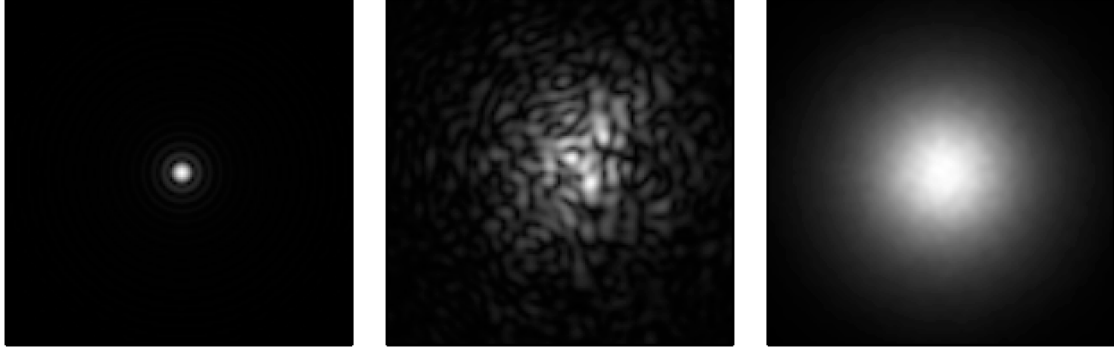


Figure 1.2: From the left, simulated images of a point source of light seen through a diffraction-limited telescope of diameter d , a short exposure of the point source through the same telescope and with atmospheric seeing with a Fried parameter given by $r_0 = 0.1d$, and seen in a long exposure with the same telescope and seeing, revealing the seeing disc.

tip-tilt mirror, a mirror which can move in two directions, is positioned earlier in the optical path and used to correct low-order wavefront errors. After reflecting off the DM, the light is refocused with a second OAP. The light is split using a beamsplitter either before or after this second OAP. Some of the light is sent to the science detector and used to image the target. The rest of the light, typically wavelengths not required for the science, is sent to a wavefront sensor.

The performance of adaptive optics can be quantified with the Strehl ratio, defined as the ratio of the peak flux of the point spread function (PSF) measured compared to that of a diffraction-limited telescope, i.e. a perfect telescope with no turbulence. At the diffraction-limit, a telescope with a circular aperture of diameter d observing at wavelength λ has an angular resolution of $1.22\lambda/d$. Current AO systems observing in the near-infrared (NIR), such as on Keck (Wizinowich et al., 2000) and Gemini (Hodapp et al., 2003), typically achieve Strehl ratios between 0.2 and 0.4. Extreme AO systems built to directly image exoplanets, such as the Gemini Planet Imager, can reach Strehl ratios of up to 0.9 (Macintosh et al., 2014). AO systems observing in the visible, such as MagAO on Magellan (Close et al., 2014), typically have Strehl ratios of ~ 0.1 -0.2.

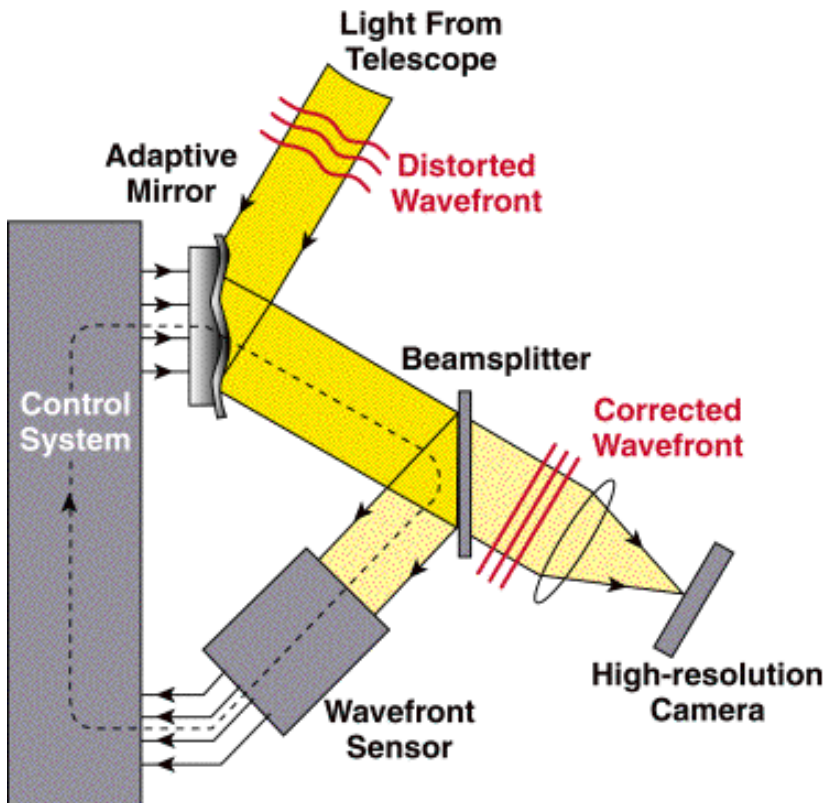


Figure 1.3: A schematic showing a basic AO system. The distorted wavefront enters the telescope, reflects off a deformable mirror which corrects high-order aberrations, and is then split by a beamsplitter. Some of the light travels to a wavefront sensor that measures the phase distortion of the wavefront. This information is then used to command the deformable mirror to take a shape that corrects the wavefront distortion. The rest of the light travels to the imaging detector. [Figure courtesy of Claire Max]

Wavefront Sensing

A wavefront sensor (WFS) is used to measure the aberrations in the wavefront. With this information, the position of the tip-tilt mirror and the DM shape can be set such that the resulting wavefront is nearly flat. In “open loop” operation, the WFS measures the wavefront before any correction has been applied. In “closed loop” operation, the wavefront error is measured by the WFS after correction by the tip-tilt mirror and DM, and the residual errors will be small.

A WFS requires a bright source, a guidestar, that can be used to measure the wavefront distortions. As the science target is often too faint to be used as a guidestar, a bright ($V < 12$) nearby star may be used, called natural guidestar AO (NGS-AO). Often, however, a sufficiently bright star will not be found nearby, resulting in NGS-AO systems having limited sky coverage (Ellerbroek & Andersen, 2008). Alternatively, an artificial guidestar created with lasers may be used, called laser guidestar AO (LGS-AO). These systems typically employ either a Rayleigh laser, which uses high-altitude backscattering from a near ultraviolet laser or a sodium laser, which uses a 589nm laser to excite a layer of sodium atoms in the upper atmosphere that originate from meteor ablation. A faint natural guidestar is typically still required for image position information, although high-order-only wavefront corrections result in significant image quality gains compared to seeing-limited imaging (Howard et al., 2018). These systems have nearly unlimited sky coverage, but the added complexity increases observing overhead time.

Two types of wavefront sensors are used in the majority of AO systems. Most common is the Shack-Hartmann WFS, which uses an array of lenses, called lenslets, of the same focal length. The aberrated wavefront enters the lenslet array and each lens images a small part of the aperture, forming multiple images of the reference star on the detector. If the incoming wavefront is plane, the imaged reference star will form a regular grid defined by the lenslet array geometry. Distortions in the wavefront, however, will displace the images from their nominal positions (see Figure 1.4). The shape of the distorted wavefront can

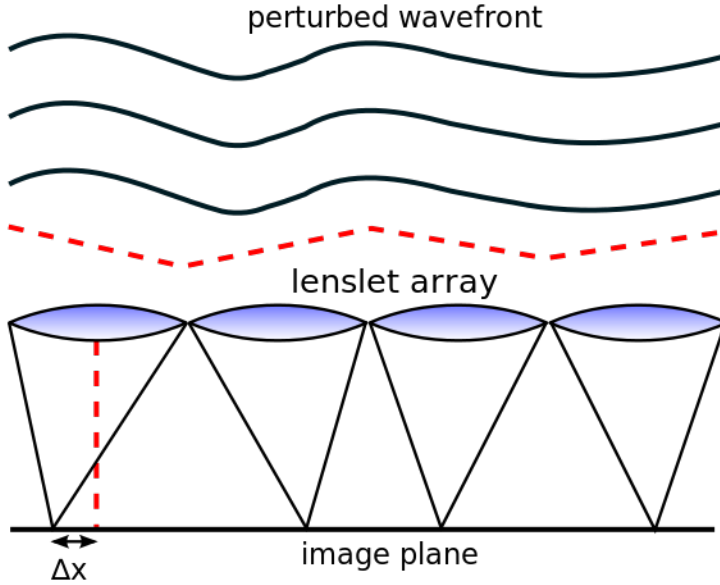


Figure 1.4: A schematic of a Shack-Hartmann WFS. The distorted wavefront is incident on the lenslet array. The position of the imaged source is displaced slightly from the nominal position due to aberrations in the wavefront. [Figure courtesy of Wikipedia Commons]

then be reconstructed from the displacement of these images. Shack-Hartmann WFS are relatively inexpensive and simple devices. They require a relatively bright reference star as the pupil is re-imaged into, in some systems, hundreds of sub-pupils, each required to be sufficiently bright to measure the incoming wavefront slope. When used in NGS-AO system, this requirement greatly limits the sky coverage possible with AO correction.

An alternative is the pyramid wavefront sensor (PWFS), illustrated in Figure 1.5. Conceived in the mid-1990s (Ragazzoni, 1996) and, due to high manufacturing cost, only used in a few instruments, such as ALFA (Kasper et al., 2000) and LBT-AO (Esposito et al., 2011), the PWFS uses a pyramidal glass prism placed at the focus of the distorted wavefront. The incoming beam is split into four by the pyramid quadrants. Each beam is deflected slightly by the pyramid, and a relay lens images the four beams into four images of the telescope pupil on a single CCD. Each sub-aperture is detected by four separate CCD pixels, and the number of sub-apertures may be as many as the number of pixels covered in a single pupil image on the detector.

If a plane wave is incident on the PWFS, the four pupils will be equally illuminated. If

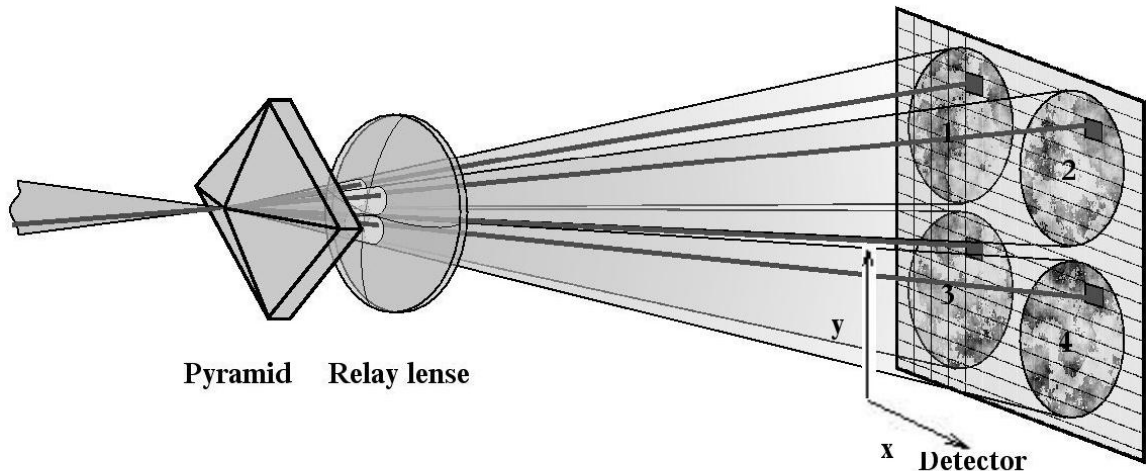


Figure 1.5: A schematic of a Pyramid WFS. The distorted wavefront is focused onto the glass pyramid. The incoming beam is split by the four quadrants of the pyramid, and a relay lens forms four images of the telescope pupil on the detector. Each sub-aperture is therefore detected by four pixels on the CCD. [Figure courtesy of S. Egner]

the wavefront is distorted, the slope of the incoming waveform will alter which quadrant of the pyramid it passes through, and the pupils will be differentially illuminated. To improve linearity (i.e. be able to detect very small wavefront aberrations), the focused beam is often modulated in a circular pattern around the pyramid apex (Fauvarque et al., 2015). The slope of the incoming wavefront at any sub-aperture can be calculated from the intensity in four corresponding pixels in each pupil image. If these intensities are given by S_1 , S_2 , S_3 , and S_4 (corresponding to the pupils imaged in Figure 1.5), the slopes of the wavefront, W , in that sub-aperture in the x- and y-direction are given by the relations

$$\frac{\delta W}{\delta x} = \delta\theta_x \frac{(S_1 + S_3) - (S_2 + S_4)}{S_1 + S_2 + S_3 + S_4} \quad (1.1.1)$$

$$\frac{\delta W}{\delta y} = \delta\theta_y \frac{(S_1 + S_2) - (S_3 + S_4)}{S_1 + S_2 + S_3 + S_4} \quad (1.1.2)$$

where θ_x and θ_y is the amplitude of modulation in the x- and y-directions.

The PWFS allows considerable optimization for observations with low-brightness reference stars. Since the sub-apertures are set by the pixels on the detector, dynamic binning of these pixels can perform lower-order wavefront corrections even with faint reference stars. In addition, the frequency and amplitude of modulation may be adjusted to increase the performance of the system. This greatly increases the sky coverage where some level of AO corrections may be applied.

The manufacturing of the pyramids, such as the for the AO system on the Large Binocular Telescope (LBT) as shown in Figure 1.6, is prohibitively expensive for an instrument on a moderately sized telescope. The final position of the pupils on the CCD and the wavefront sensing requirements of a high-order AO system demand stringent constraints on the angles of each quadrant and the sharpness of the edges and vertex (Ghigo et al., 2003). In addition, to increase the light available from a natural guidestar for wavefront sensing, often a wide range of wavelengths is used. When this “white” light is passed through the glass pyramid,

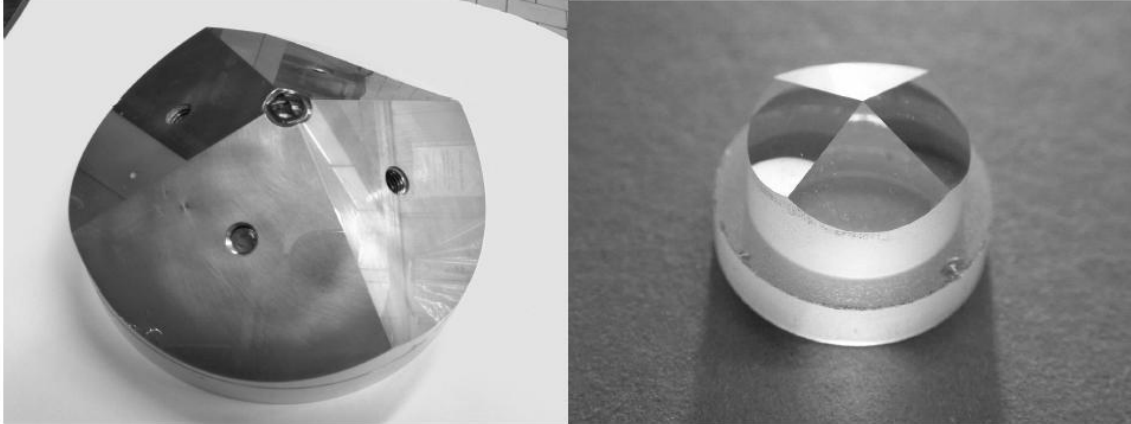


Figure 1.6: On the right, the input pyramid for the Large Binocular Telescope with diameter 13mm. On the left, the aluminum “mother pyramid” used in manufacturing, with the glass pyramid at its vertex. [Image courtesy of A. Tozzi]

significant chromatic aberrations arise in the pupil image. This is caused by the wavelength dependence of the refractive index of the glass. The pupil drift at the blue and red extremes can be as much as several CCD pixels. To reduce these aberrations, achromatic double pyramids are typically used (Tozzi et al., 2008), further increasing the potential cost.

In Chapter 2, I describe the design and construction of a reflective pyramid WFS design, costing substantially less than glass optics with reduced chromatic aberrations in the output pupil images.

1.1.2 Robo-AO

Current wide-field surveys such as Evryscope (Law et al., 2015), *Kepler* (Borucki et al., 2010), Zwicky Transient Factory (Terziv et al., 2013), and Pan-STARRS (Chambers et al., 2016) discover thousands of interesting transient events every year, such as supernovae, as well as detected several thousand planetary candidates in the past decade. For many science goals, such as precision photometry and spectroscopy, time-sensitive high-angular resolution imaging is required to understand the environment from which the transient emanates. The number of targets that require these rapid follow-ups overwhelms conventional high-resolution instruments, such as adaptive optics, and this will only increase in the coming

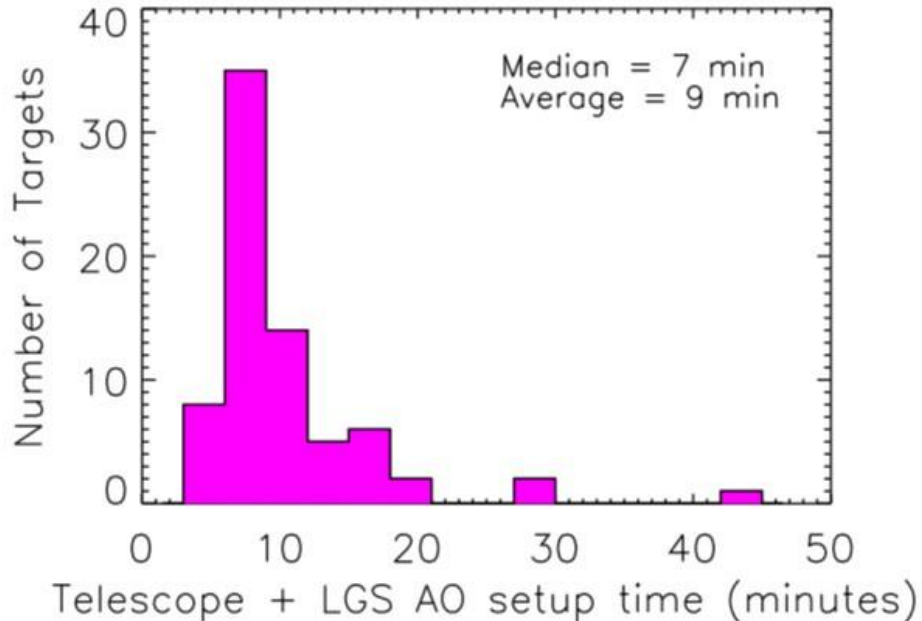


Figure 1.7: The acquisition times for the LGS-AO system on Keck. The acquisition time includes all telescope and AO overheads, including slews. The average overhead for this conventional AO system of 9 minutes is substantially longer than the 40 seconds of Robo-AO. [Image courtesy of David Le Mignant]

years with new surveys coming online, such as TESS (Ricker et al., 2014) and LSST (Tyson, 2002).

Automation of adaptive optics can vastly increase observing efficiency, resulting in an order-of-magnitude increase in the number of targets that can potentially be observed in a night. Robo-AO (Baranec et al., 2013) was conceived as a fully autonomous LGS-AO system for a small size telescope in 2009. Mounted originally on the Palomar 1.5-m telescope (see Figure 1.8), the high-order AO loop of Robo-AO was closed in 2011. Science observations began shortly thereafter, with initial AO setup overhead times of approximately 60 seconds. Further optimization in software reduced total overhead times to less than 40 seconds by 2015. Conventional systems, such as the LGS-AO system on Keck, have overhead times approximately an order-of-magnitude longer than this (see Figure 1.7).

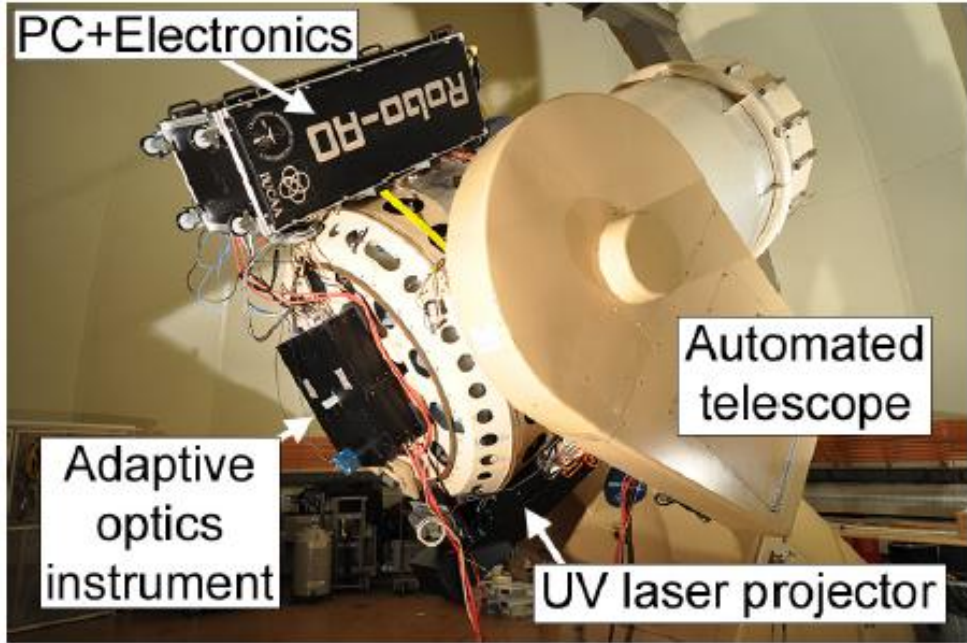


Figure 1.8: Robo-AO mounted on the automated 1.5-m telescope at Palomar Observatory.
[Image courtesy of Christoph Baranec]

Robo-AO Instrumentation

The optical design of Robo-AO is shown in Figure 1.9. Robo-AO uses a laser guidestar as a reference for the wavefront sensor. The laser consists of a pulsed, 12 Watt, 355-nanometer ultraviolet beam along the telescope line-of-sight. The ultraviolet laser is not visible to the human eye and does not produce biologically hazardous radiation levels during momentary exposures, and thus no control measures are required to avoid illuminating passing aircraft (Baranec et al., 2014a). The beam is sampled at a distance of 10 kilometers. A Shack-Hartmann wavefront sensor cycles at 1.2 kHz and feeds information to a computer driving the MEMS actuator system adapting the shape of a deformable mirror. An Andor iXon EMCCD science camera records images at 8.6 Hz. Tip-tilt errors are corrected in software using these short time frames. The EMCCD reduces the read noise from approximately $50e^-$ to $< 1e^-$, with typical EM-gains between 25 and $300\times$. The raw data is stored as frames of 1024×1024 pixels in FITS datacubes.

Robo-AO Observations

The observing sequence for a single target, described in detail in Baranec et al. (2014a), begins with a queue scheduling program that optimizes among scientific priority, slew time, telescope limits, prior observing attempts, and laser-satellite avoidance windows. The science camera, laser, and adaptive optics system are configured as the telescope slews, typically taking 40 seconds. Once pointed at the new target, the laser is acquired with a search algorithm moving a steering mirror. This process takes approximately 40 seconds, during which time the adaptive optics system is started and an observation is performed with no adaptive optics correction to estimate seeing conditions. Once the laser is acquired, the adaptive optics correction is started, removing residual atmospheric wavefront aberrations at 100Hz using a 12×12 actuator deformable mirror. The science field is imaged at 8.6Hz and saved in data cubes for later processing.

At Palomar, Robo-AO performed over 19,000 observations (see Figure 1.10), including the majority of the KOI observations, detailed in Chapter 4. In 2015, Robo-AO relocated to the Kitt Peak 2.1-m telescope for a 3-year deployment (Jensen-Clem et al., 2017). A near-infrared avalanche photodiode array camera was added to the system, enabling simultaneous visible and infrared imaging.

We describe in Chapter 2 the design and construction of Robo-SOAR, an NGS-AO analog to Robo-AO, that will observe in the South and bring automated high-resolution imaging to the entire sky.

1.2 Exoplanet Confirmation and Characterization

Two questions have persisted throughout human history: where did we come from? And, are we alone? We now have technology that is sufficiently advanced to begin to provide answers to these questions.

Until the early 1990s, the only known planets existed in a single system orbited the

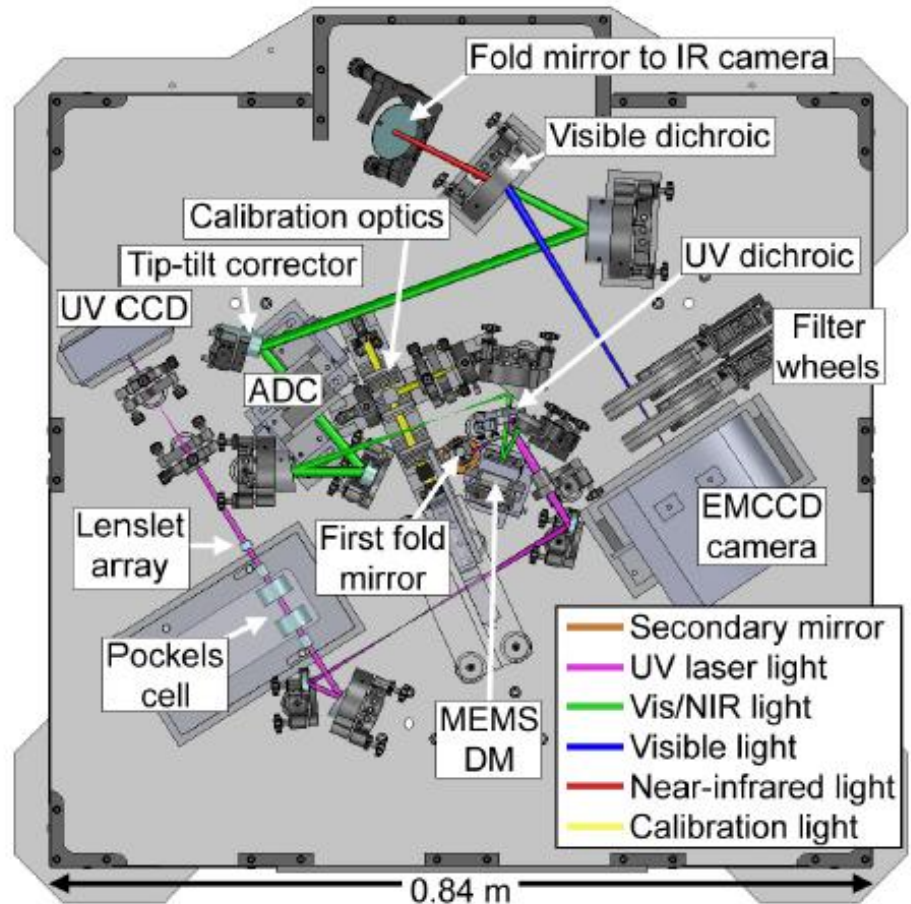


Figure 1.9: The optical design of Robo-AO. (Baranec et al., 2014a)

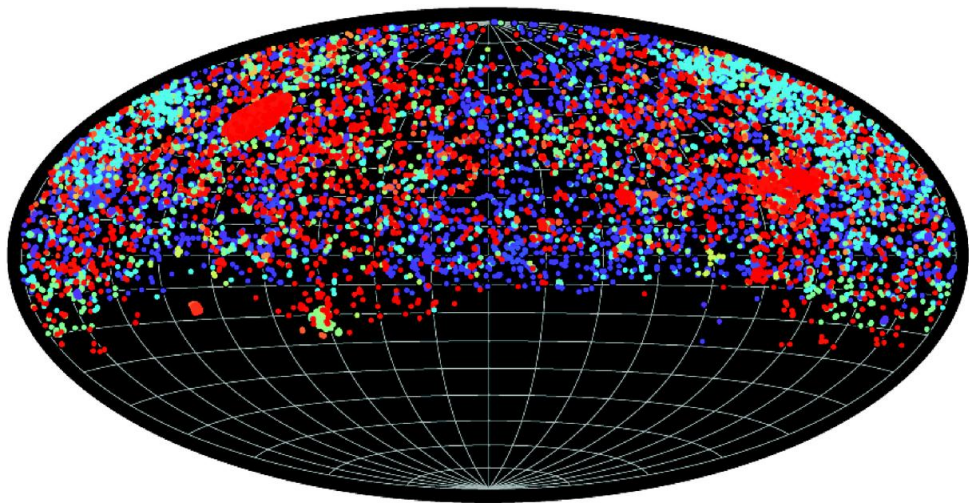


Figure 1.10: On-sky locations of the nearly 19,000 AO observations performed by Robo-AO at Palomar Observatory. Colorization is different science projects. The *Kepler* field, observed in the Robo-AO KOI survey (Chapter 4), is seen in the top left. [Image courtesy of Nicholas Law]

Sun. In only the last few decades, we have discovered thousands of other planetary systems¹ around other stars. A planet has even been detected around the nearest star (Anglada-Escudé et al., 2016). Planets, it seems, are common in the galaxy and planetary systems similar to our own are not unusual.

The most probable scenario, as far as is known, for life to exist in the galaxy is on rocky exoplanets or exomoons, warmed sufficiently by starlight or internal processes for liquid water, or alternative solvent (Schulze-Makuch et al., 2011), to subsist (Lammer et al., 2009). Studying exoplanets provides insight into the prevalence of Earth-like planets, and concurrently life, in the galaxy. Current observational resources are capable of detecting these planets and measuring the planetary radii and mass, leading to estimates of the planetary bulk densities and compositions. Future telescopes, such as the new generation of extremely large telescopes and the James Webb Space Telescope (Greene et al., 2016), will be capable in the next decade of detecting biosignatures in these planet's atmosphere, strong indicators for the presence of life. These observations will be time-intensive and limited, and a primary objective of current surveys is to detect and thoroughly vet excellent targets suitable for further study.

The diversity of exoplanet systems continues to defy our expectations. We have learned that gas giant planets can migrate into orbits of only a few days (Ngo et al., 2015); small planets abound and pack into tight, resonant orbits (Weiss et al., 2018); a type of planet with no solar system analog, sub-Neptunes, are common in the galaxy (Fressin et al., 2013); planets can orbit pairs of stars in binary star systems (Doyle et al., 2011); planets can orbit stellar remnants, such as neutron stars (Wolszczan & Frail, 1992). Studying the properties of detected planets such as these can provide insight into the mechanisms behind planetary formation and evolution.

The detection of exoplanets has been performed with a variety of techniques, summarized in Figures 1.11 and 1.12. We describe a few of the most successful techniques below and

¹3706 exoplanets as of March 2018, according to the NASA Exoplanet Archive.

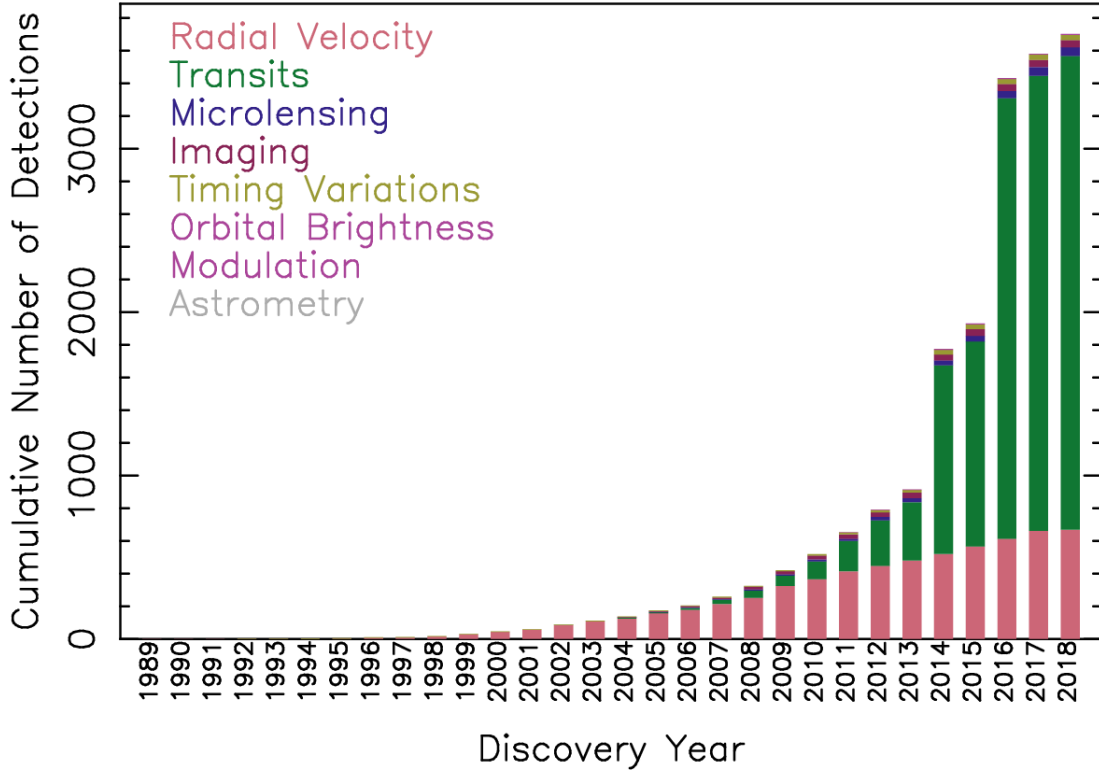


Figure 1.11: The cumulative detections of exoplanets by year and by detection technique. The radial velocity method discovered the majority of exoplanets until the discoveries by the *Kepler* telescope using the transit method were confirmed, beginning in earnest in 2013. [Image courtesy of NASA Exoplanet Archive]

note particular strengths and limitations of each.

1.2.1 Detection Techniques

Pulsar Timing Variations

The first exoplanets were detected in 1992 around a millisecond pulsar (Wolszczan & Frail, 1992). Pulsars are rapidly spinning, compact stellar remnants that emit beams of electromagnetic radiation (Pacini, 1967). The frequency of these beams as observed from Earth is very regular, even rivaling atomic clocks (Matsakis et al., 1997). The influence of planets orbiting the pulsar will introduce slight anomalies into the pulsar timing which may be used to reveal the parameters of the planetary orbit and the planetary mass.

Pulsar timing variations are sensitive to very low mass planets, down to approximately

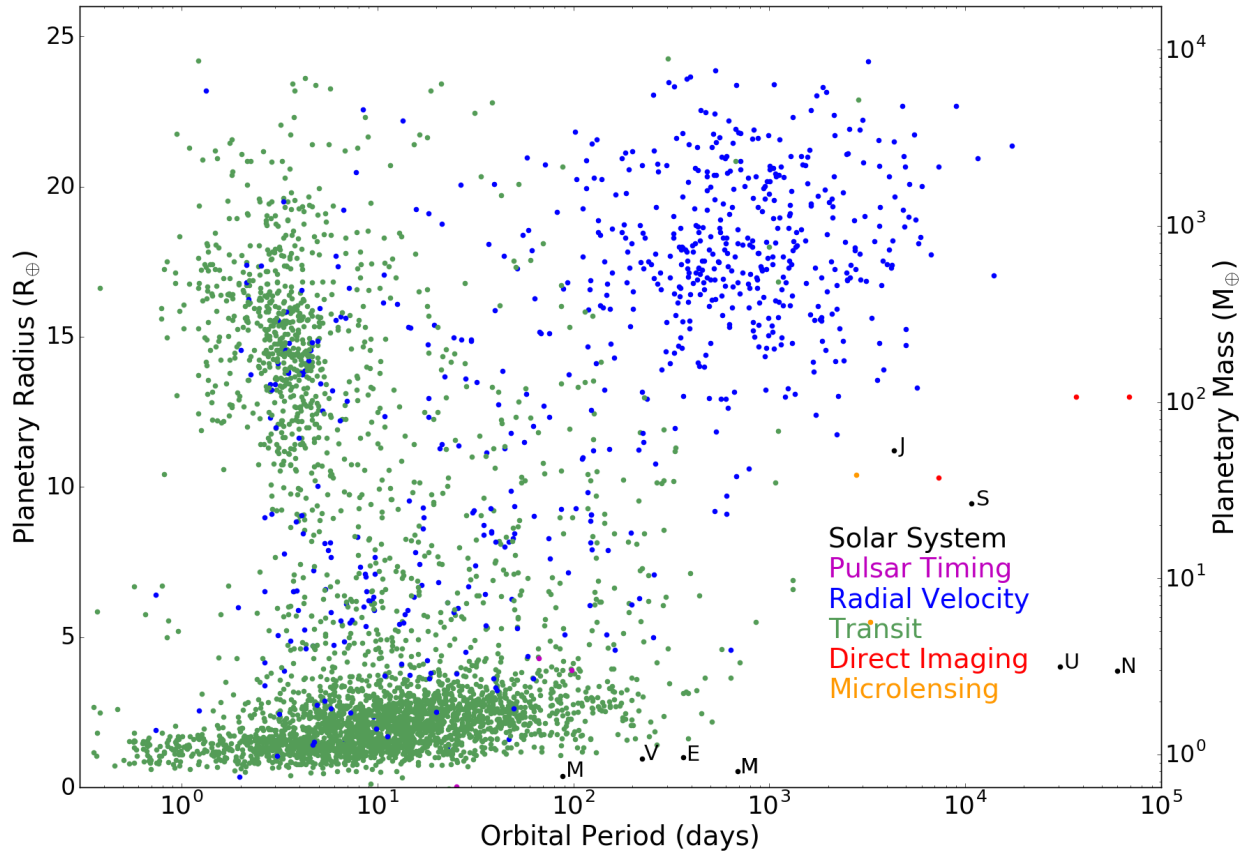


Figure 1.12: The properties of detected exoplanets colored by detection technique. Solar system planets are plotted for context. The vast majority of Earth-size exoplanets were discovered with the transit method by the *Kepler* telescope. Small planets at long-period orbits remain difficult to detect.

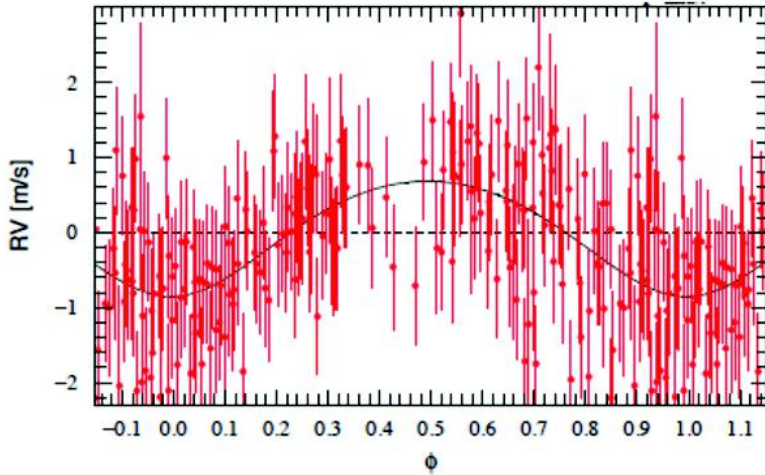


Figure 1.13: Example of a radial velocity detection of a ≥ 3.6 Earth-mass exoplanet orbiting just inside the habitable zone of the nearby K-type star, HD 85512. The velocity measurements are folded to the 58.4 day period of the planet. [Image from Pepe et al. (2011)]

0.1 Earth masses, as well as planets at long period orbits. Pulsars with orbiting planets are rare, however, and only four pulsar planetary systems have been detected to date. In recent years, variations in the timing of stellar pulsations of hot subdwarf and main-sequence stars have been used to detect several planetary candidates (Silvotti et al., 2007; Murphy et al., 2016).

Radial Velocity

The gravitational influence of an orbiting planet will induce velocity variations in the host star, typically on the order of a few meters per second. The light from the star is Doppler shifted due to these velocity variations. High-resolution spectroscopy is able to measure the line-of-sight stellar velocity using the slight shift of emission and absorption lines in the stellar spectra. With velocity measurements from observations over multiple epochs, the influence of an unseen planet on the host star can be revealed, as shown in Figure 1.13.

Radial velocity is able to place limits on a planet's minimum mass. The true planetary mass is dependent on the planet's orbital inclination. The orbital period of a planet can also be measured from the RV curve. Radial velocity is sensitive to planets at a wide-range

of orbital inclinations. Because the star-planet interaction is mediated by gravity, smaller planets result in lower stellar velocity amplitudes and are thus difficult to detect. In addition, the measurements required to detect and study a single planet are time-intensive and require a large-aperture telescope and stable, high-resolution spectrographs.

In 1995, the first exoplanet was discovered around a main-sequence star, 51 Pegasi b, using the radial velocity technique (Mayor & Queloz, 1995). This method dominated the exoplanet discovery field for over a decade and revealed many surprises, such as the existence of “hot Jupiters.” Since 2011, the number of detected exoplanets with radial velocity has declined, as telescope time has been dedicated to follow-up planets from transit surveys. New instruments in the coming years, such as NEID (Halverson et al., 2016), will be sensitive to velocity amplitudes as low as 10 cm^{-1} , consistent with an Earth-size planet orbiting at 1 AU.

Direct Imaging

The majority of exoplanets have been discovered by indirect measurements, observing their effect on more visible objects. Imaging a spatially resolved planet is an enormous challenge, as the host star emits far more light than the planet. For illustration, if a twin of our solar system were placed at 10 parsecs, Jupiter, the brightest planet, would emit only around 10^{-9} the flux of the parent star at an angular separation of $0.5''$.

Directly imaging massive, self-luminous planets is possible with boutique instruments, combining extreme adaptive optics to correct wavefront aberrations, a coronograph to reduce the intensity of light from the host star, and an integral field spectrograph to reduce speckle noise with chromatic differential imaging (Crepp et al., 2011). In addition, a large number of observing methods are used to suppress speckles, such as angular differential imaging (Sparks & Ford, 2002), statistical speckle discrimination (Labeyrie, 1995), and speckle nulling (Bordé & Traub, 2006). Current instruments, such as Gemini Planet Imager (GPI) at Gemini South (Macintosh et al., 2014) and SCExAO at Subaru (Jovanovic et al., 2015), are able to detect

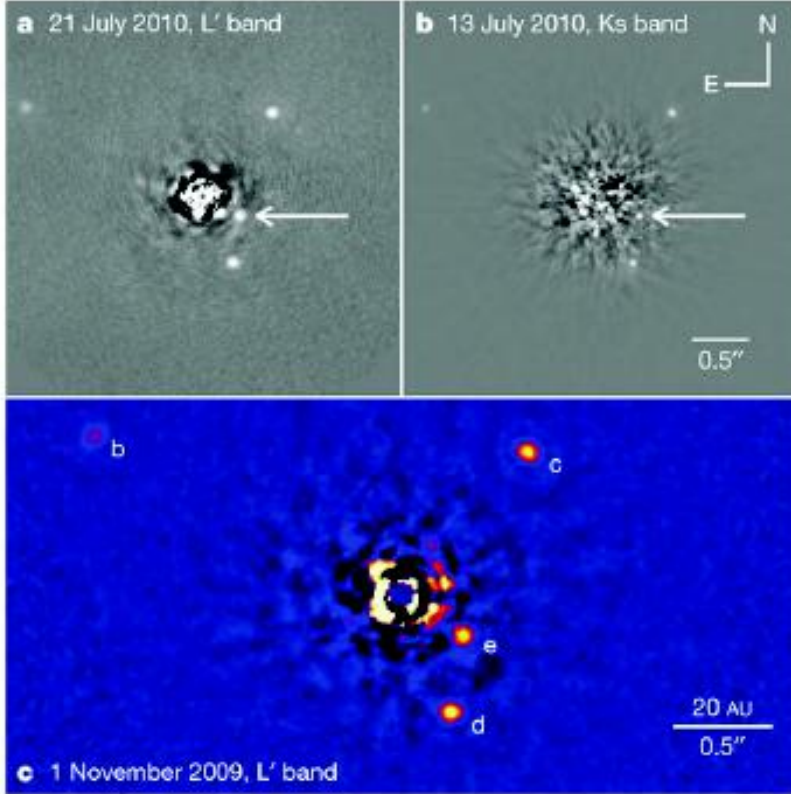


Figure 1.14: Directly imaged planets orbiting HR8799, observed in the near-infrared with Keck adaptive optics. The four planets range from 3 to 7 Jupiter masses. The light from the central star has been reduced in intensity with a coronograph. [Image from Marois et al. (2010)]

planets 10^{-5} fainter than the host star at separations of $1''$. An example of directly imaged planets is shown in Figure 1.14.

The first image of an exoplanet, the five Jupiter-mass 2M1207b which orbits a brown dwarf, came in 2004 (Chauvin et al., 2004). A total of 18 more planetary systems have been imaged in the intervening years, far fewer than was initially expected². This suggests a significant discrepancy exists between the planet mass function extrapolated from radial velocity surveys and the true giant exoplanet mass function (Bowler, 2016).

Future instruments on extremely large telescopes and the proposed coronagraphic capability for the 2.4m space-based WFIRST mission (Spergel et al., 2013) will allow imaging

²Macintosh et al. (2006) suggested that nearly 100 planets could be discovered with GPI. In the first 2.5 years of the GPI survey, one discovery has been published (Macintosh et al., 2015).

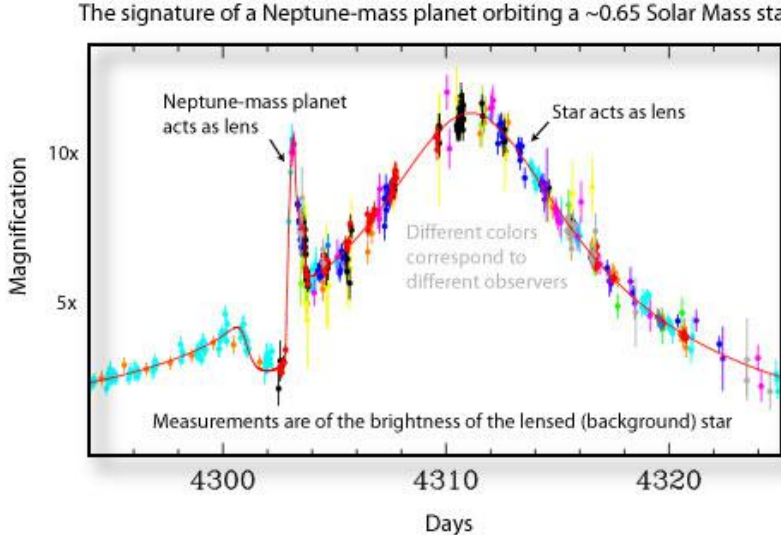


Figure 1.15: A Neptune-sized planet detected with the microlensing method. The brightness of the background star is observed. Gravity from the planet, orbiting the foreground star, contributes to the magnification of the background star. [Image from Sumi et al. (2010)]

of planets at close orbits and be sensitive to reflected starlight. At their theoretical performance limit, these instruments could even detect rocky planets in the habitable zone of nearby M-dwarfs (Guyon et al., 2012).

Microlensing

Gravitational microlensing occurs when two stars at different distances pass within ~ 1 mas of each other on the plane of the sky (Gaudi, 2012), and the gravitational field of the foreground star acts as a lens (Chwolson, 1924; Einstein, 1936). The light from the background star is then magnified, with the brightness of the star increasing over the span of a few days or weeks. If the foreground star has a planet, the gravitational field of the planet will also lens the background star, adding a detectable contribution to the lensing light curve. An example of a planet detected with microlensing is shown in Figure 1.15.

Lensing events are rare and many stars must be monitored continuously to detect planets. Most surveys observe near the galactic bulge, where the high stellar density increases the occurrence rate of microlensing events. Almost 20 microlensing planets have been published to date, primarily from the Optical Gravitational Lens Experiment (OGLE, Udalski, 2003)

and Microlensing Observations in Astrophysics (MOA, Bond et al., 2004) surveys.

Microlensing is able to detect planets at wide-orbits, low-mass planets (down to Mars-size with WFIRST), and planets around distant stars. The planetary mass can be loosely constrained from microlensing, as well as the planet's separation from the host star at the time of the lensing event. A microlensing event only happens a single time, however, and the host star is often too distant for follow-up observations, severely limiting characterization of any detected planetary system.

Astrometry

The astrometric method for detecting planets uses precise measurements of a star's position in the sky. Both components in a planet-star system orbit their mutual center of mass or barycenter. The astrometric method seeks to observe the small shift in stellar position as a star orbits the system barycenter. The variation in position is so small that ground-based telescopes, contending with the effects of atmospheric turbulence, have not yet been able to detect any planets with this method. The *Hubble Space Telescope* did use astrometry to determine the mass of a previously known planet, Gliese 876b (Benedict et al., 2002).

The *Gaia* space telescope will provide microarcsecond astrometric precision for the brightest stars, and is expected to discover approximately 20,000 long-period planets with masses between 1-15 Jupiter masses within 500 pc (Perryman et al., 2014). If extended for a 10-yr mission, the number of planet detections will more than triple.

1.2.2 Transit Method

The most successful technique in terms of planets discovered to date is the transit method, using photometry to detect the slight dip in brightness of the host star as the planet passes in front of its disk (illustrated in Figure 1.16 with an observed planetary transit shown in Figure 1.17). The depth and shape of this brightness, or transit, provides

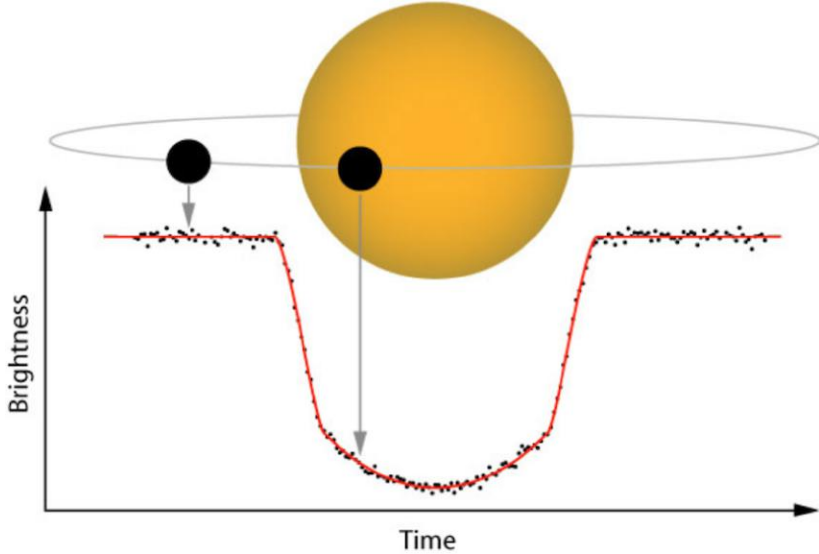


Figure 1.16: An illustration of the transit method, which detects exoplanets by looking for the small decrease in brightness of the host star as the planet orbits in front of its disk. [Image courtesy of TESS Science Team]

fundamental properties of the exoplanet. The time between successive transits provides the period of the planet. The radius of the exoplanet can be estimated from the depth of the transit or change in observed stellar flux, ΔF , using the equation

$$\frac{\Delta F}{F} = \frac{R_p^2}{R_\star^2} \quad (1.2.1)$$

where R_p is the radius of the planet and R_\star is the radius of the occulted star.

The transit method only works on the small fraction of exoplanets orbiting at inclinations which bring the planet in front of the host star (for an Earth-size planet orbiting at 1 AU, the probability of a transiting alignment is approximately 0.5%). However, the relatively large signal from a transiting planet (variations in brightness of the host star of up to several percent for giant planets) allows even small telescopes, typically observing many stars simultaneously, to detect planets at a reasonable rate.

The first transiting exoplanet, HD 209458b (Charbonneau et al., 2000), was discovered in 2000. Ground-based surveys, such as SuperWASP (Collier Cameron et al., 2007) and HATNet (Bakos et al., 2007), discovered dozens of transiting exoplanets over the coming

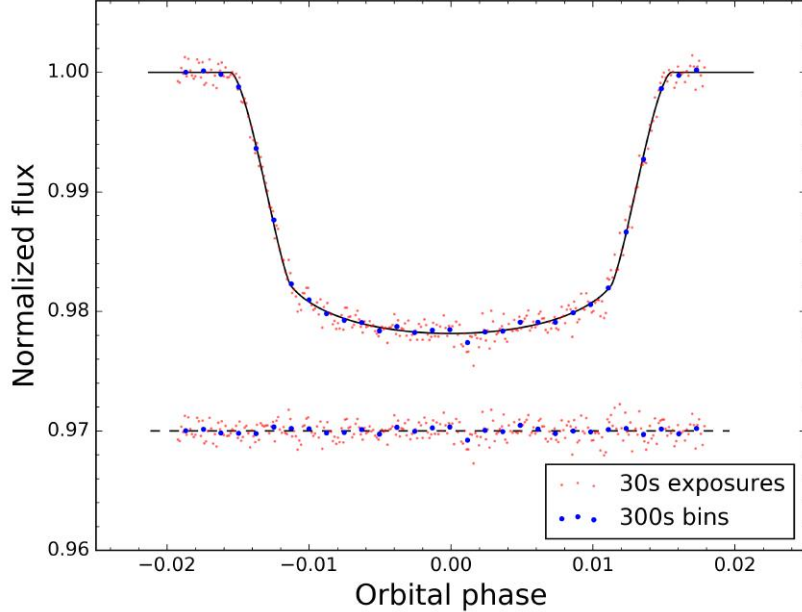


Figure 1.17: The transit of hot Jupiter, WASP-25b, as observed with the Goodman spectrograph (Clemens et al., 2004) on SOAR. The black solid line is a transit model fit with the Python package `batman` (Kreidberg, 2015). The lower dashed line shows residuals from the transit model.

decade. These discoveries were mostly gas giants orbiting at low periods, in part due to the low photometric precision (Fhring et al., 2015) achieved with small telescopes on the ground (sensitivities to flux variations of a few thousand parts per million is typical for these surveys). The inherent occurrence rate in the galaxy of Earth-like planets, i.e. rocky planets orbiting within the habitable-zone of their host star, was difficult to estimate from ground-based surveys alone. To find small planets that could maintain liquid water, exquisite photometry of thousands of stars over a multi-year baseline is required. This is only feasible with a space-based telescope.

The European Space Agency CoRoT mission (Barge et al., 2008) launched in 2006, with a primary mission of detecting terrestrial planets at low-period orbits. However, CoRoT-7b (Léger et al., 2009), with an estimated radius of $1.7R_{\oplus}$, was the only potentially rocky planet discovered. The photometric precision of the 27cm CoRoT telescope and its short 150-day observing baselines greatly limited the number of planets discovered by CoRoT (Auvergne et al., 2009).

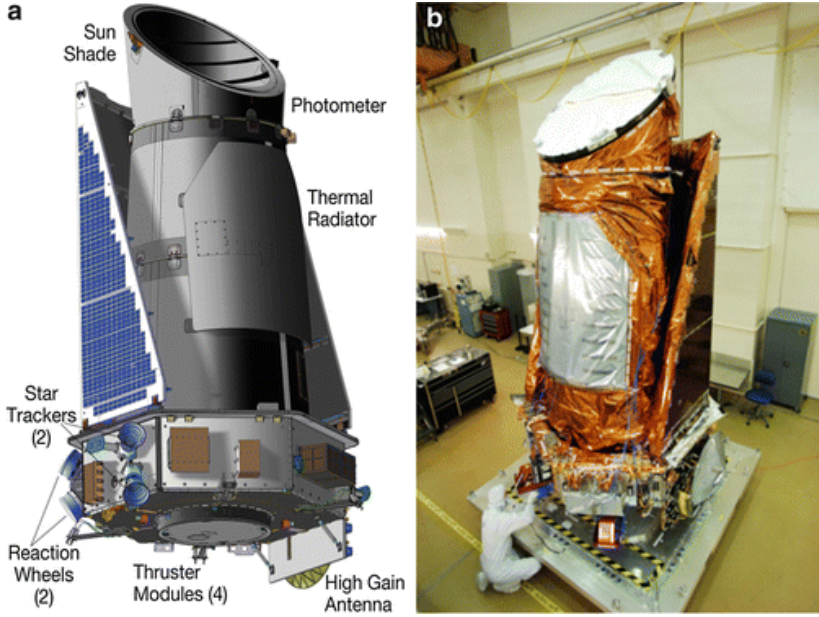


Figure 1.18: (a) A sketch of the *Kepler* telescope mated to the spacecraft. (b) The assembled flight system in a clean room with the telescope dust cover in place. The dust cover was ejected after launch. Note the person at the lower left for scale. (Courtesy of BATC)

1.2.3 *Kepler* Telescope

The *Kepler* telescope launched in 2009, and for four years observed approximately two hundred thousand stars in a 105 deg^2 field with a 1-m telescope (Caldwell et al., 2010) (shown in Figure 1.18). The sole instrument of *Kepler*, a photometer, was designed to be able to detect an Earth-sun analog system, requiring photometric precision of approximately 80 parts per million (Christiansen et al., 2012). *Kepler* has proven enormously successful, discovering more planets than every other telescope combined³, including the vast majority of terrestrial planets (see the rocky habitable-zone planets *Kepler* discovered in Figure 1.19). With the discoveries from *Kepler*, we now know that planets are ubiquitous within our galaxy (Howard et al., 2012; Burke et al., 2015).

³2649 discovered exoplanets, including 307 from the K2 mission, as of March 2018.

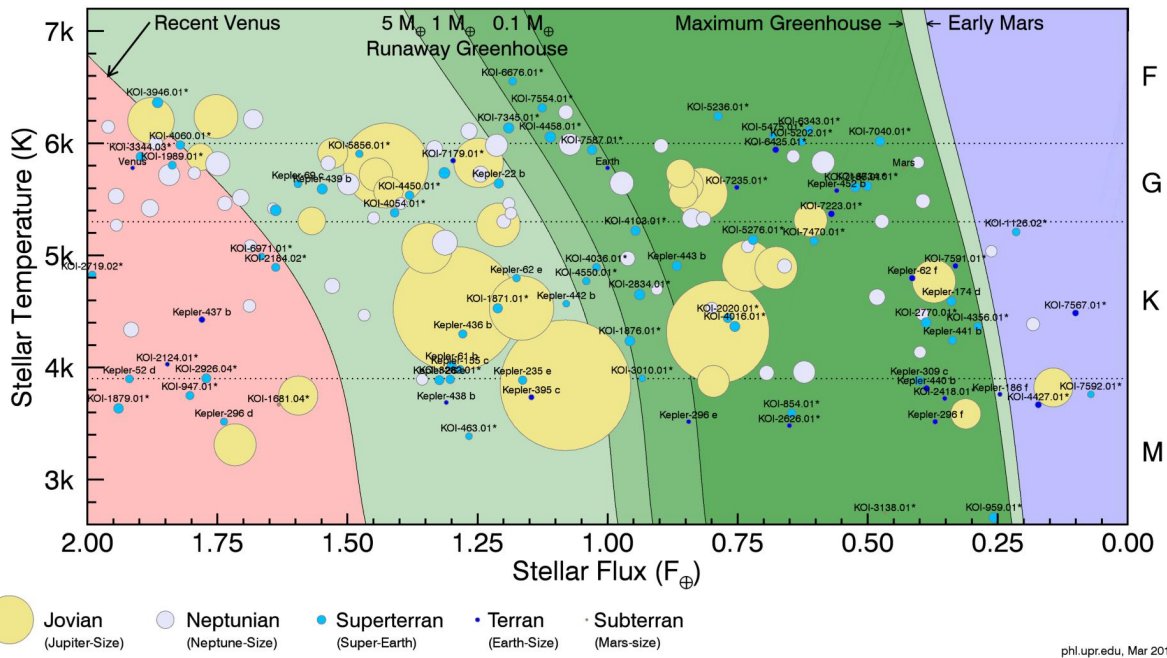


Figure 1.19: Properties of the potentially habitable exoplanet candidates discovered by *Kepler*. The effective stellar temperature of the host star is plotted on the y-axis, and the incident stellar flux at the orbit of the planet in units of Earth-flux is plotted on the x-axis. Planets with derived radii less than $2.5R_{\oplus}$ are labeled, and solar system planets are plotted for comparison. *Kepler* found 49 potentially rocky planets orbiting within the habitable-zone. [Image courtesy of the Planetary Habitability Laboratory at UPR]

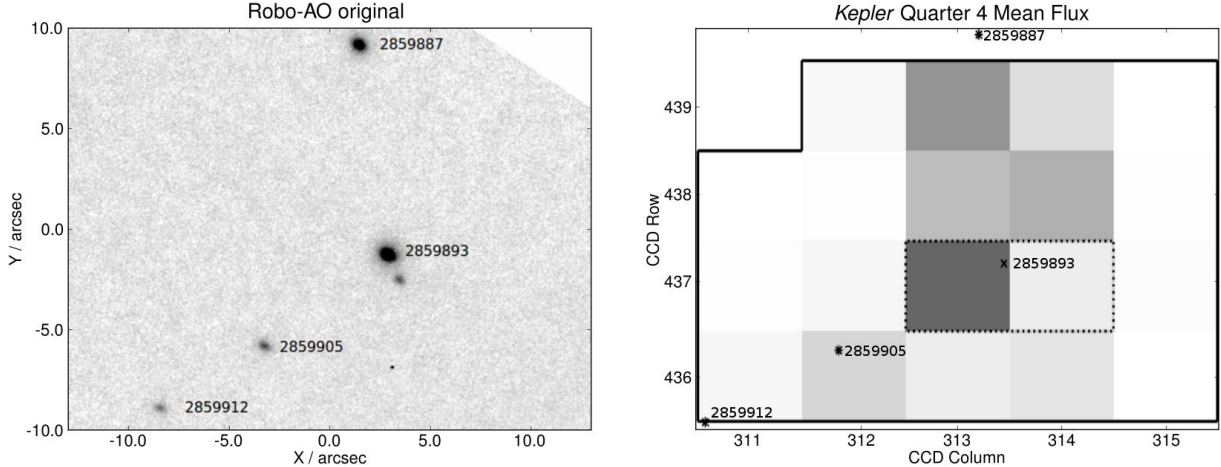


Figure 1.20: On the left, a high-resolution image from Robo-AO of KOI-4418 (KIC2859893) rotated and scaled to match the *Kepler* view of the same field, displayed on the right, with each pixel colored by the mean flux in Quarter 4. KICs in the field are marked in both images. The 1.41" binary to KOI-4418 is not visible in the ~4" pixels of *Kepler*, illustrating how real companions and background stars can blend with the KOIs, resulting in astrophysical false positives or inaccurate planetary property estimates. High-resolution follow-ups are a crucial step in the validation and characterization of *Kepler* planetary systems.

1.2.4 Photometric Contamination

The planetary candidates discovered by *Kepler* (called *Kepler* Objects of Interest, or KOIs) require substantial follow-up work for confirmation and planetary characterization. *Kepler* has exquisite photometric precision but relatively coarse spatial resolution, with an effective point-spread function of 6-10" and a pixel size of ~4" (Haas et al., 2010). In addition, while spacecraft pointing is precise to 0.2", over each observing quarter (~90 days), the stellar positions can shift on the detector by as much as 2.4" (Jenkins et al., 2010). The *Kepler* pixel response function (PRF) is the combination of the telescope's PSF, the CCD resolution, and the spacecraft's pointing jitter over each quarter. A typical PRF, with 95% encircled flux, has a radius of 16-28", or 4-7 *Kepler* pixels (Bryson et al., 2010). This large PRF leaves *Kepler* susceptible to many false positive planetary transit scenarios, i.e. a signal from a non-planetary astrophysical source that appears to be caused by a planetary transit (Brown, 2003).

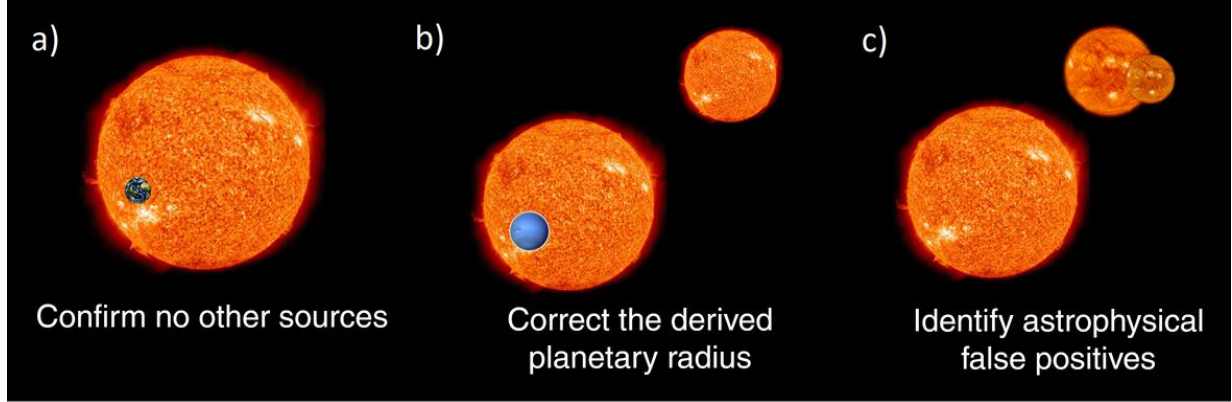


Figure 1.21: Several scenarios exist for each KOI followed up: a) no nearby star is detected, and the statistical argument that a *bona fide* planet orbits in the system is strengthened; b) a nearby star is detected, then the contaminating flux from that star can be measured and the planetary radius estimate can be corrected; c) a nearby star is detected, which is the source of a false positive planetary transit signal, such as a background eclipsing binary.

1.2.5 The Need For High-resolution Follow-up Observations

Many of these false positive scenarios can be ruled out if no nearby star to the KOI is observed. The majority of *Kepler* targets are solar-type (Batalha et al., 2013), and most form with at least one companion star (Duquennoy & Mayor, 1991; Raghavan et al., 2010). These stars are often at separations from the KOI that cannot be resolved with *Kepler*, as illustrated in Figure 1.20. Most stars within approximately 3" of the KOI are also not resolved in seeing limited surveys from the ground, such as DSS or UKIDSS images. All planetary candidates discovered with light curves produced by *Kepler* must, therefore, be independently validated by ground-based high-angular resolution observations. As illustrated in Figure 1.21, these observations help confirm and characterize these planetary candidates in several ways.

No nearby star detected

If no nearby star is detected around the KOI, this greatly reduces the false positive probability. Most *Kepler* planets have been confirmed with probabilistic validation. The principle of probabilistic validation is to demonstrate that all conceivable astrophysical false positive scenarios are negligibly likely to be the cause of a transit candidate signal compared

to the explanation of a planet transiting the presumed target star. Accurate knowledge of the target star is required for this technique, usually derived from high-resolution imaging as well as from spectroscopy and astroseismology. A single stellar source within the photometric aperture significantly increases the probability that a *bona fide* planet is present in the system (Morton et al., 2016).

Real planet in system with nearby star

If a nearby star is detected, the contaminating flux from that star can be measured and the planetary radius may be re-derived. If a target star is blended with another star (bound or line-of-sight), the true planet radius is larger than the derived planet radius because the observed transit depth is diluted by the companion star (see Figure 1.22).

In general, we do not know which star the planet is orbiting. If the planet orbits the primary star, we can correct for the transit dilution with the equation,

$$R_{p,A} = R_{p,0} \sqrt{\frac{1}{F_A}} \quad (1.2.2)$$

where $R_{p,A}$ is the corrected radius of the planet orbiting the primary star, $R_{p,0}$ is the original planetary radius estimate based on the diluted transit signal, and F_A is the fraction of flux within the aperture from the primary star.

For the case where the planet candidate is bound to the secondary star, we use the relation

$$R_{p,B} = R_{p,0} \frac{R_B}{R_A} \sqrt{\frac{1}{F_B}} \quad (1.2.3)$$

where $R_{p,B}$ is the corrected radius of the planet orbiting the secondary star bound to the primary star, R_B and R_A are the stellar radii of the secondary and primary star, respectively, and F_B is the fraction of flux within the aperture from the secondary star.

If the planet orbits the primary star, the maximum radius correction, for the case of equal brightness binary, is a factor of $\sqrt{2}$. If instead, the planet orbits the secondary star,

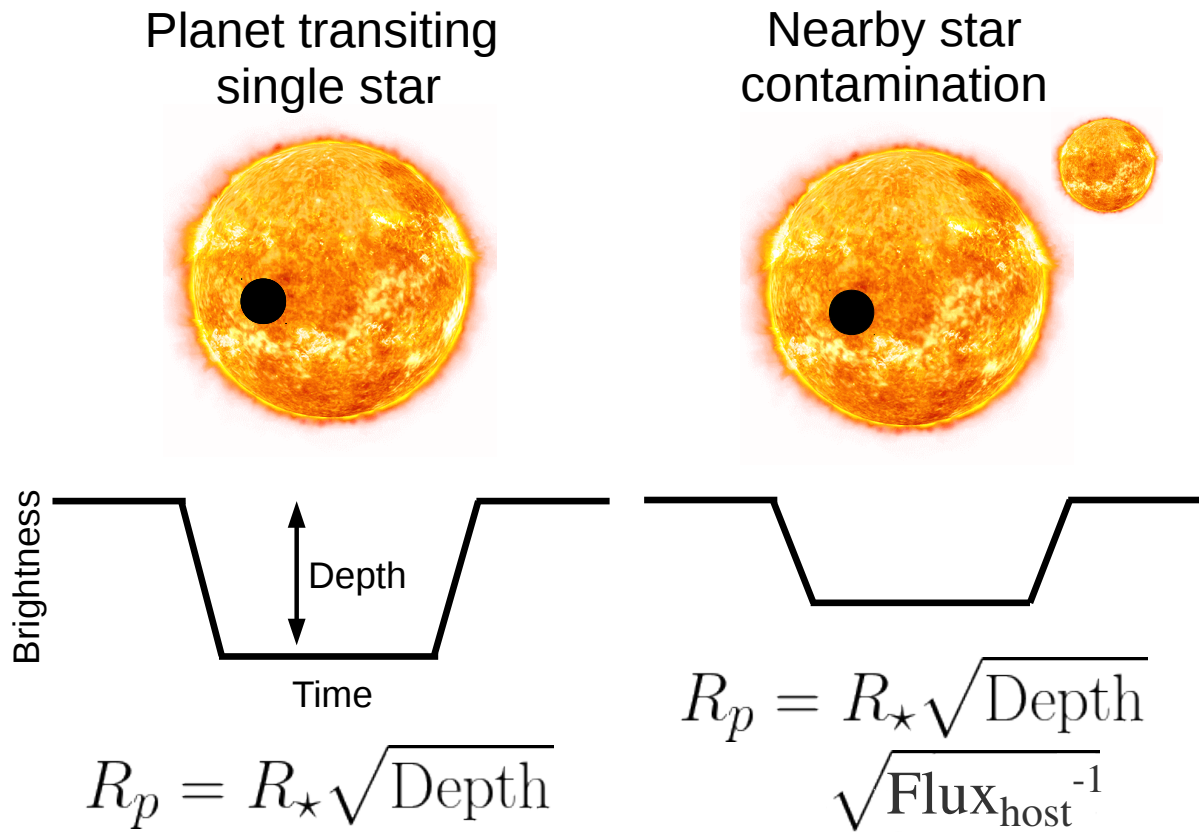


Figure 1.22: An illustration of the impact contaminating flux from a nearby star has on the transit depth of a planet. On the left, a planet transiting a single star. The radius of the planet can be derived from the depth of the transit. On the right, a planet transiting a star with a flux contribution from a nearby star. The additional flux will result in a shallower transit depth with respect to the single star system. The radius of the planet can be estimated with an additional term containing $\text{Flux}_{\text{host}}$, the fraction of the flux in the photometric aperture from the planetary host star.

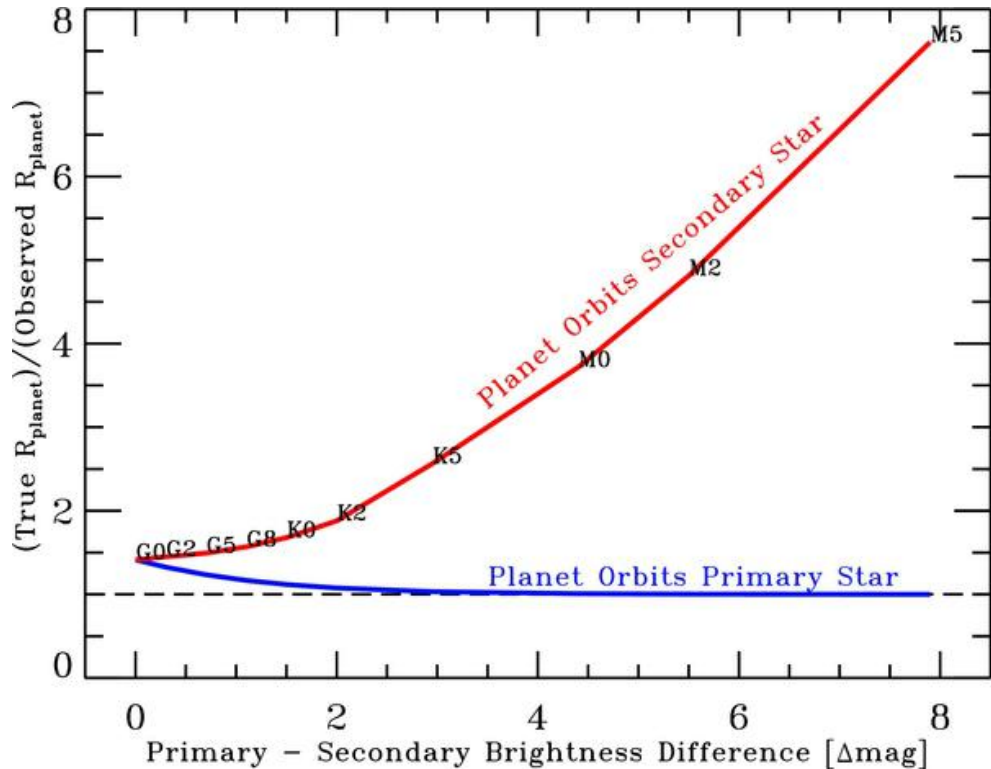


Figure 1.23: The ratio of the true planet radius to the observed planet radius for a blended binary as a function of the contrast between the companions. The blue line is the scenario where the planet orbits the primary star, and the red line is the scenario where the planet orbits the secondary star. In this example, the primary star is a G0V. Approximate spectral types of the secondary star are shown for various contrast values. [Image from Horch et al. (2014)]

the radius correction factor can vastly increase. The impact on the derived planetary radius of the two scenarios is illustrated in Figure 1.23.

These radius corrections can have an enormous impact on our understanding of the planetary candidate properties. With tight constraints on the planetary radius provided by transit observations coupled with mass measurements from either radial velocity observations or transit timing variations (Mazeh et al., 2013), the planetary bulk density may be estimated. Fitting the bulk densities to models allows the composition of the exoplanet to be inferred (Spiegel et al., 2014), as shown in Figure 1.24.

If all stars are assumed to be single, as is the case for every KOI initially, the planetary radii will be underestimated, on average, by a factor of 1.5 (Ciardi et al., 2015). The density of the planet scales with the cube of the planetary radius. Therefore an increase in the radius estimate by 1.5, typical of KOIs with detected nearby stars, will decrease the bulk density by a factor of approximately 3.4. In summary, the occurrence rate of Earth-size planets will be overestimated by as much as 15-20% if all stars are assumed single.

It is believed that the transition between rocky planets and those with a large gaseous envelope occurs rather sharply at around 1.5 to $1.6R_{\oplus}$ (Rogers, 2015; Weiss & Marcy, 2014). For example, KOI-2598.01 is a planet candidate with an original derived radius of $1.35R_{\oplus}$, using the *Kepler* light curve alone (Batalha et al., 2013). A host star was resolved in imaging using a high-angular resolution instrument into a near-equal brightness binary with a separation of approximately 1" (Baranec et al., 2016). The additional contaminating flux from this previously unknown star, blended with the primary in the *Kepler* image, diluted the transit, making it appear shallower than it would from a single star system. Since the radius estimate of the planetary candidate is directly related to the depth of the transit, as shown in Equation 1.2.1, the corrected derived radius will always be larger when a nearby star is discovered. In this case, if the planet orbits the primary star, the corrected planetary radius is $1.77R_{\oplus}$. If instead, the planet orbits the secondary star which is bound to the primary and whose stellar radius is estimated from the single-band contrast, the corrected planetary

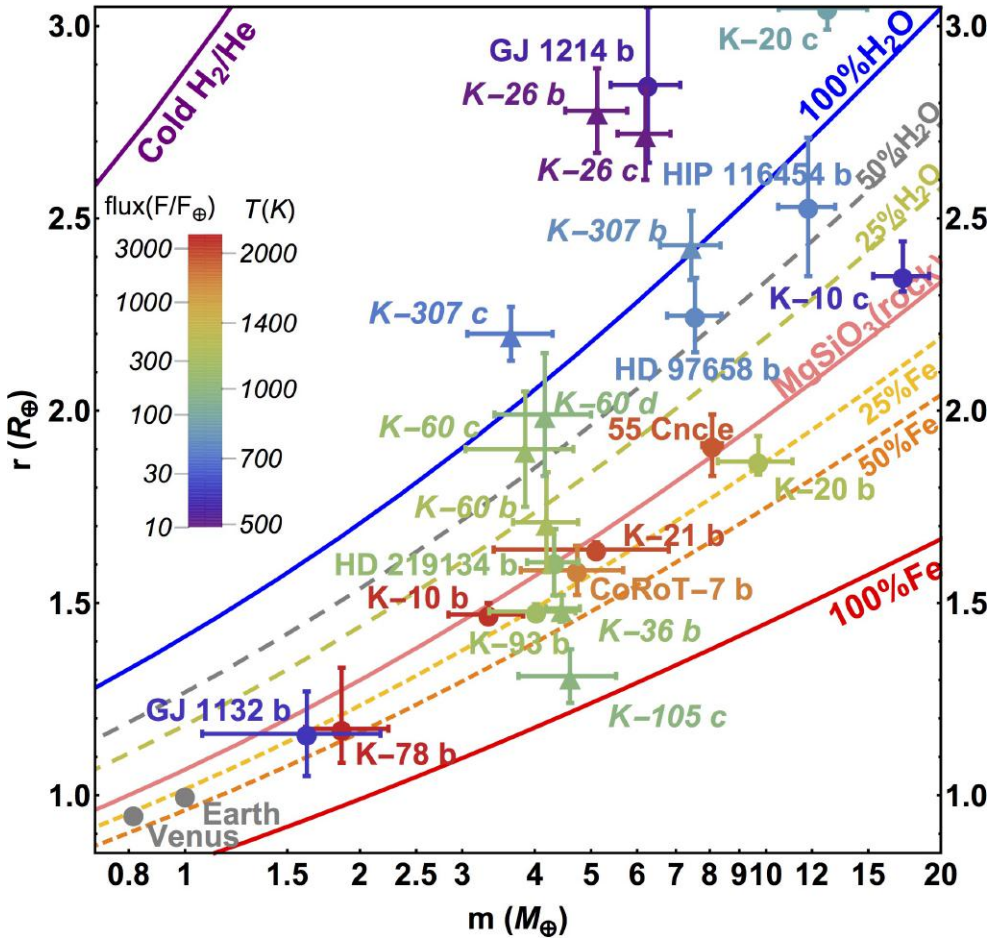


Figure 1.24: Plot of exoplanets with measured radii and masses. Only planets smaller than 20 Earth masses are plotted. Curves of different planetary composition models are plotted. The detection of a previously unknown nearby star to a planetary host star will increase the estimated planetary radius. This radius correction can significantly alter our understanding of the composition of the exoplanet. [Image from Zeng et al. (2016)]

radius is $2.0R_{\oplus}$. In either case, the estimated planetary radius is no longer consistent with a rocky planet with a thin atmosphere.

No planet in system with nearby star

As illustrated in Figure 1.25, there are several alternative scenarios which mimic a real planet orbiting the primary star:

a) a brown dwarf star orbiting the primary star. Brown dwarfs are deuterium burning stars that have approximately the same radius as Jupiter (Chabrier et al., 2009), but can have masses up to $80 M_J$. The transit depth of these systems is therefore similar to a gas giant planetary system, but radial velocity observations must be used to break the mass-radius degeneracy (Santerne et al., 2013). The majority of KOIs, however, are too faint ($V > 14$) for precision radial velocity (Fressin et al., 2013).

b) a background eclipsing binary, blended with the primary star. Their faintness with respect to the nearby KOI can reduce their deep transit depths, on the order of tens of percent when observed alone, to a depth of a few percent, consistent with the transit of a large planet (Abdul-Masih et al., 2016).

c) a grazing stellar binary. The full disks of the binary stars do not overlap each other, resulting in a distinctive V-shaped transit (Koch et al., 2007).

The false positive rate of KOIs is significantly lower than that of candidate planets from ground-based transit surveys (for example, $\sim 80\%$ for HAT-Net (Latham et al., 2009)). This is the result of the extensive vetting performed by the *Kepler* science team (Batalha et al., 2013). Before being elevated to planet candidate status, each threshold crossing event (instances when the transit detection significance for a star with a given planetary orbital period and epoch exceeds 7.1σ , over 34,000 in total over the *Kepler* mission) is checked for clear signatures of being an astrophysical false positive. A few of the tests that all KOIs must pass are:

- Comparison of the odd-numbered transit (the first, third, fifth, etc.) and even-numbered

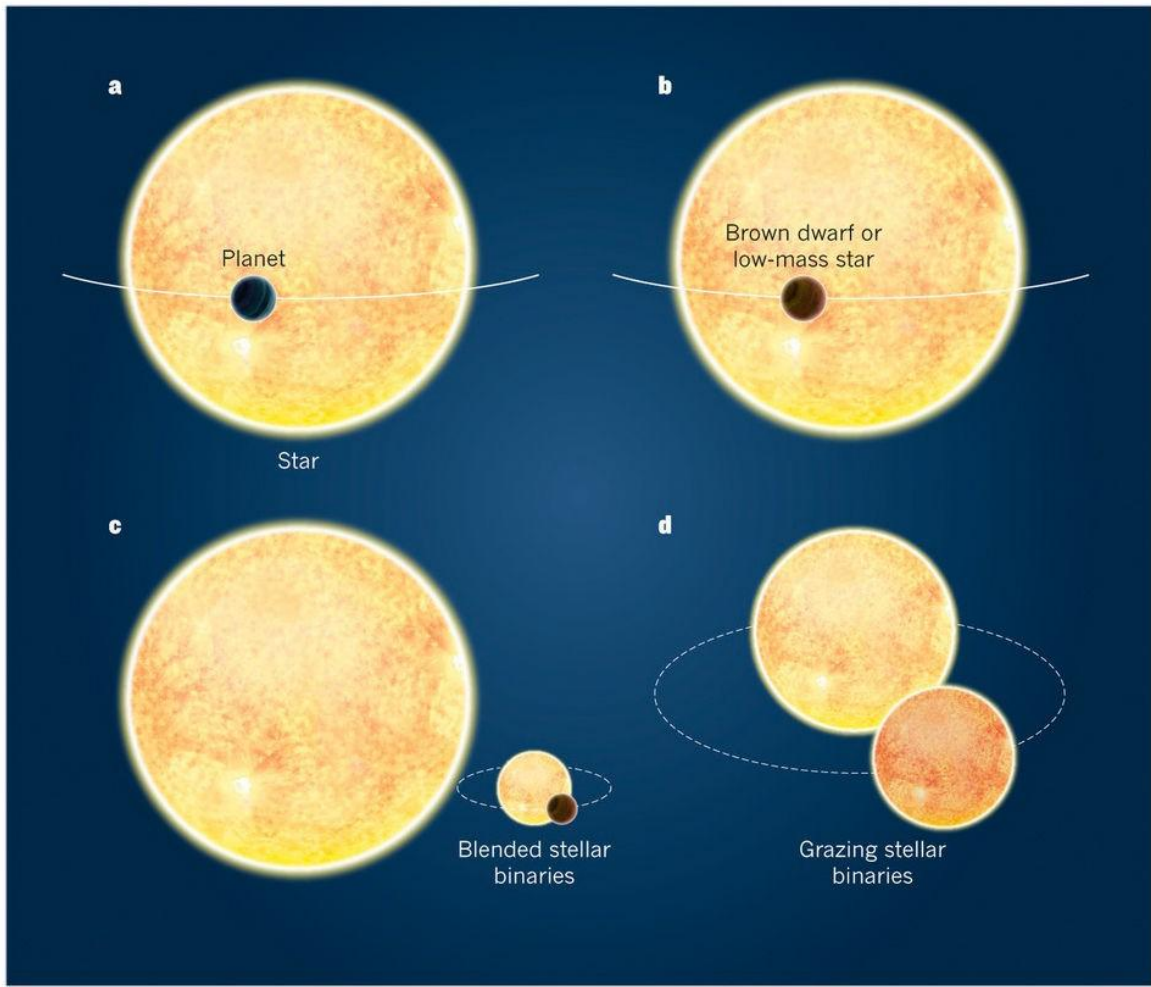


Figure 1.25: Illustrated are common false positive planetary transit scenarios. In panel a) a true planet orbiting a KOI. Several scenarios can give a similar transit signal, however: b) an orbiting brown-dwarf or low-mass star, which has a similar radii to gas-giant planets; c) a blended stellar binary, whose deep eclipse is diluted by the bright nearby star, mimicking a shallow planetary transit; d) a grazing binary star, in which the disk of the stars overlap by only a small amount during each eclipse. [Image courtesy of Santerne et al. (2013)]

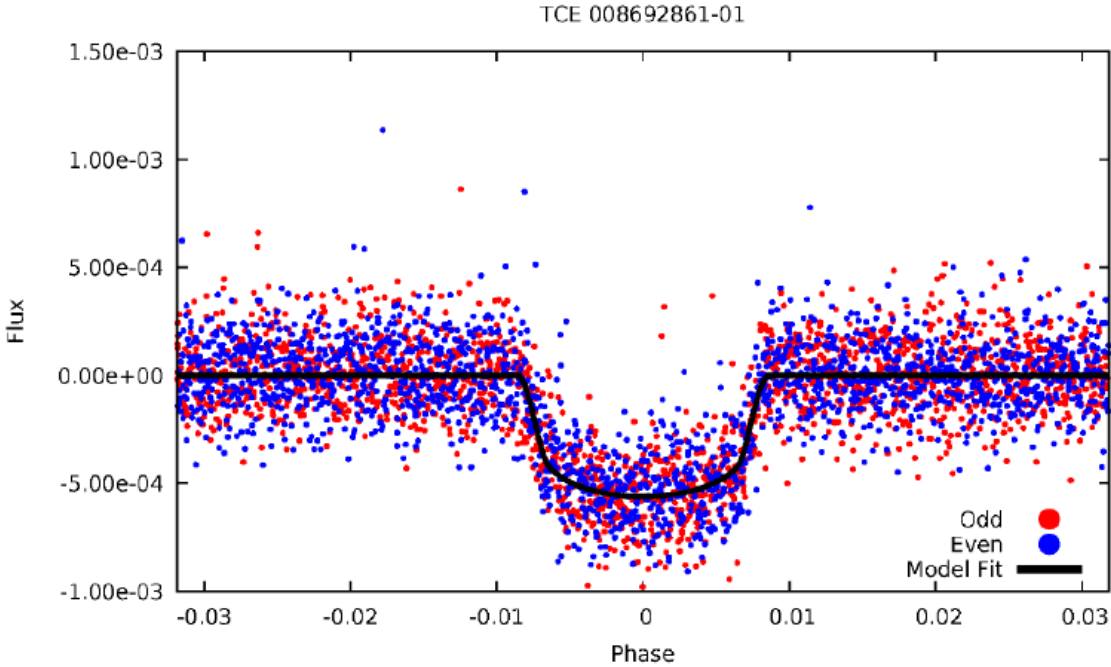


Figure 1.26: An example of the odd-even transit test used to detect near equal mass eclipsing binaries from the *Kepler* DR25 vetting reports. Points from the odd- and even-transits are shown in red and blue, respectively. A best-fit transit model is shown by the solid black line. In this example, the odd- and even-transits both fit the transit model. [Image courtesy of Jeff Coughlin]

transits (the second, fourth, sixth, etc.) can determine if the transit signal is an eclipsing binary with two nearly equal mass and size stars. In these cases, we expect slight variations in the transit depth between the two sets of transits, as the star being eclipsed alternates. An example of this test is given in Figure 1.26.

- Centroid analysis between the in- and out-of-transit point spread function. If the transit signal is from the primary host star, the difference image, produced by subtracting an in-transit image from an out-of-transit image, should result in a similar position of the primary PSF as in the original image. If instead, the transit is from a nearby blended source, the PSF position will shift slightly in the difference image, as the offset secondary source dims. An example of the centroid analysis is shown in Figure 1.27.
- Search for a significant secondary eclipse. An eclipsing binary will produce a large

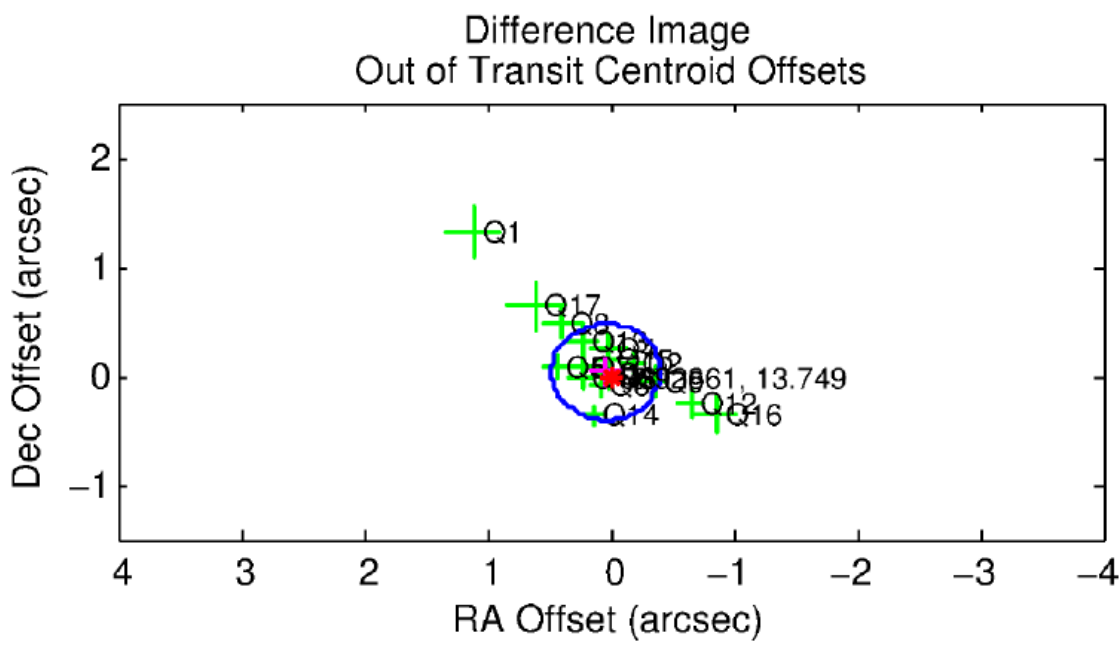


Figure 1.27: An example of the centroid test used to detect a transit signal offset from the host star from the *Kepler* DR25 vetting reports. The location of the target star is represented by the red asterisk. Individual quarterly offsets are represented by green crosses, and the blue circle is the 3σ threshold for a significant centroid offset. For this transit event, nearly all quarterly centroid measurements lie in the blue circle (Q1 is likely an anomalous outlier), and thus no significant offset is detected. [Image courtesy of Jeff Coughlin]

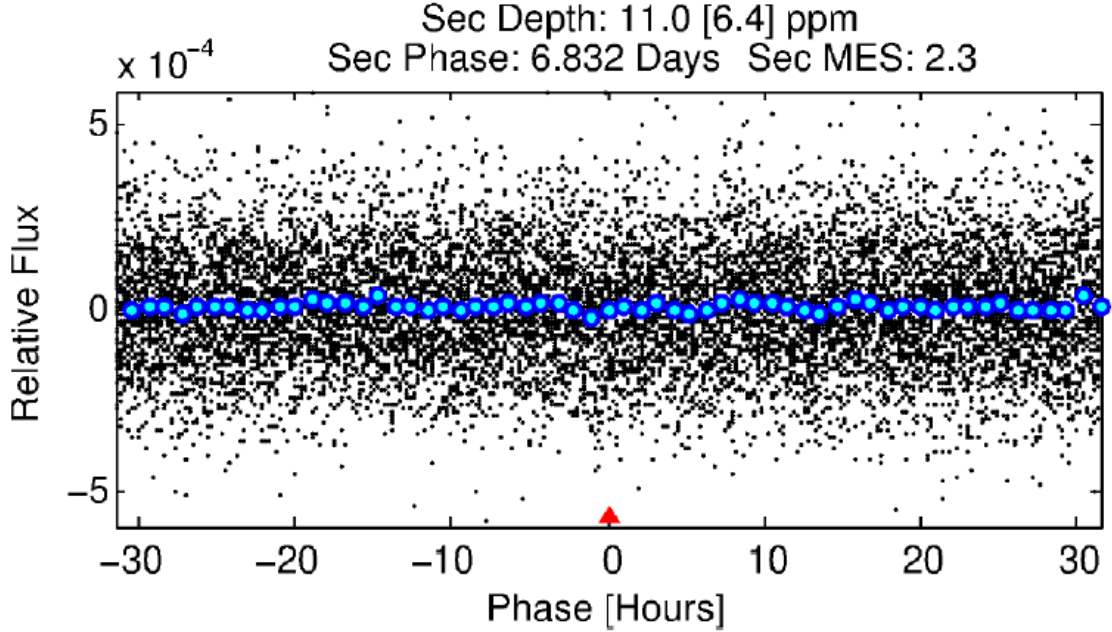


Figure 1.28: An example of the secondary eclipse test from the *Kepler* DR25 vetting reports. If the eclipsing body is self-luminous, we would expect a significant secondary eclipse in the light curve. The strongest secondary eclipse candidate of a transit event is displayed with raw *Kepler* data in black and the phase-binned averages of the data in blue. The depth of this secondary eclipse, indicated with a red triangle, is approximately 11 parts per million, and this candidate is not considered a significant secondary eclipse. [Image courtesy of Jeff Coughlin]

secondary eclipse as the eclipsing object is self-luminous. The secondary eclipse will likely be significantly shallower than the primary transit and will occur a half-phase after the primary transit if the eccentricity of the system is near zero. It is possible for hot Jupiters to have secondary eclipses due to reflected starlight, with detectable depths in the visible passband in which *Kepler* observes. To pass the test, the properties of a detected eclipse must be consistent with that expected for a planet with the estimated radius and orbital period (Angerhausen et al., 2015). An example of the secondary eclipse test is shown in Figure 1.28.

- Ephemeris matching with known transients in the field. The large *Kepler* PRF and multiple optical and electronic components in *Kepler* allow for significant contamination, in some cases with sources from opposite sides of the CCD (Coughlin et al., 2014).

If the transit signal has similar ephemerides, that is the same period and epoch, to that of a known transient source, such as an eclipsing binary, the transit is likely a false positive due to contamination. These false positive transit signals can be caused by stellar crowding, diffraction spikes, ghosting, or electronic cross-talk. An example of ephemeris matching performed on KOIs is shown in Figure 1.29.

While these vetting efforts on early catalogs were largely based on human inspection (Batalha et al., 2010), the most recent DR25 catalog has fully automated this process (Coughlin et al., 2016).

After this initial vetting, a relatively large number of false positive KOIs remain. This is in part due to a preponderance of caution by the *Kepler* team to not remove real planets from the candidate list. Notably, the candidate status of a KOI is *not* a function of its depth or shape (i.e., whether it is V-shaped, which has a high probability of being caused by an eclipsing binary but can conceivably be produced by grazing transiting planets, as well). This means that a large fraction of the deeper signals ($\sim 50\%$) can be expected to be false positives (Santerne et al., 2012, 2015). Shallower candidates have a much lower predicted false positive rate ($\sim 10\%$) (Morton & Johnson, 2011; Fressin et al., 2013), a prediction that has been confirmed by follow-up observations from the *Spitzer* space telescope (Désert et al., 2015). Lastly, it has been determined that almost all multiple-planet candidate systems are in fact real, physically associated planetary systems (Lissauer et al., 2012).

Grazing stellar binaries with periods of less than a year are unlikely to be resolved with current telescopes due to the distance to most *Kepler* host stars (on average several hundred parsecs (Kepler Mission Team, 2009)). In addition, brown dwarfs are similar in size to gas giant planets, and radial velocity measurements are required to determine their mass, not possible on most *Kepler* host stars due to their faintness. High-angular resolution observations can, however, be used to rule the primary false positive scenario, nearby background eclipsing binaries. Detection of the hundreds of false positive KOIs that are due to eclipsing binaries requires high-resolution observations of every candidate planet. We describe a

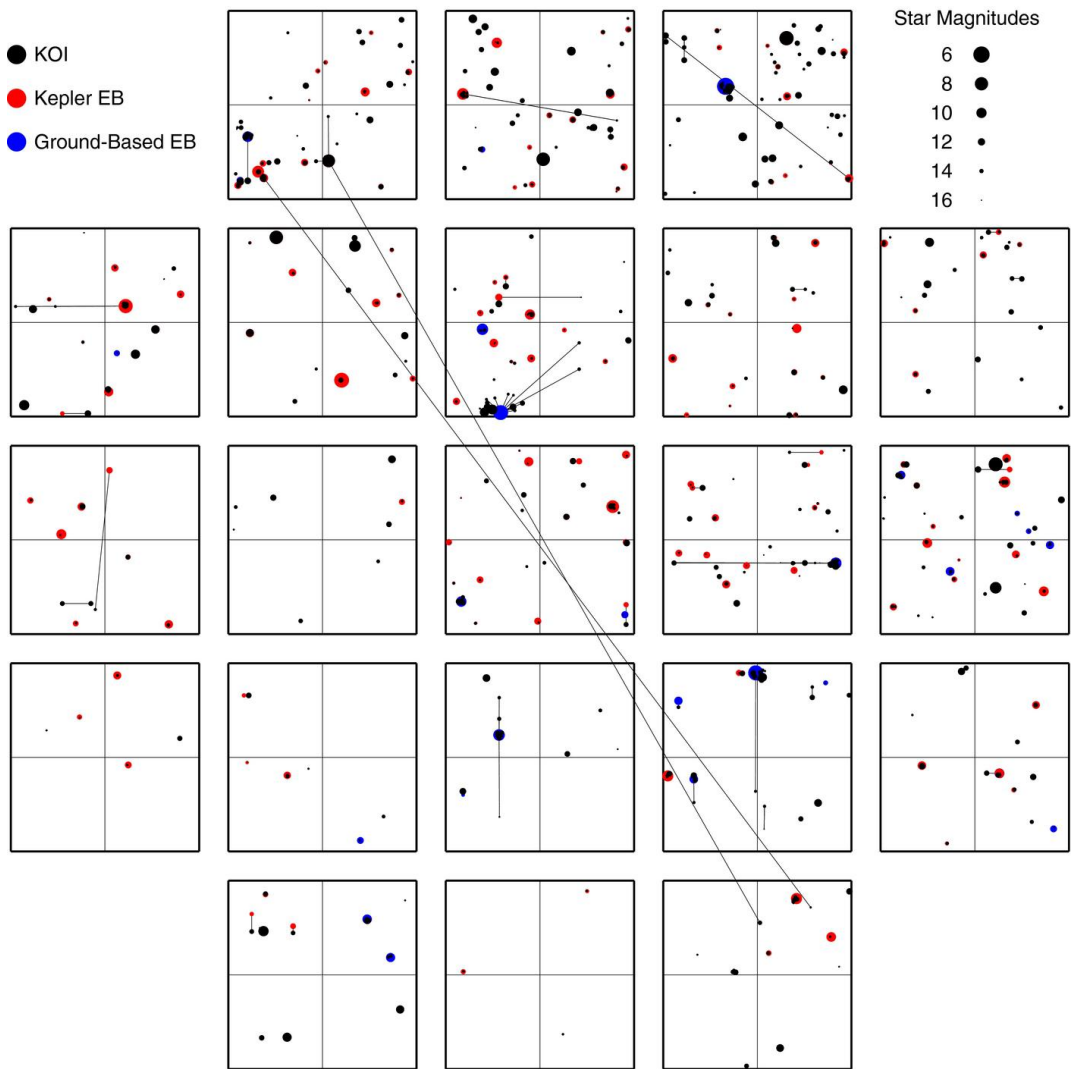


Figure 1.29: Plot of the location of each false positive KOI and the source of the transit signal. KOIs are represented by black points and eclipsing binaries are represented by red and blue points, based on the provenance of their discovery. Most pairs of KOIs and their false positive transit sources are so close that the lines connecting them are not visible. [Image courtesy of Jeff Coughlin]

survey that does just that in Chapters 4, 5, and 6.

1.3 Overview of Contents

This dissertation is divided into three sections: confirmation and characterization of exoplanets with robotic adaptive optics, multiplicity study of cool subdwarfs, and the design and construction of Robo-SOAR, a Southern robotic NGS-AO system.

In Chapter 2, I present the design and construction of Robo-SOAR. An NGS-AO analog to Robo-AO, Robo-SOAR will be a high-order AO system providing robotic AO observing to the South. The design includes a novel WFS design, a reflective version of a PWFS, which is significantly less costly than traditional glass pyramids.

In Chapter 3, I present the Robo-AO observations of 350 cool subdwarfs, an order of magnitude more targets than every other high-resolution cool subdwarf survey combined. I find these stars have significantly lower binarity rates than similar dwarf stars. I discuss how metallicity can impact binarity rates and what the results tell us about the early galaxy.

In Chapter 4, I introduce the Robo-AO KOI survey, beginning with high-resolution observations of 1629 planetary candidates. I use these observations to study the impact that stellar binarity has on planetary systems. In Chapter 5, I describe the cumulative statistics from the full survey consisting of observations of approximately 4000 *Kepler* planetary candidate hosts. I provide corrected radii estimates for over 800 planetary candidates. In Chapter 6, I continue the analysis of the results of the KOI survey, with characterization of the discovered nearby stars. I then apply more sophisticated analysis to understand how planetary systems are affected by binary stars.

Finally, I present my conclusions and potential future research avenues in Chapter 7.

1.3.1 Other Research

In addition to the projects described in the chapters below, I have also worked on several other studies in my graduate career, listed below with details of my individual contribution.

- Fulton, B. J., Collins, K. A., Gaudi, B. S., et al. 2015, ApJ, 810, 30 – Reduced and analyzed Robo-AO observations of the host star of KELT-8b, a highly inflated hot Jupiter.
- David, T. J., Stauffer, J., Hillenbrand, L. A., et al. 2015, ApJ, 814, 62 – Reduced and analyzed Robo-AO observations of HII 2407, an eclipsing binary in the Pleiades.
- Schlieder, J. E., Crossfield, I. J. M., Petigura, E. A., et al. 2016, ApJ, 818, 87 – Reduced and analyzed Robo-AO observations of the host star of K2-26, a small terrestrial planet orbiting an M-dwarf.
- Atkinson, D., Baranec, C., Ziegler, C., et al. 2017, AJ, 153, 25 – Reduced multi-band Keck-AO images used to access the probability of association of nearby stars to 104 KOIs.
- Crossfield, I. J. M., Ciardi, D. R., Petigura, E. A., et al. 2016, ApJS, 226, 7 – Reduced and analyzed Robo-AO observations of 197 planetary candidates from K2, contributing to the confirmation of 104 planets.
- Adams, E. R., Jackson, B., Endl, M., et al. 2017, AJ, 153, 82 – Reduced and analyzed Keck-AO observations of EPIC 220674823, host star to an ultra-short period planet (0.57d) and one additional planet.
- Schonhut-Stasik, J. S., Baranec, C., Huber, D., et al. 2017, ApJ, 847, 97 – Assisted in the reduction and analysis of Robo-AO and Keck-AO images of 99 astroseismic gold standard stars observed with *Kepler*.
- Howard, W. S., Law, N. M., Ziegler, C. A., Baranec, C., & Riddle, R. 2018, AJ, 155, 59 – Assisted in the use and development of a novel method to perform laser-only AO on faint KOI targets.

- Hillenbrand, L. A., Zhang, C., Riddle, R. L., et al. 2018, AJ, 155, 51 – Reduced and analyzed Robo-AO images that detected 66 candidate binary systems in the Pleiades, Praesepe, and NGC 2264 Clusters.

CHAPTER 2: ROBO-SOAR: SOUTHERN ROBOTIC NGS-AO

A common mistake that people make when trying to design something completely foolproof is to underestimate the ingenuity of complete fools.

— *The Hitchhiker’s Guide to the Galaxy*

In this chapter, I discuss the design and construction of Robo-SOAR. This chapter contains content originally from Ziegler et al. (2016).

The automation of adaptive optics observing, allowing unprecedented time-efficient observations, has been proven successful and worthwhile by the Robo-AO system (Riddle et al., 2012; Baranec et al., 2013, 2014a). Expanding this capability to the larger SOAR telescope and providing access to the Southern-Hemisphere is the purview of the Robo-SOAR instrument. Coupled with the already operational Northern Robo-AO system (Jensen-Clem et al., 2017), and planned further Northern Hemisphere systems in Hawaii and elsewhere, all-sky robotic observations of up to 1000 targets a night will be possible. This capability will be critical to follow-up planetary candidates discovered by TESS (Ricker et al., 2014), illustrated in Figure 2.1

2.1 System Capabilities

Robo-SOAR will provide in the visible (650 nm) 0.03" FWHM imaging of sources V<10 with ~20% Strehls over a 17" field-of-view. In the infrared (J- and H-bands), Robo-SOAR will provide 0.08" FWHM on sources down to V=15, with 70% bright-target Strehls. Expected typical overheads for the proven Robo-AO software are ~1 minute with an LGS system. With the simpler NGS system, we expect typical Robo-SOAR overheads to improve

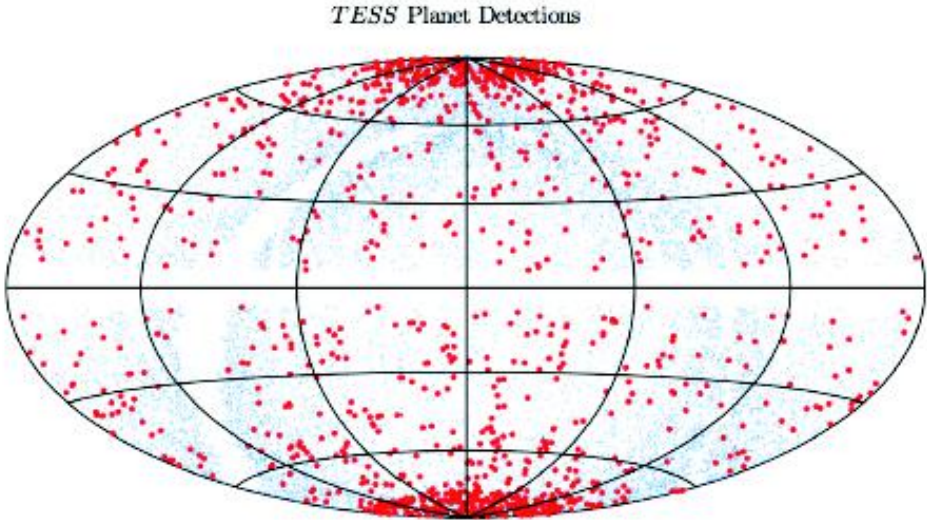


Figure 2.1: On-sky locations of simulated TESS planetary discoveries. Red dots are planets detected around the targeted stars, and blue dots are planets detected around stars in the full frame images. Robo-SOAR, in combination with Robo-AO, will be able to observe every TESS planet candidate host star in high-resolution. [Image courtesy of Sullivan et al. (2015)]

on Robo-AO, allowing observations of at least $10\times$ more targets per hours than the similar MagAO system.

Using AO-assisted speckle-imaging, Robo-SOAR will achieve diffraction-limited visible-light performance on guide stars at least as faint as $V=16$, 1-2 magnitudes fainter than non-AO-assisted speckle imaging systems. Compared to lucky imaging systems, Robo-SOAR will attain an increase in angular resolution of at least a factor of 2 and ten times more light-collection efficiency. With an optional NIR camera upgrade path, detection of companions with $2-3\times$ lower masses than other large-survey instruments is possible, including Robo-AO, as shown in Figure 2.2. Law et al. (2016) covers the science plans and capabilities of Robo-SOAR in more detail.

2.2 Optical Design

The SOAR telescope has a 4.1m primary mirror. Robo-SOAR will be mounted on the bent-Cassegrain port on the side of SOAR, taking in a beam with $F/\#$ of 16.63 and a plate scale of $3.025''/\text{mm}$. A target acquisition camera near the input will provide a

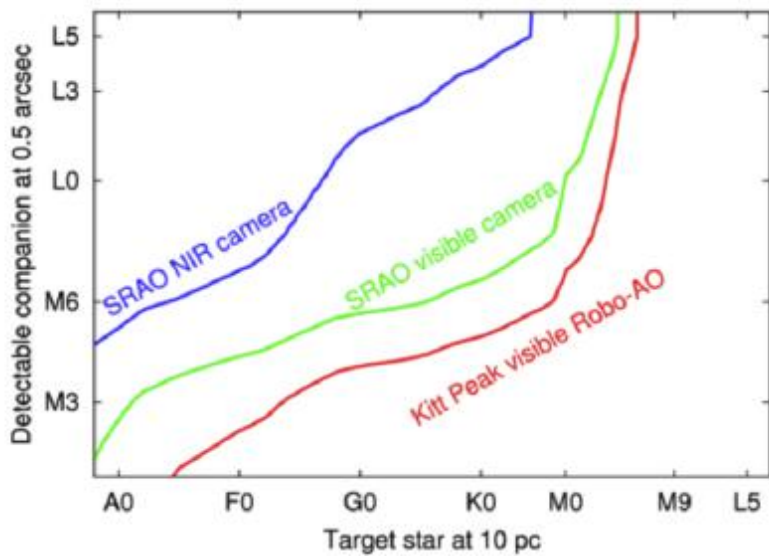


Figure 2.2: Detectable companions around typical stars in Robo-SOAR multiplicity surveys. The NIR camera is more effective at finding low-mass companions, and the visible camera will provide colors for mass estimates, improved angular resolution, and a passband that matches most large sky surveys. [Image from Law et al. (2016)]

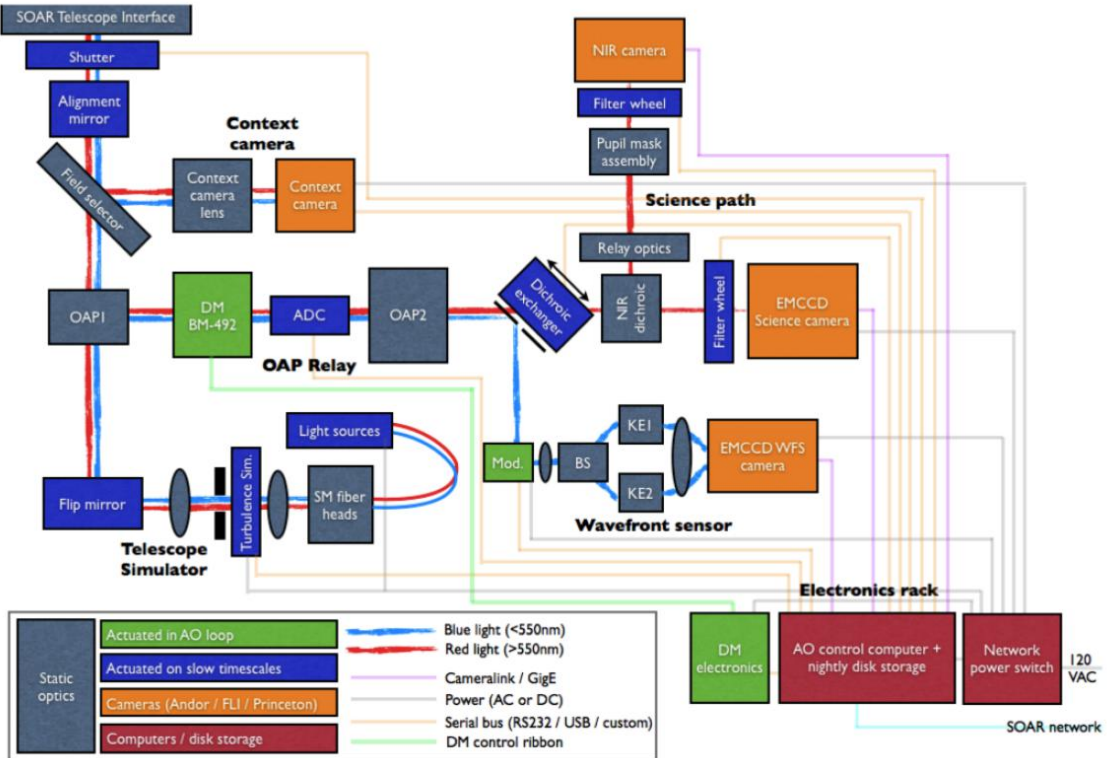


Figure 2.3: Schematic of the major components of the Robo-SOAR system and their control paths. [Image from Law et al. (2016)]

larger seeing-limited field of view to enable automated target identification and alignment. An OAP relay will provide magnification of $2.26\times$, achieving Nyquist sampling for 30 mas visible-light diffraction-limited cores on the detector. An atmospheric dispersion corrector similar to Robo-AO’s design is placed in the collimated beam after the DM and before the second OAP. Visible light science images, with field-of-view approximately 17” square, are acquired by a photon-counting Andor iXon 888 EMCCD. An optional upgrade path has NIR light sent by a dichroic into a re-imaging relay and to a Princeton Instruments 640LN NIR InGaAs-array camera. The 640LN camera is liquid-nitrogen cooled, with significantly lower read noise and dark current (15e^- and $<8\text{e}^-/\text{pix/sec}$, respectively) than traditional off-the-shelf InGaAs cameras, allowing sky background limited observations in H-band. Tip/tilt correction will be provided by SOAR’s M3 rapid-actuation mirror. The telescope simulator consists of a single-mode-fiber-fed collimated beam focused to the correct F# with rotating plastic disks to simulate turbulence. Using a dichroic, part of the light will be sent from the science path to the WFS assembly. The wavelengths extracted will be dynamically switched using an interchangeable dichroic assembly depending on the science goals.

A schematic of the system is shown in Figure 2.3. The mechanical design is shown in Figure 2.4. The full Robo-SOAR Zemax model predicts, with perfectly-built and aligned optics and no atmosphere, center-of-field Strehl ratios at 656nm of 0.99, decreasing to 0.97 at the edge of the 17” field (Figure 2.4).

2.2.1 Software Design

The success of a robotic AO system is dependent on the reliability of its software design. Robo-SOAR will be built on the existing Robo-AO software, (Riddle et al., 2012) veteran of over 5 years of robotic AO development and observing. The Robo-AO control software autonomously operates Robo-AO’s laser and safety systems, the adaptive optics control loop, the atmospheric dispersion corrector, and the science cameras. The system operates queue-scheduled, with autonomous optimal target selection and laser window avoidance.

The Robo-SOAR control software need only cover a smaller set of capabilities, as Robo-SOAR is initially planned to operate as a natural-guide-star system. The control software will be responsible for real-time wavefront reconstruction, DM control, tip/tilt removal, and queue-based scheduling. Modifications of the Robo-AO code for use in Robo-SOAR include: 1) upgrades of the system performance for the 492-actuator system; 2) alteration of the system for natural guide star operation, a new reconstructor for the dual knife-edge WFS, interface with the Andor cameras and 640LN NIR camera, interface to SOAR TCS, and automatic acquisition of guide star with the context camera along with fast tip/tilt spiral slews coupled with fast frame rate science WFS EMCCDs. The Robo-AO reduction pipeline (Law et al., 2014; Ziegler et al., 2015, 2017a) will automatically calibrate and co-add the EMCCD visible-light camera data and then perform automated PSF subtraction and companion detection.

2.3 Dual Knife-edge WFS

The Robo-SOAR WFS assembly is based on a pyramid-wavefront sensor (PWFS) (Riccardi et al., 1998), a system used on TNG, LBT, and Magellan, that has proven to effectively reach fainter guide-stars than Shack-Hartmann WFS systems (Chew et al., 2006). The glass pyramid, placed at the focal plane of the beam, splits the light into four separate paths; a relay lens produces four images of the telescope pupil on the detector. Guiding on faint stars is then achieved by allowing dynamical rebinning of detector pixels to optimize the system for low-light levels, as well as taking advantage of AO image sharpening of the WFS images. A single pyramid, however, suffers from severe chromatic aberrations, a problem that can be mitigated by employing a complex dual pyramid, as used for the LBT (Tozzi et al., 2008). The expense of glass pyramids is a result of the precise requirements on their knife-edge vertices and base angles.

We have pioneered a new mostly-reflective system that removes the chromatic aberrations at greatly reduced cost and complexity. The Robo-SOAR design uses crossed knife

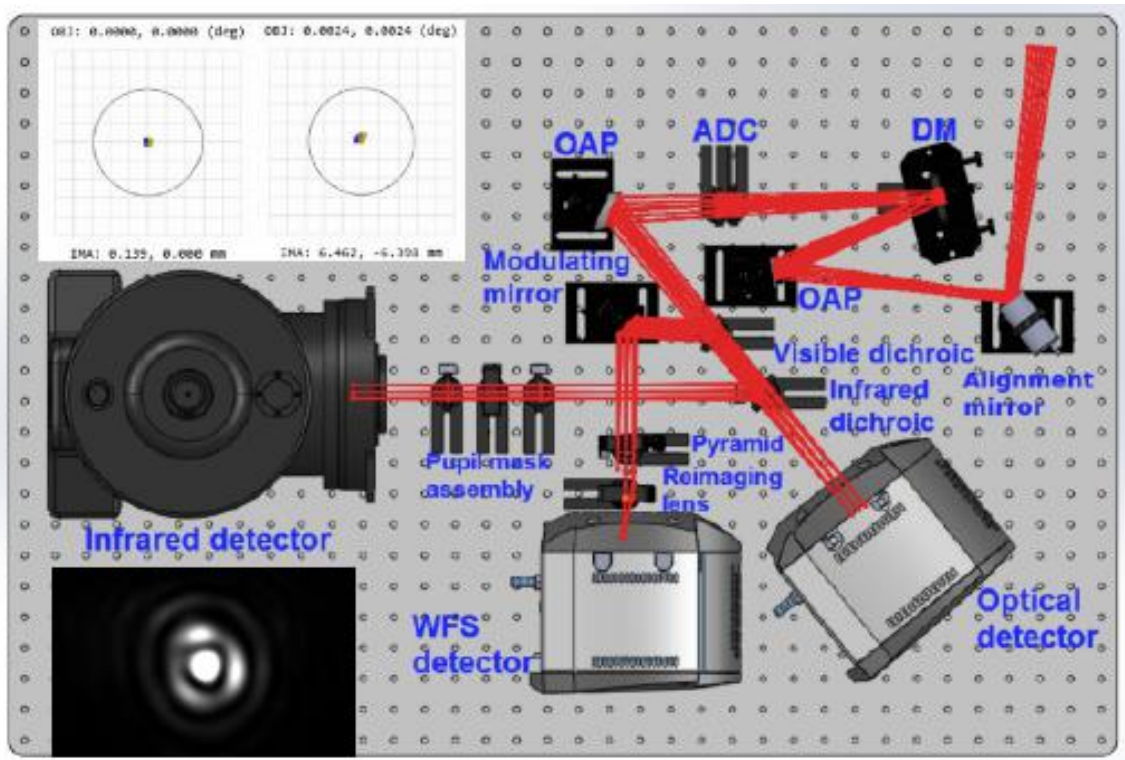


Figure 2.4: Robo-SOAR optomechanical design showing major components and beam paths. Light from the telescope enters at the top right. In the top left corner inset: Zemax-simulated spot diagrams for on-axis images (left; Strehl ratio 0.99) and corner-of-field images(right; Strehl ratio 0.97). The circle shows the diffraction-limited spot size for 656nm observations. In the bottom left corner inset: PSF output of OAP relay from system testbed.

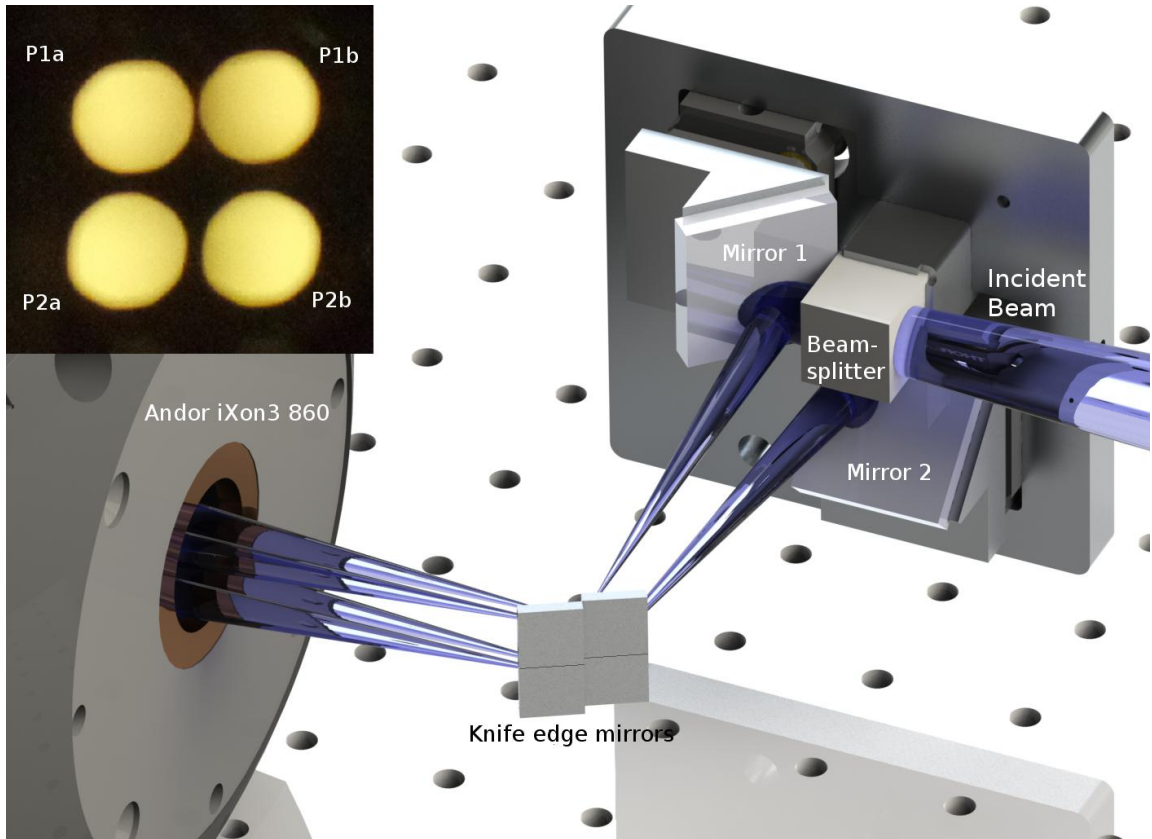


Figure 2.5: Rendering of the dual knife-edge wavefront sensor. In the upper left inset: four illuminated pupils output by the knife-edge wavefront sensor prototype with an input of diffuse light.

edges, with the light first divided by a beamsplitter and then each image focused on a mirror with a knife-edge splitting the beam, forming two pupils for each slope direction.

Diffraction simulations performed using in-house custom IDL code demonstrate similar linearity range and response to tilts for a dual knife-edge sensor compared to a traditional PWFS, but with no cross-talk between the X and Y slope measurements and lower diffraction losses. With the slopes sensed independently, as for a knife-edge sensor, the modulation required can be one-dimensional in each channel, thus reducing the cost and complexity of the required modulator. For Robo-SOAR, modulation will be introduced before entering the WFS assembly by a Physik Instrumente S-316.10D tip/tilt steering mirror driven by a Physik Instrumente E-727.3SDA piezo-controller.

The design of the system is drawn in Figure 2.5, along with the illuminated pupil images from the WFS prototype. The incoming light, redirected from the second OAP by the dichroic and increased to an F/100 beam with a large depth-of-focus using achromatic lenses, is split by a standard beamsplitter cube and directed to two plane mirrors resting on kinematic mounts which allow precise pointing of the beams. Each beam is focused on separate sets of mirror pairs, made by diamond-cutting a mirror in the middle to get a sharp outer edge. In each set, one mirror is slightly behind the other, allowing the sharp edge of the leading mirror to divide the focal plane. The edge of the back mirror is then in the shadow of the front, and thus only the edge quality of the leading mirror is important. The mutual tilt of the two mirrors separates the reflected beams, and a pair of pupil images is formed with a re-imaging lens (not shown) onto the WFS CCD: pupil images P1a and P1b are formed from the upper knife-edge mirrors fed off of Mirror 1, and, likewise, P2a and P2b are formed off of the lower knife-edge mirrors fed off of Mirror 2. With the 90° twist between the beams introduced by the beamsplitter and Mirrors 1 and 2, the parallel knife-edge mirrors are able to sense both the X and Y tilt of the incoming wavefront. The difference in intensity between P1a and P1b serves to sense the X-tilt, and the pair P2a and P2b to sense the Y-tilt. This also allows a one-dimensional modulator to be used, reducing

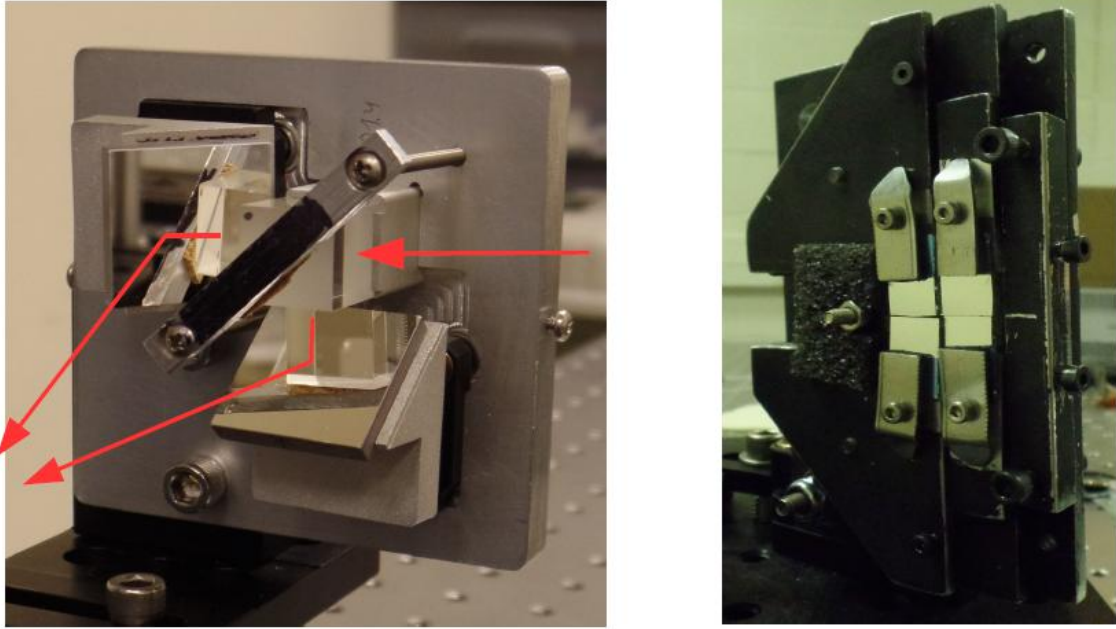


Figure 2.6: The prototype dual knife-edge wavefront sensor: the beamsplitter module (left), and the knife-edge mirror module (right).

both the cost and complexity of the system.

2.3.1 Wavefront Sensor Prototype

The prototype of the wavefront sensor assembly is shown in Figure 2.6. On the left, the incoming light (red arrow from right of image) passes through the beamsplitter cube, and both result rays are reflected toward the knife-edge module (right). The two beams cross, such that the lower beam is focused on the upper mirror pair and the upper beam on the lower mirror pair. The mirrors in the beamsplitter module, 1-inch square and silver-coated, are mounted on kinematic mirror mounts by means of the 45-degree machined bases for tip-tilt adjustment, allowing fine placement of the resulting beams on the knife-edge of the mirrors. The knife-edge module also allows tip-tilt adjustment of each pair individually as well as global tilt adjustment of the pairs with respect to each other. The resulting pupils can then be precisely placed on the detector in each quadrant in a square arrangement, shown in Figure 2.5. A lab testbed performance characterization of the WFS prototype is ongoing and is shown in Figure 2.7.

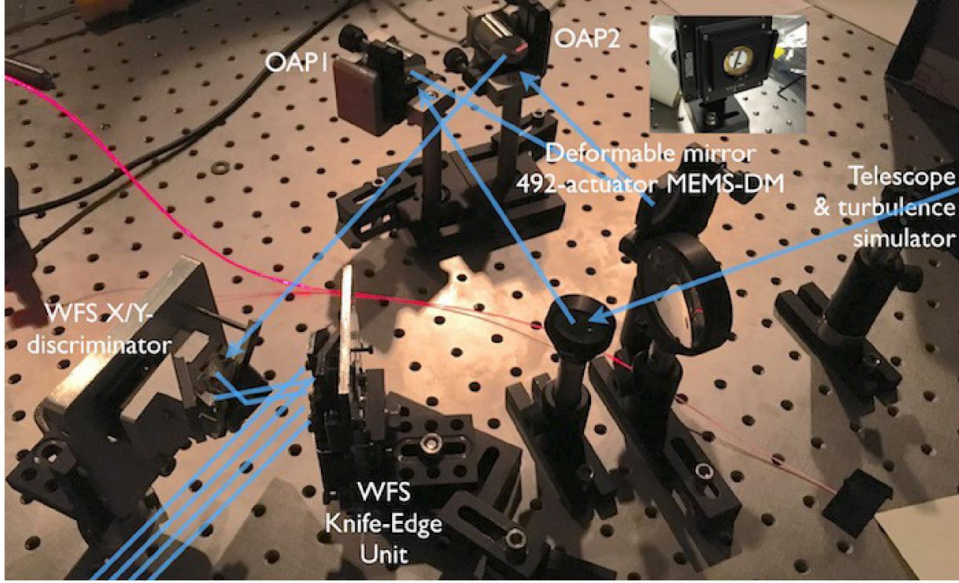


Figure 2.7: The Robo-SOAR lab testbed, before integration of the 492-DM deformable mirror. [Image from Law et al. (2016)]

2.4 Conclusions

Robo-SOAR will provide automated, moderate-order NGS-AO to the 4.1m SOAR telescope at CTIO. Along with the Northern Hemisphere Robo-AO and planned Hawaii and elsewhere systems, all-sky high-efficiency AO observations of up to 1000 targets a night will be possible, allowing large, previously infeasible surveys to be performed. With an innovative dual knife-edge WFS, similar in concept to a pyramid WFS but with reduced chromatic aberrations, Robo-SOAR can reach the diffraction limit on brighter targets.

CHAPTER 3: THE ROBO-AO COOL SUBDWARF SURVEY

There is a theory which states that if ever anyone discovers exactly what the Universe is for and why it is here, it will instantly disappear and be replaced by something even more bizarre and inexplicable. There is another theory which states that this has already happened.

— *The Hitchhiker’s Guide to the Galaxy*

In this chapter, I report the results of the largest high-resolution cool subdwarf multiplicity survey yet performed, making use of the automated Robo-AO system. This survey served as a pilot study for future kilo-target surveys, such as the Robo-AO *Kepler* survey described in Chapter 4. The results in this chapter were first presented in Ziegler et al. (2015).

Cool subdwarfs are low-mass, metal-poor stars and are remnants of the early star formation in the Milky Way. Studying their properties, including multiplicity, can give insight into how our galaxy formed, including a possible early galactic bombardment era. The efficiency of the Robo-AO system allows us to observe nearly an order-of-magnitude more systems than had previously been observed in high-resolution, and find that cool subdwarfs are significantly less likely to have companions than similar dwarf stars.

3.1 Cool Subdwarfs

Cool subdwarfs are the oldest members of the low-mass stellar population, with spectral types of G, K, and M, masses between ~ 0.6 and ~ 0.08 M_{sun} , and effective surface temperatures between ~ 4000 and ~ 2300 K (Kaltenegger & Traub, 2009). First named by Kuiper

(1939), subdwarfs are the low-luminosity, metal-poor ($[\text{Fe}/\text{H}] < -1$) spectral counterparts to the main-sequence dwarfs. On a color-magnitude diagram (see Figure 3.1), subdwarfs lie between white dwarfs and the main sequence (Adams, 1915). With decreased metal opacity, subdwarfs have smaller stellar radii and are bluer at a given luminosity than their main sequence counterparts (Sandage & Eggen, 1959).

These low-mass stars are members of the Galactic halo (Gould, 2003) and have higher systematic velocities and proper motions than disk dwarf stars. Traditionally subdwarfs have been identified using high proper motion (PM) surveys. Although 99.7% of stars in the galaxy are disk main-sequence, statistically there are more subdwarfs in these high PM surveys (Reid & Hawley, 2005). Verification and precise spectral typing of cool subdwarfs can be performed by measuring molecular lines, as defined first by Gizis (1997). Lépine et al. (2007) introduced a refined system, using spectroscopic measurements from a survey of 1,983 stars to standardize the subdwarf metallicity subclasses and spectroscopic sequence.

3.1.1 Stellar Multiplicity

The search for companions to stars of different masses can provide clues to the star formation process, as any successful model must account for both the frequency of the multiple star systems and the properties of the systems. In addition, monitoring the orbital characteristics of multiple star systems yields information otherwise unattainable for single stars, such as relative brightness and masses of the components (Goodwin et al., 2007), that lend further constraints to mass-luminosity relationships (Chabrier et al., 2000)

The multiplicity of main-sequence dwarfs has been well explored in the literature. A consistent purveying trend is that the fraction of stars with stellar companions seems to depend on the mass of the stars (see Figure 3.2). For AB-type stars, Peter et al. (2012) used a sample of 148 stars to determine a companion fraction of $\sim 70\%$. For solar-type stars (FGK-type), around 57% have companions (Duquennoy & Mayor, 1991), although Raghavan et al. (2010) have revised the fraction down to $\sim 46\%$. Fischer & Marcy (1992) looked at

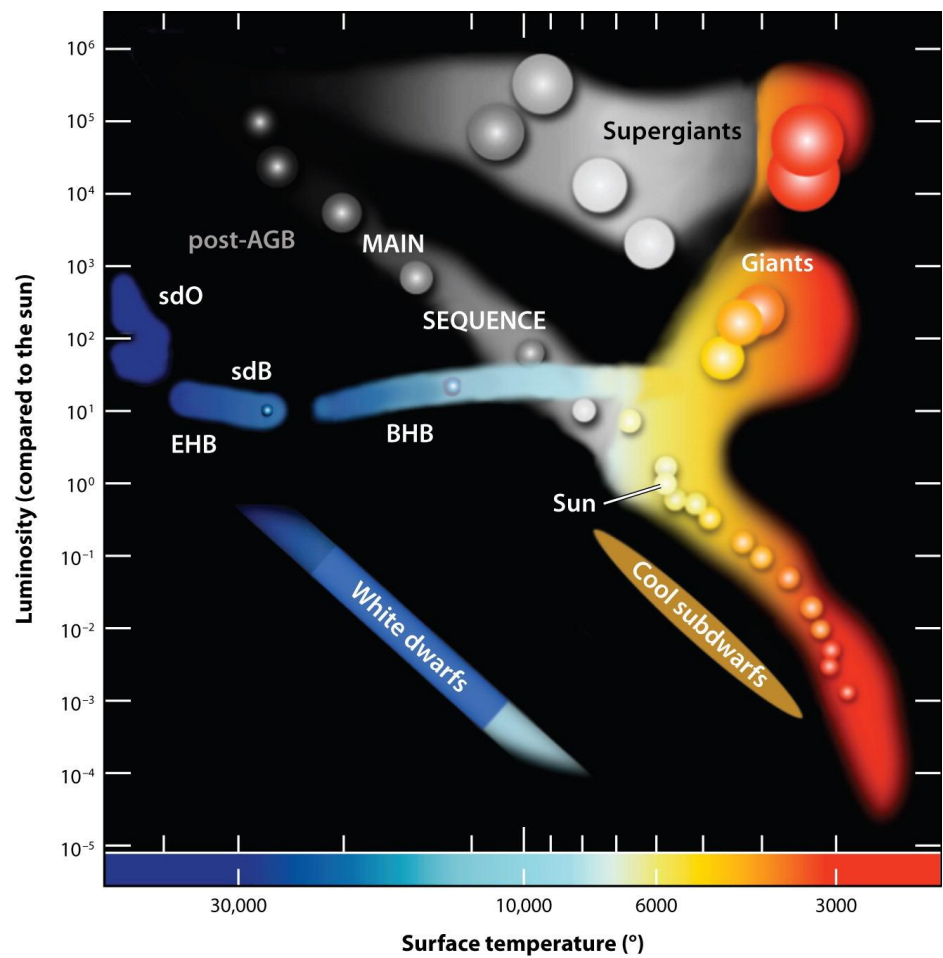


Figure 3.1: Sketch of a Hertzsprung-Russell diagram showing the approximate position of the cool subdwarfs. [Image courtesy of Heber (2009)]

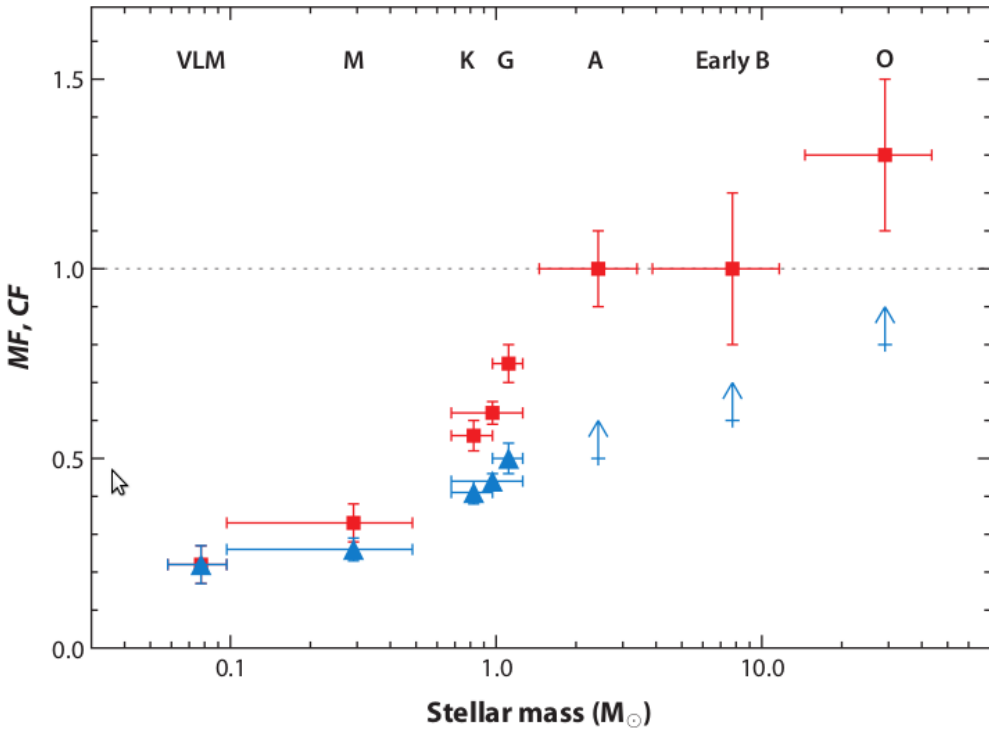


Figure 3.2: The dependency of CF (companion frequency, or the total number of stellar companions on average per star; red squares) and MF (multiplicity frequency, or the fraction of stars with gravitationally bound stellar companions; blue triangles) with primary mass for main-sequence stars and field very low-mass (VLM) objects. Horizontal error bars represent the approximate mass range for each population. The multiplicity of main-sequence stars correlates with stellar mass. [Image courtesy of Duchêne & Kraus (2013)]

M-dwarfs and found a multiplicity fraction of $42 \pm 9\%$. More recently, Janson et al. (2012) find a binary fraction for late K- to mid-M-type dwarfs of $27 \pm 3\%$ from a sample of 701 stars. For late M-dwarfs, a slightly lower fraction was found by Law et al. (2006) of $7 \pm 3\%$. Extending their previous study for mid/late M-type dwarfs, M5-M8, Janson et al. (2014) find a multiplicity fraction of 21%-27% using a sample of 205 stars.

3.1.2 Cool Subdwarf Multiplicity

Old population II stars are important probes for the early history of star formation in the galaxy (Zhang et al., 2013). The formation process of low-mass stars remains less understood than for solar-like stars. Although multiple indications suggest they form as the

low-mass tail of regular star formation (Bourke et al., 2006), other mechanisms have been proposed for some or all of these objects (Goodwin & Whitworth, 2007; Thies & Kroupa, 2007; Basu & Vorobyov, 2012). A firm binary fraction for low-metallicity cool stars could assist in constraining various formation models.

While the multiplicity of dwarf stars has been heavily studied with comprehensive surveys, detailed multiplicity studies of low-mass subdwarfs have, historically, been hindered by their low luminosity and relative rarity in the solar neighborhood. Within 10 parsecs, there are three low-mass subdwarfs, compared to 243 main-sequence stars (Monteiro et al., 2006). Subsequently, multiplicity surveys of cool subdwarfs have been relatively small. The largest, a low-limit angular resolution search by Zhang et al. (2013) mined the Sloan Digital Sky Survey (York et al., 2000, SDSS) to find 1826 cool subdwarfs, picking out subdwarfs by their PMs and identifying spectral types by fitting an absolute magnitude-spectral type relationship. They find 45 subdwarfs multiple systems in total, with 30 being wide companions and 15 partially resolved companions. When adjusting for the incompleteness of their survey, an estimate of the binary fraction of $>10\%$ is predicted. The authors note the need for a high spatial resolution imaging survey to search for close binaries (<100 AU) and put tighter constraints on the binary fraction of cool subdwarfs.

The high-resolution subdwarf surveys completed thus far have been comparatively small. Gizis & Reid (2000) detected no companions in a sample of eleven cool subdwarfs. Riaz et al. (2008) similarly found no companions in a sample of nineteen M-subdwarfs using the *Hubble Space Telescope*. Lodieu et al. (2009) reported one companion in a sample of 33 M-type subdwarfs. Jao et al. (2009) found four companions in a sample of 62 cool subdwarf systems. With the high variance in small number statistics, the relationship between dwarf and subdwarf multiplicity fractions remains inconclusive.

We describe in Chapter 3 a high-resolution survey with Robo-AO of 348 cool subdwarfs. With significantly more targets, we are able to better constrain the true binary fraction of cool subdwarfs and compare multiplicity rates between the metal-poor and solar-metallicity

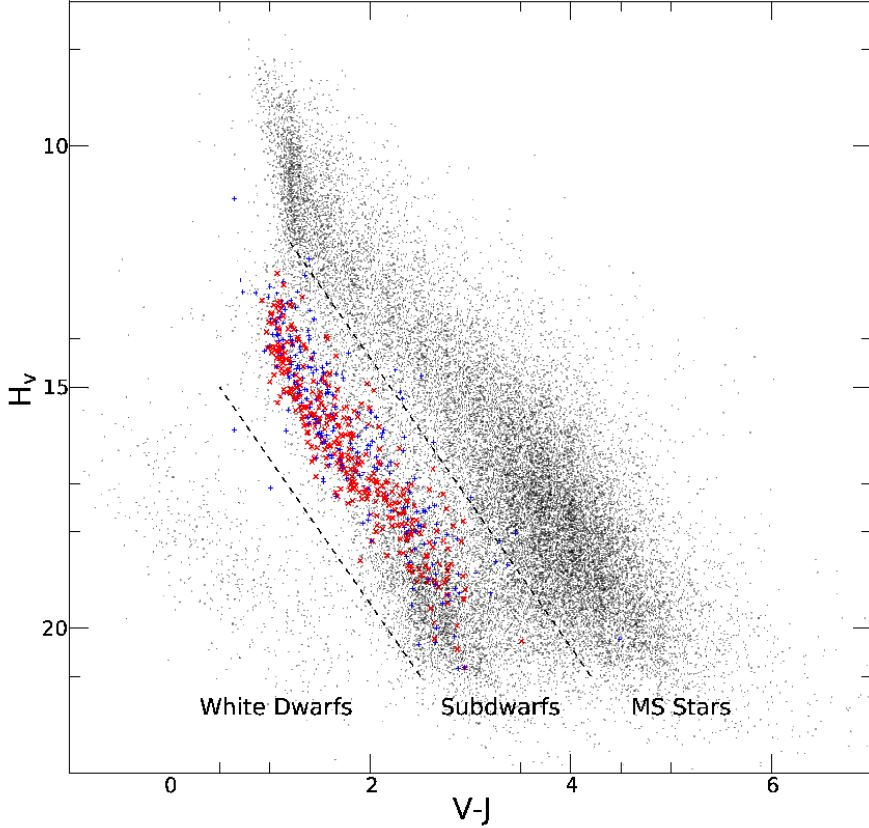


Figure 3.3: Reduced proper motion diagram of the complete rNLTT (Gould & Salim, 2003), with our observed subdwarfs in red X's, drawn from the photometric work of Marshall (2007). Unobserved candidate subdwarfs from Marshall (2007) are plotted as blue +'s. The discriminator lines, described in 3.2.1, between solar-metallicity dwarfs, metal-poor subdwarfs, and white dwarfs are at $\eta = 0$ and 5.15 , respectively, and with $b = \pm 30$. The subdwarfs plotted make use of the improved photometry of Marshall (2007).

stellar populations.

3.2 Survey Targets and Observations

3.2.1 Sample Selection

We selected targets from the 564 spectral type F- through M-subdwarf candidates studied by Marshall (2007). These targets were selected from the New Luyten Two-Tenths catalog (Luyten, 1979; Luyten & Hughes, 1980, NLTT) of high proper motion stars ($>0.18''/\text{year}$) using a reduced proper motion diagram (RPM). To distinguish subdwarf stars from their

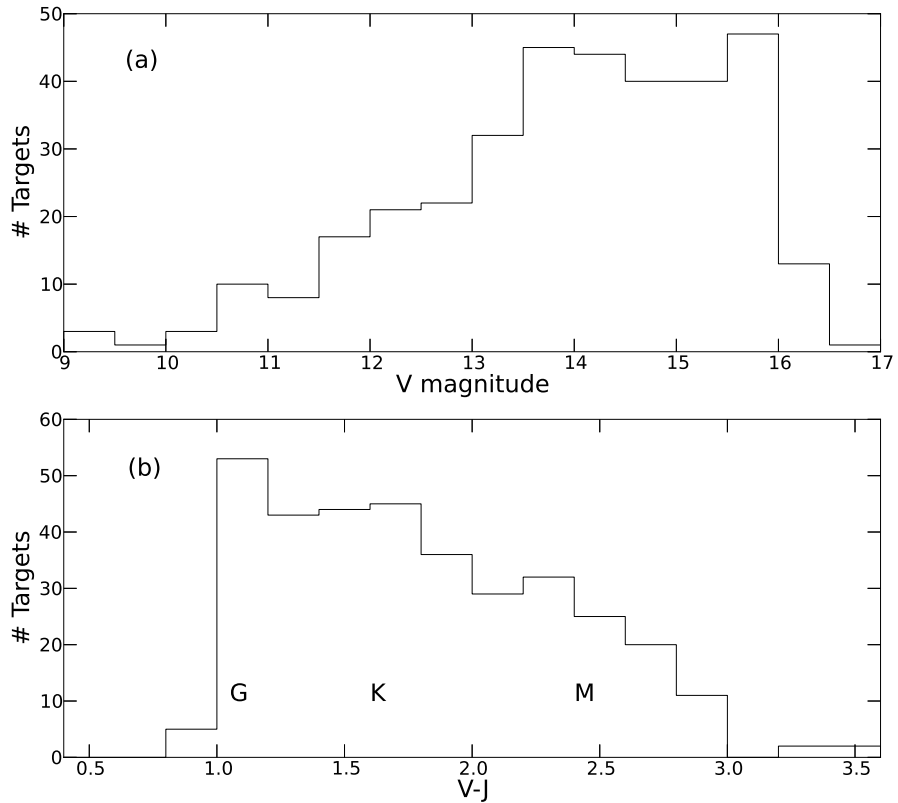


Figure 3.4: (a) Histogram of magnitudes in V band of the 348 observed subdwarfs. (b) Histogram of the $(V - J)$ colors of the observed subdwarf sample, with approximate spectral types regions G, K and M marked, using the spectral color indices of Ducati et al. (2001). Both plots use the photometry of Marshall (2007).

solar-metallicity companions on the main sequence, the RPM used a $(V - J)$ optical-infrared baseline, a technique first used by Salim & Gould (2002), rather than the shorter $(B - R)$ baseline used by Luyten. This method uses the high proper motion as a proxy for distance and the blueness of subdwarfs relative to equal luminosity dwarf stars to separate out main sequence members of the local disk and the halo subdwarfs (Marshall, 2008). The reduced proper motion, H_M , is defined as

$$H_M = m + 5\log\mu + 5 \quad (3.2.1)$$

where m is the apparent magnitude and μ is the proper motion in $''/\text{yr}$. The discriminator, η , developed by Salim & Gould to separate luminosity classes, is defined as

$$\eta(H_V, V - J, \sin b) = H_V - 3.1(V - J) - 1.47|\sin b| - 7.73 \quad (3.2.2)$$

where b is the Galactic latitude. The reduced proper motion diagram for the revised NLTT (rNLTT) catalog (Gould & Salim, 2003) and our subdwarf targets is presented in Figure 3.3. The improved photometry of Marshall (2007) placed 12 of the originally suspected subdwarfs outside the subdwarf sequence. These stars were not included in our sample. Possible dwarf contamination of our sample is expected to be small, as described in 3.3.3. Of the 552 subdwarfs confirmed by Marshall, a randomly-selected sample of 348 G-, K- and M-subdwarfs was observed by Robo-AO when available between other high priority surveys. The V-band magnitudes and $(V - J)$ colors of the observed subdwarf sample are sh

3.2.2 Observations

Robo-AO

We obtained high-angular-resolution images of the 348 subdwarfs during 32 separate nights of observations between 2012 September 3 and 2013 August 21 (UT). The observations were performed using the Robo-AO laser adaptive optics system (Baranec et al., 2013, 2014a;

Table 3.1: The specifications of the Robo-AO subdwarf survey

Filter	Sloan i' -band
FWHM resolution	0.15"
Field size	44" \times 44"
Detector format	1024 ² pixels
Pixel scale	43.1 mas / pix
Exposure time	120 seconds
Subdwarf targets	344
Targets observed / hour	20
Observation dates	September 1 2012 – August 21 2013

Riddle et al., 2012) mounted on the Palomar 60 inch telescope (see Section 1.1). The first robotic laser guide star adaptive optics system, the automatic Robo-AO system can efficiently observe large, high-resolution surveys. All images were taken using the Sloan i' -band filter (York et al., 2000) and with exposure times of 120 s. Typical seeing at the Palomar Observatory is between 0.8" and 1.8", with median around 1.1" (Baranec et al., 2014a). The typical FWHM (diffraction limited) resolution of the Robo-AO system is 0.12"-0.15". Images are recorded on an electron-multiplying CCD (EMCCD), allowing short frame rates for tip and tilt correction in software using a natural guide star ($m_V < 16$) in the field of view. Specifications of the Robo-AO system are summarized in Table 3.1.

The images were reduced by the Robo-AO imaging pipeline described in Law et al. (2009, 2014). The EMCCD output frames are dark-subtracted and flat-fielded and then, using the Drizzle algorithm (Fruchter & Hook, 2002), stacked and aligned while correcting for image motion using a star in the field. The algorithm also introduces a factor-of-two up-sampling to the images. Since the subdwarf targets are in relatively sparse stellar fields, for the majority of the images the only star visible is the target star and it was thus used to correct for the image motion.

Keck LGS-AO

Six candidate multiple systems were selected for re-imaging by the NIRC2 camera behind the Keck II laser guide star adaptive optics system (Wizinowich et al., 2000; van Dam et al., 2006a), on 2014 August 17 (UT) to confirm possible companions. The targets were selected for their low significance of detectability, either because of low contrast ratio or small angular separation. The observations were done in the K' and H bands with three 90 s exposures for two targets and three 30 second exposures for five targets in a 3-position dither pattern that avoided the noisy, lower-left quadrant. We used the narrow camera setting ($0.0099''/\text{px}$), which gave a single-frame field of view of $10'' \times 10''$.

SOAR Goodman Spectroscopy

We took spectra of 24 of the subdwarfs using the Southern Astrophysical Research Telescope (SOAR) and the Goodman Spectrograph (Clemens et al., 2004) on 2014 July 15. We observed twelve targets with companions and twelve single stars from the subdwarf sample as reference. The spectra were taken using a 930 lines/mm grating with $0.42 \text{ \AA}/\text{pixel}$, a $1.07''$ slit, and exposure times of 480 seconds.

3.3 Data Reduction and Analysis

3.3.1 Robo-AO Imaging

Target Verification

To verify that each star viewed in the image is the desired subdwarf target, we created Digital Sky Survey cutouts of similar angular size around the target coordinates. Each image was then manually checked to assure no ambiguity in the target star. The vast majority of the targets are in relatively sparse stellar regions. Four of the target stars in crowded fields whose identification was ambiguous were discarded, leaving 344 verified subdwarf targets.

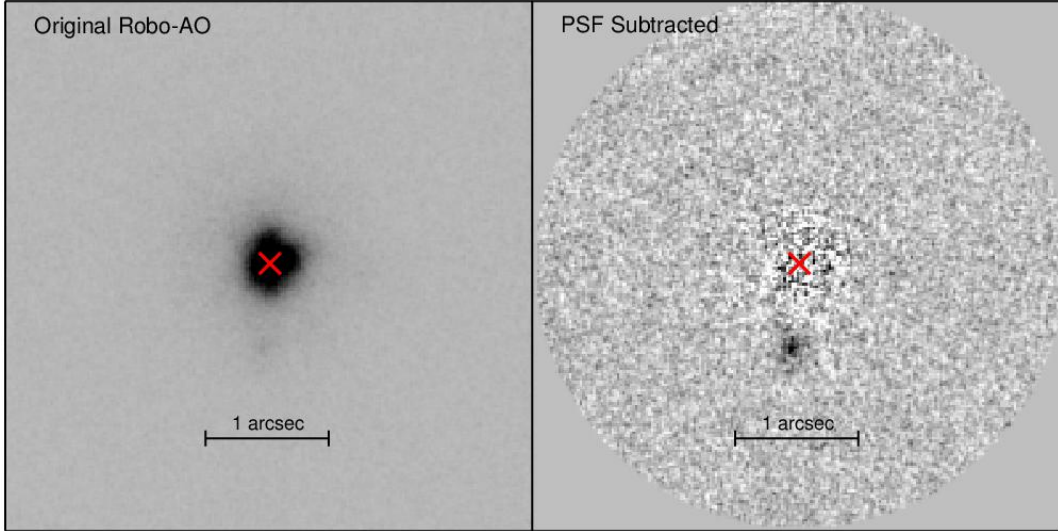


Figure 3.5: Example of PSF subtraction on NLTT31240 with companion separation of $0.74''$. The red X marks the position of the primary star’s PSF peak. Successful removal of the PSF leaves residuals consistent with photon noise.

PSF Subtraction

To locate close companions, a custom locally optimized PSF subtraction routine (Law et al., 2014) based on the Locally Optimized Combination of Images algorithm (Lafrenière et al., 2007) was applied to centered cutouts of all stars. Successful PSF subtraction requires similar reference images, taken at similar times, with similar instruments, and with reference stars of similar brightnesses. The set of subdwarf observations taken at similar times meet these criteria and were used as references, instead of dedicated reference observations, thus optimizing survey efficiency. This is made possible by the improbability of having a companion in the same position for two different targets.

For each target image and for 20 reference images selected as the closest to the target image in observation time, the region around the star was subdivided into polar sections, five up-sampled pixels in radius and 45° in angle. A locally optimized estimate of the PSF for each section was then generated using a linear combination of the reference PSFs. The algorithm begins with an average over the reference PSFs, then uses a downhill simplex algorithm to optimize the contributions from each reference image to find the best fit to

the target image. The optimization is done on several coincident sections simultaneously to minimize the probability of subtracting out a real companion, with only the central region outputted to the final PSF. This also provides smoother transitions between adjacent sections as many of the image pixels were shared in the optimization.

After iterating over all sections of the image, the final PSF is an optimal local combination of all the reference PSFs. This final PSF is then subtracted from the original reference image, leaving residuals that are consistent with photon noise. Figure 3.5 shows an example of the PSF subtraction performance.

We ran the PSF subtraction algorithm on all our targets out to a radius of $2''$. We subsequently reran the automated companion detection routine on the subtracted images to find significant ($>5\sigma$) close companions, and manually checked the results.

Automated Companion Detection

To efficiently find companions in the large data set, we developed a custom search algorithm, based on the method described in Law et al. (2014). The algorithm searches every 4-pixel diameter aperture in the image and compares the signal inside the aperture to the average noise level at that radius from the target star. The detected companions were then manually checked, eliminating spurious detections with dissimilar point spread functions (PSFs) to the target star and those having characteristics of a cosmic ray hit, such as a single bright pixel or bright streak.

Imaging Performance Metrics

The two dominant factors that effect the image performance of the Robo-AO system are seeing and target brightness. To further classify the image performance for each target an automated routine was run on all images. Described in detail in Law et al. (2014), the code uses two Moffat functions fit to the PSF to separate the widths of the core and halo. We found that the core size was an excellent predictor of the contrast performance, and used

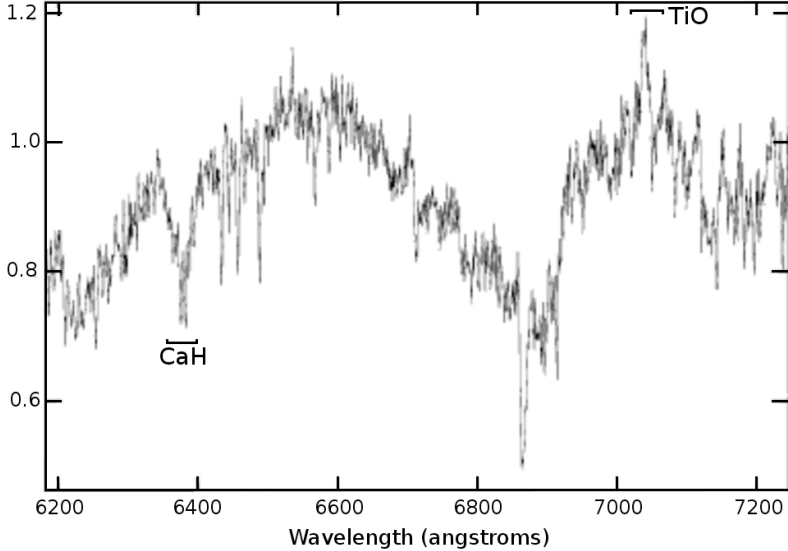


Figure 3.6: The extracted spectra for NLTT52532 showing subdwarf characteristics, most apparent the weakness of the 7050Å TiO band and strength of the 6380Å CaH band. The y-axis is given in normalized arbitrary flux units.

it to group targets into three levels (low, medium and high). Counter-intuitively, the PSF core size decreases as image quality decreases. This is caused by poor S/N on the shift-and-add image alignment used by the EMCCD detector. The frame alignment subsequently locks onto photon noise spikes, leading to single-pixel-sized spikes in the images (Law et al., 2006, 2009). The images with diffraction limited core size ($\sim 0.15''$) were assigned to the high-performance group, with smaller cores assigned to lower-performance groups. For our target observations, 32% fall in the low-performance group, 43% in the medium-performance group, and 25% in the high-performance group.

Using a companion-detection simulation with a group of representative targets, we determine the angular separation and contrast consistent with a 5σ detection. For clarity, the contrast curves of the simulated targets are fitted with functions of the form $a - b/(r - c)$ (where r is the radius from the target star and a , b , and c are fitting variables). Contrast curves for the three performance groups are shown in Section 3.4 in Figure 3.8.

Table 3.2: Full SOAR Spectroscopic Observation List

NLTT	m_v	ObsID	Companion?
2205	14.0	2014 Jul 14	yes
7301	14.9	2014 Jul 14	yes
7914	14.3	2014 Jul 14	yes
9597	12.0	2014 Jul 14	
9898	14.2	2014 Jul 14	
10022	15.8	2014 Jul 14	
10135	15.7	2014 Jul 14	
33971	12.8	2014 Jul 14	
37342	14.4	2014 Jul 14	yes
37807	12.0	2014 Jul 14	
40022	13.9	2014 Jul 14	
40313	13.7	2014 Jul 14	
41111	13.7	2014 Jul 14	
44039	11.5	2014 Jul 14	
44568	12.3	2014 Jul 14	
49486	16.0	2014 Jul 14	yes
50869	15.8	2014 Jul 14	
52377	14.5	2014 Jul 14	yes
52532	15.5	2014 Jul 14	yes
53255	15.0	2014 Jul 14	yes
55603	12.1	2014 Jul 14	yes
56818	14.0	2014 Jul 14	yes
57038	13.9	2014 Jul 14	yes
58812	14.9	2014 Jul 14	yes

Contrast Ratios

For wide companions, the binaries' contrast ratio was determined using aperture photometry on the original images. The aperture size was determined uniquely for each system based on separation and the presence of non-associated background stars.

For close companions, the estimated PSF was used to remove the blended contributions of each star before aperture photometry was performed. The locally optimized PSF subtraction algorithm attempts to remove the flux from companions using other reference PSFs with excess brightness in those areas. For detection purposes, we use many PSF core sizes for optimization, and the algorithm's ability to remove the companion light is reduced. However, the companion is artificially faint as some flux has still been subtracted. To avoid this, the PSF fit was redone excluding a six-pixel-diameter region around the detected companion. The large PSF regions allow the excess light from the primary star to be removed, while not reducing the brightness of the companion.

Separation and Position Angles

Separation angles were determined from the raw pixel positions. Uncertainties were found using estimated systematic errors due to blending between components. Typical uncertainty in the position of each star was 1-2 pixels. Position angles were calculated using a distortion solution produced using Robo-AO measurements for a globular cluster.¹

3.3.2 Previously Detected Binaries

To further realize our goal of a comprehensive cool subdwarf survey, we included in our statistics previously confirmed binary systems in the literature with separations outside of our field of view. Common proper motion is a useful indicator of wider binary systems. Wide ($>30''$) common proper motion companions among our target subdwarfs were previously

¹S. Hildebrandt (2013, private communication).

Table 3.3: Keck-AO Cool Subdwarf Observations

NLTT	m_v	ObsID	Companion?	ΔH
4817	11.4	2014 Aug 17		
7914	14.3	2014 Aug 17	yes	3.83
50869	15.8	2014 Aug 17		
52377	14.5	2014 Aug 17	yes	2.64
52532	15.5	2014 Aug 17	yes	0.53
53255	15.0	2014 Aug 17	yes	0.64
56818	14.0	2014 Aug 17	yes	0.69

identified in the Revised New Luyten Two-Tenths catalog (Salim & Gould, 2002; Chanamé & Gould, 2004, rNLTT), and a search by Lopez et al. (2012) of the Lepine and Shara Proper Motion-North catalog (Lépine & Shara, 2005, LSPM). None of our target stars overlap with the large survey of (Zhang et al., 2013), as our targets are several magnitudes brighter on average.

The target list was also cross-checked against the *Ninth Catalogue of Spectroscopic Binary Orbits* (Pourbaix et al., 2004, S_B^9), a catalog of known spectroscopic binaries available online.² While these systems were included in the total subdwarf binary numbers, the compilatory nature of this catalog leaves some uncertainty in the completeness of the spectroscopic search.

3.3.3 Goodman Spectroscopy

To further verify that the targets selected are cool subdwarfs, we took spectra of 7% of the total survey and 31% of the candidate companion systems. Past spectroscopic studies of cool subdwarfs at high resolution have proven difficult as, at the low temperatures present, a forest of molecular absorption lines conceals most atomic lines used in spectral analysis.

²<http://sb9.astro.ulb.ac.be/>

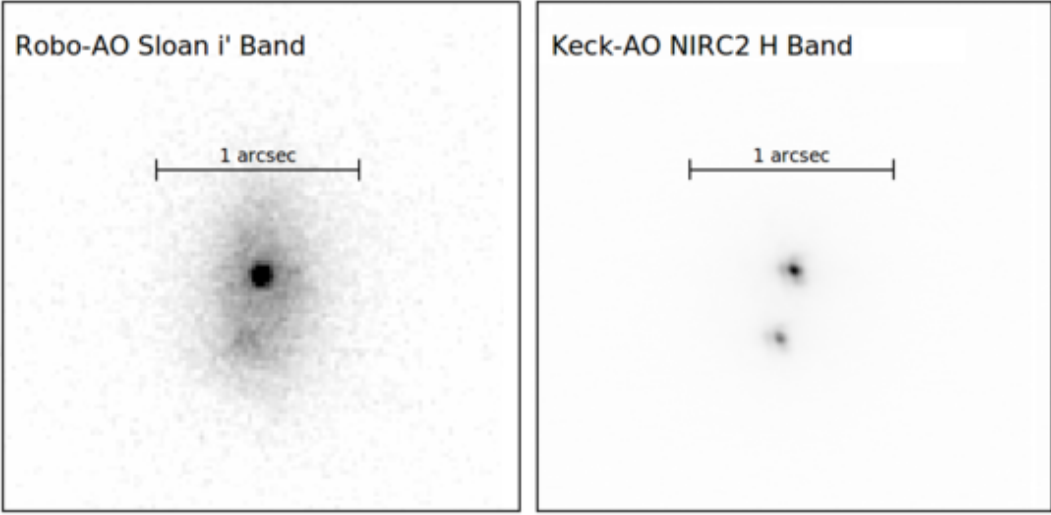


Figure 3.7: Keck-AO image confirming the Robo-AO companion to NLTT52532. The exposure times are 120 seconds for the Robo-AO image and 90 seconds for the Keck image.

Subdwarfs can be classified spectroscopically using two molecular lines (Gizis, 1997). Comparing titanium oxide (TiO) bands to metal hydride bands (typically CaH in M subdwarfs), Gizis classified two groups, the intermediate and extreme subdwarfs. As the metallicity decreases, the TiO adsorption also decreases, but the CaH remains largely unaffected for a given spectral type. This classification system was expanded and revised to include ultra subdwarfs by Lépine et al. (2007), who introduced the new useful parameter $\zeta_{TiO/CaH}$.

Spectra were taken for wavelengths 5900-7400Å, and reduced (dark-subtracted and flat-fielded) using IRAF reduction packages, particularly onedspec.apall to extract the trace of the spectrum and onedspec.dispcor for applying the wavelength calibration. A Fe+Ar arc lamp was recorded for wavelength calibration. All observed target subdwarfs were confirmed to show the spectral characteristics of subdwarf stars described above, specifically the reduced band strength of 7050Å TiO5. An example of the extracted spectra is given in Figure 3.6. The full observation list for SOAR is given in Table 3.2.

With all 24 sampled subdwarfs confirmed, spectroscopy alone gives a 95% confidence limit that the fractional dwarf contamination is below 0.12; the most likely contamination (50th percentile) below 0.03. This does not account, however, for the targets placement on a reduced proper motion diagram, which also suggests that the stars are in fact subdwarfs. We

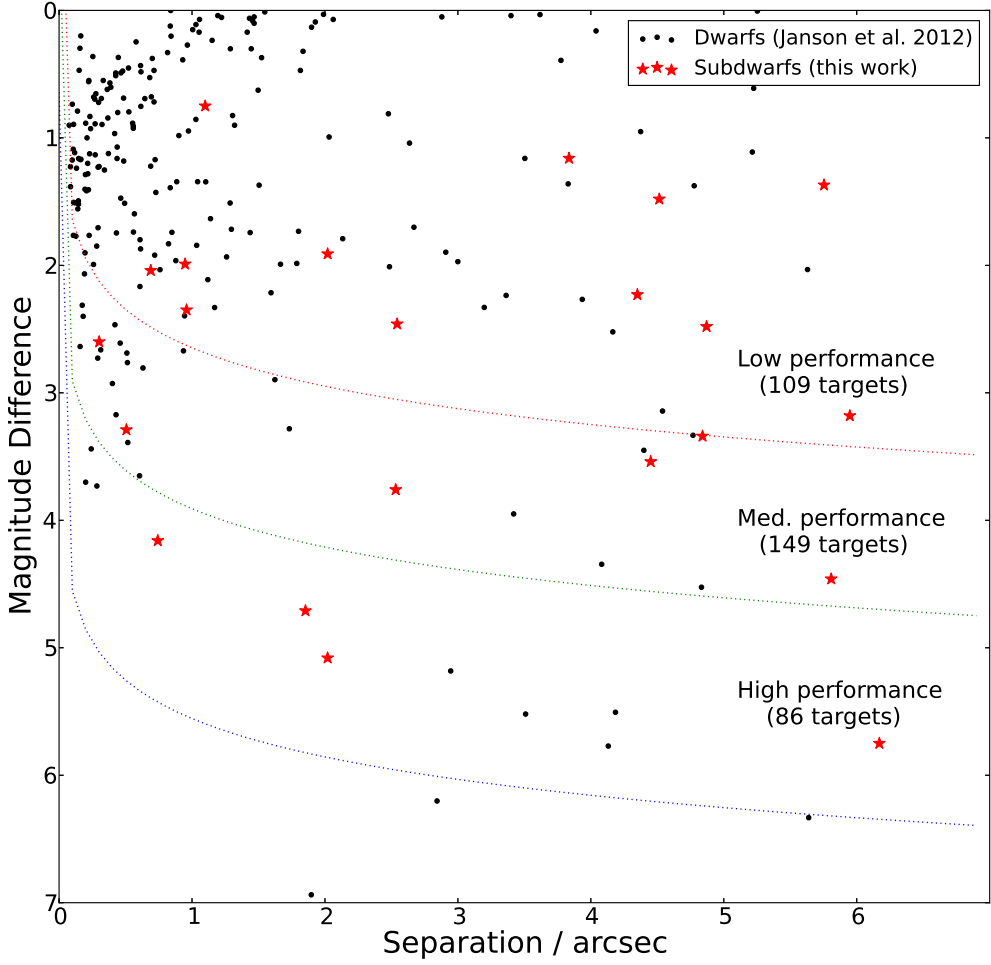


Figure 3.8: Comparison of the separation and the magnitude difference in the i-band between our subdwarf companions ($<6''$) and the dwarf companions found by Janson et al. (2012). The detectable magnitude ratios for our image performance groups are also plotted, with the number of observed subdwarf targets in each image performance group, as described in Section 4.2.5.

expect that the dwarf contamination is thus also lower than the small spectroscopic sample implies. We, therefore, consider targets not yet observed by SOAR to be probable, although unconfirmed, subdwarfs.

3.3.4 Candidate Companion Follow-ups

With either high contrast ratio or small angular separation, seven candidate subdwarf binary systems with low detection significance ($<6\sigma$) were selected for follow-up imaging using Keck II. One low-probability candidate companion star was rejected after followups

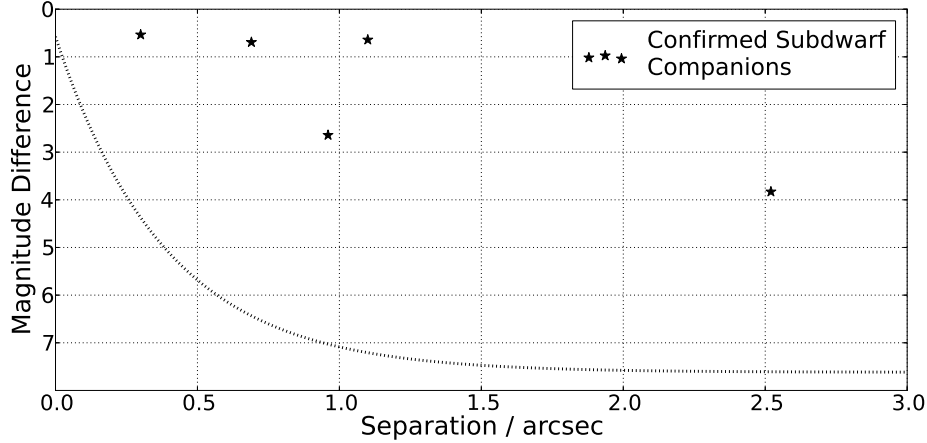


Figure 3.9: Plot of angular separation and H-band magnitude contrast for Keck confirmed subdwarf companions. The detectable magnitude ratios for the Keck images is plotted, as described in Section 4.2.5.

using Keck II, an apparent close ($\rho \simeq 0.15''$) binary to NLTT50869, probably resulting from a cosmic ray on the original Robo-AO image. A wider binary to NLTT50869, with high detection significance, was not in the image field of view. Outside of the six target stars with low significant companions, another candidate companion star, NLTT4817, was observed and had no companion inside the field of view of the Keck II image, however, had a high significance companion ($>7\sigma$) in the Robo-AO field of view. An example of the Keck II images and the Robo-AO images is given in Figure 3.7. The full Keck II observations are listed in Table 3.3, with the second to last column indicating the presence of a companion and the last column the H-band magnitude difference of the companion. Angular separations for the companions are listed in Table A.1. Confirmed companions and contrast curve for the Keck images are plotted in Figure 3.9. The area under the contrast curve was searched for all Keck images and was free of additional companions.

3.4 Discoveries

Of the 344 verified subdwarf targets observed, 43 appear to be in multiple star systems for an apparent binary fraction of $12.5\% \pm 1.9\%$, where the error is based on Poissonian statistics (Burgasser et al., 2003). This count includes 6 multiple systems first recorded in the NLTT,

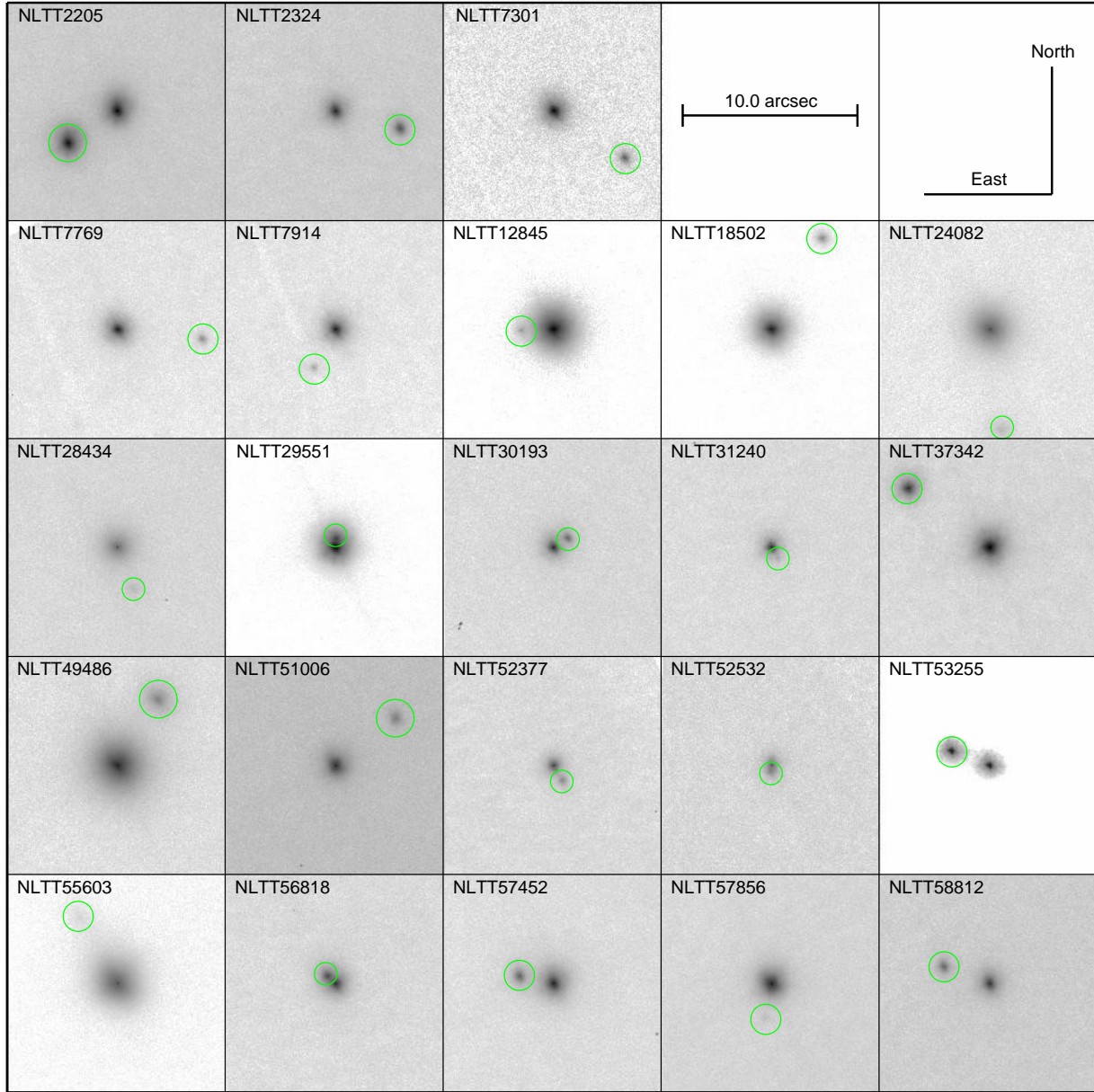


Figure 3.10: Color inverted, log-scale cutouts of the 23 multiple star systems with separations $<6''$ resolved with Robo-AO. The angular scale and orientation is similar for each cutout. The companions to NLTT 7914, 52377, 52532, and 56818 were confirmed with Keck II.

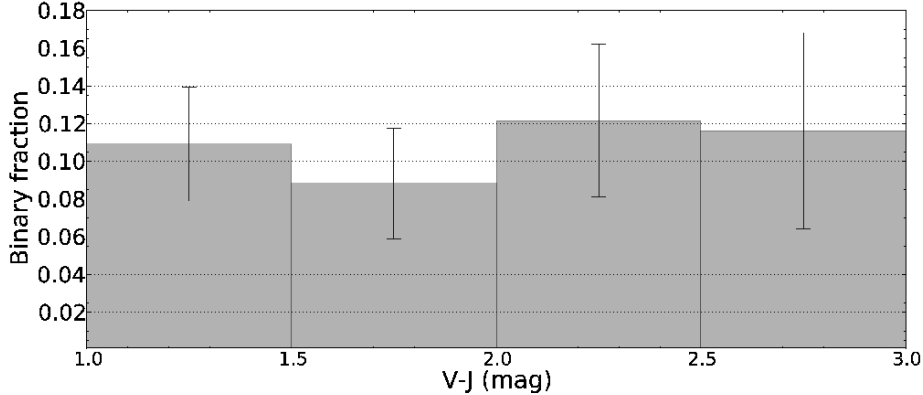


Figure 3.11: Binary fraction of the target subdwarfs binned by their $(V - J)$ color. The error bars were derived using binomial statistics.

13 systems first recorded in the rNLTT, 1 wide binary found in the LSPM (Lopez et al., 2012), 6 spectroscopic binaries, and 19 newly discovered multiple systems. We also found five new companions to already recorded binary systems, including two new triple systems, for a total of 7 triple star systems, for a triplet fraction of $2.0\%\pm.8\%$. One quarter (26%) of the companions would only be observable in a high-resolution survey ($<2.0''$ separation). The overarching dwarf trend of decreased binary fraction with later spectral types is not apparent for our sample of subdwarfs. This is seen in Figure 3.11, where the binary fraction of the target stars binned by their $(V - J)$ color is presented. Cutouts of the closest 22 multiple star systems are shown in Figure 3.10. Measured companion properties are detailed in Table A.1 in Appendix A.

3.4.1 Probability of Association

The associations of all discovered and previously recorded companions were confirmed using the Digitized Sky Survey (Reid et al., 1991, DSS) of the Palomar Observatory Sky Survey (Abell, 1959, POSS-I). Since all the targets have high proper motions, if not physically associated the systems would have highly apparent shifts in separation and position angle over the past six decades. For the widely separated systems with both stars visible in the DSS, we checked the angular separation in the DSS and our survey to confirm relatively

constant separation. For closely separated systems where both stars are merged in the DSS, we looked for a background star at the current position that does not appear in our images.

With the majority of POSS-I archival images taken between 1949 and 1956 and scanned with plate scale of $1''/\text{px}$, we can dissociate stars in the field with proper motion differences of $>16 \text{ mas/yr}$, and proper motion differences in right ascension and declination of $>8 \text{ mas/yr}$. To locate possible fake companions, we use the high-proper motion survey LSPM (Lépine & Shara, 2005), which is estimated over 99% complete in high galactic latitudes ($|b| > 15^\circ$), where most of our targets lie. Out of approximately 21 million possible associations, we identified 12,451 pairs of stars, one of our subdwarf targets and an LSPM star, which have similar (below our dissociation threshold) proper motion magnitude and direction. Known associated stars were removed from this sample. With our relatively small field of view and the large sky coverage of the LSPM, the probability of any of these pairs falling within our field of view is a remote 9.1×10^{-5} .

In addition, since our stars appear in relatively sparse stellar regions in the sky, well outside the Galactic disk, the probability of a background star appearing in a close radius to our observed star is low. Using the total number of known non-associated stars in our images, than at 95% confidence 7 of the 10 stars found within $2.5''$ of any of our background stars are associated, with 9 of 10 being the most likely number of associated stars. The small number of probable unassociated background stars in our fields and the DSS proper-motion confirmations suggest a high-likelihood for true association for all of our companion stars.

3.4.2 Photometric Parallaxes

Very few subdwarfs in our sample have accurate parallax measurements. Only 43 of the targets have published parallaxes, most with significant measurement errors. To estimate the distances to our subdwarf targets, we employed an expression for $M_R = F(R - I)$ estimated by Siegel et al. (2002) using a color-magnitude diagram and the photometric measurements by Marshall (2007).

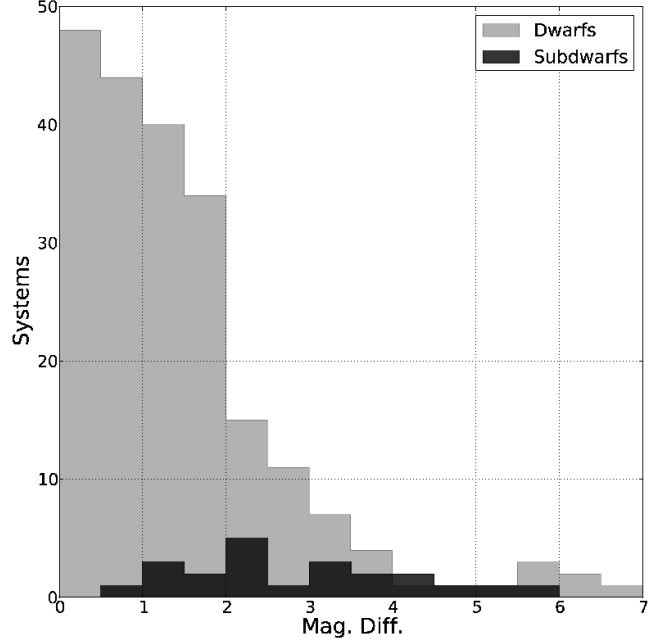


Figure 3.12: Histogram of the magnitude difference in the i-band between all our subdwarf companions and the dwarf companions found by Janson et al. (2012).

The polynomial fit found by Siegel for subdwarfs with measured parallaxes and an estimated mean [Fe/H] of -1.2, and with the Lutz & Kelker (1973) correction, is

$$M_R = 2.03 + 10 \times (R - I) - 2.21 \times (R - I)^2 \quad (3.4.1)$$

The color-absolute magnitude relation has an uncertainty of ~ 0.3 mag. In all cases, the published parallax errors are much larger than photometric errors of < 0.03 mag.

3.5 Discussion

3.5.1 Comparison to Main-Sequence Dwarfs

With comparable sample size and spectrum types, the cool dwarf survey of Janson et al. (2012) is a useful metal-rich analog to this work. The study used the Lucky Imaging technique on a sample of 761 stars, sensitive to companion separations of $0.08''$ - $6.0''$. The most striking disparity between the two samples is the lack of low-contrast ($\Delta m_i \leq 2$), close

$(\rho \leq 1'')$ companions to the subdwarf stars, a regime heavily populated by solar-metallicity dwarf companions. This is clearly seen in a plot of the companion's magnitude difference versus angular separation for the two populations, as in Figure 3.8.

The dissimilarity between contrast ratios between dwarfs and subdwarfs is further illustrated in Figure 3.12. A two-sample Kolmogorov-Smirnov test rejects the null hypothesis that the two populations are similar at a confidence of $\sim 2.8\sigma$.

The lack of close subdwarf companions has been noted previously by Jao et al. (2009) and by Abt (2008), however with significantly smaller samples. A direct comparison of orbital separations is biased by the distance variation in the two samples. With their rarity in the solar neighborhood, the subdwarf sample is overall approximately a factor of 4 further distant than the dwarf sample. If the populations were similar, this would result in a relative abundance of tight dwarf binaries, while the $6''$ limit of the Janson et al. survey reduces the number of observed wide dwarf binaries. Attempts to pick out similar systems by relative distance or by orbital separation from the two surveys results in a small statistical sample. Nonetheless, the relative lack of close stars in the subdwarfs sample, as illustrated in Figure 3.13, and confirmed at high-confidence in our survey, warrants further investigation.

3.5.2 Binarity and Metallicity

The binary fraction we have found further confirms what has been suspected by past studies: that the binary fraction of subdwarfs is substantially lower than their dwarf cousins. The largest survey of cool subdwarfs, although limited by the low angular resolution of the SDSS, Zhang et al. (2013), find a multiplicity for type late K and M subdwarfs of 2.41%, with an estimated lower bound of 10% when adjusting for survey incompleteness. This estimate and our work leave subdwarfs multiplicity rates approximately a factor of 2 to 4 lower than solar-metallicity stars of the same spectral types.

Historically, it has been a widely held view that metal-poor stars possess fewer stellar companions (Batten, 1973; Latham, 2004). A deficiency of eclipsing binaries was found in

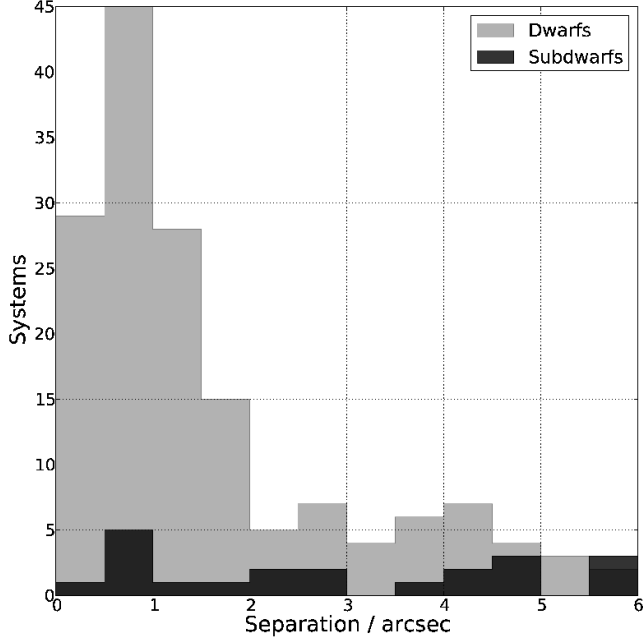


Figure 3.13: Histogram of the angular separations of our subdwarf companions and the dwarf companions found by Janson et al. (2012). Only systems resolvable in both surveys were plotted ($0.15'' < \rho < 6.0''$)

globular clusters by Kopal (1959), while Jaschek & Jaschek (1959) discovered a deficiency of spectroscopic binaries in a sample of high-velocity dwarfs. Abt & Willmarth (1987) used higher resolution CCD spectra to conclude that the frequency of spectroscopic binaries in high-velocity stars was half of metal-rich stars. Recently, however, this view has come under attack. Carney et al. (1994) used radial velocity measurements of 1464 stars, along with metallicity data (Carney et al., 1987), and found the difference in binary frequency of metal-rich and metal-poor stars to not be significant. Likewise, Grether & Lineweaver (2007) found a $\sim 2\sigma$ anti-correlation between metallicity and companion stars.

In recent years, the relationship between planetary systems and metallicity has also been explored. Fischer & Valenti (2005) found a positive correlation between planetary systems and the metallicity of the host star. This correlation has been reinforced to $\sim 4\sigma$ by Grether & Lineweaver (2007). Recently, Wang et al. (2014) found that planets in multiple-star systems occur 4.5 ± 3.2 , 2.6 ± 1.0 , and 1.7 ± 0.5 times less frequently when the companion star is separated by 10, 100, and 1000 AU, respectively.

The solution may lie in the differences between halo and thick disk stars. Latham et al. (2002) found no obvious difference between the binary fraction of the two populations, however, Chiba & Beers (2000) found a 55% multiplicity rate for thick disk stars and 12% for halo stars. Grether & Lineweaver also find that the thick disk shows a \sim 4 times higher binary fraction than halo stars, further hypothesizing that the mixing of the populations is the explanation for the perceived anti-correlation of metallicity and binarity. Similarly, Bovy et al. (2012) use spectroscopic data to chart the disk thickness, finding, instead of a bi-modal separation of the thin and thick disks, a smooth, continuous distribution. This suggests the absence of a distinct thick disk in the Milky Way.

The large difference between the M subdwarfs and thick-disk M dwarfs, apparent in our work in this paper and Janson et al. (2012), seems to imply the two populations formed under different initial conditions. Star formation in less dense regions appears to lower binary rates. Köhler et al. (2006) found a factor 3-5 difference in binary fraction between the low-density Taurus star-forming region and the dense Orion cluster. It is also possible that, as forming earlier than solar-abundance stars, the metal-poor subdwarfs could have suffered more disruptive encounters with other stars and the Galactic tide (Kaib et al., 2013). These disturbances could separate companions with separations larger than a few AU, with the tighter, more highly bound systems being less affected (Sterzik & Durisen, 1998; Abt, 2008), a theory derived from N -body simulations (Aarseth & Hills, 1972; Kroupa, 1995; Jiang & Tremaine, 2010). This, however, is contrary to our tentative result of a lack of close subdwarf companions, and the similar observations of Jao et al. (2009) and Abt (2008) that close subdwarf binaries are rare. This implies that metal-poor subdwarfs had shorter lifetimes in clusters than their younger, metal-rich cousins, either being ejected or formed in a disrupted cluster.

Another possible explanation is that a large number of low-metallicity stars in the Milky Way could have resulted from past mergers with satellite galaxies. Simulations from Abadi et al. (2006) predict that the early Galaxy underwent a period of active merging. From these

mergers, the Galaxy would inherit large numbers of metal-poor stars. Meza et al. (2005) observe a group of metal-poor stars with angular momenta similar to the cluster ω Cen, long theorized to be the core of a dwarf galaxy that merged with the Milky Way. The environment of these foreign galaxies is unknown, so star formation could be quite different than our own Galaxy. It is also possible that during the merger multiple close stellar encounters and perturbations could alter their primordial binary properties.

3.6 Conclusions

In the largest high-resolution binary survey of cool subdwarfs, we observed 344 stars with the Robo-AO robotic laser adaptive optics system, sensitive to companions at $\rho \geq 0.15''$ and $\Delta m_i \leq 6$. Of those targets, we observed 16 new multiple systems and 5 new companions to already known binary systems. When including previously recorded multiple systems, this implies a multiplicity rate for cool subdwarfs of $12.5\% \pm 1.9\%$ and a triplet fraction of $2.0\% \pm .8\%$. This is significantly lower than the observed cool subdwarf binarity of $26\% \pm 6\%$ by Jao et al. (2009) and in agreement with the completeness adjusted estimate of $> 10\%$ of Zhang et al. (2013). When comparing our results to similar surveys of non-subdwarf binarity, we note a $\sim 2.8\sigma$ difference in relative magnitude differences between companions. An apparent lack of close binaries is noted, as has been previously observed in the literature. The high efficiency of Robo-AO makes large, high-angular resolution surveys practical and will in the future continue to put tighter constraints on the properties of stellar populations.

CHAPTER 4: THE ROBO-AO KEPLER SURVEY

It is known that there are an infinite number of worlds, simply because there is an infinite amount of space for them to be in. However, not every one of them is inhabited. Therefore, there must be a finite number of inhabited worlds. Any finite number divided by infinity is as near to nothing as makes no odds, so the average population of all the planets in the Universe can be said to be zero. From this it follows that the population of the whole Universe is also zero, and that any people you may meet from time to time are merely the products of a deranged imagination.

— *The Hitchhiker’s Guide to the Galaxy*

In this chapter, I report the results of the Robo-AO KOI survey, high-angular resolution observations of every KOI with an automated LGS-AO instrument, Robo-AO. The results covered in this chapter were first presented in Ziegler et al. (2017a).

As introduced in Section 1.2, every KOI needs ground-based follow-up observations for characterization and confirmation. The challenge of performing high-angular resolution follow-up observations of the approximately 4000 planet candidates (*Kepler* objects of interest, or KOIs) discovered by *Kepler* (Borucki et al., 2010, 2011a,b; Batalha et al., 2013; Burke et al., 2014; Rowe et al., 2014; Coughlin et al., 2016; Morton et al., 2016; Mathur et al., 2017) has been met with considerable effort by the community (Howell et al., 2011; Adams et al., 2012, 2013; Lillo-Box et al., 2012, 2014; Horch et al., 2012, 2014; Marcy et al., 2014; Dressing et al., 2014; Gilliland et al., 2015; Wang et al., 2015a,b; Torres et al., 2015; Everett et al., 2015; Kraus et al., 2016; Furlan et al., 2017). Many of these surveys were performed with large-aperture telescopes, sensitive to close (tens of mas separation) and faint

(8-10 magnitudes fainter than the host star) nearby stars. However, the combined efforts of surveys with traditional high-resolution instruments—in particular, adaptive optics—has resulted in a piecemeal approach, covering less than half of the KOIs. This is in part a result of redundant observations of a small set of KOIs, as the target lists of these surveys are often biased towards bright stars. This bias also results in a high fraction of early-type stars and stars closer to the Sun, which skews any interpretations drawn from the data. In addition, disparities in the instruments and passbands of these observations may lead to inconsistent vetting as each survey has different detection sensitivities to nearby stars. The comprehensive statistics and correlations that can be derived from a homogeneous dataset of thousands of high-resolution images of multiple stellar systems hosting planets are extremely difficult to when using data from multiple surveys.

A complete, consistent high-resolution survey of all the KOIs with ground-based adaptive optics (AO) is limited by the typical overheads required with traditional systems. Taking advantage of the order-of-magnitude increase in time-efficiency provided by Robo-AO, the first robotic laser adaptive optics system, we are performing high-resolution imaging of every KOI system. The first paper in this survey, Law et al. (2014, hereafter Paper I), observed 715 *Kepler* planetary candidates, identifying 53 companions, with 43 new discoveries, for a detected companion fraction of $7.4\%\pm1.0\%$ within separations of $0.15''$ to $2.5''$. The second paper in this survey, Baranec et al. (2016, hereafter Paper II), observed 969 *Kepler* planetary candidates, identifying 202 companions, with 139 new discoveries, for a detected companion fraction of $11.0\%\pm1.1\%$ within separations of $0.15''$ to $2.5''$, and $18.1\%\pm1.3\%$ within separations of $0.15''$ to $4.0''$.

This chapter presents the observations of 1629 KOIs, around which we find 223 companions near 206 KOIs. Of these companions, 209 have not previously been imaged in high resolution. We find a companion fraction of $12.6\%\pm0.9\%$ within $4.0''$ of planetary candidate hosting stars.

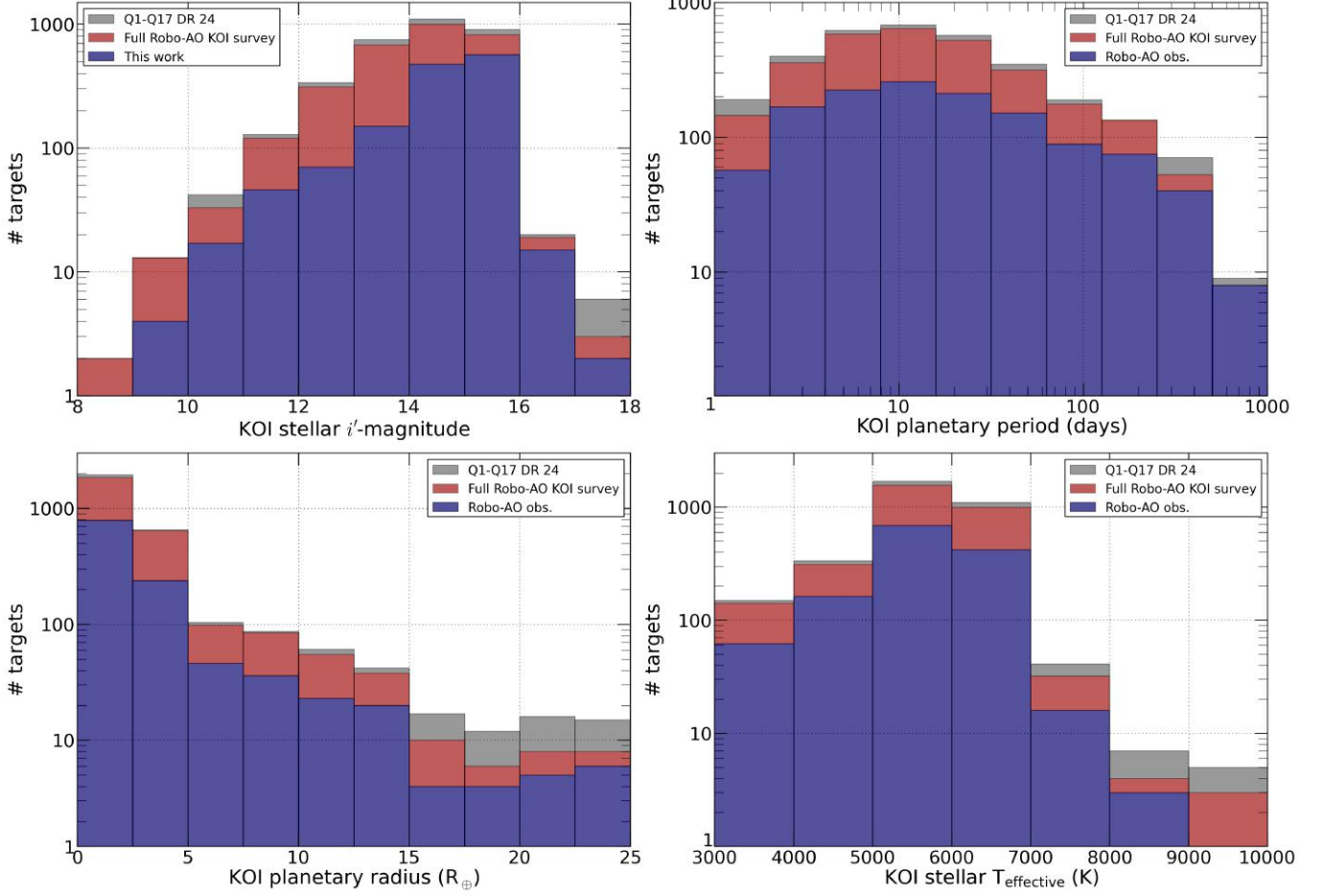


Figure 4.1: Comparison of the distribution of the Robo-AO sample in this paper as well as the combined Robo-AO survey (Paper I, Paper II, and this work) to the complete set of KOIs from Q1-Q17 (Borucki et al., 2010, 2011a,b; Batalha et al., 2013; Burke et al., 2014; Rowe et al., 2014; Coughlin et al., 2016).

4.1 Survey Targets and Observations

4.1.1 Observations

Robo-AO

We obtained high-angular-resolution images of the 1629 KOIs during 55 separate nights of observations between 2012 July 16 and 2015 June 12 (UT). The observations were performed using the Robo-AO laser adaptive optics system (Baranec et al., 2013, 2014a; Riddle et al., 2012) mounted on the Palomar 1.5-m telescope. The first robotic laser guide star adaptive optics system, the automatic Robo-AO system can efficiently perform large, high

angular resolution surveys. The AO system runs at a loop rate of 1.2 kHz to correct high-order wavefront aberrations, delivering a median Strehl ratio of 9% in the i' -band. Observations were taken in either a i' -band filter or a long-pass filter cutting on at 600 nm (LP600 hereafter). The LP600 filter approximates the *Kepler* passband at redder wavelengths, while also suppressing blue wavelengths that reduce adaptive optics performance.

Typical seeing at the Palomar Observatory is between 0.8" and 1.8", with median around 1.1" (Baranec et al., 2014a). The typical FWHM (diffraction limited) resolution of the Robo-AO system is 0.15". Images are recorded on an electron-multiplying CCD (EMCCD), allowing short frame rates for tip and tilt correction in software using a natural guide star ($m_V < 16$) in the field of view. Specifications of the Robo-AO KOI survey are summarized in Table 4.1.

Keck LGS-AO

Eight candidate multiple systems were selected for re-imaging by the NIRC2 camera behind the Keck-II laser guide star adaptive optics system (Wizinowich et al., 2006; van Dam et al., 2006b), on 2015 July 25 (UT) to confirm possible companions. The targets were selected for their low significance of detectability, either because of low contrast ratio or small angular separation. Observations were performed in the K_{prime} filter using the narrow mode of NIRC2 (9.952 mas pixel⁻¹; Yelda et al. 2010), dithering the primary target at intervals of 30 s into the 3 lowest noise quadrants, for a total exposure time of 90 s. The images were corrected for geometric distortion using the NIRC2 distortion solution of Yelda et al. (2010). Targets observed with Keck are detailed in Table 4.2. Further follow-up observations of low-significance companion detections are ongoing and will appear in future papers in this survey.

Table 4.1: The specifications of the Robo-AO KOI survey

KOI targets	1629
FWHM resolution	$\sim 0.15''$ (@600-750 nm)
Observation wavelengths	600-950 nm
Field size	$44'' \times 44''$
Detector format	1024^2 pixels
Pixel scale	43.1 mas / pix
Exposure time	90 seconds
Targets observed / hour	20
Observation dates	2012 July 16 – 2015 June 12

Gemini LGS-AO

Seven candidate multiple systems from this work and three from Paper I and Paper II, again selected for their low detection significance, were re-imaged with the adaptive optics assisted NIRI instrument (Hodapp et al., 2003) on the Gemini North telescope. Three targets were observed on 2015 July 31 (UT) and seven targets were observed on 2015 August 27, using Band 3 allocated time. Targets observed with Gemini are detailed in Table 4.3. Observations were performed with the F/32 camera, providing resolution of $21.9 \text{ mas pixel}^{-1}$ across a field of view of $22'' \times 22''$. Total integration times were 90 s in the K_{prime} band across three dithered images, used to increase dynamic range and allow sky subtraction. The common striping pattern found in NIRI images was removed using the *cleanir.py* script provided by the Gemini staff. The images were flat fielded, bad pixel corrected, and sky subtracted. The distortion solution provided by the Gemini staff was used to correct the images for distortion.

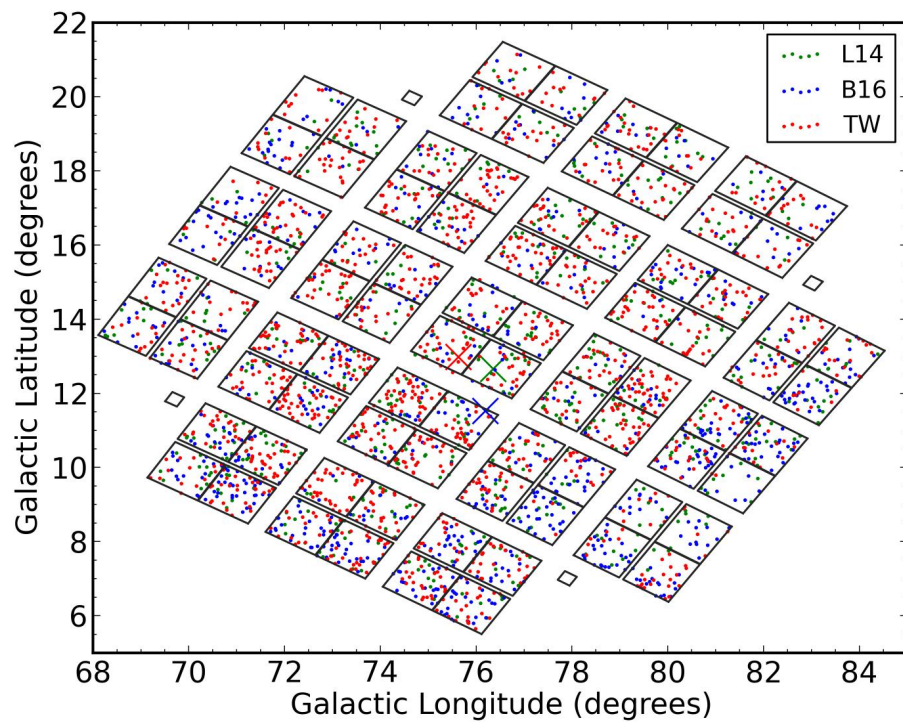


Figure 4.2: Location on sky of targeted KOIs from Paper I (L14), Paper II (B16), and this work (TW). The median coordinates of the targeted KOIs are designated by a ‘ \times ’. A projection of the *Kepler* field of view is provided for reference.

4.2 Data Reduction

With a large adaptive optics dataset acquired by Robo-AO, the data reduction process was automated as much as possible for efficiency and consistency. After initial pipeline reductions described in Section 4.2.1, the target stars were identified (Section 4.2.2), PSF subtraction performed (Section 4.2.3), nearby stars identified by visual inspection and by an automated companion search algorithm (Section 4.2.4), and constraints of the nearby star sensitivity of the survey measured (Section 4.2.5). Finally, the measurement of the properties of the detected companions is described in Section 4.2.6.

4.2.1 Imaging Pipeline

The Robo-AO imaging pipeline (Law et al., 2009, 2014) reduced the images: the raw EMCCD output frames are dark-subtracted and flat-fielded and then stacked and aligned using the Drizzle algorithm (Fruchter & Hook, 2002), which also up-samples the images by a factor of two. To avoid tip/tilt anisoplanatism effects, the image motion was corrected by using the KOI itself as the guide star in each observation.

4.2.2 Target Verification

To verify that the star viewed in the image is the desired KOI target, we created Digital Sky Survey and UKIRT (Lawrence et al., 2007) cutouts of similar angular size around the target coordinates. Each image was manually checked to assure no ambiguity in the target star and images with either poor performance or incorrect fields were removed. These bad images made up approximately 1% of all our images, and for all of the targets, additional images were available.

We select a 4" separation cutoff for our companion search to detect all nearby stars that would blend with the target KOI in a *Kepler* pixel. To facilitate the automation of the data reduction, centered 8.5" square cutouts were created around the verified target KOIs, slightly larger than the diameter of our adopted separation limit so as to not remove a portion of

the PSF of any nearby star within 4”.

4.2.3 PSF Subtraction

To identify close companions, a custom locally optimized point spread function (PSF) subtraction routine based on the Locally Optimized Combination of Images algorithm (Lafrenière et al., 2007) was applied to centered cutouts of every star. The code uses a set of twenty KOI observations, selected from the observations within the same filter closest to the target observation in time, as reference PSFs. A locally optimized PSF is generated and subtracted from the original image, leaving residuals consistent with photon noise. This procedure was performed on all KOI images out to a radius of 2” from the host star. Figure 4.3 shows an example of the PSF subtraction performance. The PSF subtracted images were subsequently run through the automated companion finding routine, as described in Section 4.2.4.

PSF Subtraction Collisions

By using other Robo-AO observations of KOIs as reference images, there is a possibility that an image used as a reference PSF will have a nearby star at a similar position with respect to its host star as the image being modeled. Only companions at separations less than 1” could potentially avoid detection by both our visual search and the automated companion detection routine. Such a scenario (a “collision”) could lead to real companions being removed from target images if they coincide with a reference star’s companion. To estimate how near to each other the companions must be for a collision to occur, we ran the PSF subtraction routine on a set of ten targets which have detected nearby stars at varying separations within 1”. We then include a copy of each target image as one of the reference PSFs. In each case, the nearby star is not detected in the subtracted image by eye or by the automated companion detection routine with a significance $>3\sigma$. The reference image is then rotated by two degrees, and the PSF subtraction routine is rerun. This process is

iterated until the nearby star is able to be detected in the subtracted image. We find on average the companion in the reference image must be within $0.05''$ of the position of the nearby star in the original image for a collision to occur.

To estimate the expected number of collisions in our analysis, we use the observed distribution of nearby stars from our survey to populate a simulated KOI survey. For each nearby star detected with separations less than $1''$, we randomly drew twenty other reference stars. We counted every time a reference star fell within $0.05''$ of the original star as a collision. With 100 simulations performed, we estimate the number of expected companions missed in our survey due to collisions is 0.44 ± 0.18 , or approximately one every two surveys.

The visual search for companions, however, will greatly reduce the number of expected companions missed in our analysis. Within our observations, we find two potential collisions (KOIs 3497 and 4098, and KOIs 6202 and 6602). Neither of these sets of colliding images was used as a reference image for each other in the initial data analysis. We reran the PSF subtraction routine for both sets using the colliding system for each as a reference image. In each case, the nearby star is only partially subtracted and is still detectable within the subtracted image. This suggests that slight alterations in the Robo-AO PSFs are sufficient to effectively eliminate the possibility that a real companion will be erroneously subtracted off by the PSF subtraction routine.

4.2.4 Companion Detection

An initial visual companion search on the original and PSF-subtracted images was performed redundantly by two people. This search yielded a preliminary companion list and filtered out bad images.

Continuing the companion search, we ran all images through a custom automated search algorithm, based on the code described in Paper I. The algorithm slides a 5-pixel diameter aperture within concentric annuli centered on the target star. For each annulus, the mean and standard deviation of the local noise is estimated using the fluxes within these apertures,

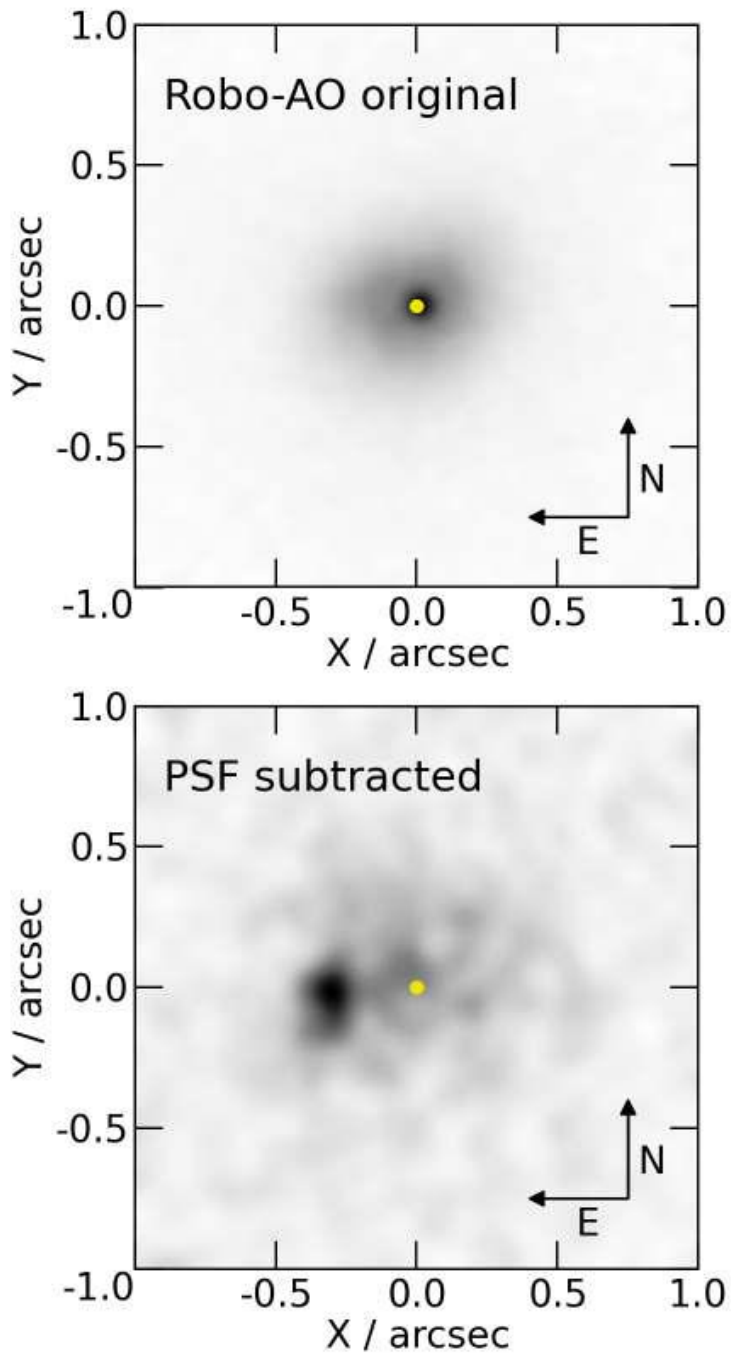


Figure 4.3: Example of PSF subtraction on KOI-5762 with companion separation of $0.34''$. The yellow circle marks the position of the primary star's PSF peak. Both images have been scaled and smoothed for clarity. Successful removal of the PSF leaves residuals consistent with photon noise. The $2''$ square field shown here is approximately equal to half the *Kepler* pixel size. The close companion to KOI-5762 was confirmed with NIRC2/Keck images.

with a sigma clip employed to remove any anomalously high signals such as those arising from a real astrophysical source. Any aperture with a summed signal greater than $+5\sigma$ compared to the local noise is considered a potential astrophysical source. These are subsequently checked manually, eliminating spurious detections with dissimilar PSFs to the target star and those having characteristics of a cosmic ray hit, such as a single bright pixel or bright streak.

4.2.5 Imaging Performance Metrics

The two dominant factors that affect the image performance of the Robo-AO system are seeing and target brightness. An automated routine was used to classify the image performance for each target. The code uses PSF core size as a proxy for image performance. Observations were binned into three performance groups, with 31% fall in the low-performance group, 41% in the medium performance group, and 28% in the high-performance group.

We determine the angular separation and contrast consistent with a 5σ detection by injecting artificial companions, a clone of the primary PSF.¹ For concentric annuli of $0.1''$ width, the detection limit is calculated by repeatedly dimming the artificial companion until the auto-companion detection algorithm (Section 4.2.4) fails to detect it. This process is subsequently performed at multiple random azimuths within each annulus, and the limiting 5σ magnitudes are averaged. For clarity, these average magnitudes for all radii measurements are fitted with functions of the form $a \times \sinh(b \times r + c) + d$ (where r is the radius from the target star and a , b , c and d are fitting variables). The limiting contrast curves from observations with Robo-AO at Palomar and Kitt Peak were determined and found to be similar. Typical contrast curves for the three performance groups are shown in Figure 5.3.

¹We find that for Robo-AO data the companion injection method provides a more realistic measure of the detection sensitivity compared to mapping the contrasts consistent with a 5σ excursion from the background noise, which results in contrast curves artificially a half-magnitude or more deeper.

4.2.6 Nearby Star Properties

Contrast Ratios

For wide, resolved companions with little PSF overlap, the companion to primary star contrast ratio was determined using aperture photometry on the original images. The aperture radius was cycled in one-pixel increments from 1-5 FWHM for each system, with background measured opposite the primary from the companion (except in the few cases where another object falls near or within this region in the image). Photometric uncertainties are estimated from the standard deviation of the contrast ratios measured for the various aperture sizes.

For close companions, the estimated PSF was used to remove the blended contributions of each star before aperture photometry was performed. The locally optimized PSF subtraction algorithm can attempt to remove the flux from companions using other reference PSFs with excess brightness in those areas. For detection purposes, we use many PSF core sizes for optimization, and the algorithm's ability to remove the companion light is reduced. However, the companion is artificially faint as some flux has still been subtracted. To avoid this, the PSF fit was redone excluding a six-pixel-diameter region around the detected companion. The large PSF regions allow the excess light from the primary star to be removed, while not reducing the brightness of the companion.

Separation and Position Angles

Separation and position angles were determined from the raw pixel positions. Uncertainties were found using estimated systematic errors due to blending between components. Typical uncertainty in the position of each star was 1-2 pixels. Position angles and the plate scale for observations at Palomar were calculated using a distortion solution produced using Robo-AO measurements for the globular cluster M15.²

²S. Hildebrandt (2013, private communication)

4.3 Discoveries

Of the 1629 KOI targets observed, 206 are apparent in multiple star systems for a nearby star fraction within 4" of $12.6\%\pm0.9\%$ ³. We also found 15 triple systems for a triplet fraction of $0.92^{+0.30}_{-0.18}\%$ ⁴, and 1 quadruple system for a quadruplet fraction of $0.06^{+0.14}_{-0.02}\%$ ¹¹. One quarter (25.8%) of the companions would only be observable in a high-resolution survey (<1.0" separation), and one half (49.8%) of the companions are too close (<2.0") for many seeing limited surveys to accurately measure binary properties (e.g. contrast ratios). The detected companion separations and contrast ratios are plotted in Figure 5.3, along with the calculated 5σ detection limits as detailed in Section 4.2.5. Cutouts of all multiple star systems are shown in Appendix F.

We confirmed six companions to eight Robo-AO detections with NIRC2 and AO on Keck-II (Wizinowich et al., 2000). In addition, two new companions were found around KOIs 2554 and 3020. These targets were selected for follow-up because of their faintness and/or closely separated detected companion. Low-sigma, visually detected companions to KOIs 1873 and 5257 were not detected. These non-detected companions are possibly a result of non-common path aberrations, as described in Section 5.1 of Paper II. These spurious detections all have similar separations and position angles with respect to the target star, facilitating their identification and manual removal. The PSF subtraction routine usually does not remove these false companions, as another star exhibiting the non-common path error is unlikely to be within the set of twenty reference images. The Keck-II observations are listed in Table 4.2 and the follow-up images are shown in Figure 4.4.

We confirmed five companions to seven KOIs observed in this paper with NIRI and AO on Gemini North. We did not detect a possible companion to KOI-2198 that was visually detected, manifesting as an elongated PSF in the Robo-AO image. We observed three KOIs

³Error based on Poissonian statistics (Burgasser et al., 2003)

⁴Error based on binomial statistics (Burgasser et al., 2003)

Table 4.2: Full Keck-AO Observation List

KOI	m_v	ObsID	Companion?	ΔK_p	Note
1447	13.2	2015 Jul 25	yes	0.63 ± 0.06	
1873	15.8	2015 Jul 25			
2117	16.2	2015 Jul 25	yes	0.53 ± 0.06	
2554	15.9	2015 Jul 25	yes	0.27 ± 0.05	Companion at $\rho=0.37''$
			yes	2.96 ± 0.10	New companion at $\rho=3.55''$
3020	13.8	2015 Jul 25	yes	1.27 ± 0.06	Companion at $\rho=0.38''$
			yes	5.01 ± 0.07	New companion at $\rho=3.86''$
3106	15.7	2015 Jul 25	yes	1.22 ± 0.13	
5257	15.5	2015 Jul 25			
5762	15.9	2015 Jul 25	yes	0.83 ± 0.08	

targeted in Paper I (KOI-327) and Paper II (KOIs 2833 and 4301) which displayed non-common path error aberrations. No companions were observed to these three targets in the follow-up observations. A new companion outside our separation cutoff ($\rho=4.24''$) was observed nearby KOI-4131. The Gemini observations are listed in Table 4.3.

4.3.1 Comparison to Other Surveys

Two detected companions (KOI-326 and KOI-841) in our survey were previously found in Lillo-Box et al. (2012), who observed 98 KOIs using the AstraLux Lucky Imaging system on the 2.2m telescope at the Calar Alto Observatory. Lillo-Box et al. (2014) also previously detected companions to KOI-3263, 3649, and 3886 in a survey of 174 KOIs. Adams et al. (2012) and Adams et al. (2013) observed 87 and 13 KOIs, respectively, with the instruments ARIES and PHARO on the MMT and Palomar telescopes, respectively. They detect companions to KOI-126 and 266 that are fainter than our survey sensitivity. Observing 87 KOIs with ARIES at the MMT, Dressing et al. (2014) previously detected companions to KOI-2813 and KOI-3111 and also detected a companion to KOI-266 ($\Delta m_{K_s}=6.32$) that is outside our detection sensitivity. Gilliland et al. (2015) found two companions to KOI-829 using the

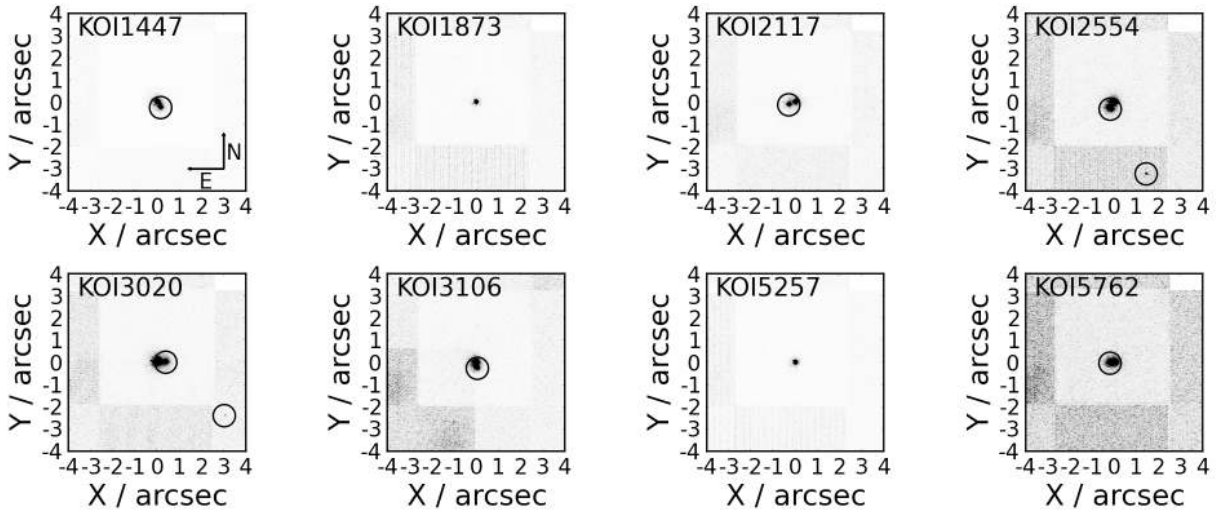


Figure 4.4: Normalized log-scale cutouts of 8 KOIs observed with the NIRC2 instrument on Keck-II, as described in Section 3.2.2. The angular scale and orientation (displayed in the first frame) is similar for each cutout, and circles are centered on the detected nearby stars.

Table 4.3: Full Gemini Observation List

KOI	m_v	ObsID	Companion?	ΔK_p	Note
327	13.1	2015 Aug 27			
2198	12.8	2015 Aug 27			
2833	12.8	2015 Aug 27			
4131	13.2	2015 Jul 31	yes	4.41 ± 0.09	Companion at $\rho=2.85''$
			yes	4.96 ± 0.11	New companion at $\rho=4.24''$
4301	13.3	2015 Aug 27			
5052	12.8	2015 Jul 31	yes	0.75 ± 0.04	
5164	12.6	2015 Aug 27			
5243	12.5	2015 Jul 31	yes	0.53 ± 0.05	Companion at $\rho=0.77''$
			yes	4.11 ± 0.09	Companion at $\rho=2.41''$
5497	11.0	2015 Aug 27			
5774	11.1	2015 Aug 27	yes	1.54 ± 0.04	

Hubble Space Telescope (HST) with Δm_{K_p} of 2.4 and 6.0 and separations of 0.11" and 3.31", respectively, which were outside the detection limits of our Robo-AO image. Wang et al. (2015a) observed 84 KOIs using the PHARO and NIRC2 instruments at Palomar and Keck, respectively, with one discovered companion (KOI-3678) appearing in our survey. Two of our targets (KOI-1411 and KOI-3823) have companions detected by Wang et al., both with $\Delta m_K > 5$, which fall outside our detection sensitivity. Wang et al. (2015b) observed 73 multiple transiting planet KOI systems at Palomar and Keck, with the only overlapping system being a companion observed near KOI-1806 which we did not detect. The companion to KOI-1806, measured by Wang et al. (2015b) as $\Delta K=1.45$ at 3.43" separation, is well within our survey sensitivity, and the reason for the non-detection is unclear. The reported companion is also not visible in UKIRT images, although it would be detectable. We detected companions to KOI-126 and 200 not detected by Howell et al. (2011); both companions are within the stated sensitivity limits for their respective targets, so the reason for the earlier non-detection is unclear. None of our nearby-star detections overlap with the discoveries of Everett et al. (2015).

Kraus et al. (2016) observed 382 KOIs with AO on the Keck-II telescope. They detected single companions to KOI-255, 1908, 2705, and 2813, and both companions to KOI-1201 that were detected in our survey. They also detected single companions to KOI-1298, 1681, 2179 2453, and 2862, and double companions to KOI-1361 and 2813, that all fall outside of our reported sensitivity.

Kolbl et al. (2015) searched for the blended spectra of KOIs with secondary stars within $\sim 0.8"$ using Keck-HIRES optical echelle spectra of 1160 California *Kepler* Survey KOIs. Of the 63 KOIs the authors found with evidence of a secondary star, we found companions to seven (KOIs 1137, 2813, 3161, 3415, 3471, 4345, 4713) and did not detect companions to eight (KOIs 1121, 1326, 1645, 3515, 3527, 3605, 3606, 3853). The companions we did not detect likely lie at small separations inside the limits of our survey sensitivity. Two of our companions (KOIs 1137 and 3415) fall within their calculated flux ratio uncertainty

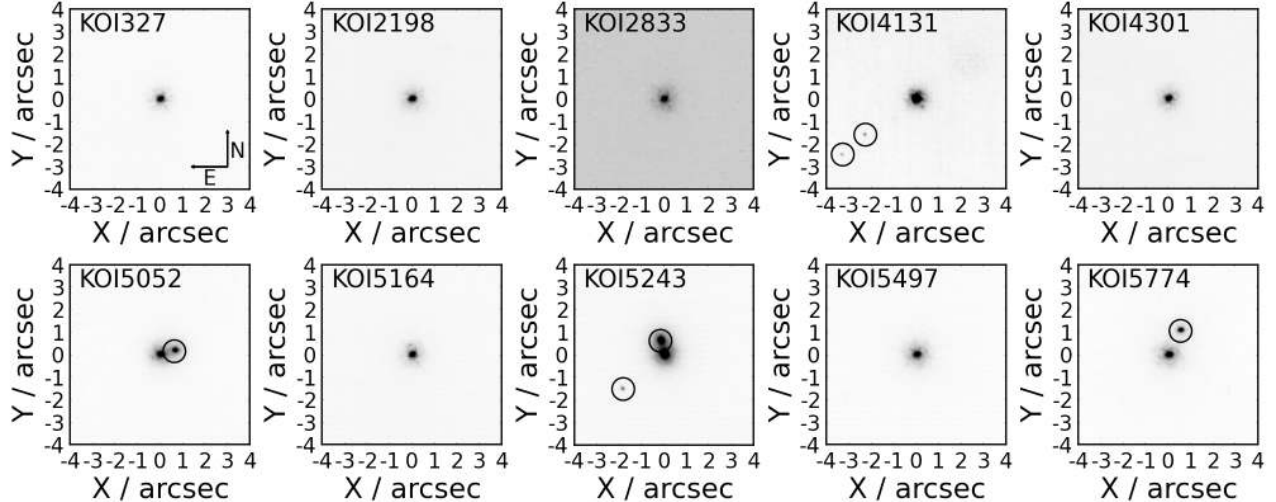


Figure 4.5: Normalized log-scale cutouts of 10 KOIs observed with the NIRI instrument on Gemini North, as described in Section 4.1.1. The angular scale and orientation (displayed in the first frame) is similar for each cutout, and circles are centered on the detected nearby stars.

and within their $\sim 0.8''$ separation limit. Without known separations and position angles, however, it is not clear that these are the same companion stars.

Nine of the widest nearby stars we detected have 2MASS (Skrutskie et al., 2006a) designations. 102 of our wide ($\rho > 2''$) nearby star detections are noted on the *Kepler* Community Follow-up Observing Program (CFOP) using J-band, $\sim 1''$ seeing-limited imaging from United Kingdom InfraRed Telescope (UKIRT) (Lawrence et al., 2007). However, with high-acuity imaging to resolve blended companions, providing greater precision photometry, and a filter that better simulates the *Kepler* bandpass, the Robo-AO survey can better evaluate the effect of the companion on the observed transit signal.

4.3.2 Multiplicity and Other Surveys

There have been multiple past high-resolution surveys of KOIs performed, allowing our results to be put into context with the overall community follow-up program. A comparison of the observed nearby-star rates from various surveys with differing methodologies may also provide convergence on the intrinsic multiplicity rate of planet-hosting stars. With varying

sensitivities between surveys, we use a lower separation cutoff than in this paper for a uniform comparison between surveys. This also has the added benefit of using only the nearest stars that have the highest probability of association. An exact comparison between surveys is still hindered, however, by the use of dissimilar instruments, passbands, and target selection criteria; in comparing results in this section we attempt to highlight major differences when comparing multiplicity rates, however, we caution that in each case there are inherent biases in the coverage of the different surveys which requires detailed analysis not covered in this work.

We find that 6.8% of KOIs have nearby stars within 2", in agreement with other visible light surveys: 6.4% in Paper I, 8.2% in Paper II, and 6.4% (Howell et al., 2011). Horch et al. (2014) found 7.0% of KOI targets had nearby stars within 1" separation, a range where we showed a 3.4% nearby star rate. Horch et al. (2014) do not report their target list, so it is not possible to identify the source of this discrepancy. It is possible that this is a result of our target selection of every KOI, resulting in a dimmer overall sample than surveys which prioritize brighter targets. The targets in this paper have a median $K_{p,med} = 14.9$, significantly fainter overall than the targets in Adams et al. (2012, $K_{p,med} = 12.2$), Dressing et al. (2014, $K_{p,med} = 13.3$), Wang et al. (2015a, $K_p < 14$), Paper I ($K_{p,med} = 13.7$), and in Paper II ($K_{p,med} = 14.2$). Horch et al. (2014) note that their *Kepler* targets mainly are between 11th and 14th magnitude. There are several reasons a brighter overall target list will inflate binarity rates: the target stars are intrinsically more luminous, which results in more physically associated companion stars as binarity correlates with luminosity (Duchêne & Kraus, 2013); the target stars are less distant, so physically associated companion of a given spectral type is brighter, thus easier to detect; brighter stars tend to have deeper detectable contrast ratios.

The disparity in multiplicity between papers in the Robo-AO survey was explored in Section 6 of Paper II as a possible result of the bias in the KOI selection process between data releases, with the median observed KOI in Paper II located nearer the Galactic plane

than in Paper I. KOIs near the Galactic plane lie in denser stellar fields, increasing the likelihood of unassociated nearby stars with the separation cutoff. Plotting the *Kepler* field of view with our targeted KOIs in Figure 4.2, the median position of KOIs in this work is closer to the center of the field than in Paper II, and further from the Galactic plane than Paper I or Paper II.

Surveys in the NIR find higher multiplicity rates within 2": 13% (Dressing et al., 2014), 17% (Adams et al., 2012), 20% (Adams et al., 2013). This is likely caused by many companions being cool, red dwarf stars that are faint in the optical (Ngo et al., 2015), and deeper, higher angular resolution imaging.

4.4 Stellar Multiplicity and *Kepler* Planet Candidates

I present in this section, the analysis originally in Paper III using the 3313 observations with Robo-AO while mounted at Palomar Observatory. A more sophisticated analysis is presented in Chapter 6.

We use this large dataset to continue our search that began in Paper I for broad-scale correlations between the observed stellar multiplicity and planetary candidate properties. Such correlations provide an avenue to constrain and test planet formation and evolution models.

All stellar and planetary properties for the KOIs in this section were obtained from the cumulative planet candidate list at the NASA Exoplanet Archive⁵ and have not been corrected for possible dilution due to the presence of nearby stars.

4.4.1 Stellar Multiplicity and KOI Number

The early and late public releases of KOIs (Borucki et al., 2011c; Batalha et al., 2013; Burke et al., 2014; Coughlin et al., 2016) could conceivably have a built-in bias, either astrophysical in origin or as a result of the initial vetting process by the *Kepler* team. This

⁵<http://exoplanetarchive.ipac.caltech.edu/>

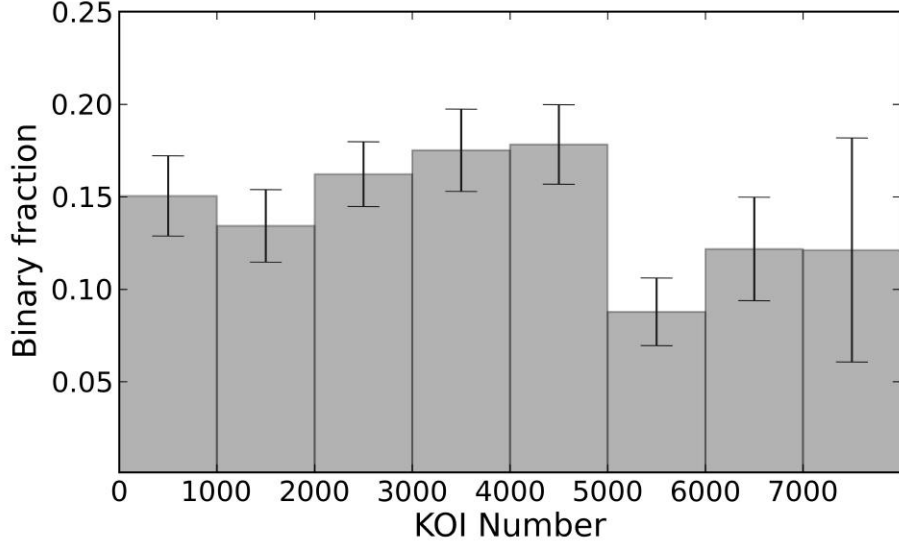


Figure 4.6: Multiplicity fraction within 4" of KOIs as a function of KOI number. A 2.9σ decrease in the fraction of nearby stars between KOIs numbered less than 5000 and greater than 5000 is apparent.

bias might appear as a variation in multiplicity with respect to KOI number. With a target list of KOIs in Paper II and this work widely dispersed in the full KOI dataset, we can search for such a trend. The fraction of KOIs with companions as a function of KOI number, as displayed in Figure 4.6, shows a sharp decrease at approximately KOI-5000. We find KOI numbers less than 5000 have a nearby star fraction of $16.1\% \pm 0.9\%$ and KOI numbers greater than 5000 have a nearby star fraction of $10.2\% \pm 1.5\%$, a 2.9σ disparity. The exact mechanism for this is unclear, however, this may be a result of better false positive detection in the later data releases due to automation of the vetting process (Mullally et al., 2015). There is no significant corresponding variation in the separations or contrasts of stellar companions between the two populations.

Stellar Multiplicity Rates and Host-star Temperature

It has been well established that stellar multiplicity correlates with stellar mass and temperature (Duchêne & Kraus, 2013). In Paper I, it was found at low significance that this trend appears to also be true for the observed KOIs. Ngo et al. (2015) found in a sample

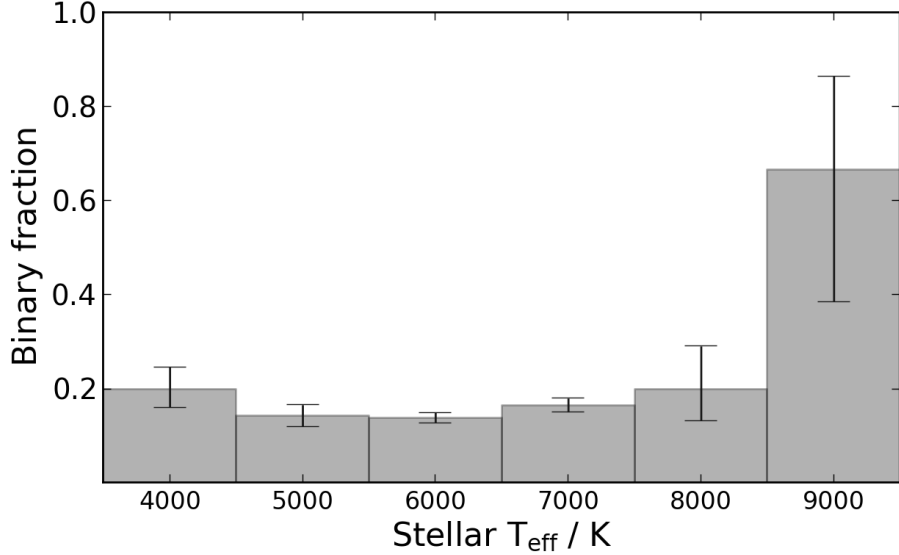


Figure 4.7: Fraction of KOIs with detected nearby ($\leq 4''$) stars as a function of stellar effective temperature.

of stars hosting close-in giant planets that, with 2.9σ significance, stars hotter than 6200 K have a companion rate two times larger than their cool counterparts. We find in the combined target sample of Paper II and this work that $14.7\% \pm 0.9\%$ of KOIs below 6200 K have a companion, compared to $17.2\% \pm 2.0\%$ above 6200 K. A Fisher exact test gives an 83% probability that the two samples are indeed from two distinct populations. The trend towards higher multiplicity with higher stellar temperatures is still visually evident, as seen in Figure 4.7. With an emphasis on solar analogs in the input catalog, the majority of KOIs are FGK-type stars (Batalha et al., 2013), thus the small number of early-type stars in our sample prevents any high significance conclusions.

4.4.2 Stellar Multiplicity and Multiple-planet Systems

Multiple star systems are thought to more commonly host single transiting planets than multiple planet systems. Perturbations from the companion star will change the mutual inclinations of planets in the same system (Wang et al., 2014), therefore a lower number of multiple transiting planet systems are expected to have stellar companions. Multiple planet systems are also subject to planet-planet effects (Rasio & Ford, 1996; Wang et al., 2015a).

In Paper I, we found a low-sigma disparity in multiplicity rates between single- and multiple-planet systems, with single-planet systems exhibiting a slightly higher nearby star fraction. With our combined sample from Paper II and this work, we revisit this result with over three times more targets. We find a slightly higher nearby star fraction for multiple planetary systems, displayed in Figure 4.8. A Fisher exact test gives an 8.7% probability of this being a chance difference. With the expectation, given the effects of stellar perturbations and the higher false positive rate for single star systems, of a higher nearby-star fraction for single-planet candidate hosting stars, even this low-significance result is surprising. A possible explanation is that the additional stellar body in the system is causing orbital migration of outer planets, moving them to shorter period orbits where *Kepler* has higher sensitivity to transit events. Also, multiple star systems have at least twice as many stars that could host transiting planets, resulting in a higher probability of observing multiple planetary transits. Lastly, with relatively low-significance, this result could also be a consequence of the “look-elsewhere” effect inherent to any multi-comparison study (Gross & Vitells, 2010); with the parameter space explored in this section, a result of this significance is expected to arise approximately 50% of the time out of pure chance.

Wang et al. (2015b) studied the influence of stellar companions on multiple-planet systems, finding a 3.2σ deficit in multiplicity rate in multi-planet systems compared to a control sample of field stars. However, they also found no significant disparity in multiplicity rates between single- and multi-planet systems.

4.4.3 Stellar Multiplicity and Close-in Planets

The presence of stellar companions is hypothesized to shape the formation and evolution of planetary systems. Overall, there is evidence that planetary formation is disrupted in close binary systems (Fragner et al., 2011; Roell et al., 2012). The third body in the system can lead to Kozai oscillations causing orbital migration of the planets (Fabrycky & Tremaine, 2007; Katz et al., 2011; Naoz et al., 2012) or tilt the circumstellar disk (Batygin,

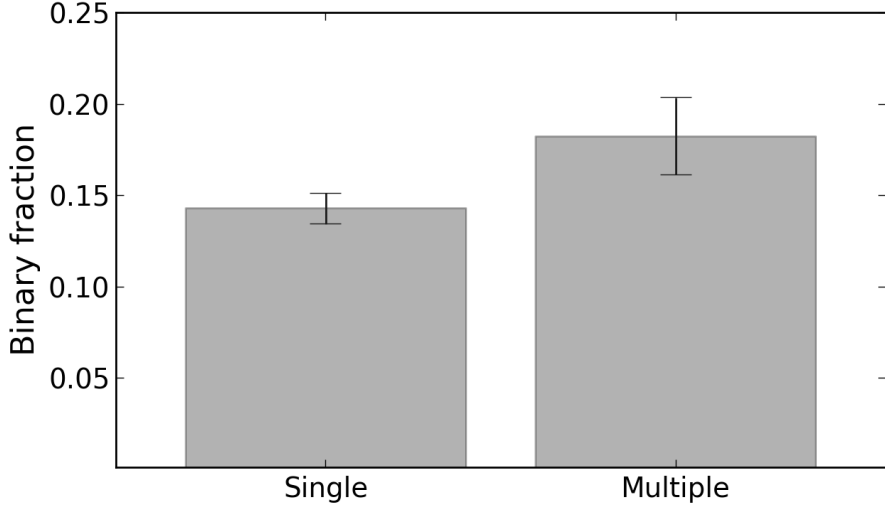


Figure 4.8: The multiplicity fraction within 4" of KOIs hosting detected single- and multiple-planetary systems.

2012). Smaller planets are also more prone to the influence of a stellar companion because of weaker planet-planet dynamical coupling (Wang et al., 2015a). These dynamical interactions between small and large planets in the same system tend to differentially eject small planets more frequently than large planets (Xie et al., 2014). The presence of a stellar companion increases the frequency of these interactions, leading to higher loss of small planets. Consequently, we would expect a correlation between binarity and planetary period for different sized planets.

We previously reported a low-significance result of stellar third bodies increasing the rate of close-in giant planets, possible evidence of orbital migration of the planet caused by the stellar companion. We revisit the discussion and analysis from Paper I in search of this correlation using the results of Paper II and this work. This analysis splits the “small” and “giant” planets at the arbitrary value of Neptune’s radius ($3.9 R_{\oplus}$). The exact value does not significantly affect the results as just 11 of the detected systems have planetary radii within 20% of the cutoff value, with 1635 small and 395 giant planets in total.

In Figure 4.9 the fraction of *Kepler* planet candidates with nearby stars is shown, with planets grouped into two different size ranges. We again see a small increase in the nearby

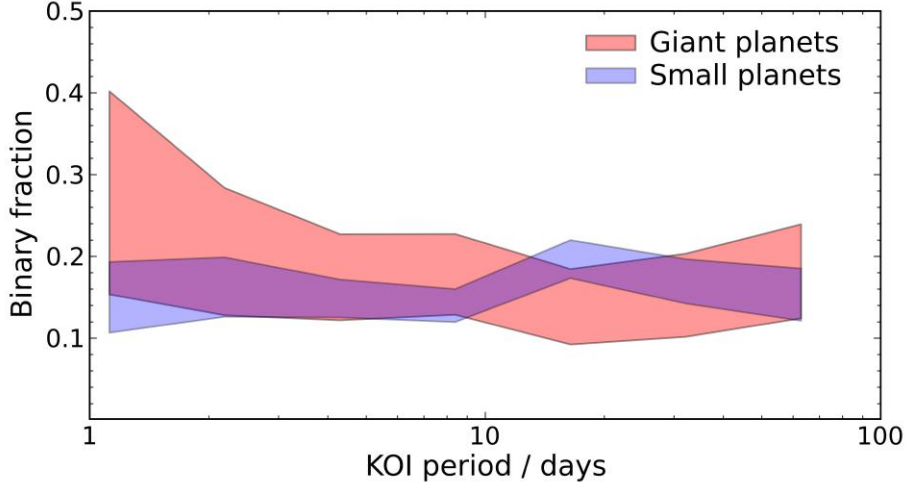


Figure 4.9: 1σ uncertainty regions for the binarity fraction as a function of KOI period for two different planetary populations.

star fraction for giants with periods < 15 days, however the $> 2\sigma$ spike at periods of 2-4 days seen in Paper I is not present. If our sample is reduced to correspond to the separation range of Paper I ($\rho < 2.5''$) in Figure 4.10, again no binarity spike at periods < 10 days is apparent.

Binning our targets into four population groups in Figure 4.11 suggests no significant difference in the binarity rate of short period giants. We also attempt to decrease the occurrence of unassociated asterisms by only using close, bright companions ($\Delta m \leq 2$, $\rho \leq 1.5''$). As in Paper I, we detected an excess of close-separation bright companions (Figure 5.3), which suggests a higher probability of association for these nearby stars. We show the binarity fraction of the four populations in Figure 4.12. As with the complete set of nearby stars, no significant differences between the four populations is evident.

Any real disparity between the populations would also manifest in the physical orbital semi-major axis, which is related to the observable periods by the stellar mass. In Figure 4.13 we plot the two population's binarity fraction as a function of the calculated semi-major axis of the planetary candidates between 0.01 and 1.0 AU. No significant giant planet binarity spike is observed as in the periods plot.

Our updated study using the targets in Paper II and this work suggests that the presence of a second stellar body in planetary systems does not appreciably affect the number of

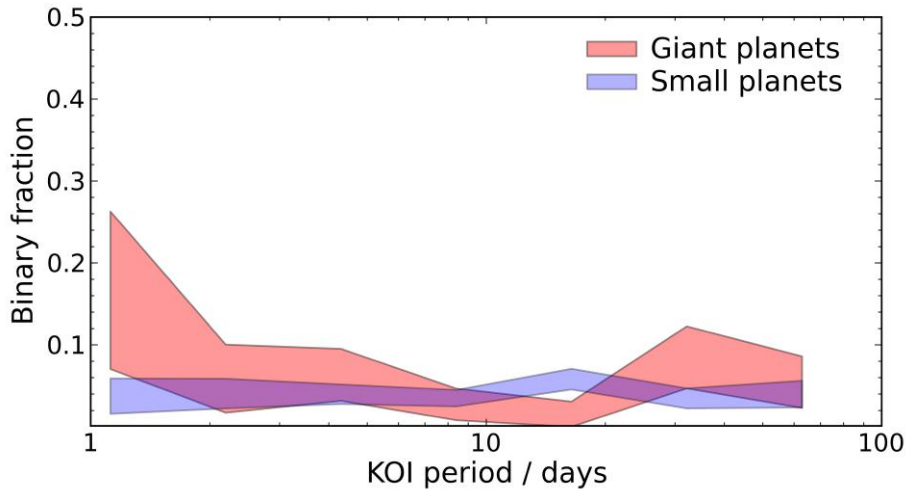


Figure 4.10: 1σ uncertainty regions for the binarity fraction as a function of KOI period for two different planetary populations, with only companions with separations $<2.5''$ used to align with Paper I.

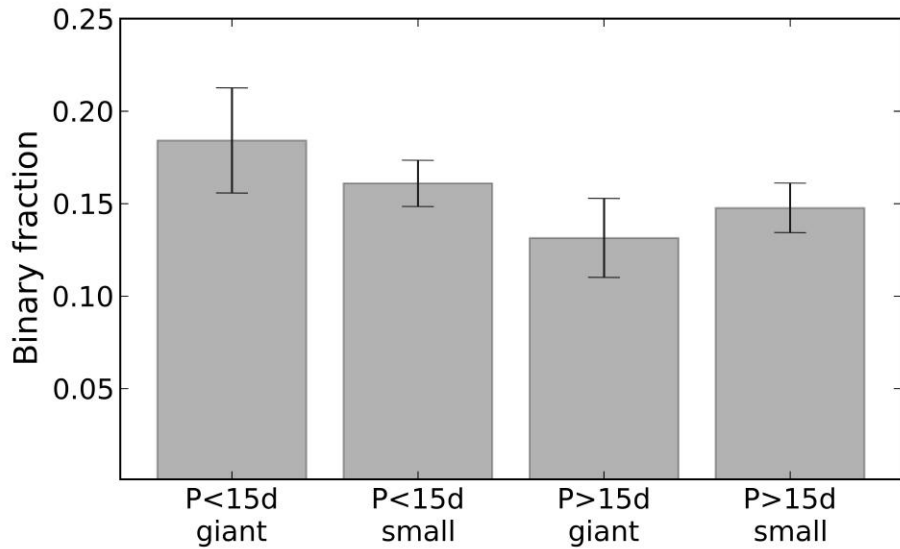


Figure 4.11: Multiplicity fraction of KOIs with four planetary populations, with all contrast ratios and separations $\leq 4''$. A planet is considered giant if its radius is equal to or larger to that of Neptune ($3.9 R_{\oplus}$). Multi-planet systems can be assigned to multiple populations.

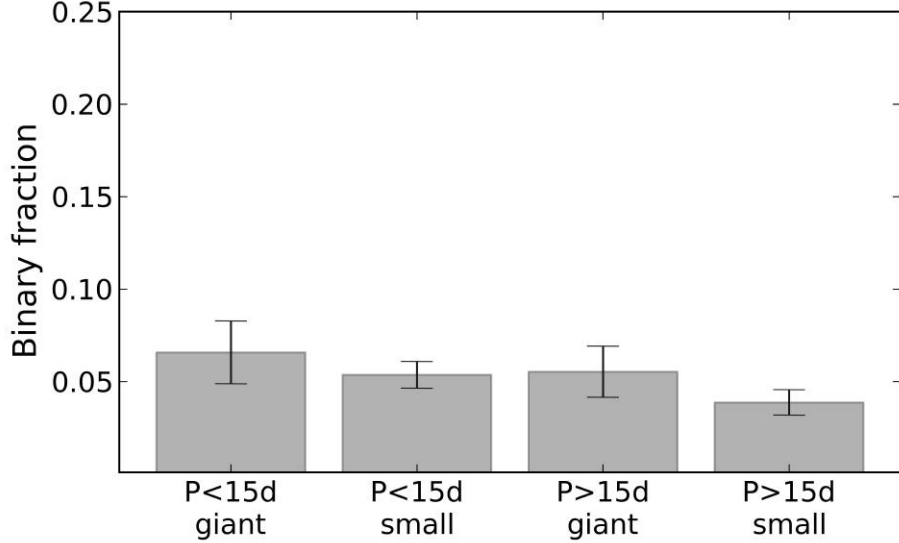


Figure 4.12: Multiplicity fraction of KOIs with four planetary populations, with only companions with $\Delta m \leq 2$ and separations $\leq 1.5''$, removing the faint nearby stars that are less likely to be physically associated.

close-in giant planets. This agrees with the analysis of Wang et al. (2015a) who find a relatively uniform multiplicity rate for planets with short and long periods. They note that our previous tentative result may have been due to short-period giants with brighter stellar companions in the visible biasing our detections. Subject to the same potential biases, the larger survey in this analysis does not indicate a period-multiplicity correlation for the two planetary populations, suggesting that our previous low-sigma result may have instead been an artifact of small-number statistics.

Kraus et al. (2016) find a 6.6σ deficit in binary stars with separation $\rho < 50$ AU in KOIs compared to field stars, again suggesting that close-in stellar companions disrupt the formation and/or evolution of planets, as had been previously hypothesized (Wang et al., 2014). Indeed, a quarter of all solar-type stars in the Milky Way are disallowed from hosting planetary systems due to the influence of binary companions.

Some evidence remains, however, that stellar binarity may encourage the presence of hot Jupiters. A recent NIR survey (Ngo et al., 2015) of exoplanetary systems with known close-in giants finds that hot Jupiter hosts are twice as likely as field stars to be found in

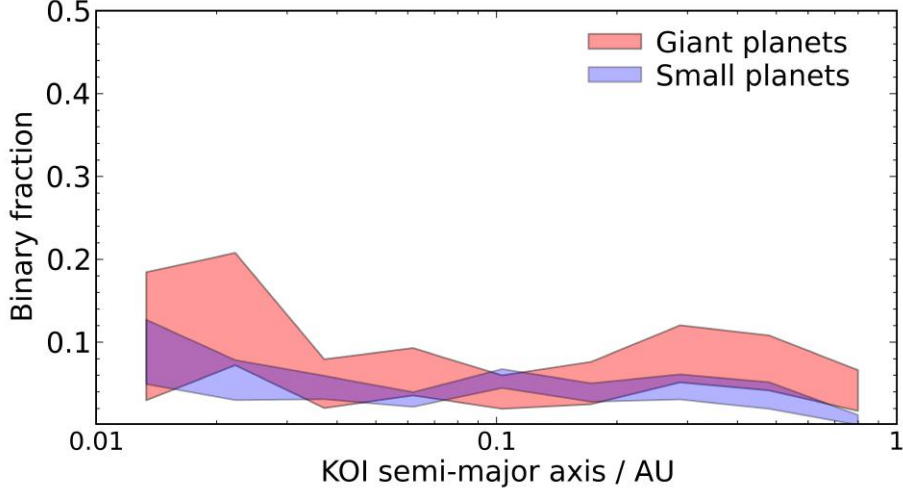


Figure 4.13: 1σ uncertainty regions for the binarity fraction as a function of KOI semi-major axis between 0.01 and 1.0 AU for two different planetary populations.

a multiple star system, with a significance of 2.8σ . However, the binarity rates of systems containing hot Jupiters remains unclear: 12% (Roell et al., 2012), 38% (Evans et al., 2016), 51% (Ngo et al., 2015).

4.5 Conclusion

We observed 1629 *Kepler* planetary candidates with the Robo-AO robotic laser adaptive optics system. We detected 206 planetary candidates with nearby stars, implying an overall nearby-star probability of $12.6\%\pm0.9\%$ at separations between $\sim0.15''$ and $4.0''$ and $\Delta m \leq 6$.

Many of our newly found companions are of particular interest, including 26 habitable zone candidates found within possible multiple star systems. In addition, we found 16 KOIs with multiple nearby stars, and 5 new candidate quadruple star systems hosting planet candidates, including KOI-4495 from Paper II. We looked at broad correlations between the presence of nearby stars and planetary characteristics. We find a higher detected companion rate of systems with multiple planets than in single-planet systems. Our previous tentative result of a deficit of close-in giant planets when a third stellar body appears in the system is not apparent in this dataset.

CHAPTER 5: CUMULATIVE STATISTICS AND CORRECTED PLANETARY RADII FROM THE ROBO-AO KEPLER SURVEY

There was one planet off in the seventh dimension that got used as a ball in a game of intergalactic bar billiards. Got potted straight into a black hole.

— *The Hitchhiker’s Guide to the Galaxy*

This chapter reports the results from observations of 532 KOIs, as well as expands the search for nearby stars around 715 KOIs observed initially in Paper I from its initial separation limit of $2.5''$ to $4.0''$. We also present the cumulative statistics from the survey, as well as derive corrected planetary radii for every candidate planet in a system with an observed nearby star. The results in this chapter were first presented in Ziegler et al. (2017b).

5.1 Cumulative Survey Targets and Observations

5.1.1 Observations

Observations in the survey were performed using the Robo-AO laser adaptive optics system (Baranec et al., 2013, 2014a; Riddle et al., 2012), see Section 1.1. The first robotic laser guide star adaptive optics system, the automatic Robo-AO system can efficiently perform large, high angular resolution surveys. The AO system runs at a loop rate of 1.2 kHz to correct high-order wavefront aberrations, delivering a median Strehl ratio of 9% in the i' -band. Observations were taken in a long-pass filter cutting on at 600 nm (LP600 hereafter). The LP600 filter approximates the *Kepler* passband at redder wavelengths, while also suppressing blue wavelengths that reduce adaptive optics performance. The LP600 passband is compared to the *Kepler* passband in Figure 5.2. We obtained high-angular-resolution images

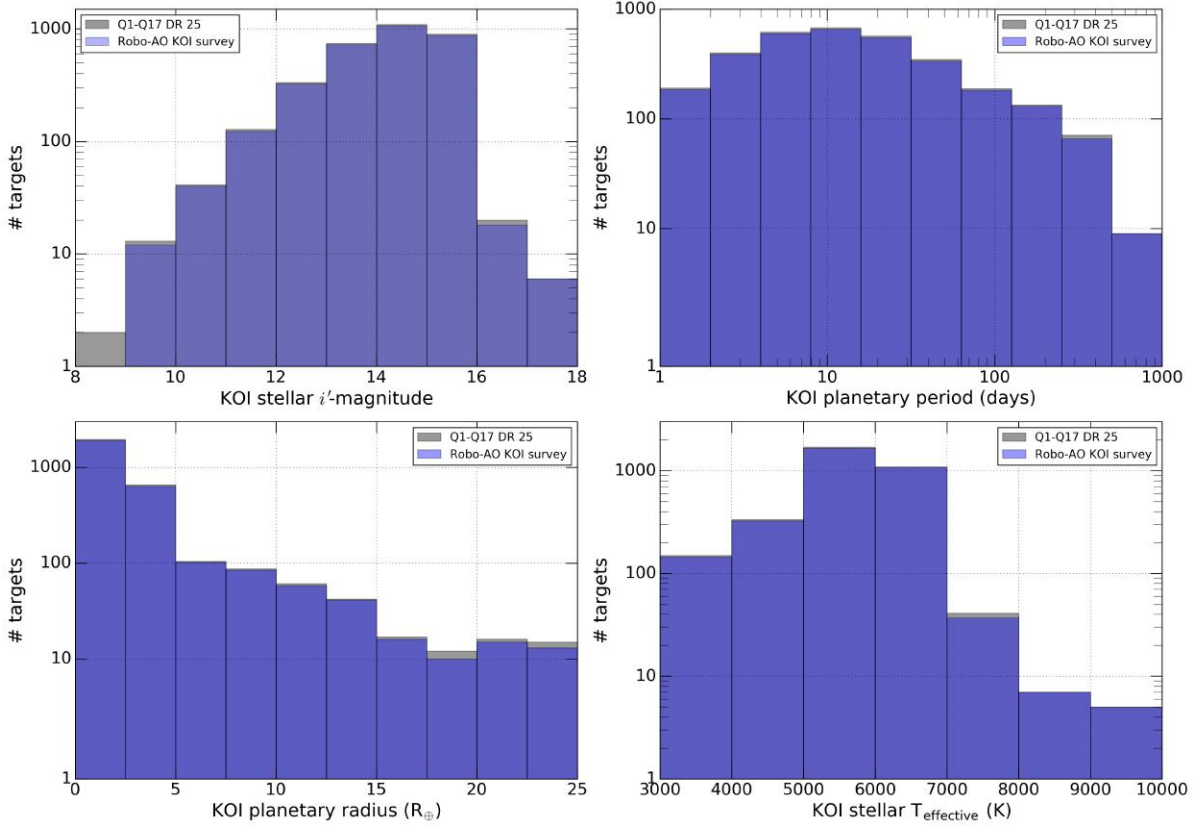


Figure 5.1: Comparison of the distribution of new Robo-AO observations in this paper as well as the combined Robo-AO survey (Law et al., 2014; Baranec et al., 2016; Ziegler et al., 2017a,b) to the complete set of KOIs from Q1-Q17 (Borucki et al., 2010, 2011a,b; Batalha et al., 2013; Burke et al., 2014; Rowe et al., 2014; Coughlin et al., 2016; Mathur et al., 2017). The Robo-AO KOI survey has observed over 95% of planetary candidate host stars detected with *Kepler*.

Table 5.1: The specifications of the Robo-AO KOI survey

KOI targets	3857
FWHM resolution	$\sim 0.15''$ (@600-750 nm)
Observation wavelengths	600-950 nm
Detector format	1024 ² pixels
Pixel scale	43 mas/pix (Palomar) 35 mas/px (Kitt Peak)
Exposure time	90 seconds
Targets observed / hour	20
Observation dates at Palomar	2012 July 16 – 2015 June 12
Observation dates at Kitt Peak	2016 June 8 – 2016 July 15

of 3313 KOIs with Robo-AO between 2012 July 16 and 2015 June 12 (UT) at the Palomar 1.8m telescope. We observed 532 additional KOIs with Robo-AO between 2016 June 8 and 2016 July 15 (UT) at the Kitt Peak 2.1m telescope.

Typical seeing at the Kitt Peak Observatory is between 0.8'' and 1.6'', with a median around 1.3'' (Jensen-Clem et al., 2017). The typical FWHM (diffraction limited) resolution of the Robo-AO system is 0.15''. Images are recorded on an electron-multiplying CCD (EMCCD), allowing short frame rates for tip and tilt correction in software using a natural guide star ($m_V < 16$) in the field of view. Specifications of the entire Robo-AO KOI survey are summarized in Table 5.1.

5.2 Data Reduction

Observations of KOIs with Robo-AO were reduced using the methods described in Section 4.2.

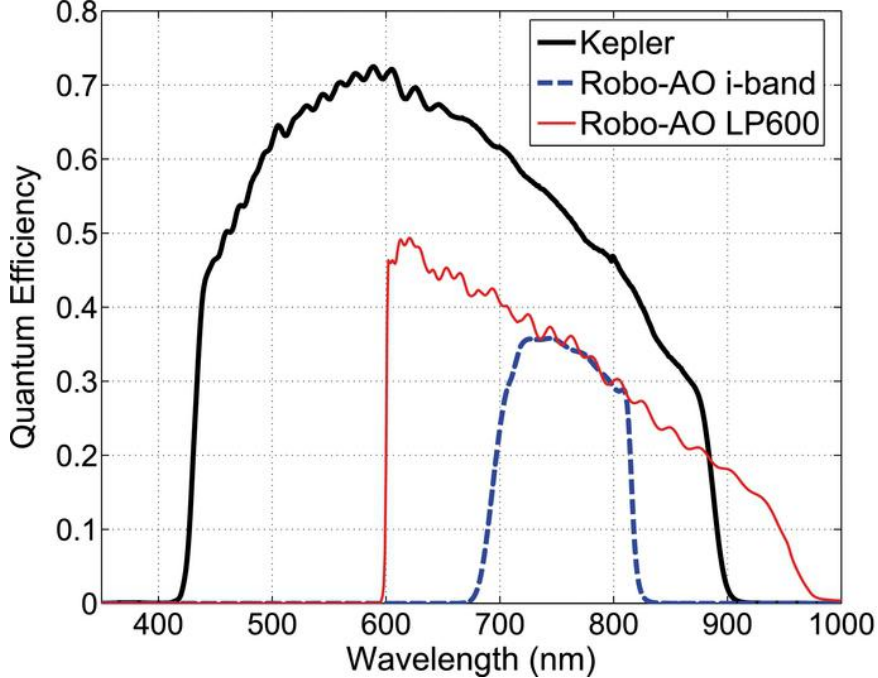


Figure 5.2: The Kepler and Robo-AO passbands. The Robo-AO curves are generated from measured reflection and transmission data from all optical components with the exception of the primary and secondary of the 60-inch telescope which are assumed to be ideal bare aluminum. [Image courtesy of Law et al. (2014)]

5.3 Discoveries and analysis

5.3.1 Robo-AO KOI Survey Cumulative Statistics

The Robo-AO KOI survey has observed 3857 KOIs and detected 610 nearby stars around 559 planetary candidate hosts, implying a nearby star fraction rate of $14.5 \pm 0.6\%$ within the Robo-AO detectability range (separations between $\sim 0.15''$ and $4.0''$ and $\Delta m \leq 6$). We also find within $4.0''$ separation, a triple star fraction of $1.2 \pm 0.2\%$ and a quadruple star fraction of $0.08^{+0.06}_{-0.03}\%$.

The detected companion separations and contrast ratios of observed nearby stars to KOIs are plotted in Figure 5.3, along with the calculated 5σ detection limits as detailed in Section 4.2.5. The properties of detected nearby stars to KOIs are listed in Table B.1. Centered cutouts of KOIs with nearby stars detected in this survey are available in Appendix F.

The nearby star fraction rate as a function of separation from the host star for the survey

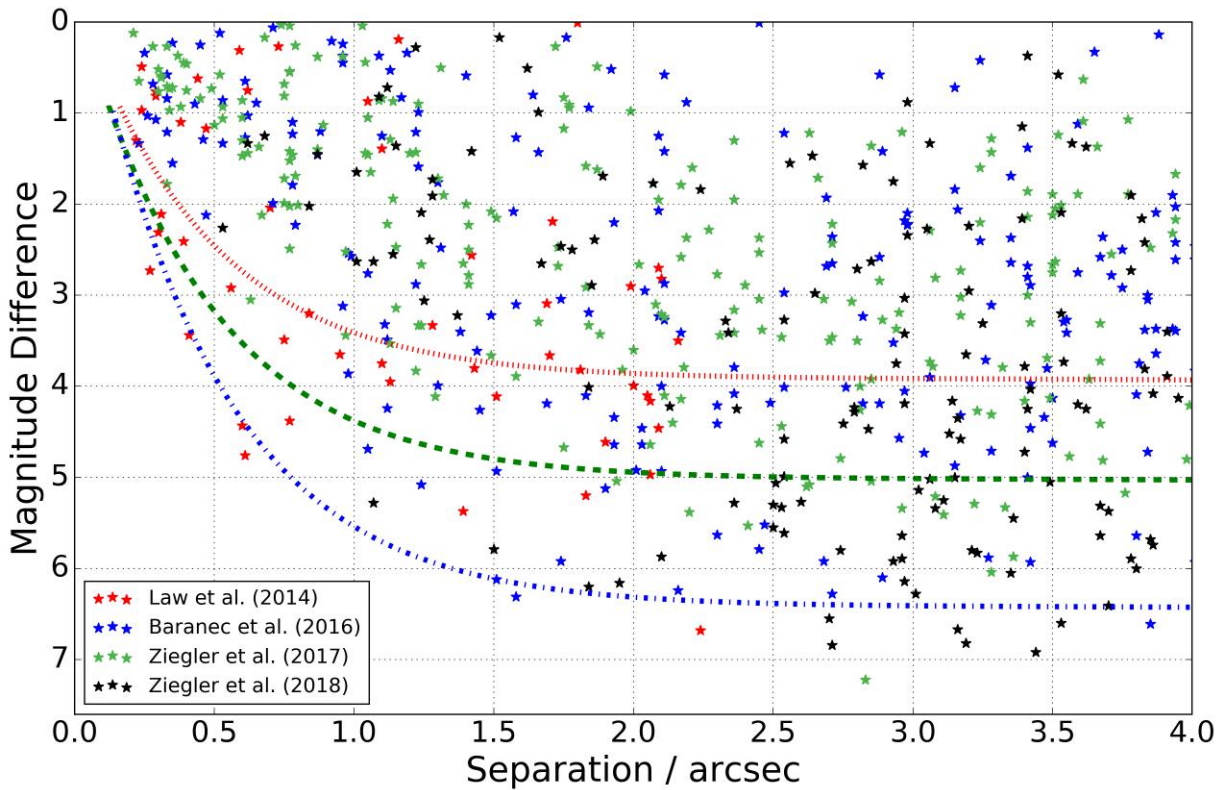


Figure 5.3: Detected nearby stars to KOIs in the Robo-AO KOI survey. Typical contrasts curves consistent with a 5σ detection on low-, medium- and high-performance images, as described in Section 4.2.5, are plotted in red, green, and blue, respectively.

to date is listed in Table 5.2 and plotted in Figure 5.4. The nearby star fraction increases linearly with separation from the host star. If all nearby stars were unbound, we would expect the rate to increase with the area enclosed. This suggests that a significant fraction of the nearby stars may be bound to the host star. It should be noted that this analysis does not account for the detection sensitivity of Robo-AO at varying separations. It is expected, however, that most nearby stars at separations $<1''$ are likely bound (Horch et al., 2014).

The properties of planetary systems in binary star systems may be impacted due to perturbations from the secondary star. We show in Table 5.3 the nearby star fraction for different planet types based on their similarity in radius to a solar system planet. We find that the nearby star rates for all four planet types are within 2σ of the total rate for the entire survey. The largest outlier rate is for the Jupiter or gas giant planets, which are known to have a large false positive fraction (Santerne et al., 2013), caused by the potential of background eclipsing binaries to mimic their deep transits. Wang et al. (2014) also find a high stellar multiplicity rate for hot Jupiters, and direct imaging surveys find that gas giants have a high rate of bound stellar companions (Ngo et al., 2016; Evans et al., 2016). It is also possible that the high nearby star rate may be due to orbital migration caused by a bound secondary star which drives gas giants to low period orbits more easily detectable by *Kepler*. In Paper III, we found a significant increase in the nearby star rate for low-period giant planets, possibly caused by orbital migration due to the secondary star (Fabrycky & Tremaine, 2007), although the significance of this effect may be small (Naoz et al., 2012; Petrovich, 2015). These migrations may also cause planet scattering, differentially ejecting smaller planets from the system (Rasio & Ford, 1996; Wang et al., 2015a).

5.3.2 Implications for *Kepler* Planet Candidates

A nearby star in the same photometric aperture as the target star will dilute the observed transit depth, resulting in underestimated radius estimates. We re-derive the estimated planetary radii for the 814 planetary candidates around the 559 KOIs with detected nearby

Table 5.2: Robo-AO KOI Survey Cumulative Nearby Star Fraction Rates

Separation (")	Systems with nearby stars	Nearby star rate (%)
<0.5	47	$1.2^{+0.20}_{-0.15}$
<1.0	121	$3.1^{+0.30}_{-0.26}$
<1.5	204	$5.3^{+0.38}_{-0.33}$
<2.0	264	$6.8^{+0.43}_{-0.38}$
<2.5	333	$8.6^{+0.47}_{-0.43}$
<3.0	411	$10.7^{+0.52}_{-0.48}$
<3.5	487	$12.6^{+0.55}_{-0.52}$
<4.0	559	$14.5^{+0.59}_{-0.55}$

Table 5.3: Nearby Star Fraction Rates By Planet Candidate Type

Planet candidate type	Planetary radius range	Systems with nearby stars	Total systems	Nearby star rate
Earths	$R_p < 1.6R_{\oplus}$	241	1480	$16.3 \pm 1.0\%$
Neptunes	$1.6R_{\oplus} < R_p < 3.9R_{\oplus}$	268	2058	$13.0 \pm 0.8\%$
Saturns	$3.9R_{\oplus} < R_p < 9R_{\oplus}$	46	338	$13.6 \pm 2.0\%$
Jupiters	$9R_{\oplus} < R_p$	47	247	$19.0 \pm 2.8\%$

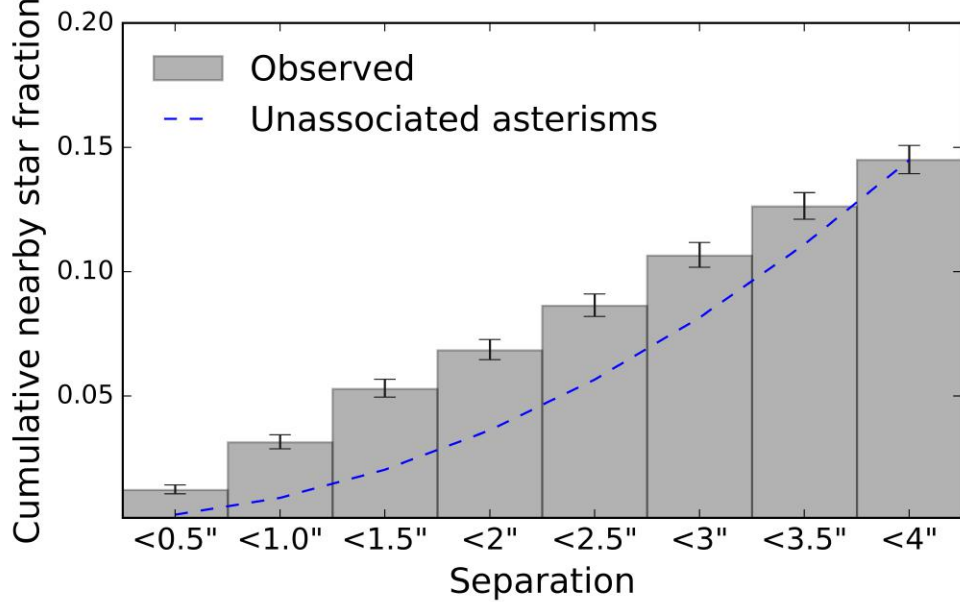


Figure 5.4: The nearby star fraction rate as a function of separation from 3857 observations of planetary candidates in the Robo-AO KOI survey. The dashed line represents a cumulative distribution that scales with the area that would be expected from non-physically-associated companions.

stars in the Robo-AO *Kepler* survey for two scenarios: 1) the planet orbits the target star; and 2) the planet orbits the secondary star which is bound to the primary star¹. For the first case, we use Equation 1.2.2. For the case where the planet candidate is bound to the secondary star, we use Equation 1.2.3.

We use the stellar radius estimates from Mathur et al. (2017) for the primary stars. The radii of secondary companions in the scenario where they are bound to the target star were estimated using the observed contrast ratio in the *Kepler* band (approximated using the LP600 bandpass) and finding the radius of an appropriately fainter star within the Dartmouth stellar models (Dotter et al., 2008). The fluxes of all observed sources within the *Kepler* aperture were summed to estimate the transit dilution. The revised planetary radius estimates of systems with detected nearby stars are detailed in Table D.1 in Appendix D.

The original derived planetary candidate radius estimates are corrected for dilution only

¹The third scenario, in which the secondary star is unbound to the primary star, is unconstrained without color information.

from nearby stars resolved in the KIC (Coughlin et al., 2016). We find that four of the nearby stars detected in our survey appear in the KIC (companions to KOIs 263, 521, 1614, and 5790). We, therefore, do not revise the radius estimates for the planetary candidates in these four systems and they are not included in the following analysis.

Of the 814 planetary candidates with nearby stars detected in this survey, approximately 29% have a corrected planetary radius at least 10% larger than the original planetary radius estimate, assuming the planet candidate orbits the primary star. If instead, the planet candidate orbits the secondary star which is bound to the primary star, almost every (99%) planetary candidate has a corrected radius greater than 10% larger than the original radius estimate.

If all planet candidates orbit the primary star, the original planetary radii derived from the *Kepler* light curves are underestimated by a factor of 1.08, on average. If all planet candidates instead orbit the secondary star which is bound to the primary, the corrected planetary radius estimates are on average a factor of 3.29 larger than those originally derived. The more realistic scenario is if we assume that the planet candidates are equally likely to be orbiting the primary or secondary stars. In this case, the radius estimates for the planetary candidate in systems with nearby stars will increase by a factor of 2.18 on average. This is significantly higher than the radius correction factor of 1.6 found by Ciardi et al. (2015) and 1.64 found by Hirsch et al. (2017). Hirsch et al. used planetary occurrence rates (Howard et al., 2012) to estimate the fraction of planets orbiting the primary and secondary star for known bound systems. It is unclear, however, if this approach results in a more accurate planetary correction factor estimate, because, as they note, the planet occurrence rates in binary systems is not well understood. Indeed, we found evidence in Paper III that binary stars significantly affect the properties of planetary systems, driving migration of large planets to low-period orbits.

A large number of unbound background stars likely inflates our estimates of the planetary correction radius factor. These stars are often much fainter than the primary star and the

Table 5.4: Planetary Candidates Likely Not Rocky Due to Nearby Stars

Object	Sep. (")	Δm (mags)	$R_{p,0}^a$ (R_\oplus)	$R_{p,prim.}^b$ (R_\oplus)	$R_{p,sec.}^c$ (R_\oplus)
0284.02	0.96	0.45	1.40	1.80	2.0
0284.04	0.96	0.45	1.41	1.82	2.1
0298.01	2.01	0.58	1.50	1.89	2.3
1214.01	0.33	1.21	1.44	1.66	2.4
1630.01	1.77	0.91	1.40	1.68	2.3
1700.01	0.29	1.07	1.54	1.8	2.6
1973.01	0.79	1.69	1.49	1.64	3.4
2163.03	0.77	0.04	1.59	2.23	2.2
2377.01	2.09	1.25	1.55	1.78	2.7
2486.01	0.24	0.49	1.42	1.82	2.0
2551.01	2.69	1.93	1.53	1.65	3.3
2580.01	0.60	0.86	1.59	1.92	2.5
2598.01	1.09	0.37	1.35	1.77	2.0
2711.02	0.52	0.12	1.43	1.97	2.0
2851.02	0.39	0.45	1.50	1.93	2.2
2896.02	0.96	0.38	1.57	2.05	2.3
3029.02	0.28	0.68	1.35	1.67	2.1
3112.01	1.87	0.49	1.41	1.8	2.1
3120.01	1.14	0.87	1.43	1.72	2.2
3214.01	0.49	0.73	1.53	1.88	2.2
3214.02	0.49	0.73	1.35	1.66	2.0
3435.01	3.06	1.33	1.58	1.8	2.8
3435.01	3.52	0.58	1.58	1.99	2.3
3928.01	2.96	1.21	1.45	1.67	2.3
4021.01	1.92	0.52	1.53	1.95	2.4
4323.01	1.12	2.22	1.59	1.69	3.2
4331.01	0.45	0.25	1.45	1.94	2.1
4463.01	2.45	0.01	1.52	2.14	2.1
4759.01	0.67	2.12	1.54	1.65	3.3
4823.01	1.40	0.59	1.51	1.9	2.3
5274.01	3.95	4.13	1.59	1.61	5.7
5762.01	0.23	0.65	1.37	1.71	2.2
6475.01	1.31	0.5	1.54	1.97	2.3
6482.01	0.52	0.58	1.53	1.93	2.4
6907.01	3.35	-0.36	1.14	1.76	1.6

^aOriginal planetary radius estimate, from NASA Exoplanet Archive.

^bEstimated planetary radius in the scenario where the planet orbits the target star, regardless whether the secondary star is bound or unbound to the target star.

^cEstimated planetary radius in the scenario where the planet orbits the secondary star, which is physically bound to the target star.

assumption that each star is equally likely to host the planet results in a large number of gas giant planets, which are inherently rare compared to terrestrial planets (Howard et al., 2012). Simulations from galactic stellar models suggest that the majority of nearby stars to KOIs at separations larger than 1" are likely unbound (Horch et al., 2014), a conclusion borne out by observations (Atkinson et al., 2017; Hirsch et al., 2017). If we limit our survey to just those likely bound nearby stars within 1", we find radius correction factors of 1.18, 1.88, and 1.54 for the scenarios where all planets orbit the primary star, all planets orbit a bound secondary star, and all planets are equally likely to orbit either star, respectively. The radius correction factors found for the set of likely bound stars is in agreement with that found by Hirsch et al. (2017), and is our recommended estimate for the true radius correction factor for *Kepler* planetary candidates with detected nearby stars.

Lastly, using the original estimates for planetary radius and the planetary radius ranges listed in Table 5.3, we find the radius correction factor for systems with nearby stars within 4" (1") for Earth-sized planets is 2.30 (1.54), for Neptune-sized planets is 2.25 (1.59), for Saturn-sized planets is 1.95 (1.67), and for Jupiter-sized planets is 1.88 (1.38), if we assume that each nearby star is bound and the planetary candidate is equally likely to orbit the primary or secondary star. Under these same assumptions, we estimate that approximately 140 previously believed rocky planet candidates ($R_{p,0} < 1.6R_{\oplus}$), or 9% of the 1480 rocky planet candidates discovered by *Kepler*, have corrected radii larger than the rocky planet cutoff at $1.6R_{\oplus}$ as described in Rogers (2015) due to nearby stars within 4". These 140 planetary candidates are therefore likely not rocky due to incorrect identification of the planetary host star and photometric contamination from nearby stars.

We also find 35 rocky planet candidates that, due to the presence of a previously undetected nearby star, are now likely not rocky if either orbiting the primary or secondary stars. We highlight these planetary candidates in Table 5.4.

5.3.3 Rocky, Habitable Zone Candidates

A primary objective of the *Kepler* mission was to estimate the occurrence rate of Earth-like planets orbiting in the habitable zone. Contamination from nearby stars has a significant effect on the derived planetary radii. Planetary radii based on *Kepler* light curves alone are underestimated by a factor of approximately 1.5 on average, as discussed in Section 5.3.2. The impact of nearby stars must, therefore, be taken into account to estimate precisely what planets are terrestrial. While the exact requirements for habitability remain unclear (Kasting et al., 1993; Selsis et al., 2007; Seager, 2013; Zsom et al., 2013), it is believed that the equilibrium temperature of the planet must allow the presence of liquid water. To be Earth-like, a planet must also be rocky: Rogers (2015) show that the transition between “rocky” and “non-rocky” occurs rather sharply at $R_P=1.6R_{\oplus}$.

We searched for potentially rocky planets, with estimated radii less than 2σ away from the rocky planet cutoff of $1.6R_{\oplus}$, residing in the habitable zone (estimated planetary equilibrium temperature ≤ 370 K) within the set of systems with newly discovered nearby stars. We find three such planetary candidates.

The two confirmed planets, KOI-701.03 and 701.04 (Kepler-62e and Kepler-62f, respectively), both reside in the habitable zone if orbiting the primary star. If instead, either one orbits the faint secondary star and that star is bound to the primary, the estimated radii of each would be much larger and it would be unlikely that they would be rocky in composition. This planet has been thoroughly vetted by Borucki et al. (2013), who concluded that the two planets are indeed rocky and orbit in the habitable zone.

KOI-7470.01 has an original radius estimate of $1.9R_{\oplus}$, near the rocky planet cutoff, and an estimated equilibrium temperature of 225 K. The undiluted radius estimate for the scenario where the planetary candidate orbits the primary is $2.59R_{\oplus}$, making it very improbable that the planet is rocky. Likewise, if the planetary candidate instead orbits the bound secondary star, it would again be unlikely to be rocky, with a planetary radius estimate of $2.70R_{\oplus}$.

5.3.4 High-order KOI multiples

Stellar multiplicity is relatively common in the galaxy. Studies with large numbers of targets and robust statistics (e.g. Duquennoy & Mayor, 1991; Raghavan et al., 2010) have provided insight into the mechanisms of star formation, but it is the rare high-order multiples that provide the most stringent test of any theory’s validity. For example, a study of high-order multiplicity of solar-type stars (Riddle et al., 2015) found that 2+2 quadruple star systems, two close pairs in a wide outer binary, are more frequent than would be expected assuming a chaotic N -body dynamics formation mechanism, necessitating an exploration for another scenario that explains the observations. The presence of any planets in a multiple star system provides similar tests for the as yet unexplained process of planetary formation. It is hypothesized that planetary formation is disrupted by the gravitational perturbations caused by a close companion (Fragner et al., 2011; Roell et al., 2012), with dynamical interactions causing orbital migration (Fabrycky & Tremaine, 2007; Katz et al., 2011; Naoz et al., 2012) or even ejection of planets from the system (Xie et al., 2014). Nonetheless, dozens of plants have been confirmed in multiple star systems, including two planets in quadruple star systems (Schwamb et al., 2013; Roberts et al., 2015).

We observed five KOIs from the Robo-AO KOI survey with Keck-AO that had four stars within 5” of the target star. These five systems, detailed in Table 5.5, were chosen for further follow-up observations to quantify the probability of physical association of the observed stars. We used the two methods described in Section 6.2.1 to determine association between the stellar components in each system. The results of these two methods are detailed in Table 5.6, along with the significance of uncertainty in distance estimates for the nearby stars compared to the KOI. All pairs with $\geq 5\sigma$ level of confidence are considered inconsistent with a gravitationally bound scenario, and pairs with $< 5\sigma$, while not necessarily physically associated, are not significantly inconsistent with this interpretation.

The gravitational association between stars within each system could potentially be ascertained from long-baseline imaging available from archival surveys. Using the Palomar

Observatory Sky Survey (POSS-I, Abell, 1959), imaged between 1949 and 1956 and scanned with plate scale of $1''/\text{px}$, we can dissociate stars in the field with proper motion differences of $>16 \text{ mas/yr}$, and proper motion differences in right ascension and declination of $>8 \text{ mas/yr}$. For the widely separated stellar pairs resolved in the POSS-I image, we checked the angular separation in the DSS and our survey to confirm relatively constant separation. For closely separated systems where both stars are merged in the POSS-I image, we looked for a background star at the current position that does not appear in our images.

In addition to POSS-I, we download data from the Two Micron All Sky Survey (2MASS, Skrutskie et al., 2006b), an infrared survey with pixel scale of $2''$, and the UKIRT Infrared Deep Sky Survey (UKIDSS, Lawrence et al., 2007), a seeing limited survey with resolution of $\sim 1''$. None of the five KOIs have been imaged by the Sloan Digital Sky Survey.

Lastly, the stellar density in the region of sky which the primary star is observed can provide an estimate for the likelihood that unassociated stars, by chance, lie nearby in our line-of-sight. We describe our measurement of the observed stellar density as a function of Galactic longitude and latitude in Section 6.2.4.

A Monte Carlo simulation was run 10^6 times for each of the five KOI observed with three nearby stars with Robo-AO to estimate the probability of n number of unassociated stars being observed within a $5''$ radius of the KOI, where n is equal to the number of observed stars and iterated down to zero. Since the stellar density model was derived from Robo-AO observations, nearby stars observed with deep, infrared imaging of Keck-AO are not considered when discussing the results.

We also run the Monte Carlo simulation 10^5 times for each of the 3857 KOIs observed in the Robo-AO KOI survey. We determine the expected number of KOIs that, by chance, have three, four, and five nearby unassociated stars as 2.02, 0.105, and 0.004, respectively. Compared to our actual observations of five KOIs with three nearby stars, we expect that on average, only two systems are purely unassociated asterisms.

Table 5.5: High-order multiple KOIs resolved using Keck-AO

KOI	m_J (mag)	ObsID	Nearby star	Det.	Significance (σ)	Separation (arcsec)	P.A. (deg.)	$\Delta LP600$ (mag)	ΔJ (mag)	ΔK_p (mag)
3214	10.9	2016 Sep 12		B	95	0.48±0.02	319±2	0.73±0.13	1.46±0.03	1.59±0.02
				C	201	1.30±0.02	199±2	2.50±0.04	2.59±0.03	2.35±0.02
				D	21	4.46±0.02	154±2	5.33±0.07	5.16±0.08	5.07±0.07
3463	13.4	2016 Sep 12		B	8	2.67±0.02	80±2	4.79±0.02	5.18±0.04	4.71±0.12
				C	13	3.64±0.02	97±2	4.41±0.04	4.22±0.06	3.96±0.08
				D	46	4.06±0.02	35±2	2.44±0.04	1.94±0.06	1.90±0.04
				E	49	5.03±0.02	213±2	2.97±0.06	2.19±0.04	1.84±0.05
				B	13	1.57±0.02	269±2			5.76±0.10
4495	14.2	2016 Oct 15		C	18	2.91±0.02	57±2	4.73±0.09	5.74±0.58 ^b	4.43±0.13
				D	38	2.95±0.02	92±2	3.90±0.06	3.38±0.07 ^b	3.24±0.07
				E	55	3.44±0.02	343±2	2.68±0.05	2.18±0.03 ^b	1.71±0.08
				F	63	5.18±0.02	50±2		2.44±0.03 ^b	2.24±0.04
				B	27	1.85±0.02	213±2	3.43±0.05		2.51±0.09
5327	12.9	2016 Oct 15		C	10	3.66±0.02	278±2	3.92±0.02	6.22±0.38 ^b	5.60±0.15
				D	38	4.06±0.02	342±2	-0.12±0.03	1.23±0.01 ^b	1.54±0.03
				B	32	2.63±0.02	145±2	5.10±0.04	4.79±0.09	4.87±0.07
6800	11.8	2016 Sep 12		C	14	2.89±0.02	117±2	5.41±0.04	6.16±0.19	5.35±0.21
				D	27	4.26±0.02	263±2	5.27±0.10	4.00±0.02 ^b	3.98±0.11

Table 5.6: Photometric distance estimates of high-order multiple KOIs

KOI	Nearby star	Sp. type ^a	R_{Sun}^a	D (pc) ^a	Sig. unassociated ^a	D (pc) ^b	Sig. unassociated ^b
3214	A ^c	G2	$1.07^{+0.06}_{-0.07}$	278^{+60}_{-61}	..	340^{+92}_{-51}	..
	B	F4	$1.28^{+0.08}_{-0.06}$	853^{+297}_{-141}	3.75	573^{+62}_{-55}	4.23
	C	K2	$0.90^{+0.03}_{-0.03}$	538^{+58}_{-89}	2.92	931^{+95}_{-123}	4.80
	D	G8	$0.97^{+0.05}_{-0.04}$	2023^{+172}_{-210}	8.31	1708^{+191}_{-173}	7.91
3463	A ^c	G7	$0.99^{+0.06}_{-0.05}$	697^{+115}_{-96}	..	591^{+98}_{-56}	..
	B	M3	$0.39^{+0.09}_{-0.08}$	1776^{+504}_{-426}	2.53	2012^{+271}_{-292}	4.87
	C	K5	$0.86^{+0.05}_{-0.03}$	3017^{+375}_{-253}	9.16	2543^{+381}_{-365}	5.35
	D	G8	$0.96^{+0.06}_{-0.04}$	1591^{+257}_{-230}	3.89	1421^{+290}_{-255}	3.25
	E	K7	$0.79^{+0.09}_{-0.10}$	1051^{+102}_{-189}	1.87	1382^{+121}_{-205}	3.85
4495	A ^c	G2	$1.05^{+0.03}_{-0.04}$	1264^{+221}_{-156}	..	1382^{+311}_{-225}	..
	B
	C	M7	$0.30^{+0.06}_{-0.05}$	669^{+142}_{-168}	4.19	780^{+234}_{-210}	2.57
	D	K0	$0.91^{+0.05}_{-0.07}$	4053^{+611}_{-752}	3.71	3188^{+452}_{-435}	4.15
	E	K7	$0.81^{+0.07}_{-0.08}$	1492^{+481}_{-319}	0.71	1728^{+222}_{-192}	1.81
	F	K2	$0.89^{+0.08}_{-0.09}$	2279^{+1126}_{-818}	1.24	2920^{+827}_{-786}	1.96
5327	A ^c	M0	$0.57^{+0.05}_{-0.06}$	711^{+92}_{-110}	..	819^{+113}_{-142}	..
	B	M3	$0.38^{+0.04}_{-0.03}$	675^{+52}_{-48}	0.69	715^{+82}_{-57}	1.27
	C	G5	$1.24^{+0.07}_{-0.06}$	4128^{+529}_{-598}	5.71	3181^{+328}_{-389}	6.07
	D	K6	$0.67^{+0.03}_{-0.05}$	957^{+128}_{-186}	1.92	1120^{+100}_{-133}	2.26
6800	A ^c	F8	$1.05^{+0.02}_{-0.03}$	501^{+69}_{-91}	..	562^{+72}_{-65}	..
	B	F7	$1.11^{+0.05}_{-0.06}$	4873^{+715}_{-698}	6.26	2481^{+511}_{-556}	3.45
	C	M8	$0.31^{+0.05}_{-0.06}$	218^{+69}_{-51}	4.10	326^{+65}_{-52}	3.63
	D	G0	$1.09^{+0.07}_{-0.05}$	2849^{+479}_{-581}	4.04	3701^{+665}_{-492}	6.38

^aEstimated using methodology described in Atkinson et al. (2017).

^bEstimated using `isochrones` software package (Morton, 2015).

^cPrimary star in system, determined to be the brightest star within 4" of KOI coordinates.

Table 5.7: Corrected radii of planetary candidates in potential high-order multiple systems

Planet candidate	Period (d)	$R_{p,i}^a$ (R_\oplus)	R_A^b (R_\oplus)	R_B^c (R_\oplus)	R_C^d (R_\oplus)	R_D^e (R_\oplus)	R_E^f (R_\oplus)
3214.01	11.5	2.59 ± 1.0	3.00	7.47	8.53
3214.02	25.1	2.02 ± 0.78	2.34	5.83	6.66
3463.01	32.5	1.32 ± 0.53	1.35	4.67
4495.01	5.93	1.49 ± 0.64	1.60	..	3.52	6.17	4.30
5327.01	5.43	2.24 ± 0.11	2.35	4.99
6800.01	5.07	72.3 ± 37	72.9	722	253

^aInitial planetary radius estimate from NASA Exoplanet Archive.

^bCorrected planetary radius estimate if planet orbits primary star A.

^cCorrected planetary radius estimate if planet orbits nearby star B.

^dCorrected planetary radius estimate if planet orbits nearby star C.

^eCorrected planetary radius estimate if planet orbits nearby star D.

^fCorrected planetary radius estimate if planet orbits nearby star E.

KOI-3214

KOI-3214 hosts planetary candidates with initial planetary radius estimates of $2.59 R_\oplus$ and $2.02 R_\oplus$ on 11.5 and 25.1-day orbits, respectively. In the Robo-AO images, three nearby stars were observed within $5''$; all three stars were reimaged by Keck-AO (see Table 3.3 for properties of nearby stars, and Figure 5.5 for a cutout of the Keck-AO image of KOI-3214 and nearby stars). Based on the observed stellar density at the Galactic latitude of KOI-3214 (0.0039 sources observed per square arcsec at $b = 8.1^\circ$), the probability of three, two, and one unassociated stars being found within $5''$ of the planetary candidate host star is 0.0035, 0.0348, and 0.2277, respectively.

Estimates of distance from stellar model fitting of multi-band photometry, shown in Table 5.6, suggest that the nearby stars at $0.48''$ (KOI-3214B) and $1.30''$ (KOI-3214C) are, while not necessarily physically associated, not significantly inconsistent with being gravitationally bound to KOI-3214A. The nearby star at $4.46''$ (KOI-3214D), however, is not

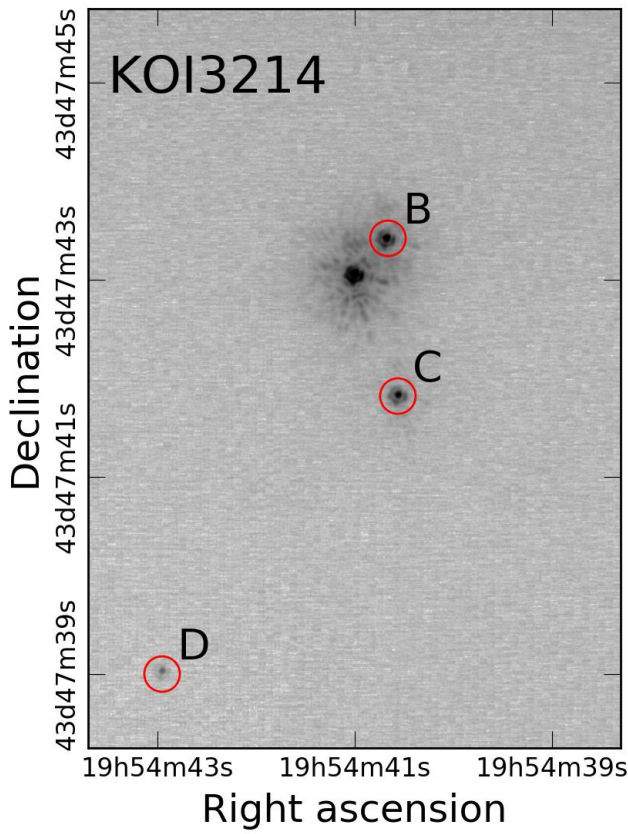


Figure 5.5: Color-inverted log-scale cutout of the Keck-AO NIRC2 K_p -band image of KOI-3214, with secondary sources labeled and circled.

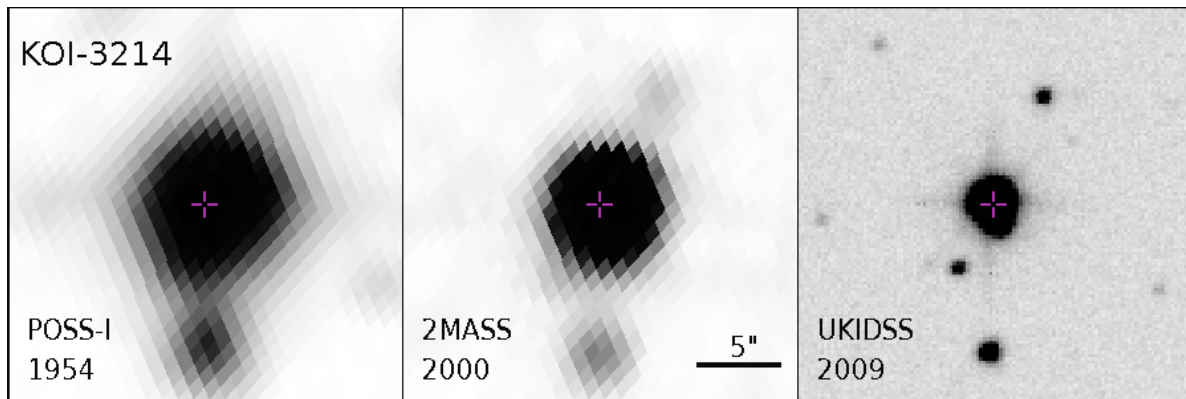


Figure 5.6: Archival images of KOI-3214 with the present day location of the target star marked with a reticle. With low proper-motion, the on-sky location of KOI-3214 has moved little over the long time baseline. All images are aligned such that north is up and east to the left and are on the same scale.

consistent with being bound to KOI-3214 and is likely a background asterism.

Archival images, see Figure 5.6, show KOI-3214 to have low proper-motion, moving little on-sky since a 1954 POSS-I image. The two nearest stars, KOI-3214B and KOI-3214C, are not visible in either the POSS-I or 2MASS images; KOI-3214C is partially blended with the primary in the UKIDSS image but has a separate central PSF. The separations and position angles between the primary and KOI-3214C are consistent with those measured in the Keck-AO image. KOI-3214D is apparent in POSS-I and 2MASS images as an extended PSF of the primary star, with a location relative to the primary consistent with the Keck-AO image. KOI-3214D is well resolved in the UKIDSS image, with a separation and position angle relative to the primary equal (within the margins of error) to those measured in Keck-AO image.

If both nearby stars are indeed physically associated with KOI-3214, the combined observations of Robo-AO and Keck-AO suggest a system consisting of a G2 primary star orbited by an F4 star at 133_{-29}^{+28} AU and a K2 star at 361_{-79}^{+78} AU. If the planetary candidates KOI-3214.01 and KOI-3214.02 orbit the target star, the contaminating flux from the secondary sources results in revised planetary radius estimates of $3.00 R_{\oplus}$ and $2.34 R_{\oplus}$, respectively. In each case, the planets are slightly more likely to be gaseous in composition, similar to Neptune, than rocky (Rogers (2015) suggests the transition between “rocky” and “non-rocky” occurs rather sharply at $R_P=1.6R_{\oplus}$). Updated radii estimates for the cases where either planet orbits one of the physically associated companion stars within 4" of the target star are shown in Table 5.7; for both planets, orbiting one of the secondary sources makes it highly likely that the planet is gaseous in composition.

KOI-3463

KOI-3463 hosts a planetary candidate with an initial planetary radius estimate of $1.3 R_{\oplus}$ on a 32.5-day orbit. In the Robo-AO images, three nearby stars were observed within 5"; all three stars were re-imaged by Keck-AO, with a fourth nearby star found just outside

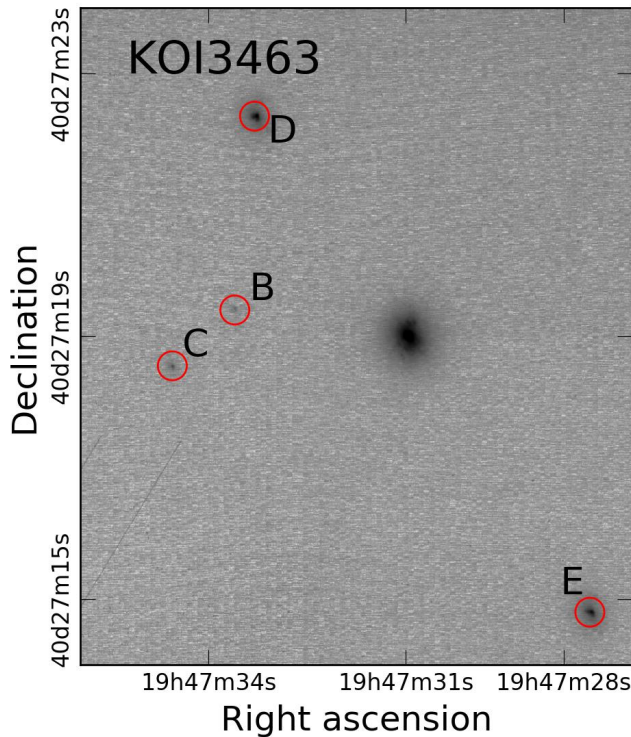


Figure 5.7: Color-inverted log-scale cutout of the Keck-AO NIRC2 K_p -band image of KOI-3463, with secondary sources labeled and circled.

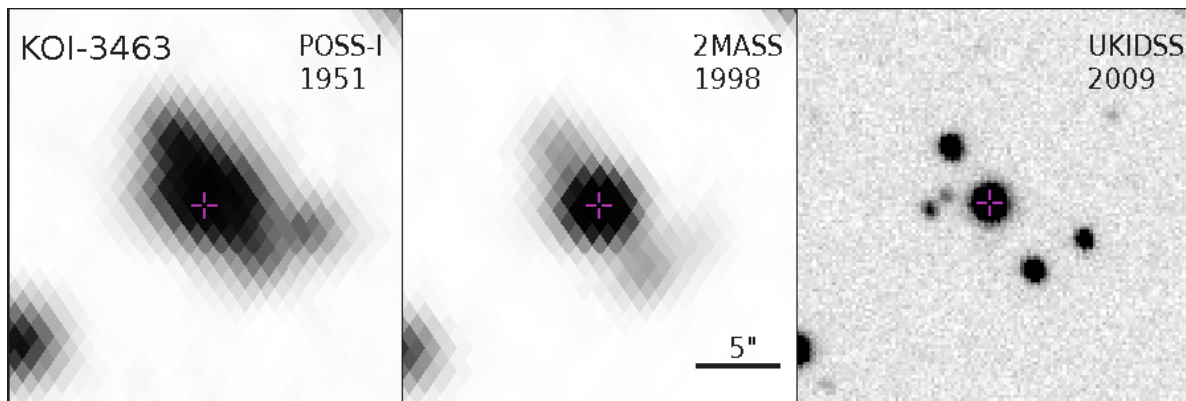


Figure 5.8: Archival images of KOI-3463 with the present day location of the target star marked with a reticle. With low proper-motion, the on-sky location of KOI-3463 has moved little over the long time baseline. All images are aligned such that north is up and east to the left and are on the same scale.

$5''$ (see Table 3.3 for properties of nearby stars, and Figure 5.7 for a cutout of the Keck-AO image of KOI-3463 and nearby stars). Based on the observed stellar density at the Galactic latitude of KOI-3463 (0.0041 sources observed per square arcsec at $b = 7.6^\circ$), the probability of three, two, and one unassociated stars being found within $5''$ of the planetary candidate host star is 0.0040, 0.0378, and 0.2345, respectively.

Estimates of distance from stellar model fitting of multi-band photometry, shown in Table 5.6, suggest that the nearby stars at $2.67''$ (KOI-3463B), $4.06''$ (KOI-3463D), and $5.03''$ (KOI-3463E) are, while not necessarily physically associated, not significantly inconsistent with being gravitationally bound to KOI-3463A. The nearby star at $3.64''$ (KOI-3214C), however, is not consistent with being bound to KOI-3463 and is likely a background asterism.

Archival images, see Figure 5.8, show KOI-3463 to have low proper-motion, moving little on-sky since a 1954 POSS-I image. The two nearest stars, KOI-3463B and KOI-3463C, are not resolved in the either the POSS-I or 2MASS images. The separations and position angles between the primary and KOI-3463D and KOI-3463E are consistent with those measured in the Keck-AO image, which does not rule out the gravitationally bound scenario for these three stars.

If all three nearby stars are indeed physically associated with KOI-3463, the combined observations of Robo-AO and Keck-AO suggest a system consisting of a G7 primary star orbited by an M3 star at 1860^{+308}_{-255} AU, a G8 star at 2829^{+468}_{-389} AU, and a K7 star at 3506^{+563}_{-482} AU. If the planetary candidate KOI-3463.01 orbits the target star, the contaminating flux from the secondary sources results in the planetary radius estimate to be revised slightly upward to $1.35 R_\oplus$, leaving the planetary candidate still possibly rocky in composition. If instead, the planetary candidate orbits KOI-3214B, the only nearby star within $4''$ and with a distance estimate not inconsistent with being bound to the primary, the revised planetary radius estimate is $4.67 R_\oplus$, resulting in a likely gaseous composition.

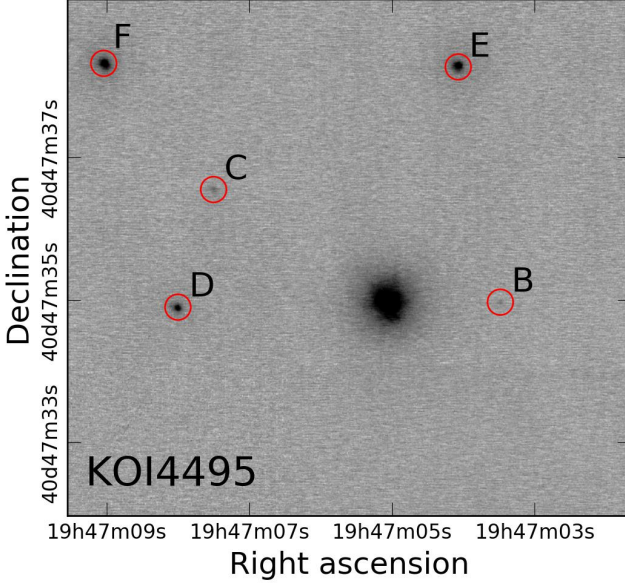


Figure 5.9: Color-inverted log-scale cutout of the Keck-AO NIRC2 K_p -band image of KOI-4495, with secondary sources labeled and circled.

KOI-4495

KOI-4495 hosts a planetary candidate with a period of 5.92 days and estimated radius of $1.49 R_{\oplus}$. In the Robo-AO images, three nearby stars were observed within $5''$. Keck-AO imaged all three stars of these previously observed stars, and resolved two new nearby stars, one just outside $5''$. Based on the observed stellar density at the Galactic latitude of KOI-4495 (0.0040 sources observed per square arcsec at $b = 7.8^{\circ}$), the probability of three, two, and one unassociated stars being found within $5''$ of the planetary candidate host star is 0.0037, 0.0365, and 0.2315, respectively.

Estimates of distance from stellar model fitting of multi-band photometry, shown in Table 5.6, suggest that the nearby stars at $2.91''$ (KOI-4495C), $2.95''$ (KOI-4495D), $3.44''$ (KOI-4495E), and $5.18''$ (KOI-4495F) are, while not necessarily physically associated, not significantly inconsistent with being gravitationally bound to KOI-3463A. The nearby star at $1.57''$ (KOI-4495B) was observed in only a single passband and cannot be characterized with photometry.

Archival images of the KOI-4495 system are shown in Figure 5.10. The four widely

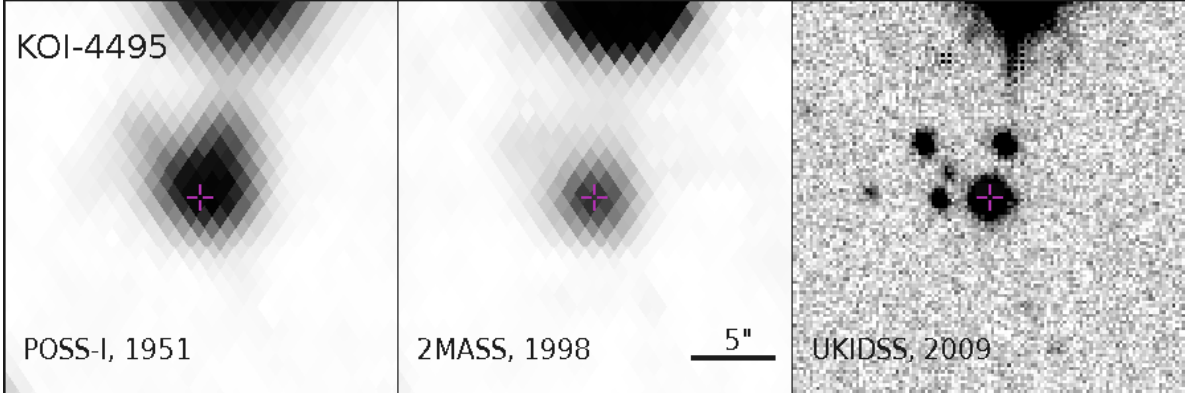


Figure 5.10: Archival images of KOI-4495 with the present day location of the target star marked with a reticle. With low proper-motion, the on-sky location of KOI-4495 has moved little over the long time baseline. All images are aligned such that north is up and east to the left and are on the same scale.

separated stars are fully resolved in the UKIDSS imaging, and KOI-4495B appears as an extension to the primary star PSF. In the POSS-I and 2MASS imaging, only KOI-4495E and KOI-4495F are detected. The separation and position angle of both are consistent with the gravitationally bound scenario.

KOI-5327

KOI-5327 hosts a $2.24 R_{\oplus}$ planetary candidate on a 5.4 day orbit. Robo-AO imaging observed three nearby stars, all of which were observed in follow-up imaging by Keck-AO. Based on the observed stellar density at the Galactic latitude of KOI-5327 (0.0026 sources observed per square arcsec at $b = 11.9^{\circ}$), the probability of three, two, and one unassociated stars being found within 5" of the planetary candidate host star is 0.0012, 0.0177, and 0.1692, respectively.

Archival images of the KOI-5327 system are shown in Figure 5.12. All three nearby stars are resolved in the UKIDSS imaging. The POSS-I imaging reveals significant proper motion shifts in the intervening years, and a clear alteration in the blended PSFs compared to the similar resolution 2MASS images. This is consistent with the primary star not being bound to either KOI-5327B and KOI-5327D.

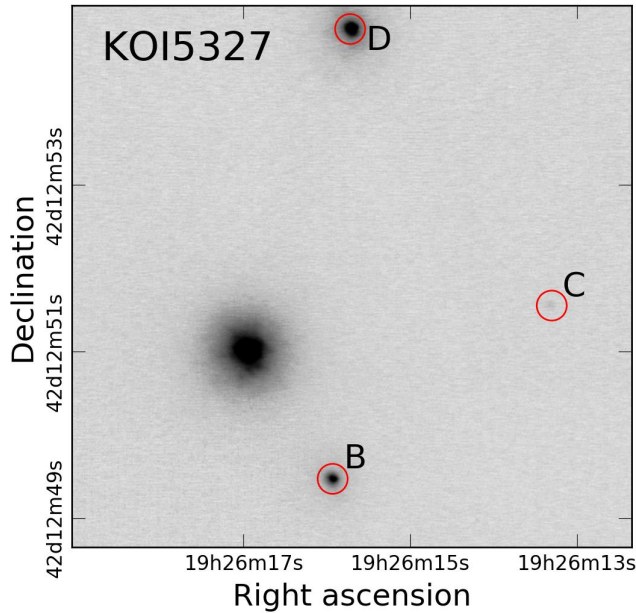


Figure 5.11: Color-inverted log-scale cutout of the Keck-AO NIRC2 K_p -band image of KOI-5327, with secondary sources labeled and circled.

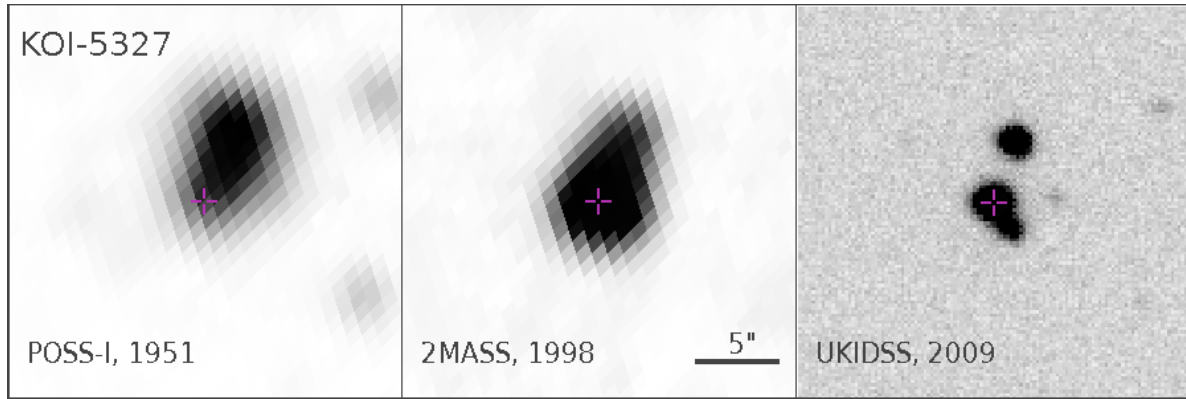


Figure 5.12: Archival images of KOI-5327 with the present day location of the target star marked with a reticle. All images are aligned such that north is up and east to the left and are on the same scale.

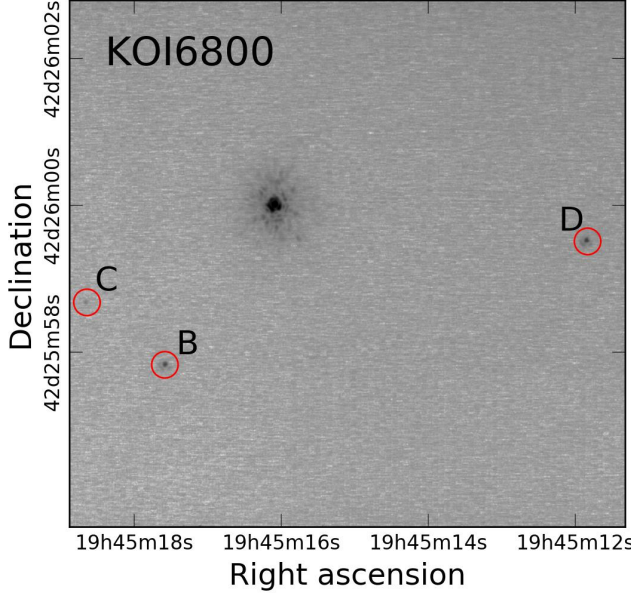


Figure 5.13: Color-inverted log-scale cutout of the Keck-AO NIRC2 K_p -band image of KOI-6800, with secondary sources labeled and circled.

KOI-6800

KOI-6800 hosts a $27.5 R_{\oplus}$ planetary candidate on a 2.5 day orbit. Robo-AO imaging observed three nearby stars, all of which were observed in follow-up imaging by Keck-AO. Based on the observed stellar density at the Galactic latitude of KOI-6800 (0.0036 sources observed per square arcsec at $b = 8.9^{\circ}$), the probability of three, two, and one unassociated stars being found within $5''$ of the planetary candidate host star is 0.0028, 0.0302, and 0.2147, respectively.

Archival images of the KOI-6800 system are shown in Figure 5.14. The three nearby stars are all resolved in the UKIDSS imaging, however, are blended with the primary in the POSS-I and 2MASS imaging. The primary star has low proper motion, and the lack of new sources in the archival images suggests that the proper motion of the nearby stars is comparable to the primary star. The archival images are consistent with the gravitationally bound scenario.

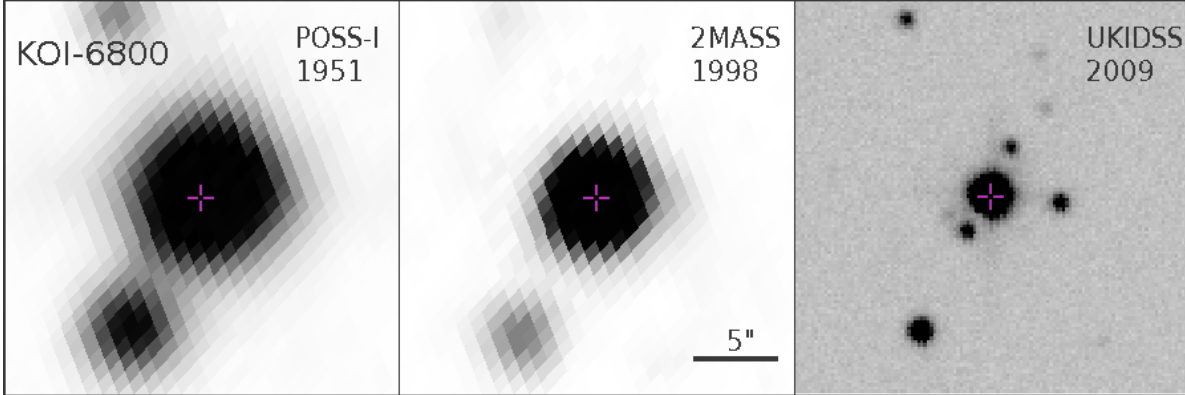


Figure 5.14: Archival images of KOI-6800 with the present day location of the target star marked with a reticle. All images are aligned such that north is up and east to the left and are on the same scale.

5.4 Conclusions

Combining the data sets from the complete Robo-AO KOI survey, we found 610 nearby stars around 559 planetary candidate hosts, from a target list of 3857 KOIs, implying a nearby star fraction rate of $14.5\% \pm 0.6\%$ within the Robo-AO detectability range (separations between $\sim 0.15''$ and $4.0''$ and $\Delta m \leq 6$). We found a nearby star fraction for Earth-sized planets of $16.3 \pm 1.0\%$, for Neptune-sized planets of $13.0 \pm 0.8\%$, for Saturn-sized planets of $13.6 \pm 2.0\%$, and for Jupiter-sized planets of $19.0 \pm 2.8\%$. We derived the corrected planetary radius for every planetary candidate with nearby stars in this survey. We found that planets in systems with likely bound nearby stars have underestimated radii by a factor of 1.54, if we assume each planet is equally likely to orbit the primary or secondary star. We found that 35 of the previously believed rocky planet candidates detected by *Kepler* are likely not rocky due to the presence of a nearby star.

We have also made the results of our survey available at a survey website.³

³<http://roboackepler.org/>

CHAPTER 6: STELLAR BINARITY AND PLANETARY SYSTEMS

The simple truth is that interstellar distance will not fit the human imagination.

— *The Hitchhiker’s Guide to the Galaxy*

In this chapter, I present an analysis of the probability of association of nearby stars to the planetary candidate hosts. I also revisit our analysis on the impact of stellar binarity to planetary systems from Chapter 4. In this analysis, I identify and remove a large fraction of the unbound asterisms, use the full set of observations from the Robo-AO KOI survey, and use the improved stellar parameters provided by the California *Kepler* survey (Johnson et al., 2017).

6.1 Observations

Robo-AO KP

Multi-band photometry of KOIs with detected nearby stars can allow characterization of each star, which can enable us to estimate the distance to each star. With these distances, we can discern whether the system is associated or a line-of-sight asterism. We performed follow-up observations in r' , i' , and z' bands of 145 KOIs with nearby stars detected by Robo-AO in previous papers in the survey were performed between 2017 March 16 and 2017 June 08 (UT) at Kitt Peak by Robo-AO. We targeted stars with surface gravity consistent with dwarf stars $\log g > 3$ and $\log g < 5$, as estimated by Mathur et al. (2017). In addition to visible photometry from Robo-AO images, we used PANSTARRs g' -band photometry (Chambers et al., 2016) for widely separated stars and extant NIR photometry from previous seeing limited and high-resolution surveys (Atkinson et al., 2017; Kraus et al., 2016; Furlan

et al., 2017). Photometry of the blended systems was obtained from the stellar properties described in Mathur et al. (2017). A list of targets observed and photometry is available in Appendix *E*.

Keck LGS-AO

Fifty-two candidate multiple systems were selected for re-imaging by the NIRC2 camera behind the Keck-II laser guide star adaptive optics system (Wizinowich et al., 2006; van Dam et al., 2006b), on 2017 Aug 8-10 (UT) to confirm possible companions. The target KOIs were selected from the entire Robo-AO survey due to the low significance of detectability of the companion star, either because of low contrast ratio or small angular separation. Of these, KOIs without previous high-resolution observations in the NIR in the literature were prioritized. Observations were performed in the K_{prime} filter using the narrow mode of NIRC2 (9.952 mas pixel $^{-1}$; Yelda et al. 2010). Ten KOIs were additionally observed in J and H filter to facilitate stellar characterization. Typically, three 30 s exposures were taken, for a total exposure time of 90 s. For increased efficiency, if a nearby star appeared to have high SNR, fewer exposures were taken. The images were corrected for geometric distortion using the NIRC2 distortion solution of Yelda et al. (2010). Targets observed with Keck are detailed in Appendix *C*. Additional NIR photometry for multi-band observations with Keck is presented in Appendix *E*.

6.2 Stellar Characterization

6.2.1 Photometric Analysis

Use of multi-band photometry allows characterization of the stars detected near KOIs, enabling estimates of the stars intrinsic brightness and approximate distances. If the distance estimates between the primary and a nearby star are in agreement, it is highly probable the two are in fact gravitationally bound.

Stellar SED fitting

To characterize the KOIs and nearby stars, we follow the analysis described in Atkinson et al. (2017). A Gaussian distribution for each available photometric color is generated using a Monte Carlo technique. Distributions are corrected for extinction using the standard relations from Cardelli et al. (1989). These distributions are then fit to age and metallicity agnostic SED models (Kraus & Hillenbrand, 2007) to determine the spectral type. We assume that all nearby stars are dwarf stars; we discuss possible background giant star contamination in Section 6.2.3. For each star, we use the intrinsic brightness of the estimated spectral type in each band compared to the observed apparent magnitudes of the star to estimate the distance to that star. The average of these estimated distances over all observed bands provides the final distance estimate. Distance uncertainties are derived from repeating the spectral fits and distance estimations using photometry in each band drawn at random from the respective Gaussian distribution. The final uncertainty is the standard deviation of the resulting distribution of distance estimates from 10,000 such fits.

The best spectral fit and distances estimate for each observed multiple system is available in Appendix *E*. For each KOI with a detected nearby star, we quantify the probability of association due to disparate distance estimates.

We combine the results of this analysis with those of Atkinson et al. (2017) and Hirsch et al. (2017) to estimate the percent of nearby stars that are bound, displayed in Figure 6.1. For results from the Robo-AO survey and from Atkinson et al. (2017), bound systems have uncertainties between the estimated distance of the primary and secondary star less than 2σ , uncertain have uncertainties between 2 and 3σ , and unbound have uncertainties greater than 3σ . The combined sample supports the conclusion of Hirsch et al. (2017) and the Robo-AO survey in Section 6.2.2 that most stars within 1" of the primary star are bound, with the percent of stars bound decreasing at wider separations.

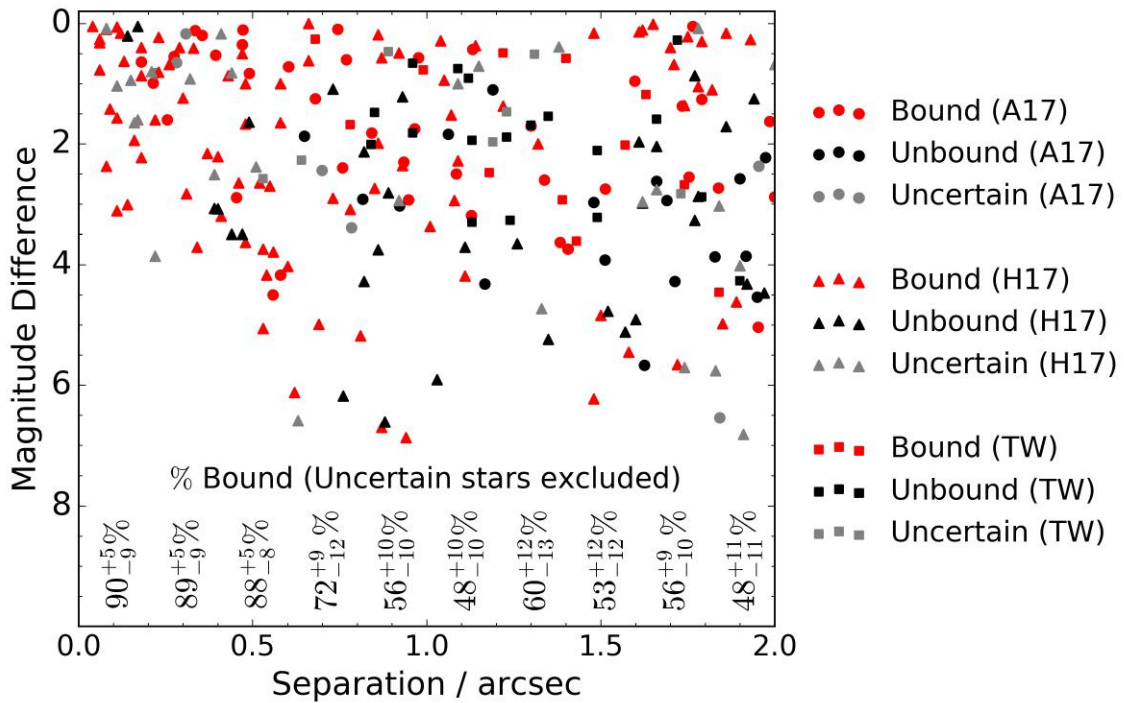


Figure 6.1: Results of association analyses of nearby stars to KOIs from Atkinson et al. (2017, A17), Hirsch et al. (2017, H17), and this work [TW], described in Section 6.2.1. The percent of nearby stars that are bound in each 0.2" bin is displayed along the bottom. Most stars within 1" of the KOI are bound, with wider separated stars more likely to be unbound.

6.2.2 Galactic Stellar Model Simulations

For nearby stars to KOIs without multi-band follow-up observations, we estimate the probability of association as a function of separation from the primary star and magnitude difference to the primary star using the TRILEGAL Galactic stellar model (Girardi et al., 2005). Following a similar analysis to Horch et al. (2014), we simulate star fields for ten one-square-degree star fields randomly distributed in the *Kepler* field of view. To match the distribution of stellar characteristics of the KOIs, we limit our sample to distances within 1300 pc, stellar effective temperatures between 3,000 and 10,000 K, and surface gravity, $\log g$, between 3.3 and 4.7. Binaries were populated at a companion rate of 46%, a fraction determined from observations for solar types stars by Duquennoy & Mayor (1991) and Raghavan et al. (2010). Orbital periods of the companion stars were drawn at random from the log-normal distribution from Duquennoy & Mayor (1991). Eccentricities were also drawn from the distribution found in Duquennoy & Mayor (1991). The semi-major axis of the orbit was determined from the stellar masses and period, and we select random values for the cosine of inclination ($\cos i$), ascending node (Ω), the angle in the orbit between the line of nodes and the semi-major axis (ω), and the time of periastron passage. The companion stars are then placed at an angular distance from the primary using by converting the true orbital distance and the distance from the solar system to the stars.

We simulate the detectable systems with Robo-AO using our average image performance (see Section 4.2.5) as a function of source brightness and a random variation caused by seeing. The simulated fraction of detected nearby stars in bins of separation and magnitude difference to the total number of observed nearby stars approximately aligned with the Robo-AO observations. A simulated *Kepler* field, with the number of nearby stars plotted limited as to be similar to the number detected in the full Robo-AO KOI survey, is displayed in Figure 6.2. Using all ten simulated fields, we determine the probability of association for a given separation and contrast. This probability density map is displayed in Figure 6.3, with observed nearby stars to KOIs from the Robo-AO survey over-plotted.

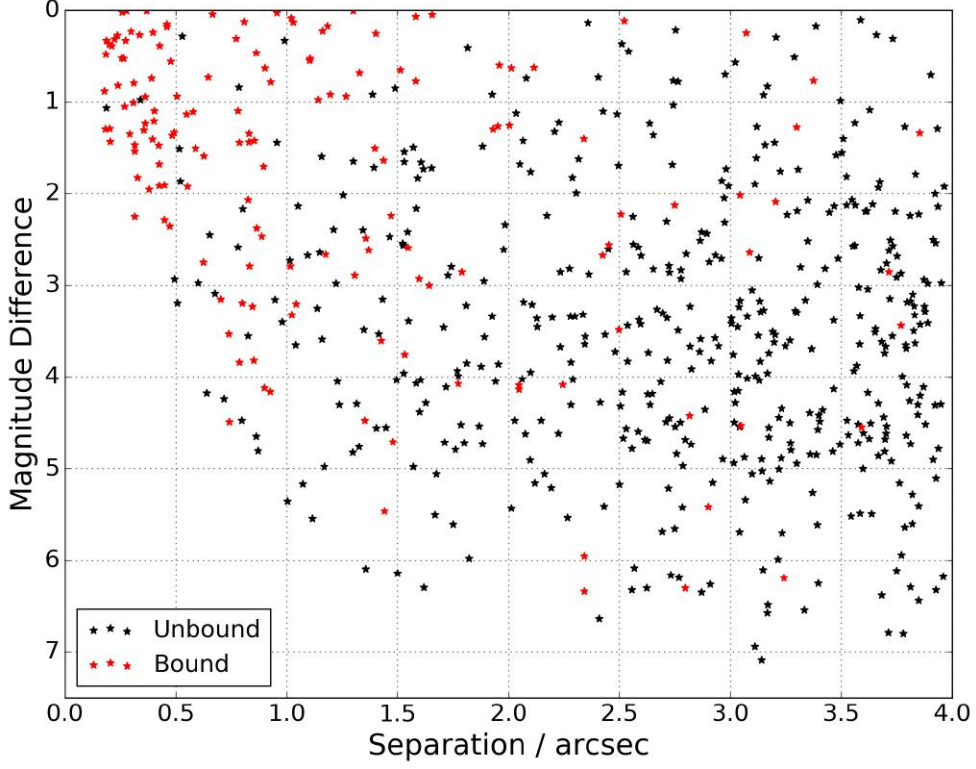


Figure 6.2: Simulated Robo-AO survey using Galactic stellar models, described in Section 6.2.2. Nearby stars that are bound to the primary star are plotted in red, and unbound asterisms are plotted in black. Bound stars are most likely to be found at small separations and near equal brightness to the target star.

The results of these simulations approximately agree with the previous simulations by Horch et al. (2014) and evidence from observations (displayed in Figure 6.1): most stars within $1''$ are expected to be bound, while wider separated companions with higher contrasts are likely unbound.

6.2.3 Expected Giant Star Contamination

It is conceivable that an unbound background giant star, observed near a KOI, has a distance estimate similar to the KOI resulting in a high probability of being bound. This is a result of our assumption that the background stars are dwarf stars. We estimate the number of expected giant stars being characterized as bound dwarf stars to the KOIs using the simulated *Kepler* fields, discussed in Section 6.2.2. We perform our stellar characterization

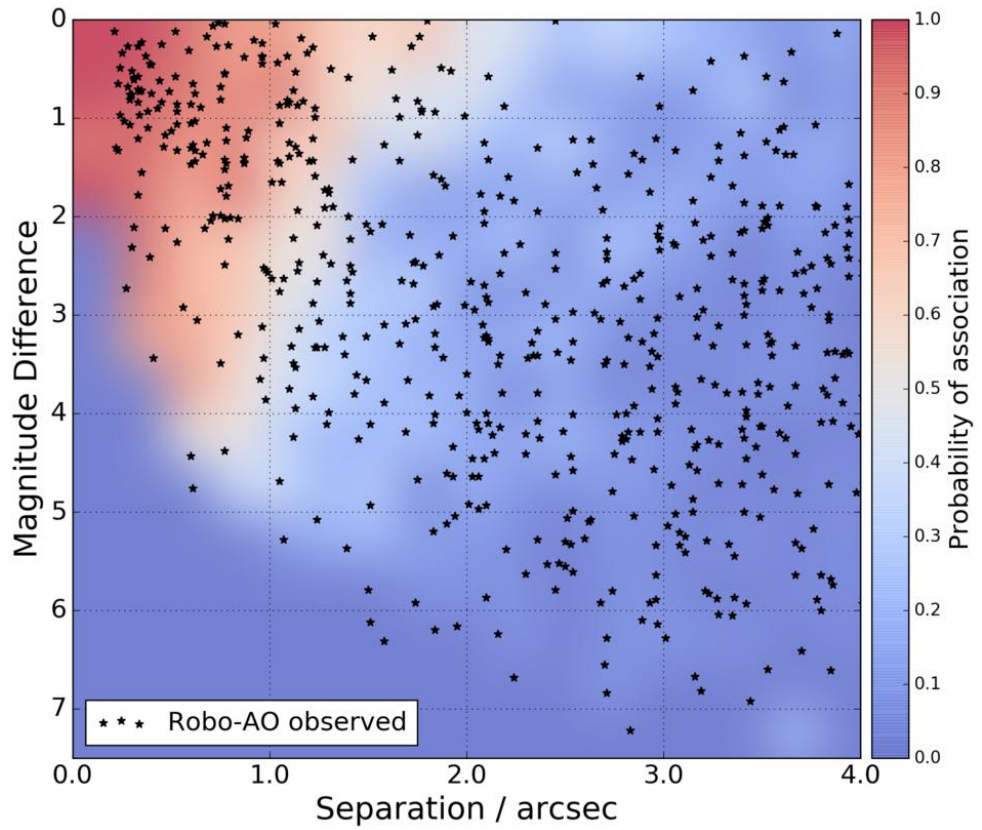


Figure 6.3: Probability of association density map derived from simulated star fields from Galactic stellar models, as described in Section 6.2.2. Observed nearby stars to KOIs from the Robo-AO survey are over-plotted.

analysis on the ten simulated fields, described in Section 6.2.1. We find a probability of approximately 20% that a single background giant star in the entire Robo-AO KOI survey will, if we assume it is a dwarf star, have an estimated probability of association with a planet host greater than 2σ in our analysis. We, therefore, expect the impact of background giant star contamination on results in this survey to be negligible.

6.2.4 Galactic Latitude and Stellar Density

The location of the KOI within the *Kepler* field may also impact the likelihood that an unbound star will be observed nearby. The large set of full frame Robo-AO images of KOIs allows us to estimate the stellar density over a statistically significant section of the sky within the *Kepler* field of view. We counted stars within 2598 full-frame images, not including the target star or any stars within 4" of the target star, to determine the observed stellar density with Robo-AO as a function of Galactic coordinates. The simulations described in Section 6.2.2 suggest that the vast majority of stars outside 4" are unbound to the target star. The observed stellar densities from the full frame Robo-AO images of KOI targets as a function of Galactic latitude are shown in Figure 6.4, with a quadratic fitting line.

We find Pearson correlation coefficients of Galactic latitude and longitude to observed stellar densities of -0.53 and -0.03, respectively. This suggests that Galactic latitude is the primary variable in estimating local stellar density. Indeed, the median Galactic latitude for KOIs with nearby stars is $b=11.2$, approximately a degree and a half closer to the Galactic disk compared the median latitude of all KOIs ($b_{med}=12.7$), while the difference in median Galactic longitude for the two populations is negligible. Apart from a higher number of nearby unbound stars, KOIs with nearby stars may on average be found at lower Galactic latitudes due in part to higher intrinsic binarity rates of thick disk stars compared to thin disk stars (Chiba & Beers, 2000; Grether & Lineweaver, 2007).

We use these stellar densities to then estimate the probability that an unbound star will, by chance, be within 4" of a KOI. We plot the KOIs with nearby stars observed in the

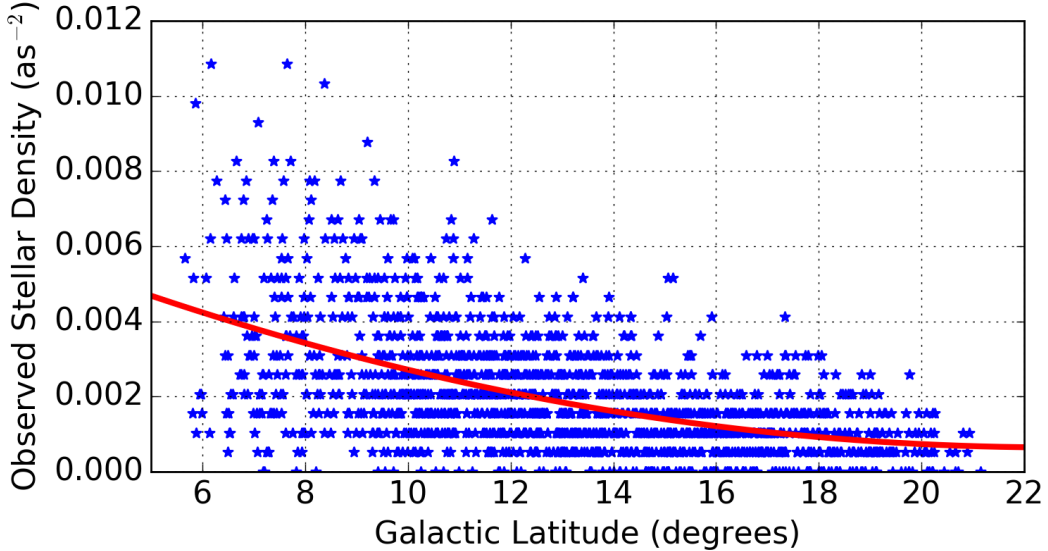


Figure 6.4: Observed stellar densities in Robo-AO full-frame images within the *Kepler* field as a function of Galactic latitude with a quadratic fit. Target stars and stars within 4" of the target star have been excluded. The distribution reveals a negative correlation between stellar density and Galactic latitude.

Robo-AO survey in Figure 6.5. We also plot the probability that an unbound star will be observed near a KOI estimated from the quadratic fit to the observed stellar densities as a function of Galactic latitude. For the entire set of 3857 targets from the Robo-AO KOI survey, we would expect on average approximately 318 unbound stars to be observed within 4" of the planetary hosts.

6.3 Stellar Binarity and Planetary Systems

We detect 610 nearby stars around 559 planetary candidate hosts from 3857 targets. With this large dataset, we can search for broad-scale correlations between the observed stellar multiplicity and planetary candidate properties. Such correlations provide an avenue to constrain and test planet formation and evolution models.

In addition to using a dataset nearly twice as large as in our previous analysis, our stellar characterization of the target and nearby stars and analysis of physical association probabilities, described in Section 6.2.1, allow us to attempt to remove the diluting impact

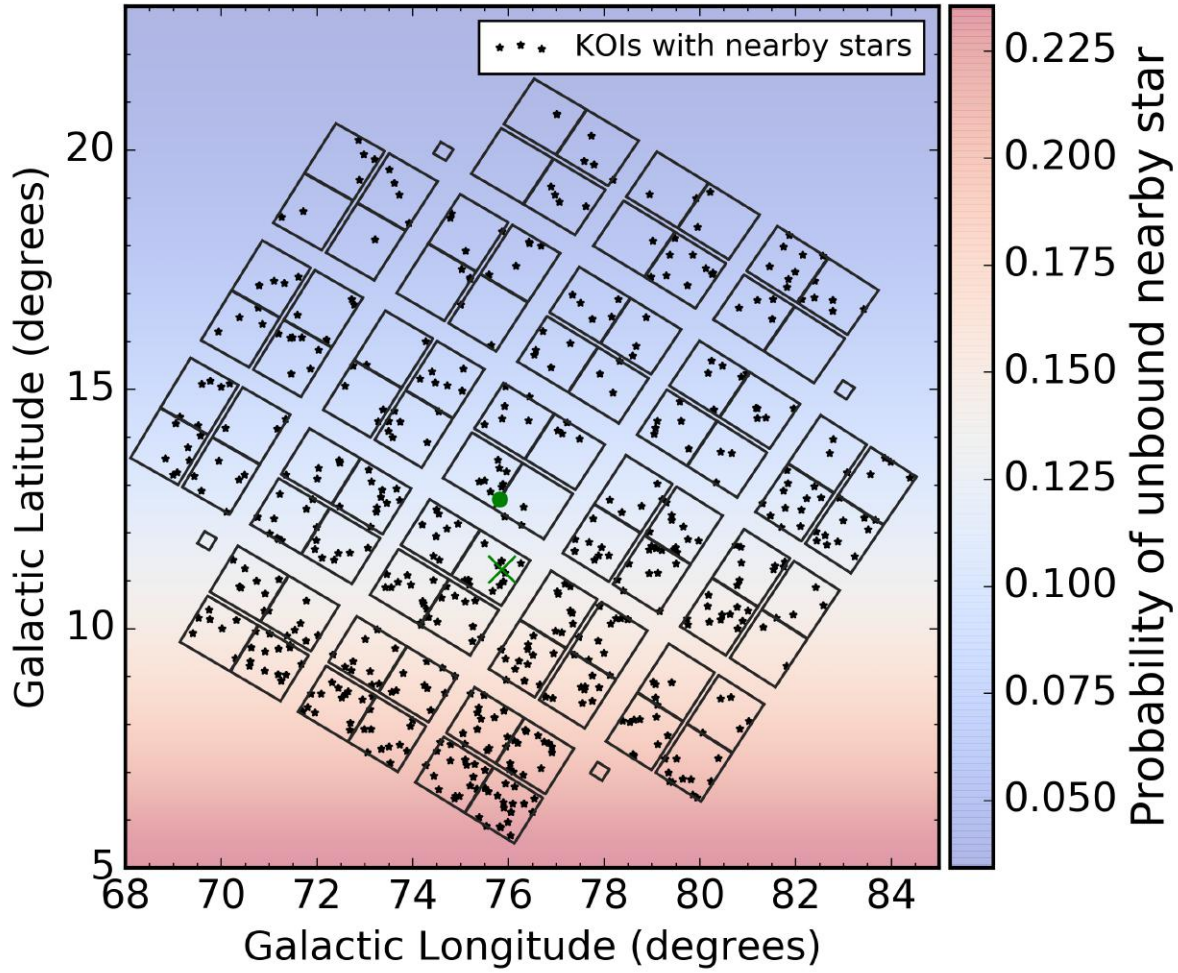


Figure 6.5: Location on the sky of KOIs with nearby stars from the Robo-AO *Kepler* survey. A projection of the *Kepler* field of view is provided for reference. The probability of an unbound star being found within $4''$ of the KOI is plotted, as determined from observed stellar densities with Robo-AO. The median sky position of all observed KOIs and KOIs with nearby stars are plotted with a green circle and \times , respectively. KOIs with nearby stars are on average closer to the Galactic disk.

of unbound nearby stars and strengthen any true correlation discovered. In addition, the California *Kepler* Survey (CKS) recently released updated stellar parameters (Johnson et al., 2017) several times more precise than those derived from photometry in the *Kepler* input catalog. These have revealed previously unknown features such as a planetary radius gap (Fulton et al., 2017). We use these parameters to search for correlations with parameters that were formerly not well constrained.

Unless noted, all stellar and planetary properties for the KOIs in this section were obtained from the cumulative planet candidate list at the NASA Exoplanet Archive¹ and have not been corrected for possible dilution due to the presence of nearby stars.

Stellar Multiplicity and KOI Number Revisited

The early and late public releases of KOIs (Borucki et al., 2011c; Batalha et al., 2013; Burke et al., 2014; Coughlin et al., 2016; Mathur et al., 2017) could conceivably have a built-in bias, either astrophysical in origin or as a result of the initial vetting process by the *Kepler* team. This bias might appear as a variation in multiplicity with respect to KOI number. In Paper III, we found a 2.9σ disparity between the multiplicity of KOIs numbered less than 5000 and greater than 5000. In the combined data set, which includes many more late release KOIs, we find KOI numbers less than 5000 have a nearby star fraction of $15.3\%\pm0.7\%$ and KOI numbers greater than 5000 have a nearby star fraction of $11.9\%\pm1.2\%$, a 2.1σ disparity. We plot the nearby star fraction rate as a function of KOI number in Figure 6.6.

The cause of this imbalance between early and late release KOIs nearby star fraction rate is not clear, but may relate to the use of automated vetting for later data releases (Mullally et al., 2015). There is no significant corresponding variation in the separations or contrasts of stellar companions between the two populations.

¹<http://exoplanetarchive.ipac.caltech.edu/>

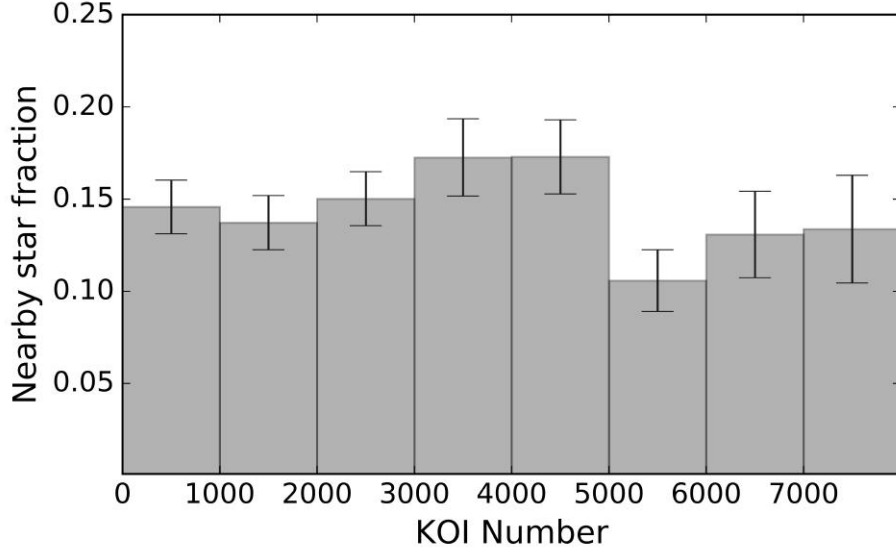


Figure 6.6: Multiplicity fraction within $4''$ of KOIs as a function of KOI number. A 2.1σ decrease in the fraction of nearby stars between KOIs numbered less than 5000 and greater than 5000 is apparent.

Stellar Multiplicity Rates and Host-star Temperature Revisited

We found that KOIs follow the correlation between multiplicity and stellar mass and temperature observed in field stars (Duchêne & Kraus, 2013) in Paper III. Restricting our sample to the likely bound nearby stars with separations less than $2.0''$ (as discussed in Section 6.2.1, we find that the trend remains for the entire set of observations from the Robo-AO KOI survey, as seen in Figure 6.7. The majority of stars in the CKS survey are solar-type, with effective stellar temperatures between 4500 and 6500 K. The trend relating multiplicity and effective temperature is expected to be negligible in that compact range of stellar temperatures, and indeed, no significant trend is apparent as seen in Figure 6.8

Stellar Multiplicity and Multiple-planet Systems Revisited

It is thought that the impact of a stellar companion to the planetary host star should perturb multiple planet systems, leading to fewer observed multiple transiting systems. Wang et al. (2014) and Picogna & Marzari (2015) suggest that perturbations from the companion star will change the mutual inclination of planets in the same system. Planets in nearby

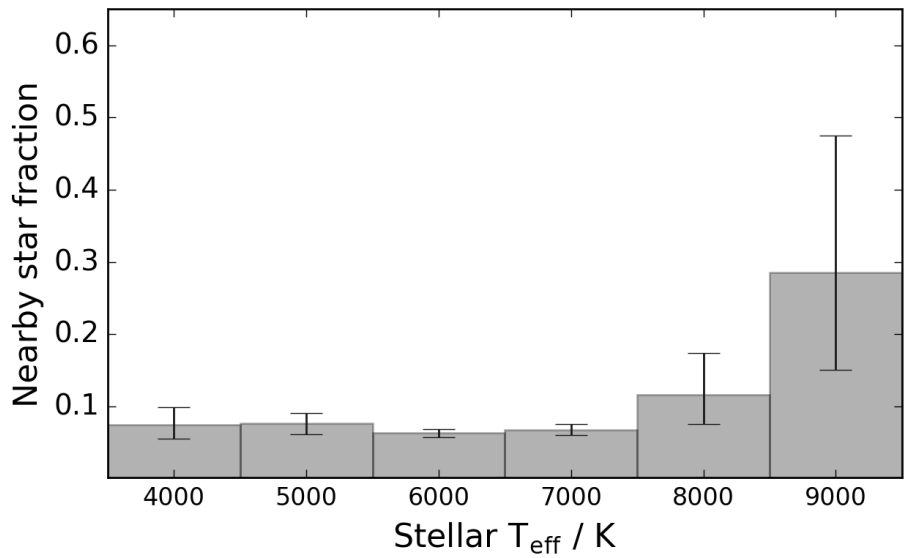


Figure 6.7: Fraction of KOIs with detected nearby ($\leq 2''$) stars as a function of stellar effective temperature.

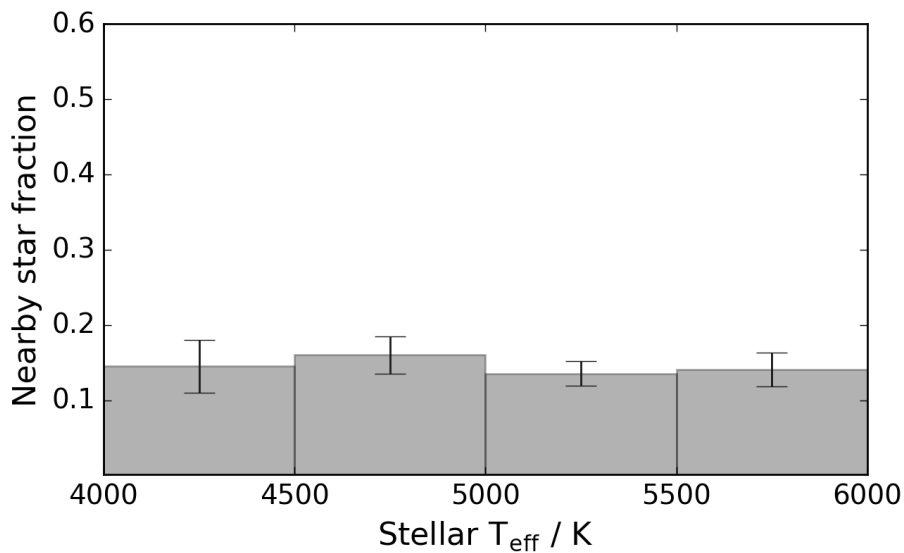


Figure 6.8: Fraction of KOIs with detected nearby ($\leq 4''$) stars as a function of stellar effective temperature, using estimates from the California *Kepler* Survey (Johnson et al., 2017).

orbits are also expected to perturb each other (Rasio & Ford, 1996; Wang et al., 2015a), possibly leading to planets being ejected out of the system (Xie et al., 2014).

We searched for evidence of a disparity in stellar multiplicity between the two planetary populations in Paper I and Paper III. In Paper I, we found single-planet systems exhibiting a slightly higher nearby star fraction. With several times more targets used in the analysis in Paper III, we found a slightly higher nearby star fraction for the multiple-planet systems. Combining all KOI targets, we again find little difference between the two populations (displayed in panel *a* in Figure 6.9): a Fischer exact test gives 87% probability the two populations are drawn from the same distribution.

The full set of KOI targets is likely highly diluted, however, by false positive planets (Morton & Johnson, 2011; Fressin et al., 2013) and unbound nearby stars (see Section 6.2.1). We, therefore, perform cuts to the set of KOI targets in an attempt to reduce these effects, shown in Figure 6.9. We find after all successive cuts, with confirmed planets with likely bound nearby stars, single-planet systems have slightly higher nearby star fraction rate than multiple-planet systems: $4.0\%\pm0.6\%$ and $3.0\%\pm0.7\%$, respectively. A Fischer exact test gives two-thirds probability (66.5%) that the two populations are indeed disparate.

It is not clear if this low-significant result is evidence of the disturbing impact of stellar companions on planetary systems. Other factors may result in a higher than expect binarity fraction of multiple planet systems, however. Companion stars can cause orbital migration with Kozai oscillations (Fabrycky & Tremaine, 2007), shifting multiple planets in the same system to shorter periods where *Kepler* has higher sensitivity to transit events. Binary stars that form together also may have mutually inclined protoplanetary disks (Müller & Kley, 2012), leading to separate transiting planetary systems around each star.

Stellar Multiplicity and Close-in Planets Revisited

It is hypothesized that the presence of a stellar companion will greatly influence the properties and architecture of planetary systems. Observational evidence suggests that planetary

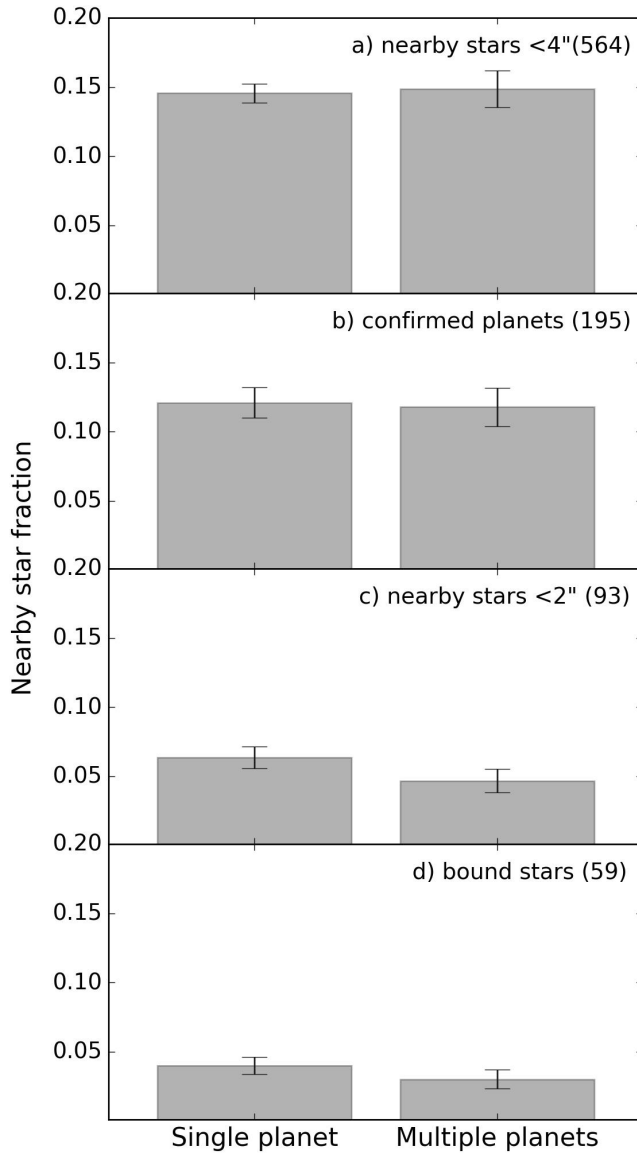


Figure 6.9: **(a)** Nearby star fraction within $4''$ of KOIs hosting single- and multiple-planetary systems. Panels **(b)-(d)** show these fractions after successive cuts to **(b)**: remove systems with unconfirmed planets; **(c)**: remove systems with nearby stars at separations greater than $2''$; **(d)**: remove systems with stars shown to be likely unbound from observations (see Section 6.2.1), and weight systems with nearby stars whose association has not been studied by the probability of association based on the separation of the nearby star from the primary star derived from observations (see Figure 6.1). The number of systems with nearby stars remaining after each successive cut is annotated in the upper right corner of each panel. In panel **(d)**, the weights of the systems with nearby stars without association determination were summed with the number of observed likely bound systems and rounded to the nearest whole number.

formation is suppressed in close binaries, resulting in a fifth of all solar-type stars being unable to host planets because of stellar interactions (Kraus et al., 2016). Perturbations from the nearby star are thought to drive planets that form at large separations inward to low-period orbits (Fabrycky & Tremaine, 2007; Katz et al., 2011; Naoz et al., 2012), with smaller planets more susceptible due to weak planet-planet dynamical coupling (Wang et al., 2015a). Interactions between planets within the same system, often caused by orbital migration caused by stellar companions, are thought to eject small planets at a greater rate than giant planets (Xie et al., 2014). We would expect then a correlation between binarity and planetary period for different sized planets.

In our analysis in Paper III, we found little evidence for a disparity in nearby star fraction for giant ($R > 3.9 R_{\oplus}$) and small ($R < 3.9 R_{\oplus}$, Neptune radius) planets at short or long periods. With the combined data set of the Robo-AO KOI survey, we find a low-significance increase in nearby star fraction for giant planets at short periods compared to small planets (see panel **a** in Figure 6.10).

We expect that our sample is heavily diluted, however, by false positive planets (hot Jupiters are expected to have a higher than average false positive rate Santerne et al. 2012) and unassociated nearby stars, as discussed in Section 6.2.1. We, therefore, remove contaminating systems in search of any possible underlying correlation. These cuts are as followed (resulting distributions are shown in Figure 6.10): remove nearby stars at separations greater than $2''$, a region where most stars are highly likely to be unbound; remove unconfirmed planets; remove systems that have been shown to be likely unbound from observations (see Section 6.2.1), and weight systems whose probability of association has not been studied by the percent likelihood of being bound based on their separation from the host star, as determined from observations.

After successive cuts, we find that giant, small planets on 1-3 day orbits have a binarity rate of $12.8\%^{+5.6\%}_{-2.8\%}$ and $2.4\%^{+1.8\%}_{-0.9\%}$ ², respectively, a 2.6σ discrepancy. No other period range

²Errors for both populations are based on Poissonian statistics (Burgasser et al., 2003).

shows a significant difference in binarity rate between the two populations.

This result agrees with the NIR survey of Ngo et al. (2015), that found hot Jupiter hosts are twice as likely as field stars to be found in multiple star systems, with a significance of 2.8σ . They, however, find that 51% of hot Jupiters are hosted by stars with stellar companions; the discrepancy in the binarity fractions found in the two surveys likely is a result of differing observational methods and limits. The binarity fraction for hot Jupiters in this survey does agree with that found by Roell et al. (2012) of 12%.

Stellar Multiplicity and Metallicity of KOIs Revisited

The relationship between stellar multiplicity and metallicity is not well understood. Early studies suggested that metal-poor stars possessed fewer stellar companions (Kopal, 1959; Jaschek & Jaschek, 1959; Batten, 1973; Abt & Willmarth, 1987), while more recent studies have suggested just the opposite (Carney et al., 1987, 1994). In particular, Grether & Lineweaver (2007) found a $\sim 2\sigma$ anti-correlation between metallicity and companion stars. Planetary systems do seem to occur more frequently in metal-rich stars (Fischer & Valenti, 2005; Grether & Lineweaver, 2007).

We can use the multiplicity fraction of planet candidate hosting stars as a function of metallicity to determine how these stars compare to field stars. For this analysis, we use the precise metallicity ($[\text{Fe}/\text{H}]$) estimates from the CKS (Johnson et al., 2017) which have typical uncertainties of 0.05 dex.

We may expect to see a correlation between metallicity and nearby star fraction rate in the full set of KOIs since our sample likely has a high number of unbound stars (see Section 6.2.1. A higher fraction of these nearby stars are from low Galactic latitudes where the observed stellar density is greater (see Section 6.2.4). Grether & Lineweaver (2007) found that stars at low b , citizens of the Galactic thick disk which have higher average metallicity (Ishigaki et al., 2012), shows a ~ 4 times higher binary fraction than halo stars.

For the set of all KOIs, the nearby star fraction within $4''$ visually appears to correlate

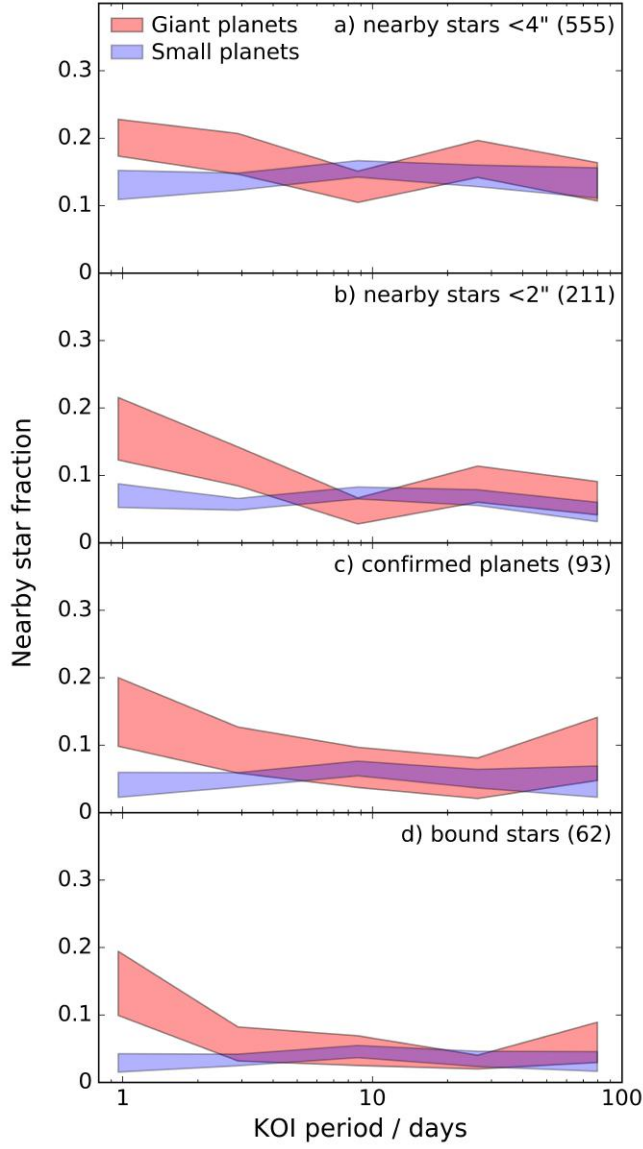


Figure 6.10: **(a)** 1σ uncertainty regions for the nearby star fraction as a function of KOI period for two different planetary populations. Panels **(b)-(d)** show these regions after successive cuts to **(b)**: remove systems with nearby stars at separations greater than $2''$; **(c)**: remove systems with unconfirmed planets; **(d)**: remove systems with stars shown to be likely unbound from observations (see Section 6.2.1), and weight systems with nearby stars whose association has not been studied by the probability of association based on the separation of the nearby star from the primary star derived from observations (see Figure 6.1). The number of systems with nearby stars remaining after each successive cut is annotated in the upper right corner of each panel. In panel **(d)**, the weights of the systems with nearby stars without association determinations were summed with the number of observed likely bound systems and rounded to the nearest whole number.

slightly with metallicity, as shown in panel **a** in Figure 6.11. A Fisher exact test suggests however with high probability ($\sim 99\%$) that sub- and super-solar metallicity KOIs are similar populations, with nearby star fraction rates of $14.1\% \pm 1.7\%$ and $14.1\% \pm 1.4\%$, respectively.

If we remove any systems with nearby stars at separations greater than $2''$, which are likely to be unbound as discussed in Section 6.2.1, we find that the nearby star fraction rate slightly decreases as metallicity increases, shown in panel **b** of Figure 6.11. With the decreased separation limit, sub-solar and super-solar metallicity KOIs have nearby star fraction rates of $7.7\% \pm 1.3\%$ and $5.9\% \pm 0.9\%$, respectively; a Fisher exact test gives a 28% probability that the two populations are distinct.

Finally, when we remove systems without confirmed planets, shown in panel **c** of Figure 6.11, no significant trend is apparent between stellar binarity of planet-hosting stars and stellar metallicity. A Fischer exact test suggests with 87% probability that sub- and super-solar are similar stellar populations, binarity rates of $5.4\% \pm 1.3\%$ and $5.9\% \pm 1.2\%$, respectively.

6.4 Conclusions

In this chapter, we performed a more sophisticated analysis of the Robo-AO survey to search for insight into the impact binary stars have on planetary systems. In particular, we removed KOIs with likely unbound nearby stars from our sample.

To identify these unbound systems, we characterized the primary and nearby star of 145 KOIs reobserved with Robo-AO in multiple visible bands. We quantified the probability of association for these systems, and derive corrected planetary radii for planetary candidates within these systems. We estimated the percent of nearby stars bound to the primary using the sample in this work and previously published datasets.

We found that giant planets at low periods are several times more likely be found in systems with stellar companions than other planets. We found that single and multiple planet systems are equally likely to orbit in binary star systems. We found that KOIs follow trends observed in field stars with respect to the relationship between stellar multiplicity

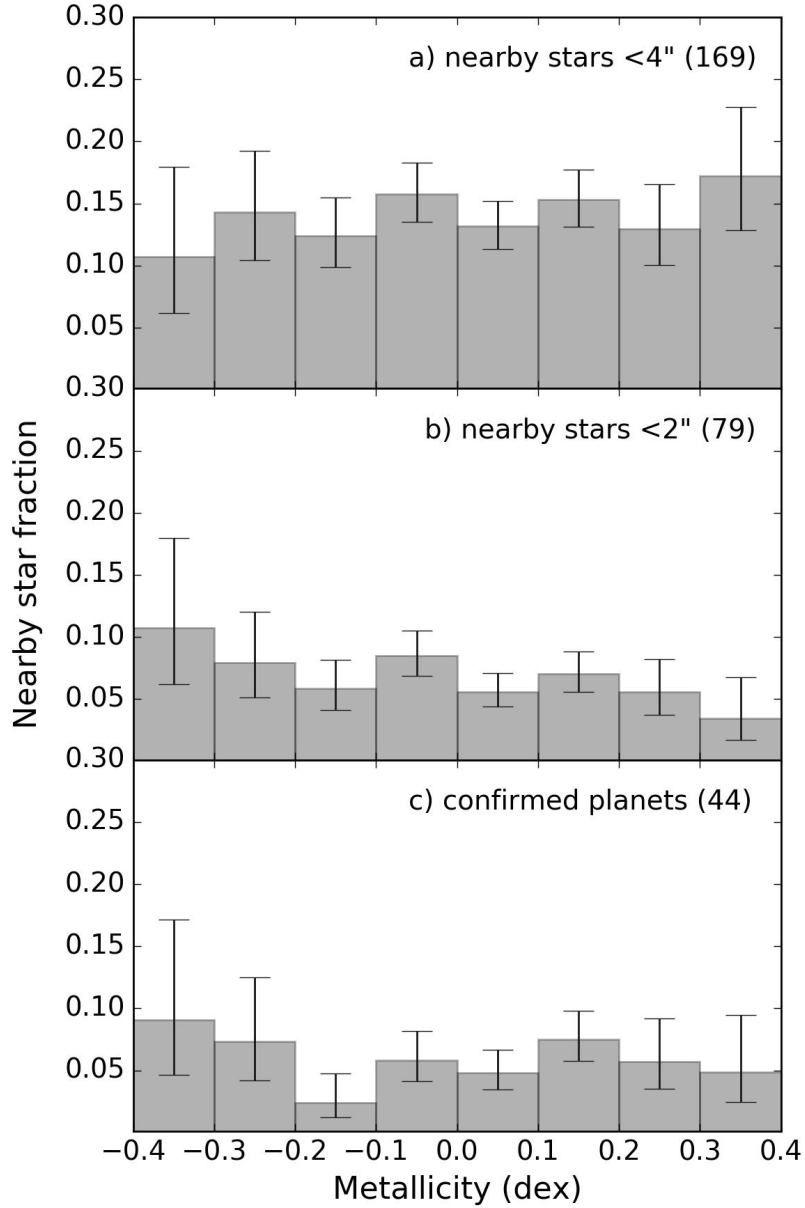


Figure 6.11: **(a)** Nearby star fraction as a function of KOI metallicity ($[\text{Fe}/\text{H}]$) using CKS estimates (Johnson et al., 2017). Panels **(b)** and **(c)** show these regions after successive cuts to **(b)**: remove systems with nearby stars at separations greater than $2''$; **(c)**: remove systems with unconfirmed planets. The number of systems with nearby stars remaining after each successive cut is annotated in the upper right corner of each panel.

and stellar effective temperature and metallicity.

CHAPTER 7: CONCLUSIONS & OUTLOOK

It is said that despite its many glaring (and occasionally fatal) inaccuracies, the Hitchhiker’s Guide to the Galaxy itself has outsold the Encyclopedia Galactica because it is slightly cheaper, and because it has the words ‘DON’T PANIC’ in large, friendly letters on the cover.

— *The Hitchhiker’s Guide to the Galaxy*

In this chapter, I summarize the results presented in this dissertation and suggest future avenues of research enabled by the work presented in this dissertation.

7.1 Robo-SOAR

Robo-SOAR is a moderate-order NGS-AO system in development for the SOAR telescope. With robotic software adapted from Robo-AO, Robo-SOAR will be capable of observing hundreds of targets a night. With an innovative, low-cost dual knife-edge WFS, similar in concept to a pyramid WFS but with reduced chromatic aberrations, Robo-SOAR can reach the diffraction limit on brighter targets.

I designed the optics of Robo-SOAR and constructed a lab testbed of the science path (Ziegler et al., 2016). I designed a glass double pyramid with reduced chromatic aberrations which would allow broadband wavefront sensing on faint targets. The manufacturing of this design, however, proved prohibitively expensive. I subsequently assisted in the conception and design of the dual knife-edge wavefront sensor, a substantially less costly reflective alternative to the glass pyramid design. The performance of this design is currently being characterized.

7.2 Cool Subdwarf Multiplicity

I discussed the observations of 348 cool subdwarf stars with Robo-AO (Ziegler et al., 2015), a pilot study for the *Kepler* survey. We found that approximately 12% of cool subdwarfs have binary companions, a fraction around three times lower than similar dwarf stars. The disparity between the two populations may be evidence of the different environments in which they formed. The lack of companions to cool subdwarfs suggests they may have formed in less dense regions, or over their long lifetimes may have had more disruptive encounters with other stars and the Galactic tide. These results are also consistent with the theory that these stars are galactic interlopers, having been formed in small, less-dense galaxies that merged with the Milky Way.

7.3 Robo-AO KOI Survey

I discussed the high-resolution observations of 3857 KOIs with Robo-AO. I wrote the last two published papers in this survey (Ziegler et al., 2017a,b), and have performed the data analysis of every observation. We found 610 stars within 4" of a planetary candidate host star. The presence of these stars contaminate the *Kepler* light curves and alter the derived planetary radius. We correct the estimated radii for over 800 planetary candidates. We find that nearby stars will, on average, increase the planetary radii by a factor of approximately 1.59. We also quantified the probability of association of 157 KOIs with nearby stars and found that the majority of systems with separations less than 1" are bound.

I also presented the results of the upcoming fifth paper in the survey. In it, I found that hot Jupiters are more likely than any other planet to be found in a binary star system. This suggests that stellar companions drive orbital migration of giant planets. I also found that single and multiple-transiting planet systems are equally likely to be found in a binary. I found that KOIs from later data releases are less likely to have a nearby star than systems from earlier data releases, possibly a result of the automation of the *Kepler* vetting pipeline. I found that KOIs follow trends observed in field stars with respect to the relationship between

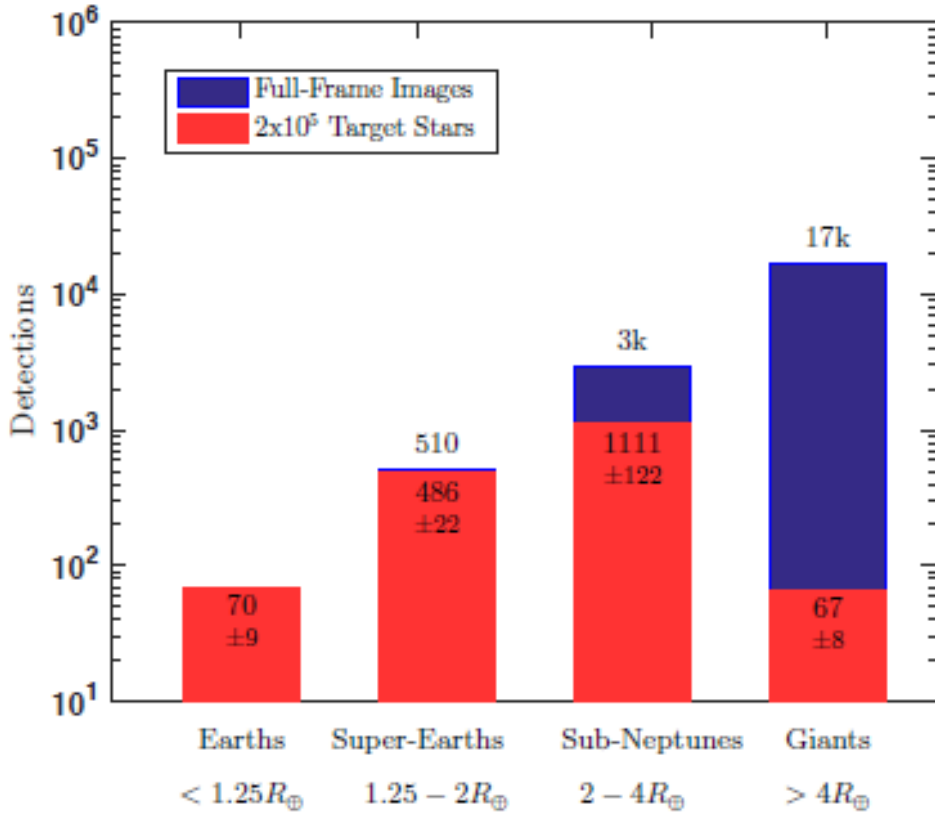


Figure 7.1: The mean numbers of planets detected in a TESS simulation around, in red, the 2×10^5 target stars observed at 2 min cadence and, in blue, the stars observed in the full-frame images observed at 30 min cadence. [Image courtesy of Sullivan et al. (2015)]

stellar multiplicity and stellar effective temperature and metallicity.

7.4 Future Outlook

7.4.1 Rapid TESS follow-ups

The TESS mission is expected to discover thousands of planets (see Figure 7.1), each requiring follow-up observations in high-resolution from the ground for confirmation and characterization. *Gaia* will improve on the resolution of seeing-limited imaging by approximately a factor of two, sensitive to the majority of stars at separations greater than one arcsecond from TESS targets (de Bruijne et al., 2014). High-resolution imaging will resolve hundreds of closer stars.

Follow-up observations of the Kepler planetary candidates have taken years to perform

(see overview in Furlan et al. (2017)). Studies performed in the interim were forced to either delay or use (often unknowingly) inaccurate data. As discoveries from TESS are of considerable interest, I am interested in building a pipeline to perform the observations and data analysis necessary to deliver corrected radius estimates for every TESS planetary candidate within a few months of announcement. Rapid follow-ups are possible as the TESS fields are anti-solar. The corrected radii estimates would be available pre-publication on a frequently updated survey website (similar to roboaokepler.org), as well as made publicly available on the NexSci ExoFOP service. These timely radius corrections would improve nearly every analysis performed using TESS planetary data over the coming decade.

7.4.2 Planetary host star identification

The properties of each planet are derived from the properties of the host star. However, over 600 Kepler planetary candidates have multiple stars within the photometric aperture of the reputed host star (Ziegler et al., 2017b). In the majority of these systems, the source of the transit signal is ambiguous (a small fraction of host stars can be identified using centroid analysis (Bryson et al., 2010)). TESS will be particularly vulnerable to host star confusion, with pixels that subtend an area on the sky 25x larger than Kepler. I am interested in a study to identify the source of the transit signal by resolving the system during the transit event with an AO system. Since only the short period around ingress or egress is required to determine the host star, many systems can be observed in a single night. This study could potentially identify and confirm the host of several dozen rocky, habitable zone planets. A few would likely be false positive eclipsing binaries. Some of the planets we find may be circumbinary, or Tatooine, planets, orbiting both components of a close stellar binary. Kepler found seven such systems, suggesting they are relatively common; however, their true occurrence rate is not known as many likely orbit unresolved close binary stars.

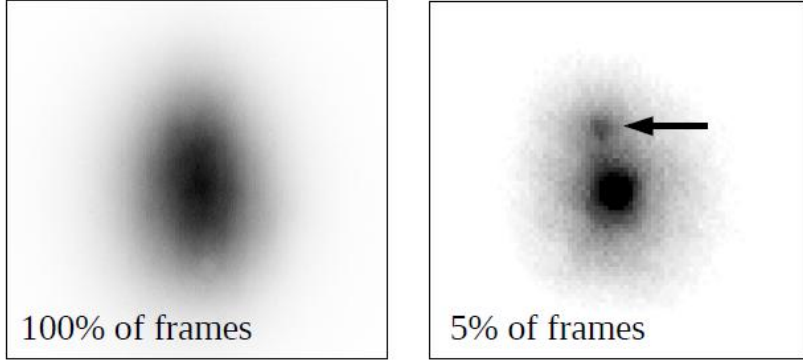


Figure 7.2: Example of lucky imaging on a binary star observed with a 1-meter telescope. The left frame is seeing limited, with 100% of frames used. The right frame uses the best 5% of frames, revealing a close binary companion ($\rho=0.3''$). This low-cost method would observe the majority of nearby stars to TESS exoplanet hosts.

7.4.3 Lucky imaging

A low-cost option for performing kilo-target high-resolution imaging surveys is lucky imaging (Law et al., 2006) using a fast frame rate camera, such as an EMCCD ($\sim \$30k$). This method uses only a small fraction of the exposures (those with the highest image quality) in each observation to reach the diffraction limit of smaller telescopes (see Figure 7.2). The instrumentation required is relatively simple, with the main expense being the camera. Around 300 of the stars found in the Robo-AO Kepler survey are not visible in seeing-limited imaging but could be detected with diffraction-limited imaging on a half-meter telescope. I am interested in a project to construct an automated lucky imaging system on a small telescope to detect hundreds of blended, nearby stars to exoplanet hosts discovered by TESS. This survey would provide preliminary corrections to the planet radii for these planets (weeks after announcement) and quickly identify potential false positives.

7.5 Final Thoughts

The era of big data in astronomy is just beginning. Future telescopes and space missions, such as LSST (Tyson, 2002), TESS (Ricker et al., 2014), and PLATO (Rauer et al., 2014), will vastly increase the number of targets requiring follow-up high-resolution observations.

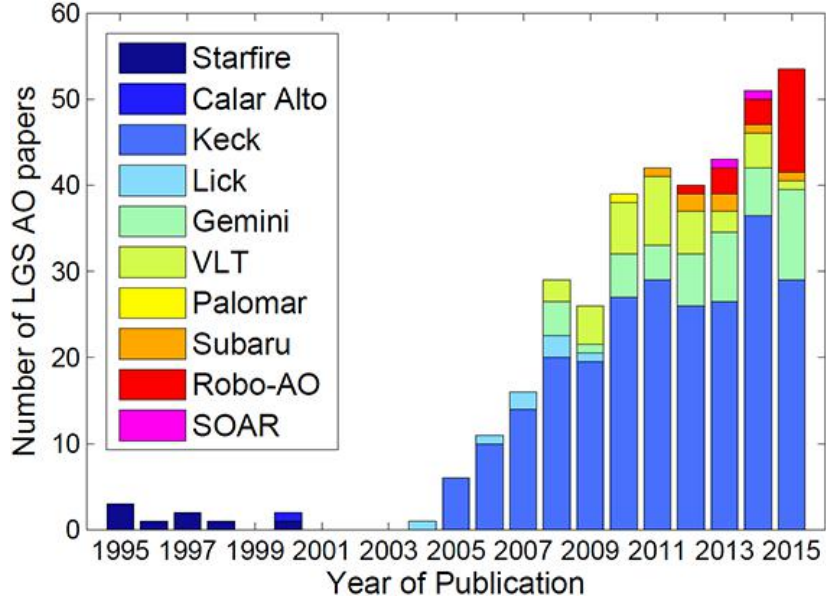


Figure 7.3: Science publications using data from LGS-AO instruments. In 2015, Robo-AO mounted on the Palomar 1.5m telescope produced the second most number of publications for any LGS-AO system, behind only Keck-AO on a 10m telescope. In 2016, Robo-AO moved to its current home on the Kitt Peak 2.1m telescope, reducing the number of science publications that year. Fully operational and with continuous dedicated time, the number of Robo-AO scientific publications has increased in 2017 and 2018. [Image courtesy of Peter Wizinowich]

The surveys performed by Robo-AO has proven that productive automated instruments on telescopes are possible, resulting in a small aperture telescope making outsized contributions to the field (see Figure 7.3). Indeed, over half of the approximately 4000 *Kepler* planetary candidates have *only* been observed in high-resolution with Robo-AO. The addition of Robo-SOAR (Chapter 2, Ziegler et al., 2016) and Robo-AO 2 (Baranec et al., 2014b) will vastly increase the number of targets that can be observed a night, and bring automated AO to the Southern sky. The tools and methods developed for the cool subdwarf survey (Chapter 3, Ziegler et al., 2015) and the *Kepler* survey (Chapter 4, Ziegler et al., 2017a,b) will make analysis of these observations feasible, and result in a multitude of new, exciting discoveries over the coming years.

APPENDIX A: PROPERTIES OF DETECTED NEARBY STARS TO COOL SUBDWARFS

In this appendix, we detail the properties of nearby stars to cool subdwarfs detected with Robo-AO, as described in Chapter 3.

Table A.1: Multiple subdwarf systems resolved using Robo-AO

NLTT	Comp	m_v	ObsID	Signif.	$\Delta i'$	ρ	ρ	P.A.	Dist	Prev Det?
	NLTT	(mag)		σ	(mag)	(")	(AU)	(deg.)	(pc)	
2045AB	..	13.5	2013 Aug 15	183.3±21.0	SB9
2205AB	2206	13.9	2013 Aug 15	52	0.18	3.37	475.5±54.3	123±2	140.9±16.1	L79
2324AB	2325	15.7	2013 Aug 16	19	1.16	3.84	138.8±15.9	254±2	36.1±4.1	L79
2324AC	..	15.7	2013 Aug 16	16	4.14	23.48	847.8±96.2	159±2	36.1±4.1	
4817AB	4814	11.4	2012 Sep 3	65	4.30	24.59	3615±413	218±2	147±16.8	S02
7301AB	7300	14.9	2012 Sep 3	30	2.48	4.87	105.7±12.1	57±2	21.7±2.5	S02
7769AB	..	14.0	2012 Sep 3	8.2	3.34	4.84	1106±126	121±2	228.6±26.2	
7914AB	..	14.3	2012 Sep 3	39 ¹	3.76	2.53 ³	424.4±48.5	150±2	167.6±19.2	
10536AB	10548	11.2	2013 Aug 15	185.7	30633±3501	85.5	164.9±18.9	S02
11015AB	11016	16.3	2013 Aug 16	42	0.94	9.24	1399±160	57±2	151.3±17.3	S02
12845AB	..	10.6	2012 Oct 3	49	4.71	1.85	149.4±17.1	92±2	80.6±9.2	
15973AB	15974	9.3	2012 Oct 7	22	3.47	6.88	303.1±34.6	227±2	44±5.0	S02
15973AC	..	9.3	2012 Oct 7	7.2	5.02	8.23	362.2±41.1	217±2	44±5.0	
17485AB	..	11.9	2012 Oct 10	191.3±21.9	SB9
18502AB	..	12.2	2013 Jan 19	25	3.18	5.95	1262±144	331±2	212.1±24.3	
18798AB	18799	14.5	2013 Jan 19	48	3.12	12.82	2270±259	172±2	177±20.2	S02
19210AB	19207	11.2	2013 Jan 20	102.5	18468±2110	285.4	180.2±20.6	S02,SB9
20691AB	..	9.6	2013 Jan 19	12	5.47	1.52	107.3±12.3	93±2	70.6±8.1	SB9
21370AB	..	13.7	2013 Jan 19	71	2.46	19.83	6603±755	322±2	332.9±38.1	SB9
24082AB	..	13.1	2013 Jan 19	4.8	4.46	5.81	1683±192	187±2	289.7±33.1	
24082AC	..	13.1	2013 Jan 19	3.8	4.17	12.00	3476±397	267±2	289.7±33.1	
25234AB	25233	13.2	2013 Jan 18	65	3.05	8.29	1175±134	287±2	141.7±16.2	S02
28434AB	..	14.9	2013 Jan 17	2.2	2.46	2.54	652.9±74.6	202±2	256.7±29.3	
29551AB	..	11.5	2012 Sep 3	8.9	3.29	0.51	104.6±12.0	355±2	206.5±23.6	
29594AB	..	13.2	2013 Apr 22	38.10	12834±1466	269	336.8±38.5	L12
30193AB	..	14.6	2013 Apr 21	12	1.99	0.95	304.8±34.8	304±2	321.5±36.7	
30838AB	30837	12.5	2013 Apr 22	11	5.69	16.25	4436±507	25±2	273±31.2	S02

Continued on next page

¹From Keck follow-up, described in Section 3.3.4

NLTT	Comp NLTT	m_v (mag)	ObsID	Signif. σ	$\Delta i'$ (mag)	ρ (")	ρ (AU)	P.A. (deg.)	Dist (pc)	Prev Det?
31240AB	..	15.0	2013 Apr 21	13	3.86	10.32	3491 ± 399	157 ± 2	338.3 ± 38.7	
31240AC	..	15.0	2013 Apr 21	5.1	4.16	0.74	251.2 ± 28.7	210 ± 2	338.3 ± 38.7	
34051AB	..	13.5	2013 Jan 19	242.3 ± 27.7	SB9
37342AB	37341	14.4	2013 Apr 22	49	1.37	5.75	123.4 ± 14.1	54 ± 2	21.4 ± 2.5	S02
45616AB	..	11.9	2012 Sep 3	125	2.59	28.31	4696 ± 536.8	113 ± 2	165.9 ± 19.0	SB9
49486AB	49487	15.9	2012 Oct 4	9.3	1.48	4.51	390.3 ± 44.6	148 ± 2	86.4 ± 9.9	S02
49819AB	49821	14.0	2013 Aug 19	340	1.12	25.28	10263 ± 1173	84 ± 2	406 ± 46.4	S02
50759AB	..	15.9	2012 Sep 13	24	2.02	13.33	3544 ± 405	26 ± 2	265.8 ± 30.4	
50759AC	50751	15.9	2012 Sep 13	297.7	79156 ± 9046	267.7	265.8 ± 30.4	S02
50869AB	..	15.8	2013 Aug 8	7.4	3.15	8.17	1707 ± 195	19 ± 2	209.0 ± 24.0	
51006AB	..	14.0	2013 Aug 8	5.2	2.23	4.35	961.8 ± 109.9	76 ± 2	221.1 ± 25.3	
52377AB	..	14.5	2012 Sep 4	568 ³	2.35	0.92 ³	561.3 ± 64.2	211 ± 2	585.3 ± 66.9	
52532AB	..	15.5	2012 Sep 4	14 ³	2.60	0.30 ³	52.82 ± 6.0	168 ± 2	175 ± 20.0	
52532AC	52538	15.5	2012 Sep 4	..	3.35	37.14	6536 ± 780	..	176 ± 21.0	L79
53255AB	..	15.0	2013 Aug 16	58 ³	0.75	1.07 ³	123.9 ± 14.2	68 ± 2	112.7 ± 12.9	
53255AC	53254	15.0	2013 Aug 16	53.8	6063 ± 694	..	112.7 ± 12.9	L79
53274AB	..	11.8	2013 Aug 17	5.0	5.75	6.17	555.9 ± 63.5	153 ± 2	90.1 ± 10.3	
55603AB	..	12.1	2013 Aug 18	2.6	3.54	4.45	886.9 ± 101.4	29 ± 2	199.2 ± 22.8	
56818AB	..	14.0	2012 Sep 3	60 ³	2.04	0.63 ³	169.8 ± 19.4	44 ± 2	246.2 ± 28.1	
57038AB	..	13.9	2013 Aug 16	210	0.19	8.14	2508 ± 286.7	335 ± 2	308.3 ± 35.2	
57452AB	..	13.6	2013 Aug 16	14	1.91	1.98	474.5 ± 54.2	77 ± 2	234.9 ± 26.9	
57856AB	..	13.2	2013 Aug 17	2.0	5.08	2.00	585.3 ± 66.9	169 ± 2	289.7 ± 33.1	
58812AB	58813	15.0	2013 Aug 16	10	1.40	2.81	743.6 ± 85.0	69 ± 2	264.4 ± 30.2	

Notes. — References for previous detections are denoted using the following codes: Pourbaix et al. 2004 (SB9); Luyten 1979 (L79); Samir et al. 2002 (S02); López et al. 2012 (L12).

APPENDIX B: PROPERTIES OF DETECTED NEARBY STARS TO KOIS

In this appendix, we give the measured properties of the 610 nearby stars detected within 4" of a *Kepler* planetary candidate, as described in Section 4.2.6.

Table B.1: Properties of detected nearby stars to planetary candidates in Robo-AO KOI survey.

KOI	Separation (")	Position angle (°)	Visible contrast (mags)	Reference
1	1.13	135	3.95	Law et al. 2014
4	3.42	75	4.46	Baranec et al. 2016
13	1.16	279	0.19	Law et al. 2014
42	1.74	35	3.04	Baranec et al. 2016
44	3.42	123	4.03	Ziegler et al. 2018
51	3.51	161	2.63	Ziegler et al. 2017
70	3.86	51	5.74	Ziegler et al. 2018
75	3.53	124	6.6	Ziegler et al. 2018
97	1.9	99	4.61	Law et al. 2014
98	0.29	140	0.76	Law et al. 2014
99	3.67	46	5.31	Ziegler et al. 2018
102	2.91	221	1.45	Ziegler et al. 2018
107	2.6	273	5.27	Ziegler et al. 2018
119	1.05	118	0.87	Law et al. 2014
120	1.62	129	0.51	Ziegler et al. 2018
126	0.34	36	0.97	Ziegler et al. 2017
129	2.1	221	5.87	Ziegler et al. 2018
141	1.1	11	1.39	Law et al. 2014
148	2.54	245	4.99	Ziegler et al. 2018
151	4.17	58	5.84	Baranec et al. 2016
155	4.01	251	3.83	Baranec et al. 2016
161	2.7	172	6.55	Ziegler et al. 2018
162	0.29	275	0.81	Law et al. 2014
162	3.23	0	5.83	Ziegler et al. 2018
163	1.22	214	-0.36	Ziegler et al. 2017
174	0.6	77	4.43	Law et al. 2014
177	0.24	215	0.97	Law et al. 2014
190	0.23	105	1.33	Baranec et al. 2016
191	1.69	94	3.09	Law et al. 2014
193	2.78	137	3.07	Ziegler et al. 2017
200	0.30	44	0.52	Ziegler et al. 2017
200	2.81	130	4.00	Ziegler et al. 2017
214	3.85	119	5.68	Ziegler et al. 2018
215	2.98	22	2.34	Ziegler et al. 2018
220	3.13	213	4.52	Ziegler et al. 2018
225	0.53	338	0.93	Ziegler et al. 2017
227	0.33	72	0.84	Baranec et al. 2016

Continued on next page

KOI	Separation (")	Position angle (°)	Visible contrast (mags)	Reference
229	1.66	264	0.99	Ziegler et al. 2018
237	3.16	208	6.67	Ziegler et al. 2018
240	2.71	272	3.46	Ziegler et al. 2017
250	3.44	275	6.92	Ziegler et al. 2018
251	3.48	123	3.80	Baranec et al. 2016
255	3.41	357	2.14	Ziegler et al. 2017
258	1.05	77	2.76	Baranec et al. 2016
263	3.34	267	0.59	Ziegler et al. 2018
268	1.81	144	3.82	Law et al. 2014
268	2.50	308	5.55	Ziegler et al. 2018
284	0.96	98	0.45	Baranec et al. 2016
285	1.51	136	6.12	Baranec et al. 2016
298	2.01	270	0.58	Baranec et al. 2016
306	2.06	243	4.16	Law et al. 2014
317	3.02	283	5.14	Ziegler et al. 2018
326	3.53	267	2.01	Ziegler et al. 2017
356	0.56	218	2.92	Law et al. 2014
379	2.04	78	1.42	Baranec et al. 2016
385	3.36	171	5.45	Ziegler et al. 2018
387	0.98	352	3.86	Baranec et al. 2016
396	1.95	183	6.16	Ziegler et al. 2018
401	1.99	268	2.9	Law et al. 2014
425	0.53	346	0.86	Baranec et al. 2016
438	3.28	181	3.11	Baranec et al. 2016
454	1.49	204	2.08	Ziegler et al. 2017
465	3.62	130	4.25	Ziegler et al. 2018
472	1.12	206	0.72	Ziegler et al. 2018
486	3.53	71	3.2	Ziegler et al. 2018
506	3.15	39	5.0	Ziegler et al. 2018
507	2.03	358	4.46	Baranec et al. 2016
509	2.79	305	4.28	Ziegler et al. 2018
509	2.94	55	3.75	Ziegler et al. 2018
510	2.45	348	2.53	Ziegler et al. 2017
511	1.28	123	3.33	Law et al. 2014
521	3.24	152	0.42	Baranec et al. 2016
532	0.97	232	3.44	Ziegler et al. 2017
541	2.80	246	3.50	Ziegler et al. 2017
558	3.16	271	2.06	Baranec et al. 2016
568	3.16	142	4.35	Ziegler et al. 2018
584	1.83	137	4.10	Baranec et al. 2016
592	2.30	150	4.21	Baranec et al. 2016
598	3.17	357	2.73	Ziegler et al. 2017
614	2.76	214	4.01	Baranec et al. 2016
626	2.74	134	5.00	Ziegler et al. 2018
628	1.83	309	5.2	Law et al. 2014

Continued on next page

KOI	Separation (")	Position angle (°)	Visible contrast (mags)	Reference
628	2.76	237	5.30	Ziegler et al. 2018
636	3.8	343	6.0	Ziegler et al. 2018
640	0.44	117	0.62	Law et al. 2014
641	2.09	278	2.07	Baranec et al. 2016
641	3.65	205	0.33	Baranec et al. 2016
644	2.77	62	1.45	Ziegler et al. 2018
645	2.98	48	2.23	Baranec et al. 2016
652	1.23	272	1.59	Baranec et al. 2016
663	3.21	61	5.8	Ziegler et al. 2018
685	3.35	268	6.05	Ziegler et al. 2018
687	0.7	13	2.04	Law et al. 2014
688	1.71	141	2.19	Law et al. 2014
697	0.71	54	0.06	Baranec et al. 2016
701	2.96	105	4.98	Ziegler et al. 2018
712	0.47	173	1.17	Law et al. 2014
730	2.04	237	2.95	Baranec et al. 2016
734	3.51	175	2.05	Ziegler et al. 2017
757	2.94	243	3.37	Ziegler et al. 2017
771	1.77	281	0.94	Ziegler et al. 2017
799	1.28	108	1.73	Ziegler et al. 2018
801	3.67	195	2.58	Baranec et al. 2016
813	3.87	137	2.09	Baranec et al. 2016
814	3.40	346	4.16	Ziegler et al. 2017
816	3.50	120	2.66	Ziegler et al. 2017
840	3.2	334	2.24	Ziegler et al. 2018
840	2.97	302	3.42	Ziegler et al. 2018
841	2.00	69	3.60	Ziegler et al. 2017
903	2.24	99	1.84	Ziegler et al. 2018
927	1.01	294	2.63	Ziegler et al. 2018
931	1.38	177	3.40	Baranec et al. 2016
944	1.14	155	2.55	Ziegler et al. 2018
959	0.68	117	1.25	Ziegler et al. 2018
976	0.25	129	0.34	Baranec et al. 2016
980	1.01	31	1.65	Ziegler et al. 2018
984	1.8	42	0.01	Law et al. 2014
987	2.05	225	4.1	Law et al. 2014
999	3.41	125	2.80	Baranec et al. 2016
1002	0.3	173	2.31	Law et al. 2014
1050	2.09	197	2.7	Law et al. 2014
1061	1.22	38	1.21	Baranec et al. 2016
1066	1.69	205	4.19	Baranec et al. 2016
1067	2.97	143	4.05	Baranec et al. 2016
1075	1.07	93	2.63	Ziegler et al. 2018
1112	2.95	172	4.57	Baranec et al. 2016
1126	1.85	302	2.89	Ziegler et al. 2018

Continued on next page

KOI	Separation (")	Position angle (°)	Visible contrast (mags)	Reference
1137	0.75	197	0.81	Ziegler et al. 2017
1150	0.39	322	2.41	Law et al. 2014
1151	0.75	309	3.49	Law et al. 2014
1152	0.59	2	0.31	Law et al. 2014
1188	3.39	202	2.16	Ziegler et al. 2018
1191	3.91	226	3.89	Ziegler et al. 2018
1193	3.08	7	2.81	Ziegler et al. 2017
1198	3.11	98	5.25	Ziegler et al. 2018
1201	2.81	236	4.26	Ziegler et al. 2017
1201	3.76	265	5.17	Ziegler et al. 2017
1214	0.33	132	1.21	Baranec et al. 2016
1254	2.98	28	0.88	Ziegler et al. 2018
1261	1.83	340	1.58	Ziegler et al. 2017
1274	1.1	241	3.75	Law et al. 2014
1279	2.74	134	5.00	Ziegler et al. 2018
1287	2.64	339	1.47	Ziegler et al. 2018
1300	0.78	357	1.79	Baranec et al. 2016
1357	3.83	167	3.38	Baranec et al. 2016
1359	1.43	333	3.8	Law et al. 2014
1366	3.4	119	4.72	Ziegler et al. 2018
1375	0.77	269	4.38	Law et al. 2014
1397	2.30	229	4.41	Baranec et al. 2016
1409	2.17	312	2.58	Ziegler et al. 2017
1441	3.06	333	3.73	Ziegler et al. 2017
1442	2.24	70	6.68	Law et al. 2014
1447	0.28	212	0.27	Ziegler et al. 2017
1450	1.74	208	2.46	Ziegler et al. 2018
1495	3.75	188	2.92	Baranec et al. 2016
1503	0.77	107	1.52	Ziegler et al. 2017
1506	1.15	14	3.14	Ziegler et al. 2017
1531	0.43	99	0.90	Baranec et al. 2016
1545	2.51	180	5.06	Ziegler et al. 2018
1546	0.62	86	1.03	Baranec et al. 2016
1546	4.15	165	3.34	Baranec et al. 2016
1546	2.93	5	3.52	Baranec et al. 2016
1558	3.61	308	1.09	Ziegler et al. 2017
1573	3.84	299	4.72	Baranec et al. 2016
1593	3.24	80	1.60	Ziegler et al. 2017
1599	2.98	207	2.22	Baranec et al. 2016
1599	3.42	316	2.89	Baranec et al. 2016
1613	0.22	184	1.3	Law et al. 2014
1614	3.37	87	-0.44	Ziegler et al. 2018
1619	2.1	226	2.82	Law et al. 2014
1627	3.41	87	0.37	Ziegler et al. 2018
1630	1.77	188	0.91	Ziegler et al. 2017

Continued on next page

KOI	Separation (")	Position angle (°)	Visible contrast (mags)	Reference
1656	1.06	189	1.65	Ziegler et al. 2017
1660	1.40	23	2.00	Ziegler et al. 2017
1661	1.37	46	3.22	Ziegler et al. 2018
1677	0.61	159	4.76	Law et al. 2014
1687	2.11	209	4.10	Ziegler et al. 2017
1692	3.19	342	6.82	Ziegler et al. 2018
1695	0.31	215	0.61	Ziegler et al. 2017
1700	0.29	289	1.07	Baranec et al. 2016
1717	0.87	305	1.46	Baranec et al. 2016
1729	3.83	210	3.81	Ziegler et al. 2018
1781	3.4	331	3.78	Ziegler et al. 2018
1784	0.33	286	0.58	Baranec et al. 2016
1792	0.53	284	1.06	Ziegler et al. 2017
1792	1.99	111	0.98	Ziegler et al. 2017
1798	3.81	186	3.75	Baranec et al. 2016
1804	2.88	168	2.84	Ziegler et al. 2017
1812	2.71	111	6.84	Ziegler et al. 2018
1820	3.78	180	5.89	Ziegler et al. 2018
1830	0.46	319	1.29	Baranec et al. 2016
1845	2.06	77	4.97	Law et al. 2014
1846	3.77	136	1.07	Ziegler et al. 2017
1853	0.96	304	0.24	Baranec et al. 2016
1855	1.5	222	5.79	Ziegler et al. 2018
1861	2.10	84	4.93	Baranec et al. 2016
1880	1.7	100	3.66	Law et al. 2014
1884	0.95	310	3.65	Law et al. 2014
1884	2.54	328	5.61	Ziegler et al. 2018
1890	0.41	142	3.44	Law et al. 2014
1891	2.09	210	4.46	Law et al. 2014
1899	1.84	342	0.94	Baranec et al. 2016
1901	3.82	105	2.16	Ziegler et al. 2018
1908	1.29	260	4.11	Ziegler et al. 2017
1916	0.27	143	2.73	Law et al. 2014
1922	3.78	195	2.73	Ziegler et al. 2018
1943	1.42	302	1.42	Ziegler et al. 2018
1950	3.35	326	1.69	Baranec et al. 2016
1972	1.05	246	1.05	Baranec et al. 2016
1973	0.79	31	1.69	Ziegler et al. 2017
1979	0.84	192	3.2	Law et al. 2014
1985	2.82	156	4.19	Baranec et al. 2016
1989	1.12	41	3.49	Baranec et al. 2016
1995	2.96	355	5.34	Ziegler et al. 2017
2009	1.51	176	4.11	Law et al. 2014
2014	3.75	267	2.50	Baranec et al. 2016
2019	4.01	105	2.61	Baranec et al. 2016

Continued on next page

KOI	Separation (")	Position angle (°)	Visible contrast (mags)	Reference
2022	3.14	71	4.16	Ziegler et al. 2018
2022	2.5	152	5.3	Ziegler et al. 2018
2025	3.49	191	5.05	Ziegler et al. 2018
2032	1.19	317	0.34	Baranec et al. 2016
2048	1.84	353	3.33	Ziegler et al. 2017
2050	3.33	215	5.33	Ziegler et al. 2017
2055	3.80	57	4.09	Baranec et al. 2016
2056	3.87	131	3.37	Baranec et al. 2016
2059	0.38	291	1.1	Law et al. 2014
2067	1.64	315	0.80	Baranec et al. 2016
2069	1.12	108	4.24	Baranec et al. 2016
2083	0.26	176	1.03	Baranec et al. 2016
2091	1.30	215	1.72	Ziegler et al. 2017
2093	2.08	352	3.10	Ziegler et al. 2017
2096	3.50	17	4.13	Baranec et al. 2016
2098	2.88	156	2.58	Baranec et al. 2016
2098	3.24	132	2.40	Baranec et al. 2016
2100	2.98	318	2.10	Baranec et al. 2016
2105	3.01	314	6.28	Ziegler et al. 2018
2115	3.59	243	2.75	Baranec et al. 2016
2117	0.33	111	0.71	Ziegler et al. 2017
2143	2.16	317	3.5	Law et al. 2014
2156	3.35	303	2.64	Baranec et al. 2016
2159	2	323	3.99	Law et al. 2014
2163	0.77	248	0.04	Ziegler et al. 2017
2169	3.59	66	4.2	Ziegler et al. 2018
2174	0.92	226	0.21	Baranec et al. 2016
2174	3.88	314	0.14	Baranec et al. 2016
2206	3.28	87	1.28	Ziegler et al. 2017
2213	3.94	91	1.67	Ziegler et al. 2017
2222	2.53	333	5.33	Ziegler et al. 2018
2247	1.90	355	5.12	Baranec et al. 2016
2283	1.05	21	1.46	Ziegler et al. 2017
2287	2.96	11	5.64	Ziegler et al. 2018
2295	2.19	78	0.88	Baranec et al. 2016
2298	1.57	194	2.08	Baranec et al. 2016
2314	4.14	201	3.45	Baranec et al. 2016
2317	1.51	110	4.93	Baranec et al. 2016
2376	0.40	213	0.46	Ziegler et al. 2017
2377	2.09	335	1.25	Baranec et al. 2016
2377	4.11	326	4.04	Baranec et al. 2016
2379	3.59	139	1.89	Ziegler et al. 2017
2380	4.01	250	2.46	Baranec et al. 2016
2413	0.31	67	2.11	Law et al. 2014
2421	1.23	290	0.99	Baranec et al. 2016

Continued on next page

KOI	Separation (")	Position angle (°)	Visible contrast (mags)	Reference
2421	4.07	132	3.87	Baranec et al. 2016
2443	1.39	163	5.37	Law et al. 2014
2445	2.10	25	3.21	Ziegler et al. 2017
2460	2.36	192	3.41	Ziegler et al. 2017
2463	0.62	125	0.75	Law et al. 2014
2469	4.18	114	2.44	Baranec et al. 2016
2474	0.61	279	0.65	Baranec et al. 2016
2482	0.31	212	0.59	Ziegler et al. 2017
2486	0.24	63	0.49	Law et al. 2014
2493	2.69	300	2.68	Baranec et al. 2016
2516	3.42	84	5.93	Baranec et al. 2016
2535	1.73	21	2.47	Ziegler et al. 2017
2542	0.88	22	1.20	Baranec et al. 2016
2547	2.79	151	4.23	Ziegler et al. 2018
2551	2.69	197	1.93	Baranec et al. 2016
2554	0.37	149	0.37	Ziegler et al. 2017
2556	3.86	238	4.08	Ziegler et al. 2018
2579	3.48	355	3.69	Ziegler et al. 2017
2580	0.60	154	0.86	Ziegler et al. 2017
2582	3.41	223	4.25	Ziegler et al. 2018
2598	1.09	75	0.37	Baranec et al. 2016
2601	1.66	14	1.43	Baranec et al. 2016
2601	1.44	297	3.61	Baranec et al. 2016
2641	1.42	195	2.56	Law et al. 2014
2641	3.54	0	3.73	Ziegler et al. 2018
2657	0.73	131	0.27	Law et al. 2014
2664	1.17	90	0.83	Baranec et al. 2016
2679	2.11	324	2.87	Baranec et al. 2016
2681	1.10	161	1.25	Baranec et al. 2016
2688	1.09	205	0.86	Ziegler et al. 2017
2705	1.84	304	3.19	Baranec et al. 2016
2707	3.28	217	4.71	Baranec et al. 2016
2707	3.87	182	3.64	Baranec et al. 2016
2711	0.52	147	0.12	Baranec et al. 2016
2722	3.27	282	5.88	Baranec et al. 2016
2729	3.94	278	2.03	Baranec et al. 2016
2743	2.36	182	3.79	Baranec et al. 2016
2744	3.50	257	2.12	Ziegler et al. 2017
2754	0.79	260	2.23	Baranec et al. 2016
2760	0.45	142	0.84	Ziegler et al. 2017
2771	3.85	312	6.61	Baranec et al. 2016
2779	0.98	61	2.54	Baranec et al. 2016
2797	0.35	222	0.72	Ziegler et al. 2017
2803	3.84	61	3.00	Baranec et al. 2016
2807	3.93	77	1.90	Baranec et al. 2016

Continued on next page

KOI	Separation (")	Position angle (°)	Visible contrast (mags)	Reference
2812	2.09	335	3.23	Baranec et al. 2016
2813	1.10	258	0.84	Ziegler et al. 2017
2836	3.94	70	3.39	Baranec et al. 2016
2837	0.35	136	0.23	Baranec et al. 2016
2838	1.74	197	5.92	Baranec et al. 2016
2848	2.30	28	5.63	Baranec et al. 2016
2851	0.39	223	0.45	Ziegler et al. 2017
2856	2.31	287	3.44	Ziegler et al. 2017
2859	0.47	282	2.12	Baranec et al. 2016
2862	0.68	20	0.17	Ziegler et al. 2017
2880	3.39	257	1.15	Ziegler et al. 2018
2896	0.96	272	0.38	Ziegler et al. 2017
2897	2.65	200	2.98	Ziegler et al. 2018
2900	2.36	85	1.30	Ziegler et al. 2017
2904	0.71	226	1.99	Baranec et al. 2016
2910	3.15	88	0.72	Baranec et al. 2016
2914	3.80	231	5.64	Baranec et al. 2016
2926	0.33	16	0.27	Ziegler et al. 2017
2927	1.39	36	2.65	Ziegler et al. 2017
2949	2.36	311	4.08	Baranec et al. 2016
2958	1.15	302	2.47	Ziegler et al. 2017
2962	1.13	68	0.53	Baranec et al. 2016
2971	0.53	209	1.33	Baranec et al. 2016
2976	2.02	198	2.66	Ziegler et al. 2017
2984	3.47	33	4.34	Baranec et al. 2016
3002	0.84	267	2.02	Ziegler et al. 2018
3020	0.38	272	0.93	Ziegler et al. 2017
3029	0.28	272	0.68	Baranec et al. 2016
3041	2.03	128	4.64	Baranec et al. 2016
3042	1.87	147	1.62	Ziegler et al. 2017
3043	1.14	68	1.94	Ziegler et al. 2017
3066	3.41	335	1.86	Ziegler et al. 2017
3069	1.93	109	2.20	Baranec et al. 2016
3073	1.30	10	1.76	Baranec et al. 2016
3106	0.30	189	0.76	Ziegler et al. 2017
3111	3.36	234	5.87	Ziegler et al. 2017
3112	1.87	151	0.49	Ziegler et al. 2017
3120	1.14	278	0.87	Ziegler et al. 2017
3136	1.83	238	2.91	Ziegler et al. 2017
3156	1.24	203	2.09	Ziegler et al. 2018
3156	3.06	288	5.02	Ziegler et al. 2018
3158	2.10	254	4.00	Baranec et al. 2016
3161	2.68	67	3.04	Ziegler et al. 2017
3190	2.68	190	5.92	Baranec et al. 2016
3214	0.49	320	0.73	Ziegler et al. 2017

Continued on next page

KOI	Separation (")	Position angle (°)	Visible contrast (mags)	Reference
3214	1.41	198	2.50	Ziegler et al. 2017
3245	1.58	184	3.10	Baranec et al. 2016
3255	3.15	44	4.87	Baranec et al. 2016
3263	0.80	276	2.01	Ziegler et al. 2017
3264	3.66	217	1.37	Ziegler et al. 2017
3277	2.45	355	5.79	Baranec et al. 2016
3277	3.41	353	5.00	Baranec et al. 2016
3284	3.94	4	2.42	Baranec et al. 2016
3288	3.17	75	4.32	Baranec et al. 2016
3288	3.50	80	4.62	Baranec et al. 2016
3309	3.71	42	2.78	Baranec et al. 2016
3324	3.84	323	3.05	Baranec et al. 2016
3335	2.40	61	2.89	Ziegler et al. 2017
3339	3.41	346	1.38	Baranec et al. 2016
3341	3.23	107	4.27	Ziegler et al. 2017
3347	3.24	295	2.20	Ziegler et al. 2017
3354	3.71	227	2.55	Ziegler et al. 2017
3372	2.36	127	1.95	Ziegler et al. 2017
3377	1.45	58	4.26	Baranec et al. 2016
3401	0.65	94	0.89	Baranec et al. 2016
3413	2.18	12	3.79	Ziegler et al. 2017
3415	0.74	89	0.03	Ziegler et al. 2017
3418	1.13	43	1.29	Ziegler et al. 2017
3432	0.66	113	1.37	Ziegler et al. 2017
3435	3.06	160	1.33	Ziegler et al. 2018
3435	3.52	301	0.58	Ziegler et al. 2018
3439	3.42	228	3.97	Baranec et al. 2016
3444	1.11	8	3.32	Baranec et al. 2016
3444	3.55	262	3.41	Baranec et al. 2016
3459	3.35	124	2.37	Baranec et al. 2016
3460	1.24	153	5.08	Baranec et al. 2016
3460	2.47	231	5.52	Baranec et al. 2016
3463	3.67	96	4.41	Ziegler et al. 2017
3463	2.74	79	4.79	Ziegler et al. 2017
3468	1.49	117	3.22	Baranec et al. 2016
3471	0.63	224	3.05	Ziegler et al. 2017
3480	0.40	210	0.75	Ziegler et al. 2017
3483	1.51	23	2.15	Ziegler et al. 2017
3486	4.16	260	4.06	Baranec et al. 2016
3497	0.78	174	1.23	Baranec et al. 2016
3500	2.54	137	4.01	Baranec et al. 2016
3533	3.08	10	5.21	Ziegler et al. 2017
3611	2.30	267	2.77	Ziegler et al. 2017
3626	1.96	310	3.82	Ziegler et al. 2017
3649	0.79	216	0.26	Ziegler et al. 2017

Continued on next page

KOI	Separation (")	Position angle (°)	Visible contrast (mags)	Reference
3660	0.60	160	1.05	Ziegler et al. 2017
3678	2.63	170	5.08	Ziegler et al. 2017
3770	1.20	34	1.44	Ziegler et al. 2017
3783	1.13	272	3.53	Ziegler et al. 2017
3790	1.28	138	1.91	Ziegler et al. 2018
3791	3.50	258	1.89	Ziegler et al. 2017
3805	3.7	199	5.37	Ziegler et al. 2018
3813	2.54	283	4.58	Ziegler et al. 2018
3813	2.13	58	4.22	Ziegler et al. 2018
3856	2.54	101	3.27	Ziegler et al. 2018
3886	0.50	116	1.13	Ziegler et al. 2017
3891	1.05	240	4.69	Baranec et al. 2016
3891	2.01	136	4.92	Baranec et al. 2016
3907	1.58	162	6.31	Baranec et al. 2016
3907	2.82	72	3.23	Baranec et al. 2016
3928	2.96	265	1.21	Ziegler et al. 2017
3946	4.27	61	5.26	Baranec et al. 2016
4004	1.93	217	4.34	Baranec et al. 2016
4021	1.92	113	0.52	Baranec et al. 2016
4053	4.11	302	5.51	Baranec et al. 2016
4062	1.49	28	3.66	Ziegler et al. 2017
4098	0.78	174	1.10	Baranec et al. 2016
4131	2.85	124	5.04	Ziegler et al. 2017
4145	2.71	237	2.36	Baranec et al. 2016
4149	1.76	63	0.17	Baranec et al. 2016
4166	3.54	157	3.29	Baranec et al. 2016
4194	2.17	290	3.41	Baranec et al. 2016
4205	2.71	66	2.65	Baranec et al. 2016
4208	0.99	234	2.57	Baranec et al. 2016
4209	0.96	203	0.37	Baranec et al. 2016
4226	2.49	267	4.18	Baranec et al. 2016
4267	1.66	194	3.29	Ziegler et al. 2017
4268	3.56	263	4.77	Ziegler et al. 2017
4274	3.26	207	3.71	Baranec et al. 2016
4274	4.54	327	4.11	Baranec et al. 2016
4287	0.61	76	1.27	Baranec et al. 2016
4313	2.88	81	4.19	Baranec et al. 2016
4323	1.12	96	2.22	Ziegler et al. 2017
4329	1.93	117	4.64	Baranec et al. 2016
4331	0.45	103	0.25	Baranec et al. 2016
4334	3.32	15	3.79	Ziegler et al. 2017
4343	0.89	138	1.13	Ziegler et al. 2017
4343	3.68	350	4.81	Ziegler et al. 2017
4345	3.17	242	3.22	Ziegler et al. 2017
4353	3.50	36	2.75	Ziegler et al. 2017

Continued on next page

KOI	Separation (")	Position angle (°)	Visible contrast (mags)	Reference
4366	2.46	303	3.38	Ziegler et al. 2017
4368	2.33	162	3.28	Ziegler et al. 2018
4389	2.88	332	0.58	Baranec et al. 2016
4399	2.16	17	6.24	Baranec et al. 2016
4405	2.95	249	3.19	Ziegler et al. 2017
4407	2.54	298	2.97	Baranec et al. 2016
4409	2.89	139	6.10	Baranec et al. 2016
4418	1.41	172	2.23	Ziegler et al. 2017
4421	2.45	322	4.62	Ziegler et al. 2017
4443	3.41	26	5.00	Baranec et al. 2016
4463	2.45	143	0.01	Baranec et al. 2016
4467	3.99	131	4.21	Ziegler et al. 2017
4495	3.06	89	3.90	Baranec et al. 2016
4495	3.41	344	2.68	Baranec et al. 2016
4495	3.04	58	4.73	Baranec et al. 2016
4523	3.94	100	2.61	Baranec et al. 2016
4526	2.53	346	4.44	Ziegler et al. 2017
4526	3.98	179	4.80	Ziegler et al. 2017
4549	0.75	149	1.99	Ziegler et al. 2017
4550	1.03	325	0.04	Ziegler et al. 2017
4567	1.31	142	2.48	Baranec et al. 2016
4575	2.97	61	2.18	Baranec et al. 2016
4580	1.58	60	1.27	Baranec et al. 2016
4582	2.71	308	6.28	Baranec et al. 2016
4582	3.55	286	3.27	Baranec et al. 2016
4590	0.87	340	0.38	Ziegler et al. 2017
4625	1.22	69	0.28	Ziegler et al. 2018
4630	3.94	53	2.17	Ziegler et al. 2017
4634	0.35	275	1.55	Baranec et al. 2016
4651	1.22	105	2.88	Baranec et al. 2016
4653	0.77	324	2.02	Ziegler et al. 2017
4655	3.17	116	3.02	Ziegler et al. 2017
4656	2.89	23	1.42	Baranec et al. 2016
4657	2.11	234	3.27	Baranec et al. 2016
4661	3.93	198	2.32	Ziegler et al. 2017
4699	4.01	285	5.93	Baranec et al. 2016
4700	3.77	49	1.89	Ziegler et al. 2017
4707	3.7	13	6.41	Ziegler et al. 2018
4710	2.70	168	3.50	Ziegler et al. 2017
4713	1.72	251	0.27	Ziegler et al. 2017
4743	3.06	98	2.29	Ziegler et al. 2017
4750	2.09	322	1.95	Ziegler et al. 2017
4759	0.67	4	2.12	Ziegler et al. 2017
4764	3.83	204	2.42	Ziegler et al. 2018
4768	1.30	159	3.99	Baranec et al. 2016

Continued on next page

KOI	Separation (")	Position angle (°)	Visible contrast (mags)	Reference
4792	3.68	318	2.36	Baranec et al. 2016
4793	2.37	225	4.25	Ziegler et al. 2018
4797	3.59	127	1.12	Baranec et al. 2016
4797	3.93	77	3.37	Baranec et al. 2016
4810	2.36	146	3.16	Ziegler et al. 2017
4812	3.15	100	1.84	Baranec et al. 2016
4813	2.54	208	1.22	Baranec et al. 2016
4813	4.03	146	3.34	Baranec et al. 2016
4823	1.40	153	0.59	Baranec et al. 2016
4871	0.96	333	3.12	Baranec et al. 2016
4881	3.42	30	3.30	Ziegler et al. 2017
4895	2.27	75	2.28	Ziegler et al. 2017
4923	0.78	123	1.46	Ziegler et al. 2017
4974	1.23	242	3.33	Ziegler et al. 2017
4993	3.49	148	4.13	Ziegler et al. 2017
5004	1.05	109	1.05	Ziegler et al. 2017
5052	0.75	285	0.68	Ziegler et al. 2017
5101	1.24	99	3.33	Ziegler et al. 2017
5143	1.22	222	3.83	Ziegler et al. 2017
5210	2.71	267	2.22	Ziegler et al. 2017
5216	3.67	96	3.31	Ziegler et al. 2017
5220	2.83	109	7.22	Ziegler et al. 2017
5220	2.89	216	3.27	Ziegler et al. 2017
5232	1.75	200	4.67	Ziegler et al. 2017
5243	0.77	17	0.55	Ziegler et al. 2017
5243	2.41	128	5.53	Ziegler et al. 2017
5274	3.95	272	4.13	Ziegler et al. 2018
5327	1.88	211	3.43	Ziegler et al. 2017
5327	3.63	277	3.92	Ziegler et al. 2017
5327	3.96	342	-0.12	Ziegler et al. 2017
5331	3.67	351	3.72	Ziegler et al. 2017
5332	2.19	7	2.37	Ziegler et al. 2017
5332	3.61	129	0.63	Ziegler et al. 2017
5340	1.24	217	2.66	Ziegler et al. 2017
5373	0.21	81	0.12	Ziegler et al. 2017
5426	2.93	152	1.75	Ziegler et al. 2018
5440	2.45	345	3.04	Ziegler et al. 2017
5454	2.07	286	1.77	Ziegler et al. 2018
5465	2.85	158	1.36	Ziegler et al. 2017
5475	3.19	70	3.65	Ziegler et al. 2018
5480	3.52	174	1.24	Ziegler et al. 2017
5482	0.62	270	1.44	Ziegler et al. 2017
5486	0.34	333	0.73	Ziegler et al. 2017
5527	2.85	236	2.63	Ziegler et al. 2018
5552	1.09	165	0.82	Ziegler et al. 2018

Continued on next page

KOI	Separation (")	Position angle (°)	Visible contrast (mags)	Reference
5553	0.97	346	2.52	Ziegler et al. 2017
5556	3.28	162	4.31	Ziegler et al. 2017
5556	3.22	247	5.29	Ziegler et al. 2017
5570	2.06	236	4.64	Ziegler et al. 2017
5578	0.33	89	1.78	Ziegler et al. 2017
5640	0.53	113	2.26	Ziegler et al. 2018
5665	2.11	91	3.24	Ziegler et al. 2017
5671	2.17	225	1.79	Ziegler et al. 2017
5672	3.17	169	4.58	Ziegler et al. 2018
5695	0.60	163	1.47	Ziegler et al. 2017
5707	2.71	239	2.43	Ziegler et al. 2017
5762	0.23	95	0.65	Ziegler et al. 2017
5774	1.32	336	1.90	Ziegler et al. 2017
5790	3.69	357	-0.67	Ziegler et al. 2018
5792	3.59	116	-0.07	Ziegler et al. 2018
5797	3.62	103	1.37	Ziegler et al. 2018
5868	2.8	94	2.71	Ziegler et al. 2018
5885	3.42	127	4.03	Ziegler et al. 2017
5889	0.77	246	1.42	Ziegler et al. 2017
5895	2.34	249	3.41	Ziegler et al. 2018
5941	1.07	216	5.28	Ziegler et al. 2018
5961	0.87	112	1.45	Ziegler et al. 2018
5993	1.25	217	3.06	Ziegler et al. 2018
6104	1.84	206	4.01	Ziegler et al. 2018
6109	0.60	322	1.30	Ziegler et al. 2017
6111	2.14	48	4.40	Ziegler et al. 2017
6120	3.85	128	2.48	Ziegler et al. 2017
6132	1.23	91	0.90	Ziegler et al. 2017
6202	0.77	322	2.49	Ziegler et al. 2017
6224	2.97	167	4.19	Ziegler et al. 2018
6256	3.05	103	2.27	Ziegler et al. 2018
6258	2.17	241	4.14	Ziegler et al. 2017
6297	2.56	103	1.55	Ziegler et al. 2018
6297	2.96	308	5.89	Ziegler et al. 2018
6311	1.75	290	0.83	Ziegler et al. 2017
6329	1.22	279	1.43	Ziegler et al. 2017
6384	3.53	285	2.09	Ziegler et al. 2018
6390	2.82	309	1.57	Ziegler et al. 2018
6415	1.75	48	1.17	Ziegler et al. 2017
6464	0.75	122	1.72	Ziegler et al. 2017
6475	1.31	57	0.50	Ziegler et al. 2017
6482	0.52	271	0.58	Ziegler et al. 2017
6483	1.41	272	2.78	Ziegler et al. 2017
6527	2.21	353	1.60	Ziegler et al. 2017
6539	1.58	175	3.89	Ziegler et al. 2017

Continued on next page

KOI	Separation (")	Position angle (°)	Visible contrast (mags)	Reference
6560	3.28	246	6.04	Ziegler et al. 2017
6560	2.20	30	5.38	Ziegler et al. 2017
6600	2.36	315	5.28	Ziegler et al. 2018
6602	0.77	322	0.54	Ziegler et al. 2017
6605	2.53	320	3.46	Ziegler et al. 2017
6610	1.73	84	2.68	Ziegler et al. 2017
6610	2.63	216	1.22	Ziegler et al. 2017
6654	1.41	195	2.88	Ziegler et al. 2017
6697	3.91	313	3.4	Ziegler et al. 2018
6706	1.04	339	1.44	Ziegler et al. 2017
6728	1.94	134	5.04	Ziegler et al. 2017
6745	3.07	72	3.78	Ziegler et al. 2017
6745	2.85	163	3.92	Ziegler et al. 2017
6783	3.25	178	3.31	Ziegler et al. 2018
6793	2.84	309	4.47	Ziegler et al. 2018
6800	2.62	145	5.10	Ziegler et al. 2017
6800	3.11	337	5.41	Ziegler et al. 2017
6835	3.08	78	5.34	Ziegler et al. 2018
6907	3.35	99	-0.36	Ziegler et al. 2018
6918	0.62	98	1.33	Ziegler et al. 2018
6925	2.66	125	1.71	Ziegler et al. 2017
7002	3.2	247	2.95	Ziegler et al. 2018
7003	3.78	285	1.9	Ziegler et al. 2018
7020	3.28	23	1.43	Ziegler et al. 2017
7032	2.74	182	5.8	Ziegler et al. 2018
7050	1.78	129	2.5	Ziegler et al. 2018
7087	1.89	165	1.69	Ziegler et al. 2018
7129	1.27	191	2.39	Ziegler et al. 2018
7205	1.04	42	0.44	Ziegler et al. 2017
7220	3.57	27	1.33	Ziegler et al. 2018
7389	1.84	291	6.2	Ziegler et al. 2018
7395	3.41	212	3.00	Ziegler et al. 2017
7408	1.67	184	2.65	Ziegler et al. 2018
7426	2.45	212	2.37	Ziegler et al. 2017
7448	0.87	260	1.40	Ziegler et al. 2017
7455	1.86	306	2.39	Ziegler et al. 2018
7470	1.52	303	0.17	Ziegler et al. 2018
7501	1.15	15	1.36	Ziegler et al. 2018
7527	2.75	98	4.41	Ziegler et al. 2018
7539	2.97	348	3.03	Ziegler et al. 2018
7540	3.67	152	5.64	Ziegler et al. 2018
7546	2.93	223	5.92	Ziegler et al. 2018
7572	2.97	16	6.14	Ziegler et al. 2018

APPENDIX C: KECK-AO OBSERVATIONS OF *KEPLER* PLANETARY CANDIDATES

In this appendix, we present the properties of nearby stars to KOIs observed with Keck-AO, as described in Section 6.1. We also present cutouts of Keck-AO observations of KOIs.

Table C.1: Keck-AO KOI Observation List and Detected Companions

KOI	ObsID	Filter	Separation (")	P.A. (deg.)	Mag. Diff. (mag)	Previous Robo-AO?
162	2017 Aug 09	Kp	0.263±0.005	127.3±2	0.164±0.034	P1
472	2017 Aug 09	Kp	0.899±0.005	206.3±2	0.359±0.010 ^a	P4
584	2017 Aug 09	Kp	1.844±0.005	135.0±2	3.167±0.007	P2
799	2017 Aug 09	Kp	1.225±0.005	110.9±2	1.539±0.014 ^a	P4
799	2017 Aug 09	Kp	0.819±0.005	152.5±2	2.429±0.009 ^a	New
799	2017 Aug 09	Kp	1.625±0.005	86.5±2	3.273±0.025 ^a	New
944	2017 Aug 09	Kp	1.126±0.005	153.2±2	2.001±0.004	P4
944	2017 Aug 09	Kp	1.77±0.005	341.4±2	4.75±0.060	New
944	2017 Aug 09	Kp	2.918±0.005	182.2±2	3.90±0.011	New
1002	2017 Aug 09	Kp	0.289±0.005	178.0±2	0.980±0.013	P1
1075	2017 Aug 09	Kp	1.007±0.005	93.4±2	1.991±0.017	P4
1503	2017 Aug 09	Kp	0.868±0.005	116.6±2	1.450±0.031	P3
1506	2017 Aug 09	Kp	1.157±0.005	11.4±2	2.211±0.019	P3
1506	2017 Aug 09	Kp	2.837±0.005	276.9±2	7.43±0.31	New
1630	2017 Aug 09	Kp	1.628±0.005	188.1±2	0.567±0.007 ^a	P3
1656	2017 Aug 09	Kp	0.957±0.005	189.0±2	1.455±0.011 ^a	P3
1660	2017 Aug 08	Kp	1.300±0.005	27.3±2	1.293±0.013 ^a	P3
1660	2017 Aug 08	Kp	3.385±0.005	254.6±2	2.657±0.11 ^a	New
1855	2017 Aug 09	Kp	1.301±0.005	76.3±2	5.048±0.116	New
1855	2017 Aug 09	Kp	1.443±0.005	224.1±2	4.633±0.032	P4
1943	2017 Aug 09	Kp	1.355±0.005	303.9±2	1.102±0.011 ^a	P4
2163	2017 Aug 09	Kp	0.667±0.005	72.6±2	0.269±0.015	New
2554	2017 Aug 09	Kp	0.343±0.005	150.5±2	0.261±0.014	P3
2554	2017 Aug 09	Kp	3.526±0.005	203.5±2	3.536±0.016	New
2580	2017 Aug 08	Kp	0.512±0.005	150.9±2	0.592±0.018	P3
2598	2017 Aug 09	Kp	0.992±0.005	76.7±2	0.249±0.013	P2
2851	2017 Aug 09	Kp	0.289±0.005	226.4±2	0.099±0.004	P3
2958	2017 Aug 09	Kp	1.187±0.005	304.8±2	3.266±0.05	P3
2958	2017 Aug 09	Kp	2.201±0.005	16.5±2	4.167±0.066	New
3029	2017 Aug 08	Kp	0.269±0.005	267.9±2	0.138±0.004	P2
3029	2017 Aug 08	Kp	1.708±0.005	355.0±2	4.358±0.028	New
3029	2017 Aug 08	Kp	2.533±0.005	3.8±2	3.715±0.015	New
3120	2017 Aug 09	Kp	1.098±0.005	278.9±2	0.803±0.013 ^a	P3
3136	2017 Aug 08	Kp	1.789±0.005	239.6±2	2.023±0.036 ^a	P3
3432	2017 Aug 09	Kp	0.599±0.005	111.4±2	1.729±0.013	P3
3460	2017 Aug 09	Kp	1.237±0.005	153.2±2	3.793±0.026	P2
3460	2017 Aug 09	Kp	2.387±0.005	232.8±2	3.719±0.007	P2

Continued on next page

KOI	ObsID	Filter	Separation (")	P.A. (deg.)	Mag. Diff. (mag)	Previous Robo-AO?
3480	2017 Aug 08	Kp	0.316±0.005	208.2±2	0.687±0.012 ^a	P3
3480	2017 Aug 08	Kp	1.173±0.005	345.3±2	4.755±0.15 ^a	New
3480	2017 Aug 08	Kp	2.767±0.005	338.7±2	4.011±0.11 ^a	New
3783	2017 Aug 09	Kp	1.129±0.005	275.1±2	3.433±0.045	P3
4208	2017 Aug 08	Kp	3.673±0.005	244.8±2	6.226±0.106	New
4323	2017 Aug 09	Kp	1.055±0.005	103.6±2	2.463±0.019	P3
4323	2017 Aug 09	Kp	1.244±0.005	36.9±2	3.023±0.03	New
4343	2017 Aug 09	Kp	0.850±0.005	141.7±2	1.431±0.011 ^a	P3
4549	2017 Aug 08	Kp	0.693±0.005	147.9±2	2.605±0.031 ^a	P3
4759	2017 Aug 09	Kp	0.647±0.005	0.0±2	2.172±0.06 ^a	P3
4759	2017 Aug 09	Kp	0.717±0.005	0.0±2	2.335±0.09 ^a	P3
4923	2017 Aug 09	Kp	0.705±0.005	126.4±2	1.827±0.009	P3
5482	2017 Aug 09	Kp	0.647±0.005	268.2±2	1.310±0.009	P3
5482	2017 Aug 09	Kp	3.713±0.005	115.4±2	4.247±0.023	New
5486	2017 Aug 10	Kp	0.307±0.005	330.9±2	2.170±0.032	P3
5553	2017 Aug 08	Kp	0.935±0.005	341.4±2	1.733±0.006 ^a	P3
5941	2017 Aug 09	Kp	0.985±0.005	218.0±2	3.406±0.01	P4
6329	2017 Aug 09	Kp	1.194±0.005	277.2±2	1.35±0.011 ^a	P3
6610	2017 Aug 09	Kp	1.241±0.005	318.9±2	3.682±0.15	New
6610	2017 Aug 09	Kp	1.650±0.005	84.5±2	2.51±0.018	P3
6610	2017 Aug 09	Kp	2.628±0.005	218.4±2	0.644±0.028	P3
6918	2017 Aug 09	Kp	0.596±0.005	99.6±2	1.080±0.026	P4
7129	2017 Aug 09	Kp	1.178±0.005	193.7±2	1.721±0.005 ^a	P4
7205	2017 Aug 09	Kp	0.887±0.005	46.8±2	0.450±0.018 ^a	P3
7389	2017 Aug 09	Kp	1.911±0.005	290.4±2	5.445±0.028	P4
Non-detections						
532	2017 Aug 09	Kp				P3
1695	2017 Aug 08	Kp				P3
2376	2017 Aug 09	Kp				P3
2482	2017 Aug 09	Kp				P3
2797	2017 Aug 08	Kp				P3
2926	2017 Aug 08	Kp				P3
4208	2017 Aug 08	Kp				P2
4653	2017 Aug 10	Kp				P3
5373	2017 Aug 09	Kp				P3
6202	2017 Aug 10	Kp				P3

References for previous Robo-AO detections are denoted using the following codes: Law et al. 2014 (P1), Baranec et al. 2016 (P2), Ziegler et al. 2017a (P3), Ziegler et al. 2017b (P4), companion not detected in Robo-AO image (New)

^aAdditional Keck NIR photometry available in Appendix E.

^bOriginal Robo-AO detection of blended close binary, resolved with Keck-AO.

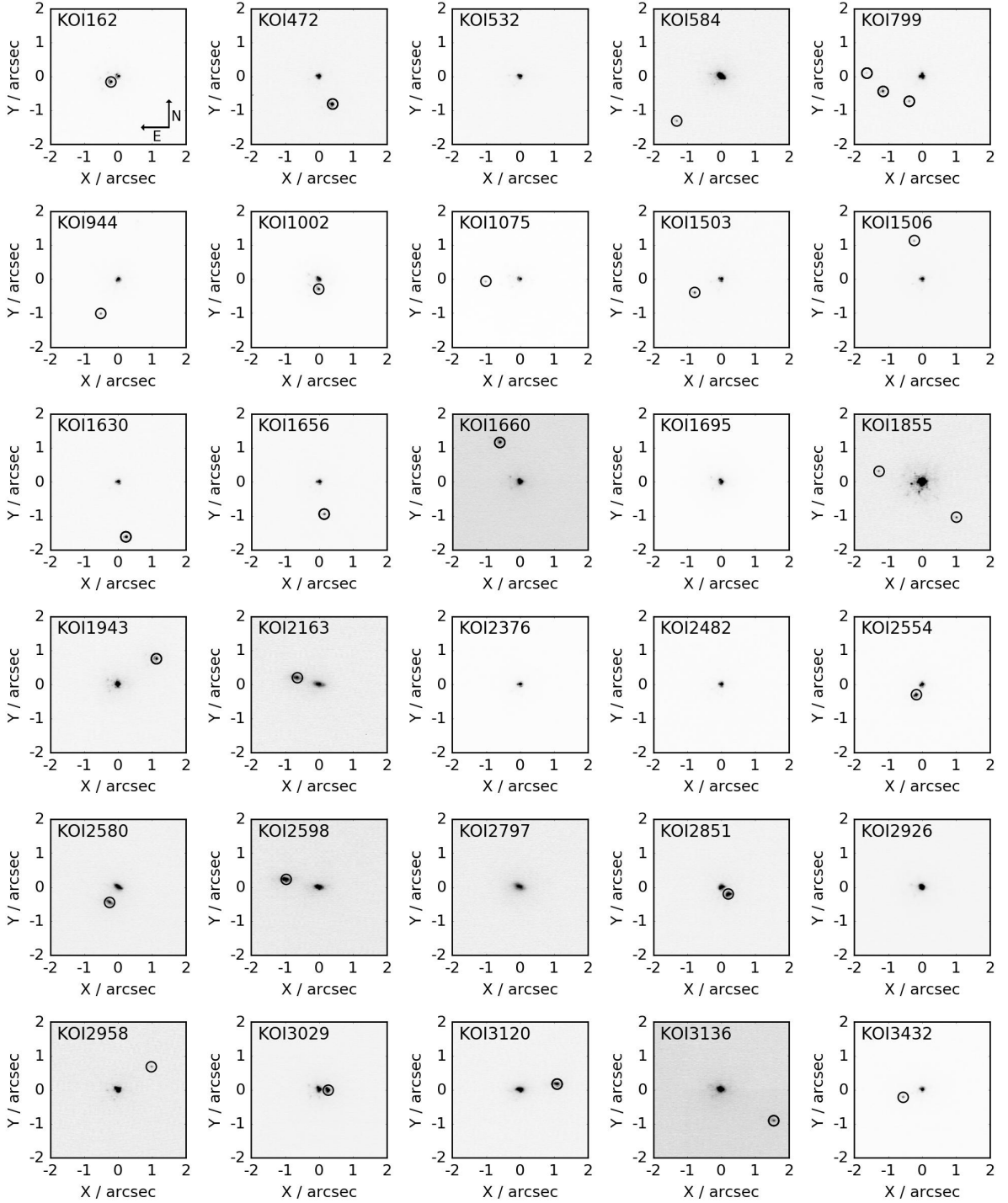


Figure C.1: Color inverted, normalized linear-scale cutouts of 30 KOIs [KOI-162 to KOI-3432] observed with the NIRC2 instrument on Keck-II, as described in Section 6.1. The angular scale and orientation (displayed in the first frame) is similar for each cutout, and circles are centered on detected nearby stars.

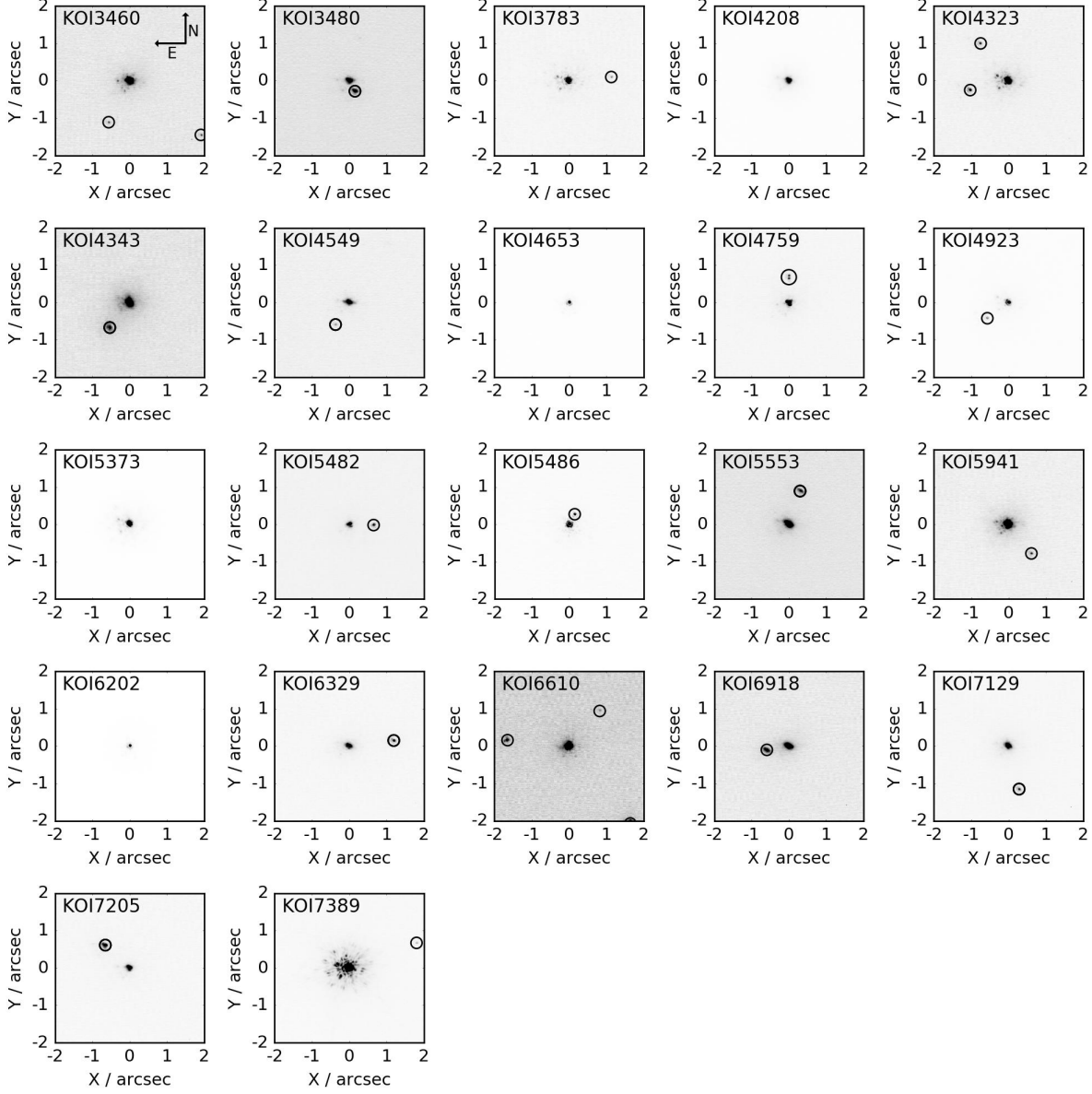


Figure C.2: Color inverted, normalized linear-scale cutouts of 22 KOIs [KOI-3460 to KOI-7389] observed with the NIRC2 instrument on Keck-II, as described in Section 6.1. The angular scale and orientation (displayed in the first frame) is similar for each cutout, and circles are centered on detected nearby stars (a single circle is centered on the close binary stars to KOI-4759).

APPENDIX D: UPDATED *KEPLER* PLANETARY CANIDATE RADII

In this appendix, we detail the implications to the derived planetary radii of planetary candidates in systems with nearby stars, as described in Section 5.3.2.

Table D.1: Implications on Derived Radius of *Kepler* Planetary Candidates

Object	Sep. (")	Δm (mags)	Reference ^a	$R_{\star,target}$ ^b (R_{\odot})	$R_{\star,secondary}$ ^c (R_{\odot})	$R_{p,0}$ ^d (R_{\oplus})	$R_{p,prim.}$ ^e (R_{\oplus})	$R_{p,sec.}$ ^f (R_{\oplus})
0001.01	1.13	3.95	P1	0.96	0.58	13.0	13.2	49.1
0004.01	3.42	4.46	P2	2.99	0.58	12.9	13.0	19.8
0013.01	1.16	0.19	P1	3.03	0.58	21.4	29.1	6.1
0042.01	1.74	3.04	P2	1.34	0.75	2.43	2.5	5.7
0044.01	3.42	4.03	P4	1.07	0.6	12.0	12.1	43.5
0070.01	3.86	5.74	P4	0.93	0.56	2.99	3.0	25.5
0070.02	3.86	5.74	P4	0.93	0.56	1.78	1.78	15.2
0070.03	3.86	5.74	P4	0.93	0.56	2.59	2.6	22.1
0070.04	3.86	5.74	P4	0.93	0.56	0.84	0.84	7.2
0070.05	3.86	5.74	P4	0.93	0.56	0.9	0.9	7.7
0075.01	3.53	6.6	P4	2.5	0.75	10.2	10.2	63.5
0097.01	1.9	4.61	P1	1.91	0.82	16.7	16.8	60.0
0098.01	0.29	0.76	P1	2.0	1.78	9.86	12.1	15.2
0099.01	3.67	5.31	P4	0.74	0.42	3.12	3.13	20.8
0102.01	2.91	1.45	P4	1.07	0.87	3.27	3.67	5.8
0102.02	2.91	1.45	P4	1.07	0.87	0.98	1.1	1.7
0107.01	2.6	5.27	P4	1.55	0.71	3.53	3.54	18.4
0119.01	1.05	0.87	P1	2.06	1.75	8.2	9.87	12.5
0119.02	1.05	0.87	P1	2.06	1.75	7.78	9.36	11.9
0120.01	1.62	0.51	P4	1.26	1.12	2.41	3.07	3.5
0126.01	0.34	0.97	P3	1.8	1.44	20.7	24.6	30.7
0126.02	0.34	0.97	P3	1.8	1.44	0.73	0.87	1.1
0129.01	2.1	5.87	P4	9.33	1.44	77.8	77.9	179
0141.01	1.1	1.39	P1	0.9	0.75	5.11	5.78	9.1
0148.01	2.54	4.99	P4	0.87	0.56	1.85	1.86	11.9
0148.02	2.54	4.99	P4	0.87	0.56	2.63	2.64	16.9
0148.03	2.54	4.99	P4	0.87	0.56	2.0	2.01	12.8
0151.01	4.17	5.84	P2	1.04	0.56	5.24	5.25	41.6
0155.01	4.01	3.83	P2	1.17	0.66	3.24	3.29	10.8
0161.01	2.7	6.55	P4	0.79	0.42	2.68	2.68	29.3
0162.01	0.29	0.81	P1	1.12	0.99	3.11	3.78	4.8
0162.01	3.23	5.83	P4	1.12	0.56	3.11	3.12	22.8
0163.01	1.22	-0.36	P3	0.77	0.56	2.08	3.22	2.0
0174.01	0.6	4.43	P1	0.7	0.49	2.59	2.61	14.2
0177.01	0.24	0.97	P1	1.03	0.89	1.78	2.11	2.9
0190.01	0.23	1.33	P2	2.34	1.71	28.3	32.2	43.4
0191.01	1.69	3.09	P1	0.89	0.6	10.9	11.2	31.5
0191.02	1.69	3.09	P1	0.89	0.6	2.25	2.31	6.5

Continued on next page

Object	Sep. (")	Δm (mags)	Reference ^a	$R_{\star,target}^b$ (R_{\odot})	$R_{\star,secondary}^c$ (R_{\odot})	$R_{p,0}^d$ (R_{\oplus})	$R_{p,prim.}^e$ (R_{\oplus})	$R_{p,sec.}^f$ (R_{\oplus})
0191.03	1.69	3.09	P1	0.89	0.6	1.2	1.23	3.5
0191.04	1.69	3.09	P1	0.89	0.6	2.07	2.13	6.0
0193.01	2.78	3.07	P3	1.0	0.66	14.4	14.8	40.2
0200.01	0.30	0.52	P3	1.5	1.39	14.3	18.2	21.5
0200.01	2.81	4.0	P3	1.5	0.75	14.3	14.5	45.5
0214.01	3.85	5.68	P4	0.94	0.56	9.06	9.08	74.3
0215.01	2.98	2.34	P4	0.94	0.71	41.6	44.0	97.5
0220.01	3.13	4.52	P4	0.83	0.56	3.55	3.58	19.4
0220.02	3.13	4.52	P4	0.83	0.56	0.88	0.89	4.8
0225.01	0.53	0.93	P3	1.24	1.01	44.7	53.3	67.0
0227.01	0.33	0.84	P2	0.47	0.42	2.45	2.96	3.9
0229.01	1.66	0.99	P4	1.08	0.91	5.81	6.88	9.1
0237.01	3.16	6.67	P4	1.03	0.49	2.6	2.6	26.9
0240.01	2.71	3.46	P3	1.05	0.66	4.14	4.22	13.1
0250.02	3.44	6.92	P4	0.54	0.66	2.64	2.64	78.8
0250.03	3.44	6.92	P4	0.54	0.66	1.21	1.21	36.1
0250.01	3.44	6.92	P4	0.54	0.66	2.83	2.83	84.5
0250.04	3.44	6.92	P4	0.54	0.66	2.13	2.13	63.6
0251.01	3.48	3.8	P2	0.51	0.24	2.54	2.58	6.9
0251.02	3.48	3.8	P2	0.51	0.24	0.8	0.81	2.2
0255.01	3.41	2.14	P3	0.51	0.36	2.47	2.64	4.9
0255.02	3.41	2.14	P3	0.51	0.36	0.75	0.8	1.5
0255.03	3.41	2.14	P3	0.51	0.36	0.57	0.61	1.1
0258.01	1.05	2.76	P2	3.13	0.36	97.0	100.7	41.1
0263.01	3.34	0.59	P4	1.54	1.37	2.51	3.16	3.7
0268.01	1.81	3.82	P1	1.36	0.75	3.02	3.06	9.8
0268.01	2.50	5.55	P4	1.36	0.58	3.02	3.03	16.7
0284.01	0.96	0.45	P2	1.1	1.01	1.93	2.49	2.8
0284.02	0.96	0.45	P2	1.1	1.01	1.4	1.8	2.0
0284.03	0.96	0.45	P2	1.1	1.01	1.22	1.57	1.8
0284.04	0.96	0.45	P2	1.1	1.01	1.41	1.82	2.1
0285.01	1.51	6.12	P2	1.67	0.66	3.63	3.64	24.1
0285.02	1.51	6.12	P2	1.67	0.66	2.31	2.31	15.4
0285.03	1.51	6.12	P2	1.67	0.66	1.91	1.91	12.7
0298.02	2.01	0.58	P2	0.79	0.75	1.62	2.04	2.5
0306.01	2.06	4.16	P1	0.82	0.56	2.14	2.16	10.0
0317.01	3.02	5.14	P4	1.4	0.66	3.02	3.03	15.3
0317.02	3.02	5.14	P4	1.4	0.66	0.99	0.99	5.0
0326.01	3.53	2.01	P3	11.54	0.66	36.0	38.7	5.6
0326.02	3.53	2.01	P3	11.54	0.66	29.7	31.9	4.6
0356.01	0.56	2.92	P1	1.77	1.04	5.95	6.15	13.8
0379.01	2.04	1.42	P2	1.68	1.28	2.78	3.13	4.6
0379.02	2.04	1.42	P2	1.68	1.28	1.83	2.06	3.0
0385.01	3.36	5.45	P4	0.89	0.56	1.59	1.6	12.4
0387.01	0.98	3.86	P2	0.66	0.49	2.46	2.49	11.0

Continued on next page

Object	Sep. (")	Δm (mags)	Reference ^a	$R_{\star,target}^b$ (R_{\odot})	$R_{\star,secondary}^c$ (R_{\odot})	$R_{p,0}^d$ (R_{\oplus})	$R_{p,prim.}^e$ (R_{\oplus})	$R_{p,sec.}^f$ (R_{\oplus})
0396.01	1.95	6.16	P4	1.31	0.58	36.9	36.9	279
0401.01	1.99	2.9	P1	0.94	0.66	4.15	4.29	11.5
0401.02	1.99	2.9	P1	0.94	0.66	4.28	4.43	11.8
0401.03	1.99	2.9	P1	0.94	0.66	1.67	1.73	4.6
0425.01	0.53	0.86	P2	0.96	0.82	14.9	17.9	22.6
0438.01	3.28	3.11	P2	0.54	0.38	2.01	2.07	6.2
0438.02	3.28	3.11	P2	0.54	0.38	1.87	1.92	5.7
0454.01	1.49	2.08	P3	0.8	0.6	2.64	2.83	5.5
0465.01	3.62	4.25	P4	1.06	0.6	5.26	5.31	21.3
0472.01	1.12	0.72	P4	0.84	0.75	3.16	3.89	4.8
0486.01	3.53	3.2	P4	1.03	0.66	2.78	2.85	8.0
0506.01	3.15	5.0	P4	1.01	0.58	3.27	3.29	18.9
0507.01	2.03	4.46	P2	0.84	0.56	3.34	3.37	17.6
0509.01	2.79	4.28	P4	0.94	0.58	2.74	2.77	12.2
0509.02	2.79	4.28	P4	0.94	0.58	3.0	3.03	13.4
0509.03	2.79	4.28	P4	0.94	0.58	2.22	2.24	9.9
0509.01	2.94	3.75	P4	0.94	0.58	2.74	2.78	9.6
0509.02	2.94	3.75	P4	0.94	0.58	3.0	3.05	10.6
0509.03	2.94	3.75	P4	0.94	0.58	2.22	2.25	7.8
0510.01	2.45	2.53	P3	1.05	0.75	2.59	2.71	6.2
0510.02	2.45	2.53	P3	1.05	0.75	2.89	3.03	6.9
0510.03	2.45	2.53	P3	1.05	0.75	2.7	2.83	6.4
0510.04	2.45	2.53	P3	1.05	0.75	3.26	3.41	7.8
0511.01	1.28	3.33	P1	0.94	0.6	2.36	2.41	7.2
0511.02	1.28	3.33	P1	0.94	0.6	1.28	1.31	3.9
0521.01	3.24	0.42	P2	1.06	0.99	4.62	5.99	6.8
0521.02	3.24	0.42	P2	1.06	0.99	1.19	1.54	1.7
0532.01	0.97	3.44	P3	0.99	0.6	2.87	2.93	8.7
0541.01	2.80	3.5	P3	0.83	0.58	2.06	2.1	7.4
0558.01	3.16	2.06	P2	0.79	0.6	2.3	2.47	4.9
0568.01	3.16	4.35	P4	0.99	0.58	1.65	1.66	7.3
0568.02	3.16	4.35	P4	0.99	0.58	0.96	0.97	4.2
0584.01	1.83	4.1	P2	0.98	0.58	2.76	2.79	10.9
0584.02	1.83	4.1	P2	0.98	0.58	2.63	2.66	10.4
0584.03	1.83	4.1	P2	0.98	0.58	1.15	1.16	4.5
0592.01	2.30	4.21	P2	1.01	0.58	2.37	2.39	9.6
0598.01	3.17	2.73	P3	0.79	0.58	2.15	2.24	5.8
0598.02	3.17	2.73	P3	0.79	0.58	1.71	1.78	4.6
0614.01	2.76	4.01	P2	1.42	0.75	11.3	11.4	37.9
0626.01	2.74	5.0	P4	1.19	0.6	2.45	2.46	12.4
0626.02	2.74	5.0	P4	1.19	0.6	0.99	0.99	5.0
0628.01	1.83	5.2	P1	1.08	0.58	2.88	2.89	17.0
0628.01	2.76	5.3	P4	1.08	0.58	2.88	2.89	17.8
0636.01	3.8	6.0	P4	2.4	0.79	55.2	55.3	289
0640.01	0.44	0.62	P1	0.85	0.75	2.43	3.04	3.5

Continued on next page

Object	Sep. (")	Δm (mags)	Reference ^a	$R_{\star,target}^b$ (R_{\odot})	$R_{\star,secondary}^c$ (R_{\odot})	$R_{p,0}^d$ (R_{\oplus})	$R_{p,prim.}^e$ (R_{\oplus})	$R_{p,sec.}^f$ (R_{\oplus})
0641.01	2.09	2.07	P2	0.65	0.56	2.73	2.93	6.5
0641.01	3.65	0.33	P2	0.65	0.6	2.73	3.6	3.9
0644.01	2.77	1.45	P4	1.1	0.89	17.1	19.2	30.5
0645.01	2.98	2.23	P2	1.26	0.87	1.95	2.07	4.0
0645.02	2.98	2.23	P2	1.26	0.87	2.01	2.13	4.1
0652.01	1.23	1.59	P2	0.82	0.66	4.43	4.92	8.3
0663.01	3.21	5.8	P4	0.55	0.22	1.37	1.37	7.8
0663.02	3.21	5.8	P4	0.55	0.22	1.58	1.58	9.0
0685.01	3.35	6.05	P4	1.58	0.6	3.07	3.08	19.0
0687.01	0.7	2.04	P1	1.69	1.12	3.13	3.36	5.7
0688.01	1.71	2.19	P1	1.97	1.35	3.54	3.77	7.1
0697.01	0.71	0.06	P2	1.45	1.39	3.62	5.05	5.0
0701.01	2.96	4.98	P4	0.66	0.42	1.98	1.99	12.6
0701.02	2.96	4.98	P4	0.66	0.42	1.33	1.34	8.5
0701.03	2.96	4.98	P4	0.66	0.42	1.72	1.73	10.9
0701.05	2.96	4.98	P4	0.66	0.42	0.57	0.57	3.6
0701.04	2.96	4.98	P4	0.66	0.42	1.43	1.44	9.1
0712.01	0.47	1.17	P1	0.84	0.75	1.11	1.29	2.0
0730.01	2.04	2.95	P2	1.25	0.75	3.46	3.57	8.3
0730.02	2.04	2.95	P2	1.25	0.75	2.68	2.77	6.4
0730.03	2.04	2.95	P2	1.25	0.75	3.57	3.69	8.6
0730.04	2.04	2.95	P2	1.25	0.75	2.42	2.5	5.8
0734.01	3.51	2.05	P3	0.91	0.71	3.08	3.3	6.6
0734.02	3.51	2.05	P3	0.91	0.71	2.54	2.73	5.5
0757.01	2.94	3.37	P3	0.85	0.58	5.76	5.89	19.1
0757.02	2.94	3.37	P3	0.85	0.58	3.86	3.95	12.8
0757.03	2.94	3.37	P3	0.85	0.58	2.65	2.71	8.8
0771.01	1.77	0.94	P3	0.98	0.87	14.1	16.9	23.0
0799.01	1.28	1.73	P4	0.97	0.75	32.4	35.6	60.5
0801.01	3.67	2.58	P2	1.11	0.75	9.73	10.2	22.5
0813.01	3.87	2.09	P2	0.77	0.75	7.34	7.86	19.8
0814.01	3.40	4.16	P3	0.73	0.49	2.32	2.35	10.7
0816.01	3.50	2.66	P3	1.08	0.75	5.52	5.75	13.5
0840.01	3.2	2.24	P4	0.79	0.6	8.99	9.54	20.4
0840.01	2.97	3.42	P4	0.79	0.58	8.99	9.18	32.6
0841.01	2.00	3.6	P3	0.82	0.58	5.0	5.09	19.0
0841.02	2.00	3.6	P3	0.82	0.58	6.5	6.62	24.7
0841.03	2.00	3.6	P3	0.82	0.58	2.19	2.23	8.3
0841.04	2.00	3.6	P3	0.82	0.58	24.0	24.4	91.2
0841.05	2.00	3.6	P3	0.82	0.58	3.71	3.78	14.1
0903.01	2.24	1.84	P4	0.83	0.66	6.96	7.57	14.1
0927.01	1.01	2.63	P4	0.92	0.66	44.0	46.0	110
0931.01	1.38	3.4	P2	1.05	0.66	13.6	13.9	42.1
0944.01	1.14	2.55	P4	0.85	0.6	4.43	4.64	10.7
0959.01	0.68	1.25	P4	0.12	0.6	2.31	2.65	24.5

Continued on next page

Object	Sep. (")	Δm (mags)	Reference ^a	$R_{\star,target}^b$ (R_{\odot})	$R_{\star,secondary}^c$ (R_{\odot})	$R_{p,0}^d$ (R_{\oplus})	$R_{p,prim.}^e$ (R_{\oplus})	$R_{p,sec.}^f$ (R_{\oplus})
0976.01	0.25	0.34	P2	1.72	1.57	78.5	103.3	110
0980.01	1.01	1.65	P4	1.94	1.39	68.0	75.1	115
0984.01	1.8	0.01	P1	0.81	0.79	2.29	3.23	3.2
0987.01	2.05	4.1	P1	0.86	0.56	1.21	1.22	5.3
0999.01	3.41	2.8	P2	0.72	0.56	2.54	2.63	7.5
0999.02	3.41	2.8	P2	0.72	0.56	2.18	2.26	6.4
1002.01	0.3	2.31	P1	1.02	0.75	1.17	1.24	2.6
1050.01	2.09	2.7	P1	0.77	0.75	1.41	1.47	5.0
1050.02	2.09	2.7	P1	0.77	0.75	1.36	1.42	4.8
1061.01	1.22	1.21	P2	0.97	0.79	2.02	2.33	3.3
1066.01	1.69	4.19	P2	0.84	0.56	9.29	9.39	43.0
1067.01	2.97	4.05	P2	1.37	0.75	49.8	50.4	177
1075.01	1.07	2.63	P4	2.31	1.37	18.7	19.5	38.8
1112.01	2.95	4.57	P2	0.97	0.58	2.33	2.35	11.5
1126.01	1.85	2.89	P4	1.0	0.66	3.6	3.72	9.3
1126.02	1.85	2.89	P4	1.0	0.66	28.2	29.2	72.8
1137.01	0.75	0.81	P3	0.86	0.75	40.7	49.5	62.5
1150.01	0.39	2.41	P1	1.04	0.75	0.9	0.95	2.1
1151.01	0.75	3.49	P1	0.85	0.58	1.22	1.24	4.2
1151.02	0.75	3.49	P1	0.85	0.58	0.94	0.96	3.3
1151.03	0.75	3.49	P1	0.85	0.58	0.67	0.68	2.3
1151.04	0.75	3.49	P1	0.85	0.58	0.76	0.78	2.6
1151.05	0.75	3.49	P1	0.85	0.58	0.8	0.82	2.8
1152.01	0.59	0.31	P1	0.49	0.42	14.4	19.1	19.1
1188.01	3.39	2.16	P4	0.81	0.6	21.8	23.3	46.8
1191.01	3.91	3.89	P4	0.91	0.58	3.29	3.34	12.9
1193.01	3.08	2.81	P3	0.92	0.6	10.4	10.8	25.7
1198.01	3.11	5.25	P4	1.33	0.6	3.42	3.43	17.4
1198.02	3.11	5.25	P4	1.33	0.6	2.2	2.21	11.2
1198.03	3.11	5.25	P4	1.33	0.6	3.02	3.03	15.4
1201.01	2.81	4.26	P3	0.42	0.22	1.01	1.02	3.7
1201.01	3.76	5.17	P3	0.42	0.22	1.01	1.01	5.6
1214.01	0.33	1.21	P2	1.05	0.87	1.44	1.66	2.4
1261.01	1.83	1.58	P3	1.59	1.17	11.2	12.4	19.0
1261.02	1.83	1.58	P3	1.59	1.17	3.69	4.1	6.3
1274.01	1.1	3.75	P1	0.82	0.58	4.53	4.6	18.4
1279.01	2.74	5.0	P4	1.07	0.58	1.94	1.95	10.6
1279.02	2.74	5.0	P4	1.07	0.58	1.08	1.09	5.9
1287.01	2.64	1.47	P4	0.81	0.71	32.1	36.0	62.2
1300.01	0.78	1.79	P2	0.53	0.42	1.2	1.31	2.4
1357.01	3.83	3.38	P2	0.95	0.6	2.87	2.93	8.8
1359.01	1.43	3.8	P1	0.85	0.58	3.19	3.24	12.7
1359.02	1.43	3.8	P1	0.85	0.58	6.45	6.55	25.8
1366.01	3.4	4.72	P4	0.94	0.56	3.04	3.06	16.0
1366.02	3.4	4.72	P4	0.94	0.56	3.88	3.91	20.4

Continued on next page

Object	Sep. (")	Δm (mags)	Reference ^a	$R_{\star,target}^b$ (R_{\odot})	$R_{\star,secondary}^c$ (R_{\odot})	$R_{p,0}^d$ (R_{\oplus})	$R_{p,prim.}^e$ (R_{\oplus})	$R_{p,sec.}^f$ (R_{\oplus})
1375.01	0.77	4.38	P1	1.29	0.66	7.25	7.31	28.3
1397.01	2.30	4.41	P2	0.49	0.23	1.89	1.91	6.8
1409.01	2.17	2.58	P3	0.85	0.6	2.94	3.07	7.1
1441.01	3.06	3.73	P3	0.99	0.6	1.9	1.93	6.6
1442.01	2.24	6.68	P1	1.0	0.49	1.13	1.13	12.1
1447.01	0.28	0.27	P3	1.69	1.52	97.5	130.1	132
1447.02	0.28	0.27	P3	1.69	1.52	20.7	27.7	28.1
1450.01	1.74	2.46	P4	1.3	0.82	59.2	62.2	120
1495.01	3.75	2.92	P2	0.93	0.66	2.74	2.83	7.7
1503.01	0.77	1.52	P3	0.94	0.75	4.6	5.14	8.2
1506.01	1.15	3.14	P3	0.83	0.58	2.92	3.0	8.9
1531.01	0.43	0.9	P2	0.93	0.79	1.16	1.39	1.8
1545.01	2.51	5.06	P4	0.96	0.56	12.6	12.7	76.2
1546.01	0.62	1.03	P2	0.89	0.75	11.9	14.0	18.9
1546.01	4.15	3.34	P2	0.89	0.58	11.9	12.2	37.0
1546.01	2.93	3.52	P2	0.89	0.58	11.9	12.2	40.0
1558.01	3.61	1.09	P3	0.95	0.79	10.7	12.5	17.2
1573.01	3.84	4.72	P2	0.92	0.56	4.22	4.25	22.7
1573.02	3.84	4.72	P2	0.92	0.56	1.38	1.39	7.4
1593.01	3.24	1.6	P3	0.91	0.75	2.08	2.31	3.9
1593.02	3.24	1.6	P3	0.91	0.75	2.14	2.37	4.0
1599.01	2.98	2.22	P2	0.97	0.75	2.9	3.08	6.6
1599.02	2.98	2.22	P2	0.97	0.75	22.3	23.7	50.6
1599.01	3.42	2.89	P2	0.97	0.66	2.9	3.0	7.7
1599.02	3.42	2.89	P2	0.97	0.66	22.3	23.1	59.4
1613.01	0.22	1.3	P1	1.31	0.99	1.31	1.49	2.1
1613.03	0.22	1.3	P1	1.31	0.99	0.85	0.97	1.3
1613.02	0.22	1.3	P1	1.31	0.99	0.9	1.03	1.4
1614.01	3.37	-0.44	P4	1.37	1.44	1.85	2.92	2.5
1619.01	2.1	2.82	P1	0.68	0.56	0.66	0.68	2.1
1627.01	3.41	0.37	P4	1.8	1.68	5.75	7.52	8.3
1627.02	3.41	0.37	P4	1.8	1.68	3.7	4.84	5.4
1627.03	3.41	0.37	P4	1.8	1.68	2.75	3.6	4.0
1630.01	1.77	0.91	P3	0.84	0.75	1.4	1.68	2.3
1656.01	1.06	1.65	P3	1.29	0.94	3.62	4.0	6.2
1660.01	1.40	2.0	P3	0.89	0.66	1.99	2.14	4.0
1661.01	1.37	3.22	P4	1.27	0.75	45.6	46.7	121
1677.01	0.61	4.76	P1	1.25	0.6	2.92	2.94	12.7
1687.01	2.11	4.1	P3	0.78	0.6	1.65	1.67	8.5
1692.01	3.19	6.82	P4	0.89	0.42	2.85	2.85	31.5
1692.02	3.19	6.82	P4	0.89	0.42	0.84	0.84	9.3
1695.01	0.31	0.61	P3	1.49	1.37	2.19	2.74	3.4
1700.01	0.29	1.07	P2	0.8	0.71	1.54	1.8	2.6
1717.01	0.87	1.46	P2	1.17	0.91	2.43	2.73	4.2
1729.01	3.83	3.81	P4	0.86	0.58	16.0	16.2	63.4

Continued on next page

Object	Sep. (")	Δm (mags)	Reference ^a	$R_{\star,target}^b$ (R_{\odot})	$R_{\star,secondary}^c$ (R_{\odot})	$R_{p,0}^d$ (R_{\oplus})	$R_{p,prim.}^e$ (R_{\oplus})	$R_{p,sec.}^f$ (R_{\oplus})
1781.01	3.4	3.78	P4	0.72	0.49	3.47	3.52	13.8
1781.02	3.4	3.78	P4	0.72	0.49	2.2	2.23	8.7
1781.03	3.4	3.78	P4	0.72	0.49	3.46	3.51	13.7
1784.01	0.33	0.58	P2	1.04	0.94	8.8	11.1	13.1
1792.02	0.53	1.06	P3	1.07	0.91	0.77	0.9	1.2
1792.03	0.53	1.06	P3	1.07	0.91	1.32	1.55	2.1
1792.01	0.53	1.06	P3	1.07	0.91	4.55	5.34	7.4
1792.02	1.99	0.98	P3	1.07	0.91	0.77	0.91	1.2
1792.03	1.99	0.98	P3	1.07	0.91	1.32	1.56	2.1
1792.01	1.99	0.98	P3	1.07	0.91	4.55	5.39	7.2
1798.01	3.81	3.75	P2	1.03	0.6	39.9	40.6	132
1804.01	2.88	2.84	P3	0.69	0.56	5.1	5.28	15.9
1812.01	2.71	6.84	P4	2.02	0.66	63.5	63.6	485
1820.01	3.78	5.89	P4	0.88	0.49	1.63	1.63	13.9
1820.02	3.78	5.89	P4	0.88	0.49	0.97	0.97	8.3
1830.01	0.46	1.29	P2	0.8	0.66	2.22	2.54	3.8
1830.02	0.46	1.29	P2	0.8	0.66	3.56	4.07	6.1
1845.01	2.06	4.97	P1	1.67	0.75	3.97	3.99	17.6
1845.02	2.06	4.97	P1	1.67	0.75	10.7	10.7	47.4
1846.01	3.77	1.07	P3	0.8	0.71	3.79	4.44	6.4
1853.01	0.96	0.24	P2	1.05	1.01	2.4	3.22	3.5
1855.01	1.5	5.79	P4	0.61	0.36	3.45	3.46	29.3
1861.01	2.10	4.93	P2	1.33	0.6	3.56	3.58	15.7
1880.01	1.7	3.66	P1	0.54	0.36	1.28	1.3	4.7
1884.01	0.95	3.65	P1	0.8	0.56	4.37	4.45	16.8
1884.02	0.95	3.65	P1	0.8	0.56	1.73	1.76	6.7
1884.01	2.54	5.61	P4	0.8	0.49	4.37	4.38	36.0
1884.02	2.54	5.61	P4	0.8	0.49	1.73	1.73	14.3
1890.01	0.41	3.44	P1	1.6	0.89	1.75	1.79	4.9
1891.01	2.09	4.46	P1	0.81	0.56	2.18	2.2	11.9
1891.02	2.09	4.46	P1	0.81	0.56	1.35	1.36	7.4
1899.01	1.84	0.94	P2	1.18	0.99	2.81	3.35	4.3
1899.02	1.84	0.94	P2	1.18	0.99	1.08	1.29	1.7
1901.01	3.82	2.16	P4	1.65	1.06	3.56	3.8	6.6
1908.01	1.29	4.11	P3	0.6	0.42	1.34	1.36	6.4
1908.02	1.29	4.11	P3	0.6	0.42	1.16	1.17	5.5
1916.01	0.27	2.73	P1	1.27	0.79	2.42	2.52	5.5
1916.02	0.27	2.73	P1	1.27	0.79	2.08	2.16	4.7
1916.03	0.27	2.73	P1	1.27	0.79	1.01	1.05	2.3
1922.01	3.78	2.73	P4	1.14	0.75	2.38	2.47	5.7
1922.03	3.78	2.73	P4	1.14	0.75	4.22	4.39	10.1
1943.01	1.42	1.42	P4	1.64	1.21	3.09	3.48	5.0
1950.01	3.35	1.69	P2	0.76	0.58	3.44	3.79	6.3
1972.01	1.05	1.05	P2	1.34	1.06	2.88	3.38	4.3
1972.02	1.05	1.05	P2	1.34	1.06	1.0	1.17	1.5

Continued on next page

Object	Sep. (")	Δm (mags)	Reference ^a	$R_{\star,target}^b$ (R_{\odot})	$R_{\star,secondary}^c$ (R_{\odot})	$R_{p,0}^d$ (R_{\oplus})	$R_{p,prim.}^e$ (R_{\oplus})	$R_{p,sec.}^f$ (R_{\oplus})
1973.01	0.79	1.69	P3	0.59	0.56	1.49	1.64	3.4
1979.01	0.84	3.2	P1	0.99	0.66	1.38	1.42	4.1
1985.01	2.82	4.19	P2	0.73	0.49	2.24	2.26	10.5
1989.01	1.12	3.49	P2	0.95	0.6	2.28	2.33	7.3
1995.01	2.96	5.34	P3	0.86	0.49	29.2	29.3	197
2009.01	1.51	4.11	P1	0.97	0.58	2.23	2.26	9.0
2014.01	3.75	2.5	P2	0.88	0.66	24.3	25.5	60.3
2019.01	4.01	2.61	P2	0.9	0.6	2.66	2.78	6.2
2022.01	3.14	4.16	P4	0.96	0.58	1.92	1.94	8.0
2022.02	3.14	4.16	P4	0.96	0.58	1.9	1.92	7.9
2022.01	2.5	5.3	P4	0.96	0.56	1.92	1.93	13.0
2022.02	2.5	5.3	P4	0.96	0.56	1.9	1.91	12.8
2025.01	3.49	5.05	P4	1.47	0.71	3.29	3.31	16.4
2025.02	3.49	5.05	P4	1.47	0.71	2.8	2.81	13.9
2025.03	3.49	5.05	P4	1.47	0.71	1.81	1.82	9.0
2032.01	1.19	0.34	P2	1.55	1.44	2.08	2.74	3.0
2048.01	1.84	3.33	P3	0.79	0.58	2.12	2.17	7.4
2048.02	1.84	3.33	P3	0.49	0.25	576.1	589.4	1392
2050.01	3.33	5.33	P3	0.84	0.49	1.6	1.61	11.0
2050.02	3.33	5.33	P3	0.84	0.49	0.74	0.74	5.1
2055.01	3.80	4.09	P2	1.12	0.6	2.56	2.59	9.2
2055.02	3.80	4.09	P2	1.12	0.6	1.79	1.81	6.4
2055.03	3.80	4.09	P2	1.12	0.6	1.48	1.5	5.3
2055.04	3.80	4.09	P2	0.83	0.56	1.26	1.27	5.6
2056.01	3.87	3.37	P2	0.93	0.6	2.07	2.12	6.5
2059.01	0.38	1.1	P1	0.75	0.6	0.79	0.92	1.2
2059.02	0.38	1.1	P1	0.75	0.6	0.44	0.51	0.7
2067.01	1.64	0.8	P2	1.39	1.2	1.77	2.15	2.7
2069.01	1.12	4.24	P2	1.36	0.71	3.7	3.74	13.8
2083.01	0.26	1.03	P2	1.18	0.97	2.53	2.98	3.9
2091.01	1.30	1.72	P3	0.76	0.97	2.12	2.33	6.5
2093.01	2.08	3.1	P3	8.77	0.97	20.8	21.3	9.8
2093.02	2.08	3.1	P3	8.77	0.97	12.3	12.6	5.8
2093.03	2.08	3.1	P3	8.77	0.97	10.0	10.3	4.7
2096.01	3.50	4.13	P2	0.82	0.56	1.94	1.96	9.0
2098.01	2.88	2.58	P2	1.26	0.79	2.26	2.36	4.9
2098.02	2.88	2.58	P2	1.26	0.79	2.21	2.31	4.8
2098.01	3.24	2.4	P2	1.26	0.82	2.26	2.38	4.7
2098.02	3.24	2.4	P2	1.26	0.82	2.21	2.33	4.6
2100.01	2.98	2.1	P2	0.91	0.71	1.22	1.31	2.7
2105.01	3.01	6.28	P4	0.98	0.49	1.25	1.25	11.4
2115.01	3.59	2.75	P2	0.76	0.56	2.69	2.79	7.4
2117.01	0.33	0.71	P3	0.69	0.6	1.84	2.27	2.8
2143.01	2.16	3.5	P1	0.84	0.58	1.01	1.03	3.6
2156.01	3.35	2.64	P2	0.43	0.24	1.66	1.73	3.2

Continued on next page

Object	Sep. (")	Δm (mags)	Reference ^a	$R_{\star,target}$ ^b (R_{\odot})	$R_{\star,secondary}$ ^c (R_{\odot})	$R_{p,0}$ ^d (R_{\oplus})	$R_{p,prim.}$ ^e (R_{\oplus})	$R_{p,sec.}$ ^f (R_{\oplus})
2159.01	2	3.99	P1	1.09	0.6	1.32	1.34	4.6
2159.02	2	3.99	P1	1.09	0.6	1.33	1.35	4.7
2163.01	0.77	0.04	P3	1.02	0.99	1.76	2.47	2.4
2163.02	0.77	0.04	P3	1.02	0.99	1.6	2.24	2.2
2163.03	0.77	0.04	P3	1.02	0.99	1.59	2.23	2.2
2169.01	3.59	4.2	P4	0.84	0.56	0.92	0.93	4.3
2169.02	3.59	4.2	P4	0.84	0.56	0.68	0.69	3.2
2169.03	3.59	4.2	P4	0.84	0.56	0.64	0.65	3.0
2169.04	3.59	4.2	P4	0.84	0.56	0.37	0.37	1.7
2174.01	0.92	0.21	P2	0.64	0.6	2.44	3.3	3.4
2174.02	0.92	0.21	P2	0.64	0.6	2.05	2.77	2.9
2174.03	0.92	0.21	P2	0.64	0.6	1.71	2.31	2.4
2174.04	0.92	0.21	P2	0.64	0.6	0.96	1.3	1.3
2174.01	3.88	0.14	P2	0.64	0.6	2.44	3.34	3.4
2174.02	3.88	0.14	P2	0.64	0.6	2.05	2.81	2.8
2174.03	3.88	0.14	P2	0.64	0.6	1.71	2.34	2.4
2174.04	3.88	0.14	P2	0.64	0.6	0.96	1.32	1.3
2206.01	3.28	1.28	P3	0.96	0.79	1.64	1.88	2.8
2213.01	3.94	1.67	P3	0.78	0.79	1.6	1.76	3.9
2222.01	2.53	5.33	P4	5.55	0.79	14.0	14.0	23.3
2247.01	1.90	5.12	P2	0.61	0.38	0.79	0.79	5.3
2283.01	1.05	1.46	P3	0.61	0.56	16.4	18.4	32.8
2287.01	2.96	5.64	P4	0.67	0.38	0.98	0.98	7.6
2287.02	2.96	5.64	P4	0.67	0.38	0.79	0.79	6.1
2295.01	2.19	0.88	P2	0.8	0.75	0.52	0.62	0.9
2298.01	1.57	2.08	P2	0.53	0.36	0.7	0.75	1.3
2298.03	1.57	2.08	P2	0.53	0.36	0.36	0.39	0.7
2298.02	1.57	2.08	P2	0.53	0.36	0.63	0.67	1.2
2314.01	4.14	3.45	P2	0.95	0.6	2.67	2.73	8.5
2317.01	1.51	4.93	P2	1.04	0.58	1.23	1.24	6.7
2376.01	0.40	0.46	P3	0.84	0.79	2.34	3.01	3.5
2377.01	2.09	1.25	P2	0.82	0.71	1.55	1.78	2.7
2377.01	4.11	4.04	P2	0.82	0.56	1.55	1.57	6.9
2379.01	3.59	1.89	P3	1.02	0.75	20.8	22.5	39.2
2380.01	4.01	2.46	P2	0.96	0.71	1.59	1.67	3.8
2413.02	0.31	2.11	P1	0.72	0.58	1.47	1.57	3.3
2413.01	0.31	2.11	P1	0.72	0.58	1.49	1.59	3.4
2421.01	1.23	0.99	P2	0.53	0.49	0.55	0.65	1.0
2421.02	1.23	0.99	P2	0.53	0.49	0.48	0.57	0.8
2421.01	4.07	3.87	P2	0.53	0.32	0.55	0.56	2.0
2421.02	4.07	3.87	P2	0.53	0.32	0.48	0.49	1.7
2443.01	1.39	5.37	P1	1.0	0.56	1.01	1.01	6.7
2443.02	1.39	5.37	P1	1.0	0.56	1.0	1.0	6.6
2445.01	2.10	3.21	P3	0.9	0.6	12.0	12.3	35.9
2460.01	2.36	3.41	P3	0.64	0.49	1.51	1.54	5.7

Continued on next page

Object	Sep. (")	Δm (mags)	Reference ^a	$R_{\star,target}^b$ (R_{\odot})	$R_{\star,secondary}^c$ (R_{\odot})	$R_{p,0}^d$ (R_{\oplus})	$R_{p,prim.}^e$ (R_{\oplus})	$R_{p,sec.}^f$ (R_{\oplus})
2463.01	0.62	0.75	P1	1.17	1.01	1.04	1.27	1.6
2469.01	4.18	2.44	P2	0.8	0.6	2.34	2.46	5.7
2474.01	0.61	0.65	P2	0.8	0.75	42.0	52.3	66.1
2482.01	0.31	0.59	P3	0.9	0.79	2.44	3.07	3.5
2486.01	0.24	0.49	P1	1.24	1.08	1.42	1.82	2.0
2493.01	2.69	2.68	P2	0.77	1.08	1.6	1.67	8.1
2516.01	3.42	5.93	P2	2.08	0.75	1.43	1.43	7.9
2535.01	1.73	2.47	P3	0.79	0.6	2.96	3.11	7.4
2542.01	0.88	1.2	P2	0.36	0.24	0.67	0.77	0.9
2547.01	2.79	4.23	P4	1.0	0.58	1.48	1.49	6.1
2551.01	2.69	1.93	P2	0.72	0.58	1.53	1.65	3.3
2554.01	0.37	0.37	P3	0.51	0.42	13.7	17.9	17.6
2554.02	0.37	0.37	P3	0.51	0.42	0.94	1.23	1.2
2556.01	3.86	4.08	P4	0.93	0.58	1.5	1.52	6.2
2579.01	3.48	3.69	P3	1.24	0.71	1.53	1.56	4.9
2579.02	3.48	3.69	P3	1.24	0.71	1.66	1.69	5.3
2579.03	3.48	3.69	P3	1.24	0.71	1.6	1.63	5.1
2580.01	0.60	0.86	P3	0.86	0.75	1.59	1.92	2.5
2582.01	3.41	4.25	P4	1.37	0.71	2.01	2.03	7.4
2598.01	1.09	0.37	P2	1.01	0.94	1.35	1.77	2.0
2601.01	1.66	1.43	P2	1.37	1.04	1.64	1.85	2.7
2601.01	1.44	3.61	P2	1.37	0.75	1.64	1.67	4.8
2641.01	1.42	2.56	P1	1.08	0.75	0.84	0.88	2.0
2641.01	3.54	3.73	P4	1.08	0.66	0.84	0.85	2.9
2657.01	0.73	0.27	P1	0.84	0.79	0.58	0.77	0.8
2664.01	1.17	0.83	P2	0.79	0.75	2.66	3.22	4.5
2679.01	2.11	2.87	P2	2.67	0.75	29.6	30.7	32.2
2681.01	1.10	1.25	P2	0.76	0.6	6.01	6.9	9.7
2681.02	1.10	1.25	P2	0.76	0.6	2.07	2.37	3.4
2688.01	1.09	0.86	P3	0.59	0.56	5.15	6.21	8.7
2705.01	1.84	3.19	P2	0.39	0.22	1.24	1.27	3.1
2707.01	3.28	4.71	P2	1.15	0.6	3.21	3.23	14.8
2707.02	3.28	4.71	P2	1.15	0.6	1.68	1.69	7.7
2707.03	3.28	4.71	P2	1.15	0.6	2.69	2.71	12.4
2707.01	3.87	3.64	P2	1.15	0.66	3.21	3.27	10.0
2707.02	3.87	3.64	P2	1.15	0.66	1.68	1.71	5.2
2707.03	3.87	3.64	P2	1.15	0.66	2.69	2.74	8.4
2711.01	0.52	0.12	P2	1.11	1.06	1.62	2.23	2.2
2711.02	0.52	0.12	P2	1.11	1.06	1.43	1.97	2.0
2722.01	3.27	5.88	P2	1.2	0.58	1.51	1.51	11.0
2722.02	3.27	5.88	P2	1.2	0.58	1.44	1.44	10.5
2722.03	3.27	5.88	P2	1.2	0.58	1.21	1.21	8.8
2722.04	3.27	5.88	P2	1.2	0.58	1.27	1.27	9.2
2722.05	3.27	5.88	P2	1.2	0.58	1.17	1.17	8.5
2729.01	3.94	2.03	P2	1.12	0.79	1.96	2.11	3.8

Continued on next page

Object	Sep. (")	Δm (mags)	Reference ^a	$R_{\star,target}^b$ (R_{\odot})	$R_{\star,secondary}^c$ (R_{\odot})	$R_{p,0}^d$ (R_{\oplus})	$R_{p,prim.}^e$ (R_{\oplus})	$R_{p,sec.}^f$ (R_{\oplus})
2743.01	2.36	3.79	P2	0.88	0.58	1.32	1.34	5.1
2744.01	3.50	2.12	P3	1.45	0.99	4.85	5.18	9.4
2744.02	3.50	2.12	P3	1.45	0.99	2.84	3.03	5.5
2754.01	0.79	2.23	P2	0.97	0.75	0.74	0.79	1.7
2760.01	0.45	0.84	P3	0.78	0.75	2.69	3.25	4.6
2771.01	3.85	6.61	P2	1.54	0.58	1.91	1.91	15.1
2779.01	0.98	2.54	P2	0.86	0.6	1.88	1.97	4.4
2797.01	0.35	0.72	P3	1.08	0.97	1.65	2.03	2.5
2803.01	3.84	3.0	P2	0.94	0.6	0.53	0.55	1.4
2807.01	3.93	1.9	P2	1.28	0.89	2.34	2.54	4.2
2812.01	2.09	3.23	P2	1.03	0.66	2.61	2.68	7.6
2813.01	1.10	0.84	P3	12.56	0.66	14.8	17.9	1.4
2836.01	3.94	3.39	P2	0.76	0.56	1.22	1.25	4.4
2837.01	0.35	0.23	P2	2.27	2.02	2.88	3.87	3.8
2838.01	1.74	5.92	P2	1.1	0.56	0.92	0.92	7.1
2838.02	1.74	5.92	P2	1.1	0.56	0.81	0.81	6.3
2848.01	2.30	5.63	P2	1.46	0.66	1.55	1.55	9.4
2851.01	0.39	0.45	P3	0.97	0.89	2.27	2.93	3.3
2851.02	0.39	0.45	P3	0.97	0.89	1.5	1.93	2.2
2856.01	2.31	3.44	P3	1.09	0.66	2.88	2.94	8.7
2859.01	0.47	2.12	P2	0.72	0.58	0.7	0.75	1.6
2859.02	0.47	2.12	P2	0.72	0.58	0.65	0.69	1.5
2859.03	0.47	2.12	P2	0.72	0.58	0.57	0.61	1.3
2859.05	0.47	2.12	P2	0.72	0.58	0.66	0.71	1.5
2859.04	0.47	2.12	P2	0.72	0.58	0.57	0.61	1.3
2862.01	0.68	0.17	P3	0.51	0.42	1.64	2.23	2.0
2880.01	3.39	1.15	P4	0.87	0.75	1.22	1.42	2.1
2896.01	0.96	0.38	P3	1.51	1.39	31.1	40.6	44.6
2896.02	0.96	0.38	P3	1.26	1.17	1.57	2.05	2.3
2897.01	2.65	2.98	P4	0.88	0.6	23.1	23.8	64.3
2900.01	2.36	1.3	P3	0.77	0.6	2.08	2.37	3.4
2904.01	0.71	1.99	P2	1.76	1.21	2.23	2.4	4.1
2910.01	3.15	0.72	P2	0.85	0.75	1.8	2.22	2.7
2914.01	3.80	5.64	P2	2.57	0.87	2.89	2.9	13.2
2926.01	0.33	0.27	P3	0.56	0.49	2.21	2.95	2.9
2926.05	0.33	0.27	P3	0.56	0.49	3.47	4.63	4.6
2926.03	0.33	0.27	P3	0.56	0.49	2.38	3.18	3.2
2926.04	0.33	0.27	P3	0.56	0.49	2.25	3.0	3.0
2926.02	0.33	0.27	P3	0.56	0.49	2.2	2.94	2.9
2927.01	1.39	2.65	P3	1.03	0.75	2.31	2.41	5.9
2949.01	2.36	4.08	P2	1.34	0.71	1.04	1.05	3.6
2949.02	2.36	4.08	P2	1.34	0.71	0.87	0.88	3.1
2958.01	1.15	2.47	P3	1.03	0.75	1.89	1.98	4.5
2962.01	1.13	0.53	P2	1.04	0.94	0.93	1.18	1.4
2971.01	0.53	1.33	P2	1.47	1.17	1.26	1.43	2.1

Continued on next page

Object	Sep. (")	Δm (mags)	Reference ^a	$R_{\star,target}^b$ (R_{\odot})	$R_{\star,secondary}^c$ (R_{\odot})	$R_{p,0}^d$ (R_{\oplus})	$R_{p,prim.}^e$ (R_{\oplus})	$R_{p,sec.}^f$ (R_{\oplus})
2971.02	0.53	1.33	P2	1.47	1.17	1.65	1.88	2.8
2976.01	2.02	2.66	P3	0.63	0.49	1.94	2.02	5.4
2984.01	3.47	4.34	P2	1.36	0.66	1.12	1.13	4.1
3002.01	0.84	2.02	P4	1.13	0.79	1.31	1.41	2.5
3020.01	0.38	0.93	P3	1.97	1.63	1.9	2.27	2.9
3029.01	0.28	0.68	P2	0.99	0.89	2.24	2.77	3.4
3029.02	0.28	0.68	P2	0.99	0.89	1.35	1.67	2.1
3041.01	2.03	4.64	P2	1.08	0.58	1.15	1.16	5.3
3042.01	1.87	1.62	P3	0.97	0.75	1.91	2.11	3.4
3043.01	1.14	1.94	P3	1.1	0.79	1.07	1.16	2.0
3043.02	1.14	1.94	P3	0.86	0.66	0.73	0.79	1.5
3066.01	3.41	1.86	P3	0.76	0.66	2.1	2.28	4.7
3069.01	1.93	2.2	P2	1.1	0.75	1.88	2.0	3.7
3073.01	1.30	1.76	P2	0.84	0.66	1.18	1.29	2.3
3106.01	0.30	0.76	P3	1.0	0.87	1.08	1.32	1.6
3111.02	3.36	5.87	P3	1.1	0.56	0.66	0.66	5.0
3111.01	3.36	5.87	P3	1.1	0.56	0.92	0.92	7.0
3112.01	1.87	0.49	P3	0.8	0.75	1.41	1.8	2.1
3120.01	1.14	0.87	P3	1.15	0.99	1.43	1.72	2.2
3136.01	1.83	2.91	P3	0.69	0.56	0.93	0.96	3.0
3156.02	1.24	2.09	P4	1.5	1.04	44.8	47.9	86.5
3156.03	1.24	2.09	P4	1.5	1.04	77.2	82.6	149
3156.04	1.24	2.09	P4	1.5	1.04	35.9	38.4	69.4
3156.01	1.24	2.09	P4	1.5	1.04	27.8	29.8	53.8
3156.02	3.06	5.02	P4	1.5	0.71	44.8	45.0	214
3156.03	3.06	5.02	P4	1.5	0.71	77.2	77.5	369
3156.04	3.06	5.02	P4	1.5	0.71	35.9	36.1	172
3156.01	3.06	5.02	P4	1.5	0.71	27.8	27.9	133
3158.02	2.10	4.0	P2	0.72	0.49	0.65	0.66	2.8
3158.03	2.10	4.0	P2	0.72	0.49	0.65	0.66	2.8
3158.04	2.10	4.0	P2	0.72	0.49	0.62	0.63	2.7
3158.05	2.10	4.0	P2	0.72	0.49	0.95	0.96	4.2
3158.01	2.10	4.0	P2	0.72	0.49	0.5	0.51	2.2
3161.01	2.68	3.04	P3	1.67	0.94	54.5	56.2	128
3190.01	2.68	5.92	P2	1.21	0.58	0.86	0.86	6.3
3214.01	0.49	0.73	P3	1.79	1.52	1.53	1.88	2.2
3214.02	0.49	0.73	P3	1.79	1.52	1.35	1.66	2.0
3214.01	1.41	2.5	P3	1.79	1.1	1.53	1.6	3.1
3214.02	1.41	2.5	P3	1.79	1.1	1.35	1.42	2.8
3245.01	1.58	3.1	P2	1.3	0.75	1.09	1.12	2.7
3255.01	3.15	4.87	P2	0.68	0.42	1.56	1.57	9.2
3263.01	0.80	2.01	P3	0.44	0.25	7.71	8.29	12.0
3264.01	3.66	1.37	P3	0.64	0.58	1.36	1.54	2.6
3277.01	2.45	5.79	P2	2.48	0.82	3.19	3.2	15.1
3277.01	3.41	5.0	P2	2.48	0.94	3.19	3.21	12.2

Continued on next page

Object	Sep. (")	Δm (mags)	Reference ^a	$R_{\star,target}^b$ (R_{\odot})	$R_{\star,secondary}^c$ (R_{\odot})	$R_{p,0}^d$ (R_{\oplus})	$R_{p,prim.}^e$ (R_{\oplus})	$R_{p,sec.}^f$ (R_{\oplus})
3284.01	3.94	2.42	P2	0.52	0.36	0.97	1.02	2.1
3288.01	3.17	4.32	P2	0.98	0.58	3.35	3.38	14.6
3288.01	3.50	4.62	P2	0.98	0.58	3.35	3.37	16.8
3309.01	3.71	2.78	P2	0.86	0.6	5.91	6.13	15.4
3324.01	3.84	3.05	P2	0.79	0.58	2.37	2.44	7.3
3335.01	2.40	2.89	P3	1.09	0.75	2.29	2.37	6.1
3339.01	3.41	1.38	P2	0.93	0.75	2.55	2.89	4.4
3341.01	3.23	4.27	P3	1.35	0.66	2.13	2.15	7.5
3341.02	3.23	4.27	P3	1.35	0.66	1.48	1.49	5.2
3347.01	3.24	2.2	P3	0.79	0.6	1.49	1.59	3.3
3354.01	3.71	2.55	P3	0.9	0.66	1.33	1.39	3.3
3372.02	2.36	1.95	P3	1.05	0.75	2.37	2.56	4.5
3372.01	2.36	1.95	P3	1.05	0.75	2.28	2.46	4.3
3377.01	1.45	4.26	P2	0.51	0.23	0.99	1.0	3.2
3401.01	0.65	0.89	P2	1.2	1.01	1.96	2.35	3.0
3401.02	0.65	0.89	P2	1.07	0.94	2.2	2.64	3.5
3413.01	2.18	3.79	P3	1.03	0.6	57.1	57.9	193
3415.01	0.74	0.03	P3	1.38	1.37	1.77	2.49	2.5
3418.01	1.13	1.29	P3	1.06	0.87	3.85	4.4	6.5
3432.01	0.66	1.37	P3	1.45	1.12	2.36	2.67	3.9
3435.01	3.06	1.33	P4	0.89	0.75	1.58	1.8	2.8
3435.01	3.52	0.58	P4	0.89	0.79	1.58	1.99	2.3
3439.01	3.42	3.97	P2	1.14	0.66	2.19	2.22	8.0
3444.01	1.11	3.32	P2	0.53	0.36	0.76	0.78	2.4
3444.02	1.11	3.32	P2	0.53	0.36	4.98	5.1	15.9
3444.03	1.11	3.32	P2	0.53	0.36	0.5	0.51	1.6
3444.04	1.11	3.32	P2	0.53	0.36	0.74	0.76	2.4
3444.01	3.55	3.41	P2	0.53	0.36	0.76	0.78	2.5
3444.02	3.55	3.41	P2	0.53	0.36	4.98	5.09	16.6
3444.03	3.55	3.41	P2	0.53	0.36	0.5	0.51	1.7
3444.04	3.55	3.41	P2	0.53	0.36	0.74	0.76	2.5
3459.01	3.35	2.37	P2	0.86	0.6	1.75	1.85	3.8
3460.01	1.24	5.08	P2	1.51	0.71	2.25	2.26	11.0
3460.01	2.47	5.52	P2	1.51	0.66	2.25	2.26	12.6
3463.01	3.67	4.41	P3	1.06	0.6	1.42	1.43	6.2
3463.01	2.74	4.79	P3	1.06	0.58	1.42	1.43	7.1
3468.01	1.49	3.22	P2	2.44	1.28	3.22	3.3	7.6
3471.01	0.63	3.05	P3	2.19	1.28	36.7	37.8	89.9
3480.01	0.40	0.75	P3	0.74	0.66	1.15	1.41	1.8
3483.01	1.51	2.15	P3	1.24	0.82	2.08	2.22	3.9
3486.01	4.16	4.06	P2	0.89	0.58	1.63	1.65	7.0
3497.01	0.78	1.23	P2	0.34	0.24	0.8	0.92	1.1
3500.01	2.54	4.01	P2	2.48	1.1	3.78	3.83	10.8
3500.02	2.54	4.01	P2	2.48	1.1	1.57	1.59	4.5
3533.01	3.08	5.21	P3	0.99	0.56	53.9	54.1	337

Continued on next page

Object	Sep. (")	Δm (mags)	Reference ^a	$R_{\star,target}$ ^b (R_{\odot})	$R_{\star,secondary}$ ^c (R_{\odot})	$R_{p,0}$ ^d (R_{\oplus})	$R_{p,prim.}$ ^e (R_{\oplus})	$R_{p,sec.}$ ^f (R_{\oplus})
3611.01	2.30	2.77	P3	1.0	0.71	44.4	46.0	116
3626.01	1.96	3.82	P3	0.9	0.58	62.2	63.2	237
3649.01	0.79	0.26	P3	1.34	1.21	73.3	98.0	99.5
3660.01	0.60	1.05	P3	0.8	0.71	38.8	45.6	65.2
3678.01	2.63	5.08	P3	1.04	0.58	9.09	9.13	52.8
3770.01	1.20	1.44	P3	1.24	0.94	7.31	8.22	12.2
3783.01	1.13	3.53	P3	1.94	1.01	72.2	73.5	195
3791.01	3.50	1.89	P3	1.39	0.99	7.23	7.84	13.3
3791.02	3.50	1.89	P3	1.39	0.99	5.94	6.44	10.9
3805.01	3.7	5.37	P4	13.55	0.99	539.2	541.1	468
3813.01	2.54	4.58	P4	1.21	0.6	6.9	6.95	28.6
3813.01	2.13	4.22	P4	1.21	0.66	6.9	6.97	26.7
3856.01	2.54	3.27	P4	3.35	0.66	95.2	97.5	86.9
3886.01	0.50	1.13	P3	12.7	0.66	43.7	50.8	4.5
3891.01	1.05	4.69	P2	2.78	0.66	79.0	79.5	164
3891.01	2.01	4.92	P2	2.78	0.66	79.0	79.4	182
3907.01	1.58	6.31	P2	1.77	0.66	5.82	5.83	39.9
3907.01	2.82	3.23	P2	1.77	0.99	5.82	5.97	14.8
3928.01	2.96	1.21	P3	1.71	1.37	1.45	1.67	2.3
3946.01	4.27	5.26	P2	1.35	0.6	3.28	3.29	16.6
4004.01	1.93	4.34	P2	1.01	0.58	1.41	1.42	6.1
4021.01	1.92	0.52	P2	1.42	1.35	1.53	1.95	2.4
4021.02	1.92	0.52	P2	1.42	1.35	1.02	1.3	1.6
4053.01	4.11	5.51	P2	1.03	0.56	0.85	0.85	5.8
4062.01	1.49	3.66	P3	1.12	0.66	36.0	36.6	117
4098.01	0.78	1.1	P2	2.57	1.9	2.39	2.79	3.4
4131.01	2.85	5.04	P3	2.91	1.9	2.07	2.08	13.8
4131.02	2.85	5.04	P3	2.91	1.9	4.41	4.43	29.5
4145.01	2.71	2.36	P2	1.0	0.75	0.96	1.01	2.2
4149.01	1.76	0.17	P2	1.23	1.17	1.71	2.33	2.4
4149.02	1.76	0.17	P2	1.23	1.17	1.82	2.48	2.6
4166.01	3.54	3.29	P2	0.97	0.6	2.41	2.47	7.0
4194.01	2.17	3.41	P2	0.72	0.56	1.29	1.32	4.9
4205.01	2.71	2.65	P2	0.9	0.66	0.88	0.92	2.3
4208.01	0.99	2.57	P2	0.73	0.58	1.23	1.29	3.3
4209.01	0.96	0.37	P2	0.7	0.66	2.35	3.07	3.4
4226.01	2.49	4.18	P2	1.44	0.75	1.63	1.65	5.8
4267.01	1.66	3.29	P3	1.45	0.82	1.36	1.39	3.6
4268.01	3.56	4.77	P3	0.51	0.22	0.59	0.59	2.3
4274.01	3.26	3.71	P2	0.95	0.58	1.08	1.1	3.7
4274.01	4.54	4.11	P2	0.95	0.58	1.08	1.09	4.4
4287.01	0.61	1.27	P2	1.67	1.35	1.29	1.48	2.2
4287.02	0.61	1.27	P2	1.67	1.35	0.85	0.97	1.4
4313.01	2.88	4.19	P2	0.85	0.56	82.6	83.5	380
4323.02	1.12	2.22	P3	1.51	1.04	0.89	0.95	1.8

Continued on next page

Object	Sep. (")	Δm (mags)	Reference ^a	$R_{\star,target}$ ^b (R_{\odot})	$R_{\star,secondary}$ ^c (R_{\odot})	$R_{p,0}$ ^d (R_{\oplus})	$R_{p,prim.}$ ^e (R_{\oplus})	$R_{p,sec.}$ ^f (R_{\oplus})
4323.01	1.12	2.22	P3	1.51	1.04	1.59	1.69	3.2
4329.01	1.93	4.64	P2	1.25	0.66	1.02	1.03	4.6
4331.01	0.45	0.25	P2	1.73	1.68	1.45	1.94	2.1
4334.01	3.32	3.79	P3	0.74	0.56	1.1	1.12	4.9
4343.01	0.89	1.13	P3	1.3	1.01	1.73	2.01	2.6
4343.01	3.68	4.81	P3	1.3	0.6	1.73	1.74	7.4
4345.01	3.17	3.22	P3	1.46	0.82	26.6	27.3	67.5
4353.01	3.50	2.75	P3	0.98	0.66	3.92	4.07	9.7
4366.01	2.46	3.38	P3	0.73	0.56	1.0	1.02	3.7
4368.01	2.33	3.28	P4	2.56	1.28	2.37	2.43	5.5
4368.02	2.33	3.28	P4	2.14	1.2	58.7	60.1	152
4389.01	2.88	0.58	P2	0.86	0.75	1.27	1.6	1.8
4399.01	2.16	6.24	P2	0.82	0.49	1.42	1.42	15.2
4405.01	2.95	3.19	P3	0.99	0.66	1.39	1.43	4.2
4407.01	2.54	2.97	P2	1.32	0.79	0.6	0.62	1.5
4409.01	2.89	6.1	P2	1.29	0.58	1.06	1.06	7.9
4418.01	1.41	2.23	P3	0.9	0.66	3.19	3.39	6.9
4421.01	2.45	4.62	P3	1.2	0.6	0.61	0.61	2.6
4421.02	2.45	4.62	P3	1.2	0.6	0.62	0.62	2.6
4443.01	3.41	5.0	P2	1.44	0.66	1.22	1.23	5.6
4463.01	2.45	0.01	P2	0.82	0.79	1.52	2.14	2.1
4467.01	3.99	4.21	P3	0.82	0.56	1.42	1.43	6.8
4495.01	3.06	3.9	P2	0.98	0.58	1.39	1.41	5.1
4495.01	3.41	2.68	P2	0.98	0.66	1.39	1.45	3.4
4495.01	3.04	4.73	P2	0.98	0.58	1.39	1.4	7.4
4523.01	3.94	2.61	P2	1.16	0.75	1.03	1.08	2.3
4526.01	2.53	4.44	P3	1.33	0.66	2.72	2.74	10.6
4526.02	2.53	4.44	P3	1.33	0.66	2.09	2.11	8.1
4526.01	3.98	4.8	P3	1.33	0.66	2.72	2.74	12.4
4526.02	3.98	4.8	P3	1.33	0.66	2.09	2.1	9.6
4549.01	0.75	1.99	P3	0.86	0.66	1.16	1.25	2.4
4550.01	1.03	0.04	P3	0.79	0.75	1.84	2.58	2.5
4567.01	1.31	2.48	P2	0.99	0.71	8.1	8.5	19.1
4567.02	1.31	2.48	P2	0.99	0.71	1.11	1.17	2.6
4575.01	2.97	2.18	P2	1.7	1.12	1.98	2.11	3.8
4580.01	1.58	1.27	P2	1.84	1.44	1.23	1.41	2.0
4582.01	2.71	6.28	P2	0.88	0.49	0.35	0.35	3.5
4582.01	3.55	3.27	P2	0.88	0.58	0.35	0.36	1.1
4590.01	0.87	0.38	P3	0.83	0.75	1.75	2.28	2.4
4625.01	1.22	0.28	P4	0.7	0.66	21.3	28.3	30.6
4630.01	3.94	2.17	P3	1.52	1.04	2.46	2.62	4.9
4634.01	0.35	1.55	P2	1.04	0.79	0.98	1.09	1.7
4651.01	1.22	2.88	P2	1.01	0.66	0.77	0.8	2.0
4653.01	0.77	2.02	P3	1.16	0.82	1.07	1.15	2.1
4655.01	3.17	3.02	P3	0.79	0.58	1.15	1.19	3.5

Continued on next page

Object	Sep. (")	Δm (mags)	Reference ^a	$R_{\star,target}$ ^b (R_{\odot})	$R_{\star,secondary}$ ^c (R_{\odot})	$R_{p,0}$ ^d (R_{\oplus})	$R_{p,prim.}$ ^e (R_{\oplus})	$R_{p,sec.}$ ^f (R_{\oplus})
4656.01	2.89	1.42	P2	1.69	1.28	1.39	1.57	2.3
4657.01	2.11	3.27	P2	0.77	1.28	0.54	0.55	4.1
4657.02	2.11	3.27	P2	0.77	1.28	0.77	0.79	5.9
4661.01	3.93	2.32	P3	0.84	0.6	1.01	1.07	2.2
4699.01	4.01	5.93	P2	1.34	0.58	1.08	1.08	7.2
4700.02	3.77	1.89	P3	0.78	0.58	1.83	1.98	3.6
4700.01	3.77	1.89	P3	0.78	0.58	1.2	1.3	2.3
4707.01	3.7	6.41	P4	1.44	0.58	1.05	1.05	8.1
4710.01	2.70	3.5	P3	0.86	0.58	1.3	1.33	4.5
4743.01	3.06	2.29	P3	0.75	0.58	20.5	21.7	48.5
4750.01	2.09	1.95	P3	0.84	0.66	1.93	2.08	4.0
4759.01	0.67	2.12	P3	0.95	0.71	1.54	1.65	3.3
4764.01	3.83	2.42	P4	0.75	0.58	1.45	1.53	3.6
4768.01	1.30	3.99	P2	0.65	0.49	1.44	1.46	7.0
4792.01	3.68	2.36	P2	1.07	0.75	0.91	0.96	2.0
4793.01	2.37	4.25	P4	0.92	0.58	0.89	0.9	4.0
4797.01	3.59	1.12	P2	0.7	0.6	1.26	1.47	2.1
4797.01	3.93	3.37	P2	0.7	0.56	1.26	1.29	4.9
4810.01	2.36	3.16	P3	1.04	0.66	3.17	3.26	8.9
4812.01	3.15	1.84	P2	0.85	0.66	0.71	0.77	1.4
4813.01	2.54	1.22	P2	0.6	0.56	0.82	0.94	1.6
4813.01	4.03	3.34	P2	0.6	0.49	0.82	0.84	3.2
4823.01	1.40	0.59	P2	2.01	1.83	1.51	1.9	2.3
4871.01	0.96	3.12	P2	1.16	0.75	0.6	0.62	1.7
4871.02	0.96	3.12	P2	1.25	0.75	0.76	0.78	2.0
4881.01	3.42	3.3	P3	1.58	0.89	1.16	1.19	3.1
4881.02	3.42	3.3	P3	1.58	0.89	1.16	1.19	3.1
4895.01	2.27	2.28	P3	0.93	0.71	1.1	1.17	2.5
4895.02	2.27	2.28	P3	0.96	0.71	1.85	1.96	4.1
4923.01	0.78	1.46	P3	1.47	1.16	1.4	1.57	2.4
4974.01	1.23	3.33	P3	0.78	1.16	2.98	3.05	21.0
5004.01	1.05	1.05	P3	1.02	0.87	2.0	2.35	3.2
5052.01	0.75	0.68	P3	12.61	0.87	444.1	550.1	51.8
5101.01	1.24	3.33	P3	1.5	0.87	1.64	1.68	4.5
5216.01	3.67	3.31	P3	0.89	0.58	2.56	2.62	7.8
5220.01	2.83	7.22	P3	8.83	0.58	18.4	18.4	33.7
5220.01	2.89	3.27	P3	8.83	0.58	18.4	18.8	5.6
5232.01	1.75	4.67	P3	1.06	0.58	1.82	1.83	8.6
5243.01	0.77	0.55	P3	2.22	1.95	116.1	147.0	166
5243.01	2.41	5.53	P3	2.22	0.82	116.1	116.5	548
5274.01	3.95	4.13	P4	1.4	0.75	1.59	1.61	5.7
5327.01	1.88	3.43	P3	0.57	0.36	2.09	2.13	6.6
5327.01	3.63	3.92	P3	0.57	0.32	2.09	2.12	7.2
5327.01	3.96	-0.12	P3	0.57	0.56	2.09	3.04	2.8
5331.01	3.67	3.72	P3	0.82	0.58	1.17	1.19	4.7

Continued on next page

Object	Sep. (")	Δm (mags)	Reference ^a	$R_{\star,target}$ ^b (R_{\odot})	$R_{\star,secondary}$ ^c (R_{\odot})	$R_{p,0}$ ^d (R_{\oplus})	$R_{p,prim.}$ ^e (R_{\oplus})	$R_{p,sec.}$ ^f (R_{\oplus})
5332.01	2.19	2.37	P3	1.05	0.75	1.09	1.15	2.4
5332.01	3.61	0.63	P3	1.05	0.94	1.09	1.36	1.6
5340.01	1.24	2.66	P3	1.01	0.71	1.79	1.87	4.5
5373.01	0.21	0.12	P3	3.86	0.71	5.0	6.88	1.3
5426.01	2.93	1.75	P4	1.23	0.89	1.78	1.95	3.2
5440.01	2.45	3.04	P3	0.94	0.6	1.75	1.8	4.7
5454.01	2.07	1.77	P4	0.76	0.58	2.62	2.87	5.0
5465.01	2.85	1.36	P3	0.9	0.75	1.12	1.27	2.0
5475.01	3.19	3.65	P4	1.29	0.75	2.41	2.45	7.6
5475.02	3.19	3.65	P4	1.29	0.75	0.97	0.99	3.1
5480.01	3.52	1.24	P3	1.46	1.2	5.78	6.64	9.6
5482.01	0.62	1.44	P3	0.86	0.71	2.96	3.33	5.3
5486.01	0.34	0.73	P3	3.36	0.71	23.5	28.8	8.5
5527.01	2.85	2.63	P4	1.02	0.71	72.3	75.4	175
5552.01	1.09	0.82	P4	0.99	0.87	2.1	2.55	3.3
5553.01	0.97	2.52	P3	0.84	0.6	2.32	2.43	5.5
5556.01	3.28	4.31	P3	1.01	0.58	1.86	1.88	7.9
5556.01	3.22	5.29	P3	1.01	0.56	1.86	1.87	11.9
5570.01	2.06	4.64	P3	0.82	0.56	2.28	2.3	13.3
5578.01	0.33	1.78	P3	2.46	1.68	3.0	3.28	5.1
5640.01	0.53	2.26	P4	4.89	1.68	9.56	10.1	9.9
5665.01	2.11	3.24	P3	1.75	0.97	1.33	1.36	3.3
5671.01	2.17	1.79	P3	1.13	0.82	1.73	1.89	3.1
5672.01	3.17	4.58	P4	1.68	0.75	65.3	65.7	241
5695.01	0.60	1.47	P3	1.23	0.94	70.4	79.0	119
5707.01	2.71	2.43	P3	1.17	0.79	2.88	3.03	6.3
5762.01	0.23	0.65	P3	0.8	0.75	1.37	1.71	2.2
5774.01	1.32	1.9	P3	1.62	1.12	96.2	104.2	173
5790.01	3.69	-0.67	P4	0.71	0.75	3.71	6.27	4.8
5792.01	3.59	-0.07	P4	0.72	0.71	8.71	12.5	11.9
5797.01	3.62	1.37	P4	2.06	1.57	136.3	154.4	221
5868.01	2.8	2.71	P4	1.48	0.91	1.89	1.97	4.2
5885.01	3.42	4.03	P3	0.95	0.58	1.87	1.89	7.4
5889.01	0.77	1.42	P3	1.12	0.89	2.42	2.73	4.2
5895.01	2.34	3.41	P4	0.96	0.6	1.16	1.18	3.6
5941.01	1.07	5.28	P4	0.81	0.49	60.5	60.7	420
5961.01	0.87	1.45	P4	0.52	0.38	25.2	28.4	41.2
5993.01	1.25	3.06	P4	1.42	0.87	29.9	30.8	77.3
6104.01	1.84	4.01	P4	0.92	0.58	2.38	2.41	9.6
6104.02	1.84	4.01	P4	0.92	0.58	2.9	2.94	11.7
6109.01	0.60	1.3	P3	1.3	0.99	81.6	93.1	129
6109.02	0.60	1.3	P3	2.64	1.83	1.9	2.17	2.7
6111.01	2.14	4.4	P3	2.67	1.83	3.63	3.66	19.0
6120.01	3.85	2.48	P3	1.01	0.75	1.7	1.78	4.1
6120.02	3.85	2.48	P3	0.99	0.71	1.67	1.75	3.9

Continued on next page

Object	Sep. (")	Δm (mags)	Reference ^a	$R_{\star,target}^b$ (R_{\odot})	$R_{\star,secondary}^c$ (R_{\odot})	$R_{p,0}^d$ (R_{\oplus})	$R_{p,prim.}^e$ (R_{\oplus})	$R_{p,sec.}^f$ (R_{\oplus})
6132.01	1.23	0.9	P3	1.65	1.37	13.0	15.6	19.6
6132.02	1.23	0.9	P3	1.65	1.37	5.83	6.99	8.8
6132.03	1.23	0.9	P3	1.65	1.37	4.03	4.83	6.1
6224.02	2.97	4.19	P4	1.69	0.79	2.69	2.72	8.8
6256.01	3.05	2.27	P4	0.71	0.58	1.37	1.45	3.4
6258.01	2.17	4.14	P3	1.73	0.82	0.72	0.73	2.3
6297.01	2.56	1.55	P4	0.97	0.75	34.0	37.9	59.7
6297.01	2.96	5.89	P4	0.97	0.56	34.0	34.1	297
6311.01	1.75	0.83	P3	2.32	1.83	119.6	144.8	167
6329.01	1.22	1.43	P3	2.11	1.57	2.06	2.32	3.3
6384.01	3.53	2.09	P4	0.8	0.6	2.79	2.99	5.9
6390.01	2.82	1.57	P4	1.53	1.16	81.5	90.6	141
6415.01	1.75	1.17	P3	0.98	0.79	4.64	5.37	7.5
6464.02	0.75	1.72	P3	1.03	0.79	1.94	2.13	3.6
6464.03	0.75	1.72	P3	1.05	0.79	3.39	3.72	6.2
6464.01	0.75	1.72	P3	1.05	0.79	21.6	23.7	39.5
6475.01	1.31	0.5	P3	0.71	0.66	1.54	1.97	2.3
6482.01	0.52	0.58	P3	0.93	0.87	1.53	1.93	2.4
6483.01	1.41	2.78	P3	1.86	1.08	112.2	116.5	243
6527.01	2.21	1.6	P3	1.62	1.21	2.92	3.24	5.0
6539.01	1.58	3.89	P3	1.49	0.75	2.04	2.07	6.2
6600.01	2.36	5.28	P4	0.96	0.56	0.69	0.69	4.6
6602.01	0.77	0.54	P3	0.78	0.56	41.6	52.7	48.8
6605.01	2.53	3.46	P3	2.21	1.16	2.39	2.44	6.3
6654.01	1.41	2.88	P3	1.12	0.75	2.47	2.56	6.4
6706.01	1.04	1.44	P3	1.79	1.37	4.3	4.84	7.2
6745.01	3.07	3.78	P3	1.29	0.71	2.78	2.82	8.8
6745.01	2.85	3.92	P3	1.29	0.71	2.78	2.82	9.4
6783.01	3.25	3.31	P4	0.93	0.6	1.31	1.34	4.0
6793.01	2.84	4.47	P4	0.8	0.56	0.79	0.8	4.4
6800.01	2.62	5.1	P3	1.27	0.6	54.9	55.2	273
6800.01	3.11	5.41	P3	1.27	0.58	54.9	55.1	304
6907.01	3.35	-0.36	P4	0.71	0.75	1.14	1.76	1.6
6918.01	0.62	1.33	P4	0.76	0.6	6.17	7.02	10.3
6925.01	2.66	1.71	P3	0.53	0.38	0.94	1.03	1.7
7002.01	3.2	2.95	P4	0.94	0.66	1.3	1.34	3.7
7003.01	3.78	1.9	P4	1.59	1.1	1.35	1.46	2.4
7020.01	3.28	1.43	P3	1.47	1.16	72.8	81.9	125
7032.01	2.74	5.8	P4	0.94	0.56	0.61	0.61	5.3
7050.01	1.78	2.5	P4	1.05	0.75	0.76	0.8	1.8
7087.01	1.89	1.69	P4	1.75	1.28	88.6	97.5	154
7129.01	1.27	2.39	P4	1.08	0.75	1.74	1.83	3.8
7205.01	1.04	0.44	P3	1.43	1.37	39.8	51.4	60.6
7220.01	3.57	1.33	P4	0.95	0.75	0.97	1.1	1.6
7389.01	1.84	6.2	P4	7.91	0.75	11.0	11.0	18.1

Continued on next page

Object	Sep. (")	Δm (mags)	Reference ^a	$R_{\star,target}$ ^b (R_{\odot})	$R_{\star,secondary}$ ^c (R_{\odot})	$R_{p,0}$ ^d (R_{\oplus})	$R_{p,prim.}$ ^e (R_{\oplus})	$R_{p,sec.}$ ^f (R_{\oplus})
7408.01	1.67	2.65	P4	0.53	0.38	19.1	19.9	48.5
7426.01	2.45	2.37	P3	0.81	0.6	0.97	1.02	2.3
7448.01	0.87	1.4	P3	1.66	1.28	1.66	1.87	2.7
7455.01	1.86	2.39	P4	2.07	1.35	2.44	2.57	5.1
7470.01	1.52	0.17	P4	0.99	0.94	1.9	2.59	2.7
7501.01	1.15	1.36	P4	2.89	0.94	89.5	101.5	62.0
7527.01	2.75	4.41	P4	3.15	0.94	134.4	135.6	309
7539.01	2.97	3.03	P4	0.81	0.58	1.3	1.34	3.9
7540.01	3.67	5.64	P4	0.94	0.56	0.92	0.92	7.4
7546.01	2.93	5.92	P4	3.46	0.56	4.9	4.91	12.1
7572.01	2.97	6.14	P4	4.23	0.56	1.59	1.59	3.6

^aReference for nearby star detection: (P1, Law et al., 2014), (P2, Baranec et al., 2016), (P3, Ziegler et al., 2017a),(P4, Ziegler et al., 2017b).

^bPrimary stellar radius estimate from Mathur et al. (2017).

^cEstimated radius of secondary stellar companion in the scenario where it is bound to the primary star, using absolute magnitude difference in the *Kepler* band and the Dartmouth stellar models (Dotter et al., 2008).

^dOriginal planetary radius estimate, from NASA Exoplanet Archive.

^eEstimated eclipsing object radius in the scenario where it is physically bound to the target star, corrected for transit dilution caused by the presence of nearby stars.

^fEstimated eclipsing object radius in the scenario where it is bound to the companion star, correcting for transit dilution by nearby stars and using the stellar radius estimate of the companion in this table.

APPENDIX E: CHARACTERIZATION OF MULTI-BAND IMAGED KOI SYSTEMS

In this appendix, we present the results of multi-band photometry of KOIs with nearby stars and characterize the stars within each systems, as described in Section 6.2.1.

Table E.1: Characterization of KOIs and nearby stars

KOI	Sep. (")	Est. Prim. ^a SpT	Prim. Dist. (pc)	Est. Sec. ^a SpT	Sec. Dist. (pc)	$\sigma_{unassoc}$	$\Delta m_g^{\prime b}$	$\Delta m_r^{\prime c}$	$\Delta m_i^{\prime c}$	$\Delta m_z^{\prime c}$	Δm_J^d	Δm_H^d	Δm_K^d
1	1.13	G2	202^{+34}_{-41}	K7	275^{+63}_{-41}	1.62	3.98 ± 0.04	3.77 ± 0.03	3.59 ± 0.03	2.8 ± 0.1	2.5 ± 0.1	2.36 ± 0.01^f	
4	3.42	F3	349^{+59}_{-71}	F5	1999^{+393}_{-344}	7.61	4.71 ± 0.01	4.61 ± 0.03	4.43 ± 0.02	4.23 ± 0.01			
13	1.16	B8	786^{+132}_{-159}	A4	414^{+90}_{-65}	3.33	0.24 ± 0.01	0.29 ± 0.05		0.18 ± 0.03			0.14 ± 0.01^f
42	1.74	F9	95^{+16}_{-19}	K2	137^{+30}_{-22}	1.92	2.86 ± 0.03	2.68 ± 0.02	2.54 ± 0.02	2.21 ± 0.03			1.87 ± 0.01^f
70	3.86	G6	272^{+46}_{-55}	K7	1086^{+171}_{-217}	6.68	5.75 ± 0.04	5.2 ± 0.04	4.54 ± 0.12	4.44 ± 0.02			4.14 ± 0.03^f
75	3.47	G0	162^{+27}_{-33}	G2	3224^{+577}_{-594}	9.94	6.92 ± 0.23	6.62 ± 0.12	6.58 ± 0.24	6.65 ± 0.1			6.51 ± 0.04^f
97	1.9	F5	573^{+96}_{-116}	F5	3712^{+726}_{-642}	7.95	4.36 ± 0.03	4.27 ± 0.05	4.26 ± 0.07				
155	4.01	G1	516^{+87}_{-104}	K4	1227^{+155}_{-271}	4.61	4.33 ± 0.05	4.38 ± 0.17	4.04 ± 0.19	3.76 ± 0.19			
163	1.22	G8	361^{+61}_{-73}	G8	414^{+84}_{-70}	0.74		0.55 ± 0.02	0.49 ± 0.02	0.43 ± 0.09			
191	1.69	G3	904^{+152}_{-183}	F6	3828^{+726}_{-677}	6.73		2.78 ± 0.07	2.81 ± 0.03	2.68 ± 0.19	2.58 ± 0.06^g	2.61 ± 0.05^g	2.62 ± 0.06^g
200	2.81	G0	795^{+134}_{-161}	K7	1494^{+116}_{-380}	3.54	4.66 ± 0.37	4.98 ± 0.72	4.63 ± 0.27		3.43 ± 0.03		
229	1.66	G2	884^{+149}_{-179}	F0	3467^{+647}_{-621}	6.47		1.62 ± 0.11	1.59 ± 0.1		1.5 ± 0.01		
255	3.41	K7	273^{+46}_{-55}	G6	2603^{+241}_{-635}	9.53		2.23 ± 0.07	2.5 ± 0.17	2.62 ± 0.17	2.81 ± 0.04		3.66 ± 0.01^f
268	1.81	F5	236^{+40}_{-48}	K7	273^{+58}_{-44}	0.78		4.81 ± 0.03	4.11 ± 0.01	3.75 ± 0.01	3.05 ± 0.06^g	2.65 ± 0.06^g	2.55 ± 0.13^g
268	2.5	F5	236^{+40}_{-48}	M1	365^{+10}_{-119}	2.36		6.51 ± 0.07	5.59 ± 0.06	4.96 ± 0.07	3.81 ± 0.12^g	3.35 ± 0.13^g	3.98 ± 0.13^g
387	0.98	K3	231^{+39}_{-47}	G5	2086^{+389}_{-374}	8.74		3.31 ± 0.09	3.17 ± 0.1	3.35 ± 0.1			4.05 ± 0.04
401	1.99	G6	488^{+82}_{-99}	K7	552^{+116}_{-90}	0.67		3.43 ± 0.02	2.95 ± 0.02	2.62 ± 0.02	2.06 ± 0.06^g		1.63 ± 0.06^g
454	1.49	G8	624^{+105}_{-126}	F6	2863^{+567}_{-490}	6.95		2.06 ± 0.01	2.11 ± 0.01	2.18 ± 0.02			
472	1.12	G2	1026^{+173}_{-208}	F3	2629^{+496}_{-467}	4.77		0.87 ± 0.01	0.91 ± 0.03	1.01 ± 0.41			
506	1.13	G1	909^{+153}_{-184}	K1	2099^{+407}_{-365}	4.29		3.63 ± 0.07	3.3 ± 0.05	3.14 ± 0.05			
510	2.45	G5	679^{+114}_{-137}	K7	733^{+149}_{-123}	0.41	3.61 ± 0.01	2.97 ± 0.03	2.41 ± 0.01	2.21 ± 0.19	1.84 ± 0.01		
511	1.28	G1	723^{+122}_{-146}	K7	769^{+167}_{-121}	0.33		3.53 ± 0.04	3.16 ± 0.04	3.01 ± 0.28	2.22 ± 0.06^g	1.81 ± 0.01^g	1.7 ± 0.01^g
598	3.17	G8	626^{+105}_{-127}	G5	2796^{+486}_{-525}	6.98	3.05 ± 0.03	2.99 ± 0.06	2.86 ± 0.03	2.6 ± 0.06	2.79 ± 0.02		
628	1.83	G1	629^{+106}_{-127}	F2	6419^{+621}_{-1549}	9.64		3.75 ± 0.05	3.49 ± 0.02	3.24 ± 0.03			3.87 ± 0.06^g
641	2.09	K5	170^{+29}_{-34}	M1	157^{+44}_{-18}	0.41	2.23 ± 0.03	2.01 ± 0.03	1.72 ± 0.13	1.59 ± 0.11	1.04 ± 0.01		
641	3.65	K5	170^{+29}_{-34}	M0	99^{+33}_{-8}	2.75	0.85 ± 0.03	0.55 ± 0.04	0.28 ± 0.11	0.14 ± 0.06	-0.32 ± 0.01		
652	1.23	K0	310^{+52}_{-63}	K7	352^{+70}_{-60}	0.69		2.03 ± 0.01	1.46 ± 0.01	1.26 ± 0.01	1.28 ± 0.17		0.9 ± 0.43
688	1.71	F4	972^{+164}_{-197}	F8	1484^{+348}_{-217}	2.21		1.96 ± 0.01	1.84 ± 0.01	1.94 ± 0.03	1.55 ± 0.06^g		1.37 ± 0.06^g
757	2.94	K0	893^{+150}_{-181}	G5	6741^{+673}_{-1612}	8.94	3.81 ± 0.05	3.68 ± 0.09	3.38 ± 0.07	3.29 ± 0.14	3.82 ± 0.1		
799	1.23 ^h	G2	1036^{+174}_{-210}	G0	2182^{+430}_{-375}	3.85		1.97 ± 0.03	1.89 ± 0.04	1.78 ± 0.16	1.65 ± 0.02^h	1.55 ± 0.02^h	1.54 ± 0.01^h
799	0.82 ^h	G2	1036^{+174}_{-210}	M2	924^{+182}_{-159}	0.62					3.07 ± 0.02^h	2.63 ± 0.02^h	2.43 ± 0.01^h
799	1.63 ^h	G2	1036^{+174}_{-210}	K2	3011^{+627}_{-494}	5.25				3.67 ± 0.04^h	3.37 ± 0.07^h	3.27 ± 0.03^h	
801	3.67	G2	922^{+155}_{-186}	G8	1895^{+377}_{-323}	3.74	2.78 ± 0.07	2.97 ± 0.06	2.75 ± 0.02	2.7 ± 0.08	2.35 ± 0.02		
840	3.2	K0	596^{+100}_{-121}	B8	15397^{+4786}_{-1434}	9.19	1.75 ± 0.18	2.01 ± 0.04	1.85 ± 0.02		2.81 ± 0.02		
840	2.97	K0	596^{+100}_{-121}	F1	8229^{+1413}_{-1558}	9.56	3.11 ± 0.18	3.19 ± 0.32	2.58 ± 0.08		3.54 ± 0.02		

Continued on next page

KOI	Sep.	Est. Prim. ^a	Prim. Dist.	Est. Sec. ^a	Sec. Dist.	$\sigma_{unassoc}$	$\Delta m_{g'}^b$	$\Delta m_{r'}^c$	Δm_i^c	Δm_z^c	Δm_J^d	Δm_H^d	Δm_K^d	
	(")	SpT	(pc)	SpT	(pc)									
	984	1.8	G6	191 ⁺³² ₋₃₉	K4	99 ⁺¹⁶ ₋₁₉	3.48	-0.05±0.01	-0.01±0.01	0.04±0.02			0.15±0.01 ^f	
	1112	2.95	G0	874 ⁺¹⁴⁷ ₋₁₇₇	K7	1367 ⁺³⁵⁷ ₋₁₇₄	2.31		4.47±0.16		3.6±0.14 ^g	2.95±0.08 ^g	2.75±0.07 ^g	
	1150	0.39	G2	491 ⁺⁸³ ₋₉₉	G0	1223 ⁺²⁴⁸ ₋₂₀₅	4.61		2.11±0.04	2.08±0.04	2.05±0.03			
	1151	0.75	G4	449 ⁺⁷⁵ ₋₉₁	K7	741 ⁺¹⁶³ ₋₁₁₆	2.63		3.99±0.05	3.28±0.03	3.29±0.16		2.55±0.06 ^g	
	1193	3.08	G5	998 ⁺¹⁶⁸ ₋₂₀₂	K3	1641 ⁺³³⁶ ₋₂₇₄	2.63	3.82±0.02	3.17±0.06	2.95±0.03	2.56±0.09	2.31±0.02	2.4±0.06 ^g	
	1274	1.1	G8	335 ⁺⁵⁶ ₋₆₈	K7	593 ⁺¹¹⁴ ₋₁₀₄	3.02		4.09±0.38	3.76±0.1	3.53±0.09	2.8±0.06 ^g	2.5±0.06 ^g	
	1359	1.43	G1	1103 ⁺¹⁸⁶ ₋₂₂₃	K5	1650 ⁺⁶⁰⁵ ₋₉₀	1.98		3.81±0.04	3.61±0.11	3.42±0.11		2.16±0.06 ^g	
	1546	2.93	G2	774 ⁺¹³⁰ ₋₁₅₆	G6	2572 ⁺⁶⁶⁸ ₋₃₃₀	5.6	4.17±0.09	3.64±0.07	3.5±0.05	3.27±0.3	3.22±0.06 ^g	3.02±0.07 ^g	
	1573	3.84	G0	778 ⁺¹³¹ ₋₁₅₇	G9	3352 ⁺⁸³⁴ ₋₄₅₆	6.52	4.84±0.09	4.91±0.09	4.82±0.1	4.69±0.49	4.1±0.06		
	1593	3.24	G2	1361 ⁺²²⁹ ₋₂₇₅	K1	1378 ⁺¹⁷⁶ ₋₃₀₃	0.07	2.0±0.05	2.16±0.05	1.82±0.07		1.17±0.02		
	1599	2.98	G2	880 ⁺¹⁴⁸ ₋₁₇₈	G0	2179 ⁺⁴⁵⁰ ₋₃₆₀	4.58	2.65±0.01	2.51±0.03	2.34±0.02	2.24±0.07	1.95±0.03		
	1599	3.42	G2	880 ⁺¹⁴⁸ ₋₁₇₈	F0	6303 ⁺⁸³⁸ ₋₁₃₆₃	8.59	2.71±0.01	2.85±0.06	2.74±0.05	2.72±0.03	2.79±0.03		
	1619	2.1	K2	118 ⁺²⁰ ₋₂₄	M1	163 ⁺²³ ₋₃₄	1.77		3.58±0.01	2.84±0.04	2.48±0.04	2.06±0.13	2.06±0.01 ^f	
	1630	1.63 ^h	G4	991 ⁺¹⁶⁷ ₋₂₀₀	K1	928 ⁺¹⁹¹ ₋₁₅₄	0.35		1.29±0.02	1.18±0.02	1.09±0.06	0.70±0.01 ^h	0.58±0.02 ^h	0.56±0.01 ^h
	1656	0.96 ^h	G1	1003 ⁺¹⁶⁹ ₋₂₀₃	F2	3322 ⁺⁷⁵⁸ ₋₄₉₉	5.70		1.67±0.03	1.82±0.02	2.01±0.21	1.72±0.02 ^h	1.50±0.01 ^h	1.46±0.01 ^h
	1729	3.83	G9	761 ⁺¹²⁸ ₋₁₅₄	K3	2394 ⁺⁵⁰⁸ ₋₃₈₆	5.55	4.42±0.13	3.99±0.16	3.67±0.23	3.47±0.18	3.31±0.05		
	1781	3.64	K2	141 ⁺²⁴ ₋₂₉	M3	111 ⁺¹⁹ ₋₂₁	1.31		4.98±0.07	3.77±0.05		2.58±0.1	2.43±0.04	2.32±0.01 ^f
	1792	1.99	G8	188 ⁺³² ₋₃₈	F4	655 ⁺¹⁵⁸ ₋₉₃	5.84		0.97±0.04	1.08±0.04	1.19±0.04	1.36±0.01		1.4±0.02
	1845	3.04	K0	406 ⁺⁶⁸ ₋₈₂	F8	4966 ⁺¹⁷⁷⁸ ₋₃₀₀	8.18		4.47±0.03	4.75±0.07	4.68±0.13	4.26±0.07 ^g	4.83±0.04	4.4±0.09 ^g
	1845	3.04	K0	406 ⁺⁶⁸ ₋₈₂	F8	4966 ⁺¹⁷⁷⁸ ₋₃₀₀	8.18		4.47±0.03	4.75±0.07	4.68±0.13	4.26±0.07 ^g	4.83±0.04	4.4±0.09 ^g
	1853	0.96	G1	545 ⁺⁹² ₋₁₁₀	A2	2485 ⁺⁴³⁴ ₋₄₆₅	7.05		0.56±0.01	0.66±0.01	0.94±0.15			
	1908	1.29	K4	338 ⁺⁵⁷ ₋₆₈	M1	861 ⁺⁸² ₋₂₀₉	5.04		4.3±0.23	3.95±0.05	3.45±0.05		2.85±0.04	3.22±0.01 ^f
	1943	1.35 ^h	G0	525 ⁺⁸⁸ ₋₁₀₆	F8	1000 ⁺²¹³ ₋₁₆₁	3.34		1.63±0.03	1.54±0.05	1.46±0.05	1.18±0.02 ^h	1.11±0.02 ^h	1.10±0.01 ^h
	1995	2.96	G5	969 ⁺¹⁶³ ₋₁₉₆	B8	83457 ⁺¹⁸²³⁹ ₋₁₃₁₀₁	10.41	5.02±0.21	5.28±0.2	5.33±0.28	5.58±0.32	5.95±0.49		
	2032	1.19	G2	298 ⁺⁵⁰ ₋₆₀	F2	613 ⁺¹⁰⁵ ₋₁₁₆	3.8		0.3±0.04	0.32±0.05	0.36±0.05		0.38±0.03	0.41±0.01
	2059	0.38	K2	185 ⁺³¹ ₋₃₇	K7	172 ⁺¹⁵ ₋₄₂	0.4		1.22±0.08	1.07±0.06	0.91±0.04		0.1±0.04	0.53±0.15 ^g
	2093	2.08	F5	1752 ⁺²⁹⁵ ₋₃₅₄	F7	5105 ⁺¹⁹⁴⁷ ₋₂₂₆	4.75	4.6±0.4	3.38±0.02	3.27±0.02	3.14±0.12			
	2098	2.88	G1	634 ⁺¹⁰⁷ ₋₁₂₈	K4	653 ⁺¹⁴⁰ ₋₁₀₄	0.16	3.01±0.02	2.7±0.01	2.48±0.01	2.24±0.02	1.56±0.01		
	2098	3.24	G1	634 ⁺¹⁰⁷ ₋₁₂₈	G2	1796 ⁺¹⁹⁷ ₋₄₁₇	5.48	2.49±0.02	2.58±0.05	2.41±0.04	2.38±0.04	2.3±0.01		
	2100	2.98	G0	834 ⁺¹⁴⁰ ₋₁₆₉	K5	736 ⁺²³² ₋₆₆	0.65	3.36±0.11	2.8±0.07	2.3±0.05	2.28±0.12	1.44±0.01		
	2105	3.01	F9	657 ⁺¹¹¹ ₋₁₃₃	K0	3892 ⁺³⁷⁶ ₋₉₃₉	8.3	5.52±0.24	5.69±0.14	5.1±0.11		4.99±0.15		
	2156	3.35	M0	290 ⁺⁴⁹ ₋₅₉	G3	4722 ⁺⁹⁶⁴ ₋₇₈₉	9.53		2.3±0.05	2.79±0.09	3.12±0.11	3.61±0.07		3.94±0.01 ^f
	2159	2.0	G1	529 ⁺⁸⁹ ₋₁₀₇	M0	624 ⁺¹⁷⁵ ₋₇₁	0.86		5.08±0.11	4.26±0.18		3.48±0.02	2.63±0.06 ^g	2.47±0.06 ^g
	2169	3.59	G8	223 ⁺³⁷ ₋₄₅	M2	283 ⁺⁵⁶ ₋₄₈	1.29		5.43±0.03	4.34±0.04	3.8±0.02	3.17±0.01	2.93±0.03	2.78±0.01 ^f
	2206	3.28	G4	1026 ⁺¹⁷³ ₋₂₀₇	G7	1418 ⁺²⁸⁸ ₋₂₃₈	1.73	1.66±0.06	1.55±0.07	1.38±0.07		1.22±0.01		
	2213	3.94	G9	728 ⁺¹²² ₋₁₄₇	G7	1721 ⁺³¹⁷ ₋₃₁₁	4.42	1.49±0.01	1.91±0.08	1.84±0.08		1.79±0.03	1.71±0.1	
	2295	2.19	G8	151 ⁺²⁵ ₋₃₁	K3	175 ⁺²³ ₋₃₈	0.83		1.05±0.01	1.05±0.04	1.02±0.02	0.7±0.12		0.92±0.01 ^f

Continued on next page

KOI	Sep. (")	Est. Prim. ^a SpT	Prim. Dist. (pc)	Est. Sec. ^a SpT	Sec. Dist. (pc)	$\sigma_{unassoc}$	$\Delta m_{g'}^b$	$\Delta m_{r'}^c$	Δm_i^c	$\Delta m_{z'}^c$	Δm_J^d	Δm_H^d	Δm_K^d
2298	1.57	K2	309^{+52}_{-62}	K7	430^{+94}_{-67}	1.75		2.29 ± 0.01	2.02 ± 0.01	1.89 ± 0.01			1.3 ± 0.02
2380	4.01	G2	695^{+117}_{-140}	A9	4352^{+889}_{-726}	7.81	2.35 ± 0.06	2.49 ± 0.13	2.52 ± 0.16	2.58 ± 0.13			
2443	1.39	F9	712^{+120}_{-144}	K7	1741^{+336}_{-304}	4.55		5.61 ± 0.11	5.01 ± 0.08	4.66 ± 0.08	4.13 ± 0.07^g		3.63 ± 0.06^g
2535	1.73	K1	512^{+86}_{-104}	M1	771^{+2}_{-236}	2.42		3.46 ± 0.04	2.83 ± 0.05	2.13 ± 0.11	2.51 ± 0.01		
2542	0.88	M2	151^{+25}_{-30}	M4	120^{+37}_{-12}	1.16		1.64 ± 0.06	1.49 ± 0.03	1.21 ± 0.07	0.89 ± 0.06^g		0.6 ± 0.05^g
2547	2.79	G0	700^{+118}_{-141}	K3	2118^{+443}_{-347}	5.41		4.98 ± 0.04	4.62 ± 0.09	4.33 ± 0.22	3.93 ± 0.03		
2598	0.99 ^h	G0	733^{+123}_{-148}	F7	999^{+259}_{-129}	1.62		0.72 ± 0.02	0.77 ± 0.03	0.97 ± 0.08			0.25 ± 0.01^h
2807	3.93	F5	916^{+154}_{-185}	G5	1091^{+177}_{-214}	0.96	2.16 ± 0.01	2.06 ± 0.02	1.99 ± 0.02	1.83 ± 0.05	1.57 ± 0.04	1.31 ± 0.05	1.32 ± 0.06
2856	2.31	G2	1191^{+200}_{-241}	G6	4750^{+765}_{-935}	6.65	3.98 ± 0.02	4.01 ± 0.3	3.7 ± 0.15		3.5 ± 0.05		
2862	0.68	K7	382^{+64}_{-77}	M0	310^{+60}_{-54}	1.13		0.34 ± 0.06	0.26 ± 0.03	0.24 ± 0.09			0.00 ± 0.06
2880	3.39	G8	1020^{+172}_{-206}	K5	1017^{+190}_{-182}	0.01	2.0 ± 0.09	1.8 ± 0.13	1.6 ± 0.14	1.47 ± 0.23	0.75 ± 0.01		0.64 ± 0.1
2910	3.15	K0	662^{+111}_{-134}	A5	4137^{+971}_{-603}	7.64	0.51 ± 0.01	0.6 ± 0.02	0.75 ± 0.03	0.98 ± 0.05	1.17 ± 0.01		
2914	3.8	F4	492^{+83}_{-100}	G2	3887^{+704}_{-711}	8.5		5.92 ± 0.02	5.74 ± 0.06	5.62 ± 0.19	5.52 ± 0.04		
2927	1.39	G2	1479^{+249}_{-299}	K4	1894^{+435}_{-283}	1.31		3.29 ± 0.08	2.93 ± 0.16	2.49 ± 0.08			
2949	2.36	G1	499^{+84}_{-101}	G2	3010^{+632}_{-490}	7.68	4.4 ± 0.12	4.38 ± 0.03	4.15 ± 0.07	3.98 ± 0.12	4.29 ± 0.02		3.86 ± 0.1
2976	2.02	G7	1063^{+179}_{-215}	G6	3991^{+748}_{-712}	6.32	3.37 ± 0.15	3.17 ± 0.16	2.61 ± 0.07		2.82 ± 0.05		
3002	0.84	G2	474^{+80}_{-96}	A7	3092^{+463}_{-632}	8.24		2.07 ± 0.02	2.01 ± 0.04	2.35 ± 0.37			
3066	3.41	G8	967^{+163}_{-196}	K5	1430^{+231}_{-281}	2.12	2.85 ± 0.03	2.83 ± 0.09	2.56 ± 0.06		1.82 ± 0.03		
3069	1.93	G3	866^{+146}_{-175}	K2	1006^{+207}_{-167}	0.81		2.51 ± 0.04	2.31 ± 0.02	2.04 ± 0.03	1.57 ± 0.06^g	1.31 ± 0.06^g	1.26 ± 0.06^g
3073	1.3	G7	589^{+99}_{-119}	G2	1695^{+256}_{-345}	5.4		1.85 ± 0.01	1.69 ± 0.02	1.63 ± 0.05	1.75 ± 0.01		
3120	1.09 ^h	G1	1013^{+170}_{-205}	F5	2104^{+337}_{-415}	3.87		1.14 ± 0.09	0.75 ± 0.08		0.83 ± 0.03^h	0.79 ± 0.02^h	0.80 ± 0.01^h
3136	1.79 ^h	K1	751^{+126}_{-152}	K5	1523^{+383}_{-205}	3.57		3.05 ± 0.13	2.88 ± 0.06		2.34 ± 0.03^h	2.21 ± 0.04^h	2.02 ± 0.03^h
3158	2.1	K2	31^{+5}_{-6}	M0	54^{+9}_{-10}	3.04		3.41 ± 0.09	2.9 ± 0.04	2.38 ± 0.06	2.44 ± 0.04		2.23 ± 0.06
3190	2.68	G5	240^{+40}_{-49}	K2	1309^{+660}_{-53}	5.33		6.31 ± 0.09	6.15 ± 0.23	5.94 ± 0.23	5.43 ± 0.04		3.96 ± 0.03
3277	2.45	F5	590^{+99}_{-119}	F9	4528^{+869}_{-794}	8.37	5.72 ± 0.09	5.61 ± 0.18	5.49 ± 0.13	5.31 ± 0.22			
3277	3.41	F5	590^{+99}_{-119}	G6	2371^{+471}_{-405}	6.51	5.21 ± 0.09	4.82 ± 0.11	4.96 ± 0.04	4.24 ± 0.05	4.21 ± 0.03		
3288	3.17	G5	601^{+101}_{-122}	K3	2030^{+408}_{-344}	5.87	4.72 ± 0.04	4.49 ± 0.06	4.51 ± 0.05		3.78 ± 0.04		
3288	3.5	G5	601^{+101}_{-122}	K0	3340^{+176}_{-907}	8.39	4.04 ± 0.04	4.84 ± 0.03	4.65 ± 0.04				
3309	3.71	G8	561^{+94}_{-113}	G6	2228^{+460}_{-369}	6.44	2.98 ± 0.04	3.05 ± 0.05	2.89 ± 0.06		2.9 ± 0.01		2.82 ± 0.01^f
3324	3.84	G5	1287^{+216}_{-260}	F8	5517^{+1526}_{-645}	6.39	3.23 ± 0.01	3.04 ± 0.04	3.24 ± 0.07		2.69 ± 0.04		
3341	3.23	G0	980^{+165}_{-198}	K4	2602^{+622}_{-371}	4.78	5.46 ± 0.71	5.02 ± 0.2	4.72 ± 0.1	4.41 ± 0.23	3.73 ± 0.07		
3418	1.13	G2	1200^{+202}_{-243}	A5	7522^{+1521}_{-1266}	7.83		1.75 ± 0.05	1.94 ± 0.05				
3439	3.42	F2	1272^{+214}_{-257}	G3	3250^{+612}_{-578}	4.76	4.38 ± 0.02	4.22 ± 0.08	3.94 ± 0.05	3.77 ± 0.18	3.44 ± 0.1		
3459	3.35	G1	1106^{+186}_{-224}	F2	5344^{+1219}_{-804}	6.97	2.54 ± 0.02	2.4 ± 0.14	2.39 ± 0.3		2.26 ± 0.02		
3468	1.49	G0	667^{+112}_{-135}	A9	5077^{+1057}_{-833}	8.25		3.24 ± 0.05	3.22 ± 0.03	3.18 ± 0.04			
3497	0.78	K4	181^{+30}_{-37}	M0	224^{+46}_{-37}	1.14		1.86 ± 0.02	1.68 ± 0.01	1.45 ± 0.01			1.31 ± 0.47
3791	3.5	F5	824^{+139}_{-167}	F5	1844^{+376}_{-308}	4.13	2.16 ± 0.03	2.02 ± 0.02	1.94 ± 0.02	1.9 ± 0.01	1.78 ± 0.01		

Continued on next page

KOI	Sep. (")	Est. Prim. ^a SpT	Prim. Dist. (pc)	Est. Sec. ^a SpT	Sec. Dist. (pc)	$\sigma_{unassoc}$	$\Delta m_{g'}^b$	$\Delta m_{r'}^c$	Δm_i^c	Δm_z^c	Δm_J^d	Δm_H^d	Δm_K^d
3856	2.54	G1	450^{+76}_{-91}	A2	6267^{+1058}_{-1199}	9.6	3.31 ± 0.1	3.32 ± 0.02	3.27 ± 0.02	3.31 ± 0.04	3.42 ± 0.01		
3928	2.96	F5	672^{+113}_{-136}	F6	958^{+179}_{-171}	1.91	1.4 ± 0.06	1.41 ± 0.03	1.33 ± 0.03	1.3 ± 0.03	1.09 ± 0.01		
4004	1.93	G4	334^{+56}_{-68}	M1	391^{+108}_{-45}	0.81		4.84 ± 0.03	3.81 ± 0.03	3.33 ± 0.01	3.42 ± 0.01		2.37 ± 0.08^g
4053	4.11	G0	405^{+68}_{-82}	K2	2768^{+413}_{-568}	8.36	6.16 ± 0.01	6.25 ± 0.21	6.03 ± 0.18	5.72 ± 0.19			
4166	3.54	G5	947^{+159}_{-192}	K5	1636^{+321}_{-282}	2.89	4.3 ± 0.05	4.12 ± 0.58	3.77 ± 0.61		2.67 ± 0.02		
4343	0.85 ^h	G1	573^{+96}_{-116}	F3	1737^{+378}_{-274}	5.39		1.45 ± 0.03	1.48 ± 0.01	1.56 ± 0.02	1.43 ± 0.02^h	1.47 ± 0.03^h	1.43 ± 0.01^h
4343	3.68	G1	573^{+96}_{-116}	G2	6585^{+776}_{-1493}	9.69	5.84 ± 0.02	5.57 ± 0.13	5.1 ± 0.14	5.21 ± 0.34	5.34 ± 0.2		
4366	2.46	G6	991^{+167}_{-201}	G8	4128^{+756}_{-749}	6.7	3.51 ± 0.08	3.64 ± 0.08	3.59 ± 0.06	3.5 ± 0.31			
4407	2.54	F9	209^{+35}_{-42}	K4	271^{+62}_{-40}	1.36		3.18 ± 0.02	2.91 ± 0.02	2.73 ± 0.01	2.28 ± 0.49^g	1.95 ± 0.71^g	1.89 ± 0.34^g
4443	3.41	F3	1077^{+181}_{-218}	K5	1548^{+423}_{-184}	1.87	5.96 ± 0.1	4.87 ± 0.07	4.91 ± 0.06	3.96 ± 0.11	3.53 ± 0.02		
4463	2.45	G8	651^{+110}_{-132}	K5	441^{+40}_{-108}	2.16		0.03 ± 0.03	0.15 ± 0.01	0.27 ± 0.04	0.16 ± 0.1^g	0.24 ± 0.08^g	0.25 ± 0.07^g
4495	3.06	G1	1178^{+198}_{-238}	K1	3168^{+738}_{-466}	4.85	4.45 ± 0.15	4.23 ± 0.16	4.07 ± 0.17	3.83 ± 0.43	3.38 ± 0.03		
4495	3.41	G1	1178^{+198}_{-238}	F8	3415^{+1097}_{-293}	4.9	2.89 ± 0.15	2.85 ± 0.05	2.79 ± 0.08	2.68 ± 0.07	2.17 ± 0.03		
4582	2.71	G3	232^{+39}_{-47}	F5	5347^{+893}_{-1030}	10.18		5.92 ± 0.09	5.87 ± 0.09	5.79 ± 0.14			6.09 ± 0.03^f
4582	3.55	G3	232^{+39}_{-47}	F0	2131^{+374}_{-398}	8.85	2.52 ± 0.04	2.81 ± 0.13	2.93 ± 0.16	3.0 ± 0.19	3.09 ± 0.01		3.4 ± 0.01^f
4630	3.94	G2	883^{+149}_{-179}	F3	3539^{+737}_{-581}	6.46	2.33 ± 0.08	2.24 ± 0.04	2.13 ± 0.13		2.06 ± 0.13		
4655	3.17	G2	1191^{+200}_{-241}	M1	853^{+57}_{-302}	1.69	3.45 ± 0.16		3.53 ± 0.58		2.3 ± 0.03		
4661	3.93	K0	515^{+87}_{-104}	K7	586^{+66}_{-135}	0.72	3.26 ± 0.02	2.79 ± 0.09	2.59 ± 0.04	2.21 ± 0.1	1.54 ± 0.07	1.36 ± 0.06	1.41 ± 0.08
4699	4.01	F4	621^{+105}_{-126}	K1	3208^{+414}_{-702}	7.68	6.85 ± 0.06	6.33 ± 0.12	5.95 ± 0.14	5.47 ± 0.16	5.54 ± 0.09		
4713	1.72	G5	530^{+89}_{-107}	F3	1023^{+186}_{-187}	3.46		0.32 ± 0.02	0.28 ± 0.01	0.24 ± 0.03	0.03 ± 0.01		
4750	2.09	G2	1367^{+230}_{-276}	A9	8147^{+1898}_{-1197}	7.53	2.33 ± 0.06	2.5 ± 0.02	2.67 ± 0.04		2.34 ± 0.02		
4759	0.64 ^h	G1	993^{+167}_{-201}	K1	1762^{+470}_{-217}	2.91		2.34 ± 0.23^i	2.27 ± 0.18^i		2.65 ± 0.08^h	2.37 ± 0.07^h	2.17 ± 0.06^h
4759	0.71 ^h	G1	993^{+167}_{-201}	K3	1921^{+424}_{-281}	3.34		2.34 ± 0.23^i	2.27 ± 0.18^i		2.75 ± 0.10^h	2.53 ± 0.08^h	2.34 ± 0.09^h
4823	1.4	G9	246^{+41}_{-50}	G8	297^{+51}_{-57}	1.02		0.7 ± 0.01	0.58 ± 0.01	0.59 ± 0.01			
4881	3.42	F7	644^{+108}_{-130}	A2	6420^{+1814}_{-723}	8.32	3.69 ± 0.05	3.31 ± 0.1	3.06 ± 0.06	2.86 ± 0.11	2.73 ± 0.01		
5101	1.24	F4	681^{+115}_{-138}	A1	6479^{+1308}_{-1092}	8.74		3.07 ± 0.06	3.27 ± 0.05				
5640	0.53	G9	157^{+26}_{-32}	K7	241^{+45}_{-43}	2.31		3.1 ± 0.03	2.58 ± 0.02	2.33 ± 0.04			
5665	2.11	F9	227^{+38}_{-46}	K1	394^{+150}_{-18}	2.66		3.29 ± 0.01	3.06 ± 0.01	2.92 ± 0.01	3.23 ± 0.01		2.27 ± 0.02
5790	3.69	K1	682^{+115}_{-138}	F8	948^{+340}_{-57}	1.64	-0.96 ± 0.02	-0.6 ± 0.07	-0.52 ± 0.09	0.52 ± 0.15	-0.52 ± 0.02	-0.41 ± 0.06	-0.35 ± 0.07
5885	3.42	G5	865^{+146}_{-175}	A3	21222^{+3990}_{-3779}	10.07	4.0 ± 0.03	4.0 ± 0.05	3.94 ± 0.05	4.1 ± 0.11	4.46 ± 0.12		
6104	1.84	G2	825^{+139}_{-167}	K7	1037^{+418}_{-30}	1.12		4.49 ± 0.03	4.46 ± 0.03	3.28 ± 0.12			
6111	2.14	F4	669^{+113}_{-135}	B8	13444^{+3749}_{-1549}	9.21	3.33 ± 0.2	3.56 ± 0.02	3.91 ± 0.09	3.93 ± 0.2			
6120	3.85	G2	1176^{+198}_{-238}	G7	2386^{+428}_{-439}	3.71	2.84 ± 0.02	2.71 ± 0.09	2.48 ± 0.06		2.1 ± 0.21		
6132	1.23	G0	846^{+142}_{-171}	G1	1250^{+285}_{-188}	2.06		1.54 ± 0.05	1.47 ± 0.04	1.18 ± 0.06			
6256	3.05	K1	691^{+116}_{-140}	F0	5951^{+1644}_{-696}	8.1	1.63 ± 0.03	1.55 ± 0.11	1.66 ± 0.25		2.15 ± 0.02		
6329	1.19 ^h	F4	993^{+167}_{-201}	F7	1492^{+281}_{-265}	2.18		2.06 ± 0.07	1.97 ± 0.06		1.48 ± 0.02^h	1.37 ± 0.02^h	1.35 ± 0.01^h
6384	3.53	G2	1453^{+245}_{-294}	F0	7628^{+613}_{-1926}	8.02	2.07 ± 0.03	2.05 ± 0.1	1.94 ± 0.08	1.77 ± 0.13	2.11 ± 0.03		

Continued on next page

KOI	Sep. (")	Est. Prim. ^a SpT	Prim. Dist. (pc)	Est. Sec. ^a SpT	Sec. Dist. (pc)	$\sigma_{unassoc}$	$\Delta m_{g'}^b$	$\Delta m_{r'}^c$	$\Delta m_{i'}^c$	$\Delta m_{z'}^c$	Δm_J^d	Δm_H^d	Δm_K^d
6475	1.31	K7	147^{+25}_{-30}	K5	218^{+42}_{-38}	2.09		0.42 ± 0.05	0.51 ± 0.05	0.62 ± 0.05			
6600	2.36	G1	158^{+27}_{-32}	M2	193^{+51}_{-24}	1.03		5.91 ± 0.08	5.19 ± 0.04	4.45 ± 0.06	3.6 ± 0.03		3.05 ± 0.03
6783	3.25	G2	1230^{+207}_{-249}	G2	5058^{+924}_{-920}	6.66	3.94 ± 0.15	3.52 ± 0.23	3.21 ± 0.11		3.1 ± 0.07		
6793	2.84	G7	659^{+111}_{-133}	B8	39018^{+6303}_{-7663}	10.8	4.09 ± 0.03	3.55 ± 0.16	3.23 ± 0.13	3.49 ± 0.24	4.72 ± 0.11		
7129	1.18^h	G1	611^{+103}_{-124}	K2	867^{+147}_{-166}	1.90		2.84 ± 0.01	2.48 ± 0.01	2.19 ± 0.03	1.92 ± 0.01^h	1.78 ± 0.02^h	1.72 ± 0.01^h
7205	0.89^h	G2	647^{+109}_{-131}	F5	1070^{+227}_{-173}	2.65		0.46 ± 0.02	0.47 ± 0.05	0.59 ± 0.02			0.45 ± 0.02^h
7546	2.93	A6	965^{+162}_{-195}	F2	9286^{+1410}_{-1886}	9.11		6.54 ± 0.06	6.12 ± 0.09	5.96 ± 0.14	5.81 ± 0.08		
7572	2.97	A3	408^{+69}_{-82}	K1	615^{+177}_{-67}	2.1		5.46 ± 0.01	5.16 ± 0.01	5.0 ± 0.03	4.27 ± 0.01		

^aMethodology described in Section 6.2.1.

^bFrom PANSTARRs (Chambers et al., 2016).

^cFrom observations at Robo-AO KP described in Section 6.1.

^dFrom UKIRT (Lawrence et al., 2007) unless noted.

^eFrom California *Kepler* Survey (Johnson et al., 2017).

^fFrom Kraus et al. (2016).

^gFrom Atkinson et al. (2017).

^hFrom Keck NIRC-2 observations, as described in Section 6.1.

ⁱBlended Robo-AO photometry of close binary resolved with Keck-AO, not used in stellar characterization.

APPENDIX F: CUTOUTS OF KOIS WITH NEARBY STARS OBSERVED WITH ROBO-AO

In this appendix, we provide cutouts of KOIs with nearby stars detected with Robo-AO, as described in Chapter 4.

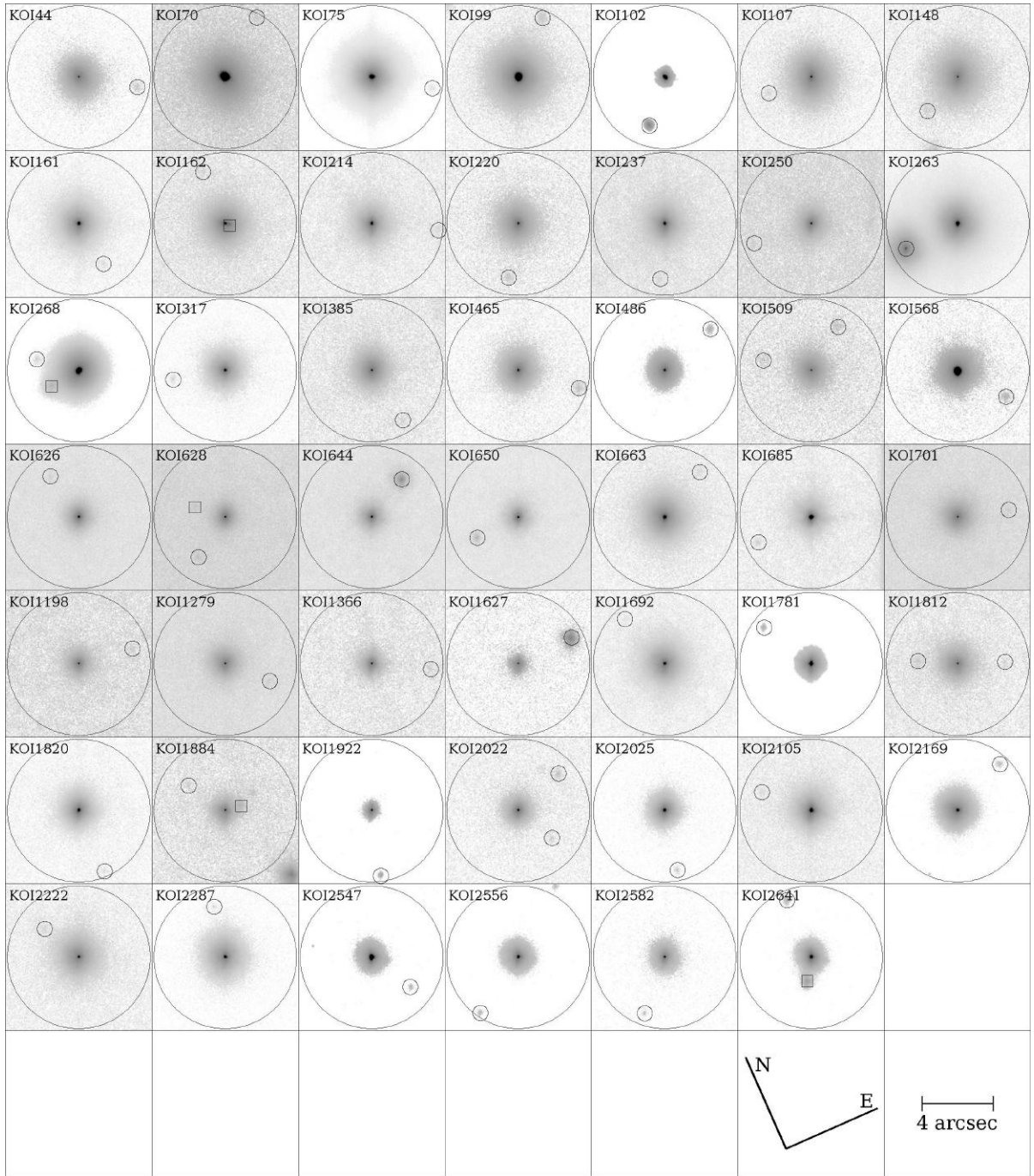


Figure F.1: Color inverted, normalized log-scale cutouts of 48 multiple KOI systems with separations outside 2.5" and within 4" resolved with Robo-AO at Palomar from the Law et al. (2014) target list. The angular scale and orientation are similar for each cutout. The smaller circles are centered on the detected nearby star, and the larger circle is the limit of the survey's 4" separation range. Squares are centered on companions with separations less than 2.5" found in Law et al. (2014) from Robo-AO at Palomar.

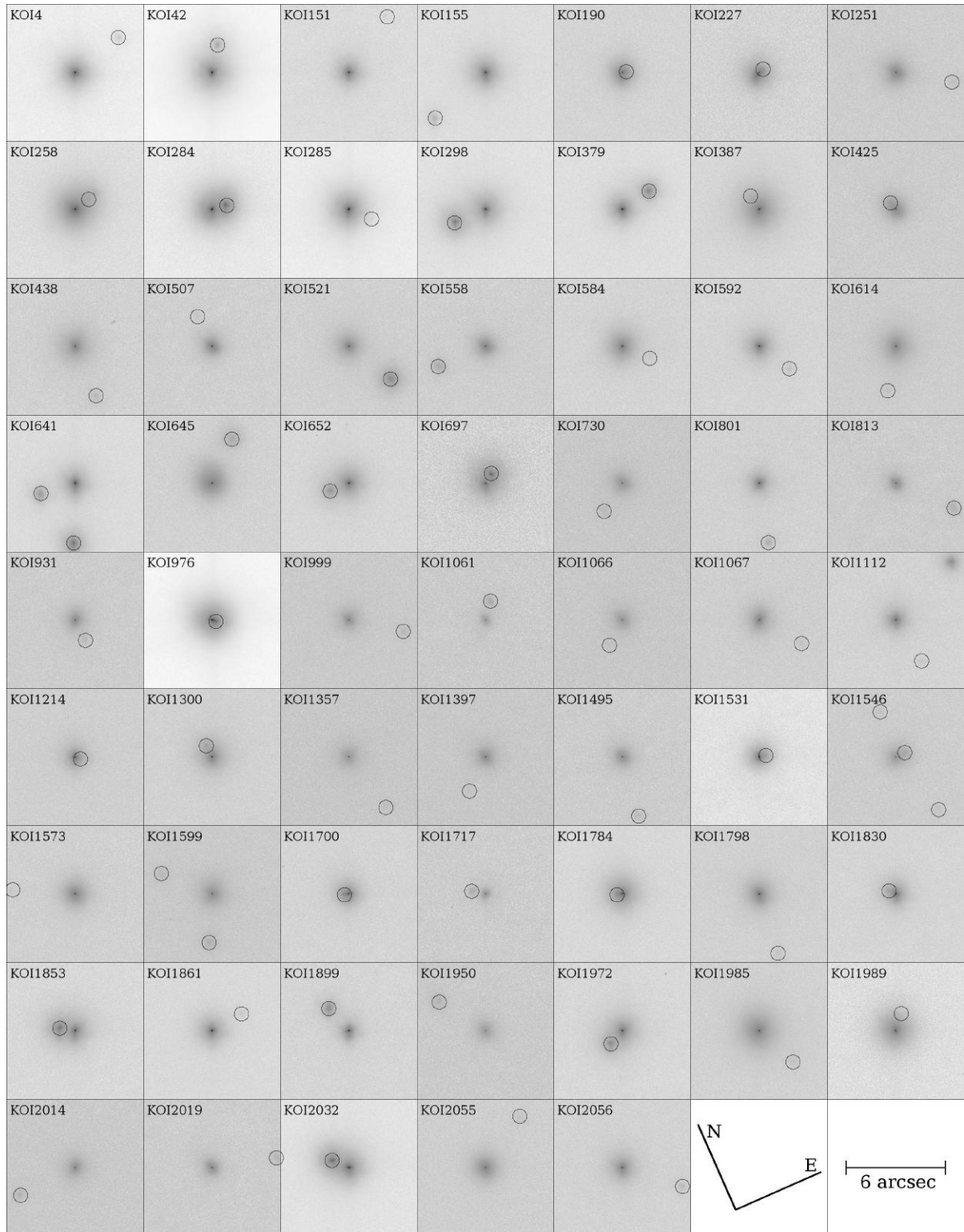


Figure F.2: Color inverted, normalized log-scale cutouts of 61 multiple KOI systems [KOI-4 to KOI-2056] with separations $<4''$ resolved with Robo-AO from Baranec et al. (2016). The angular scale and orientation is similar for each cutout. The smaller circles are centered on the detected nearby star.

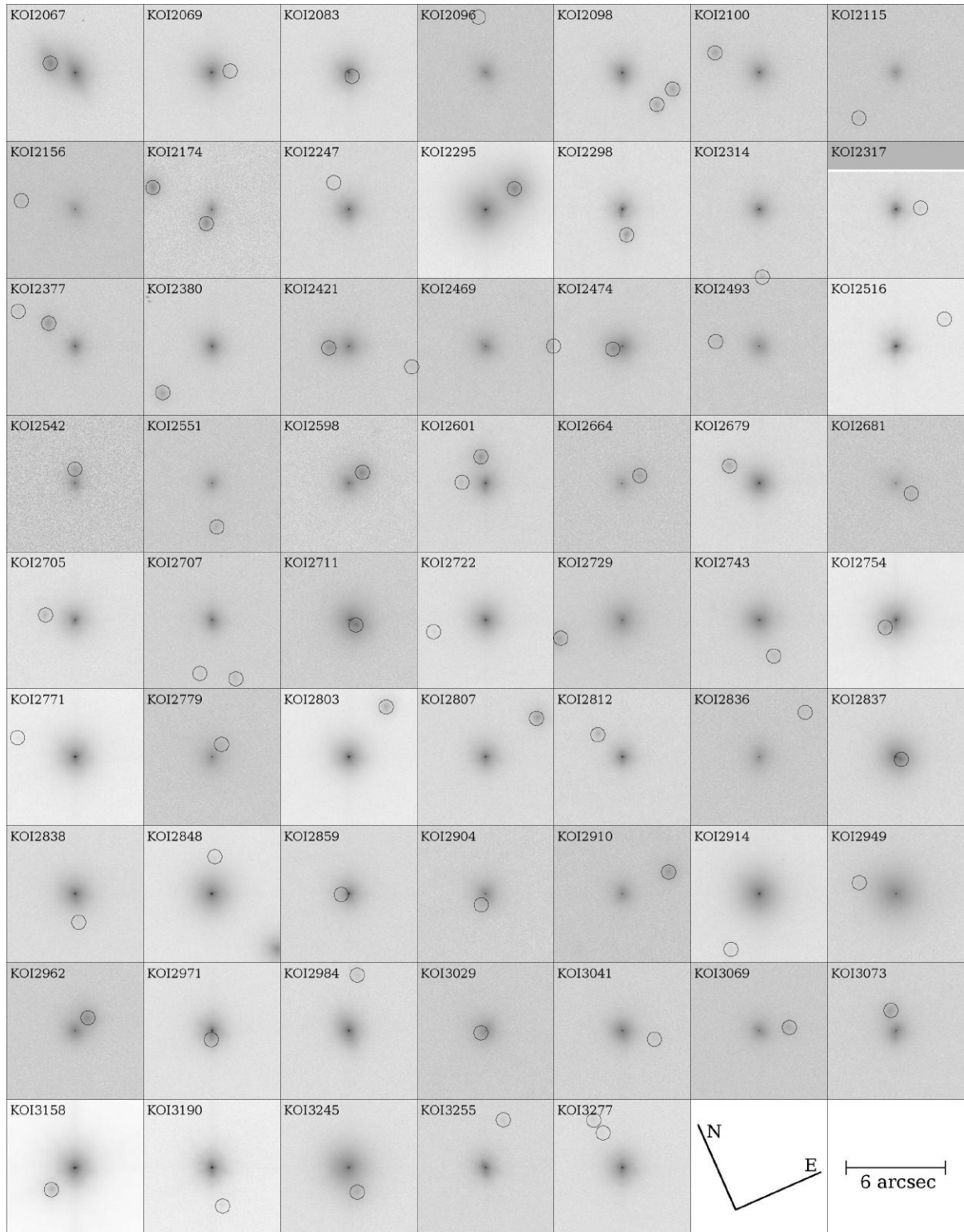


Figure F.3: Color inverted, normalized log-scale cutouts of 61 multiple KOI systems [KOI-2067 to KOI-3277] with separations $<4''$ resolved with Robo-AO from Baranec et al. (2016). The angular scale and orientation is similar for each cutout. The smaller circles are centered on the detected nearby star.

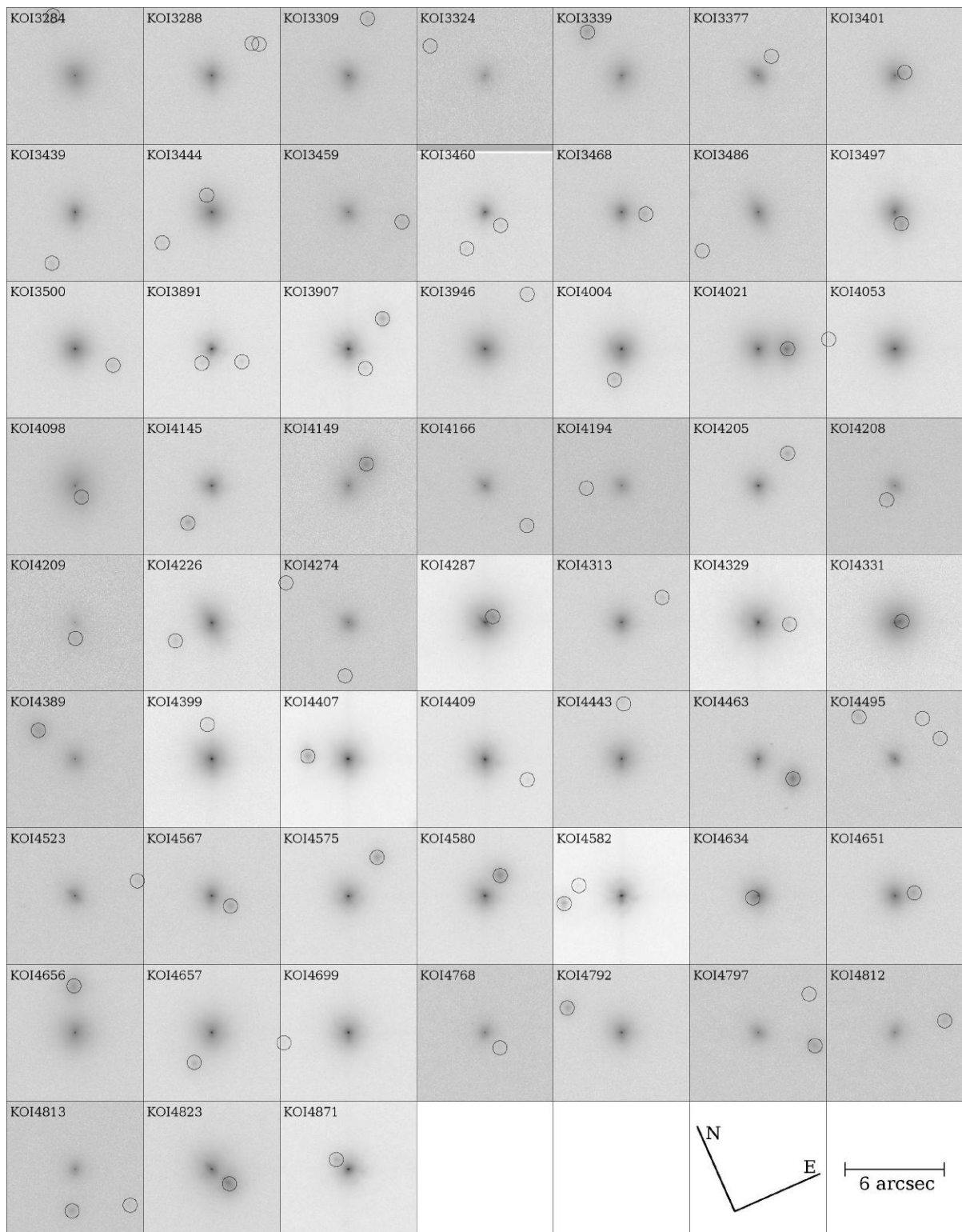


Figure F.4: Color inverted, normalized log-scale cutouts of 59 multiple KOI systems [KOI-3284 to KOI-4871] with separations $<4''$ resolved with Robo-AO from Baranec et al. (2016). The angular scale and orientation is similar for each cutout. The smaller circles are centered on the detected nearby star.

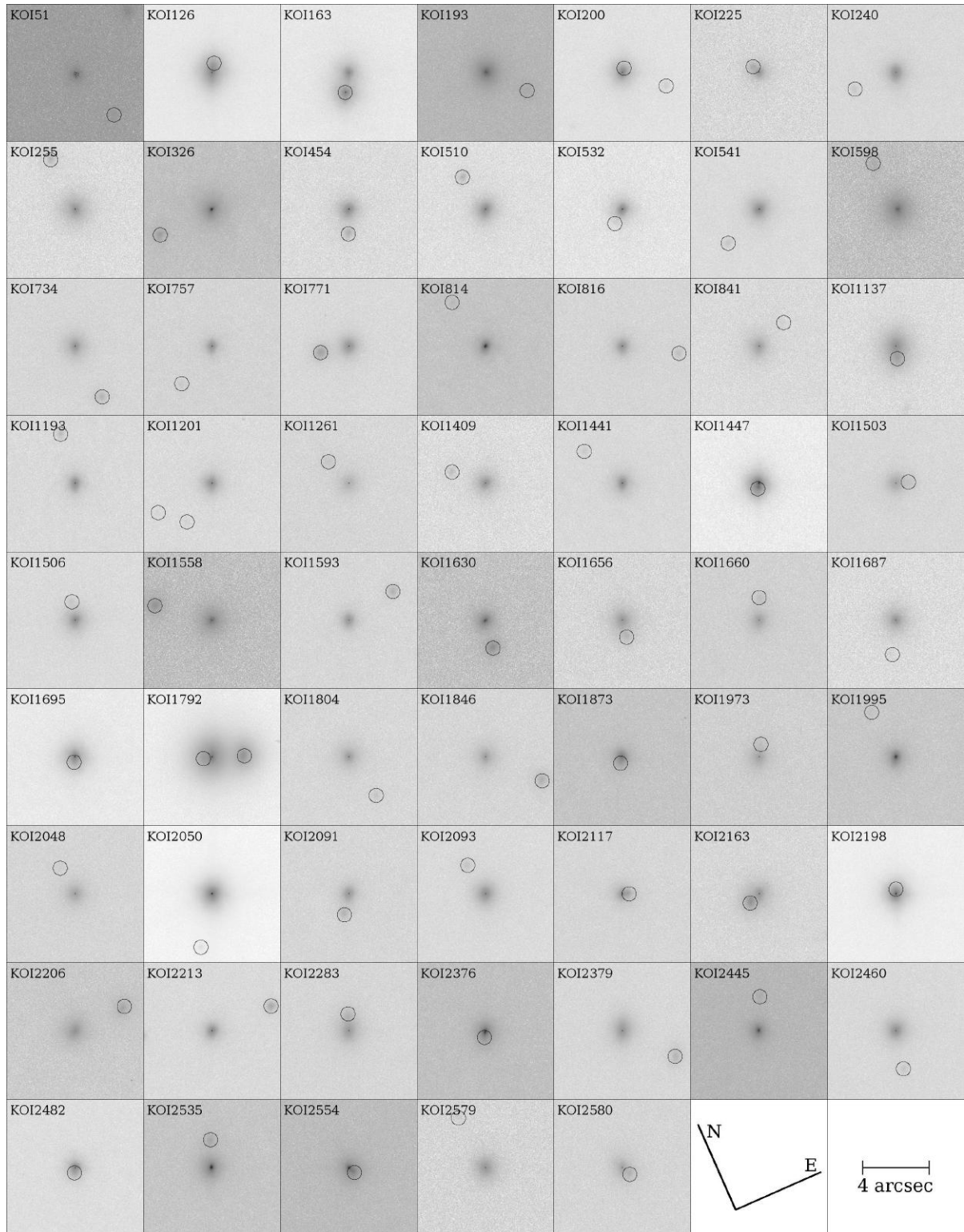


Figure F.5: Color inverted, normalized log-scale cutouts of 61 multiple KOI systems [KOI-51 to KOI-2688] with separations $<4''$ resolved with Robo-AO in Ziegler et al. (2017a). The angular scale and orientation is similar for each cutout. The smaller circles are centered on the detected nearby star, and the larger circle is the limit of the survey's 4'' separation range.

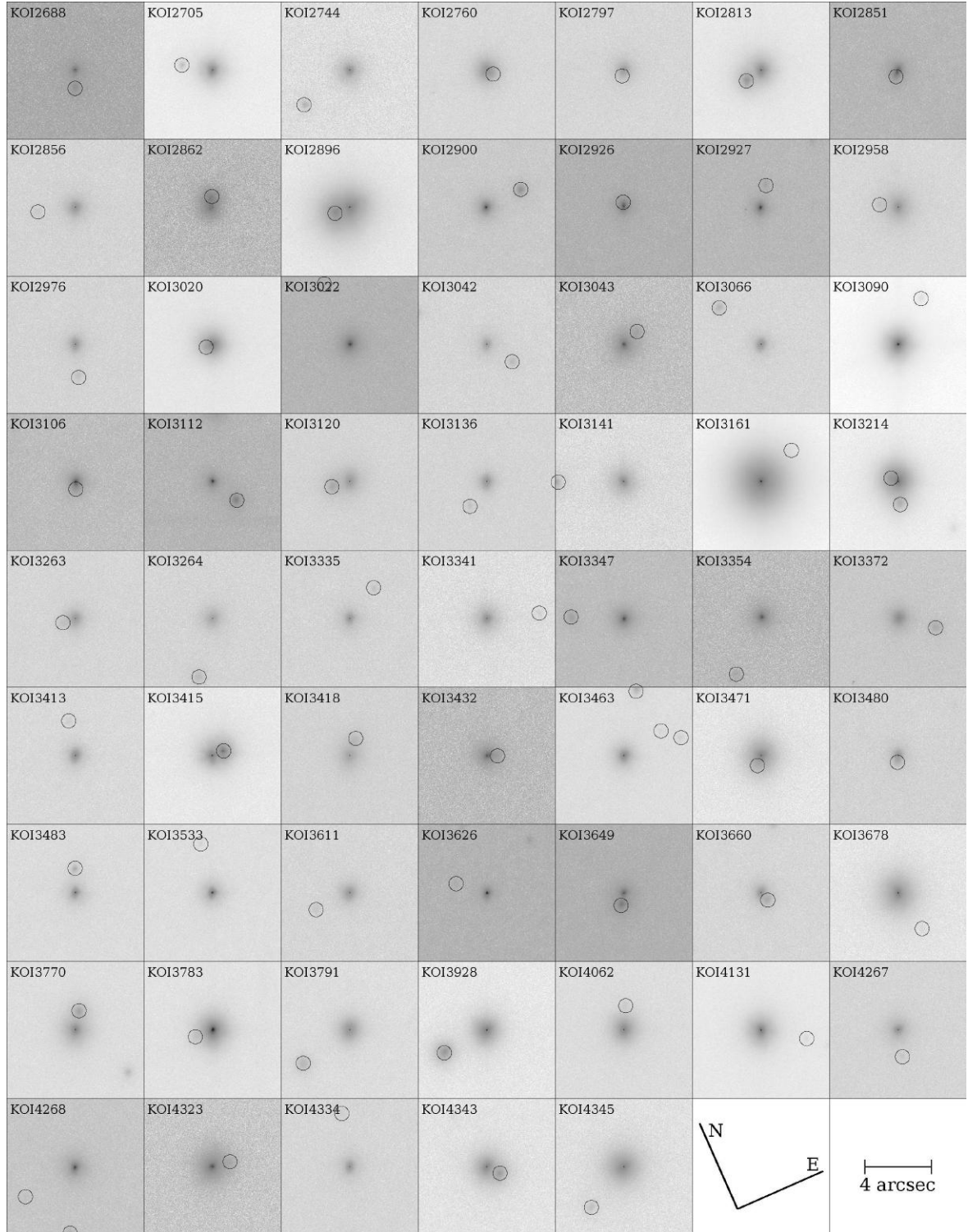


Figure F.6: Color inverted, normalized log-scale cutouts of 61 multiple KOI systems [KOI-2744 to KOI-4405] with separations $< 4''$ resolved with Robo-AO in Ziegler et al. (2017a). The angular scale and orientation is similar for each cutout. The smaller circles are centered on the detected nearby star, and the larger circle is the limit of the survey's $4''$ separation range.

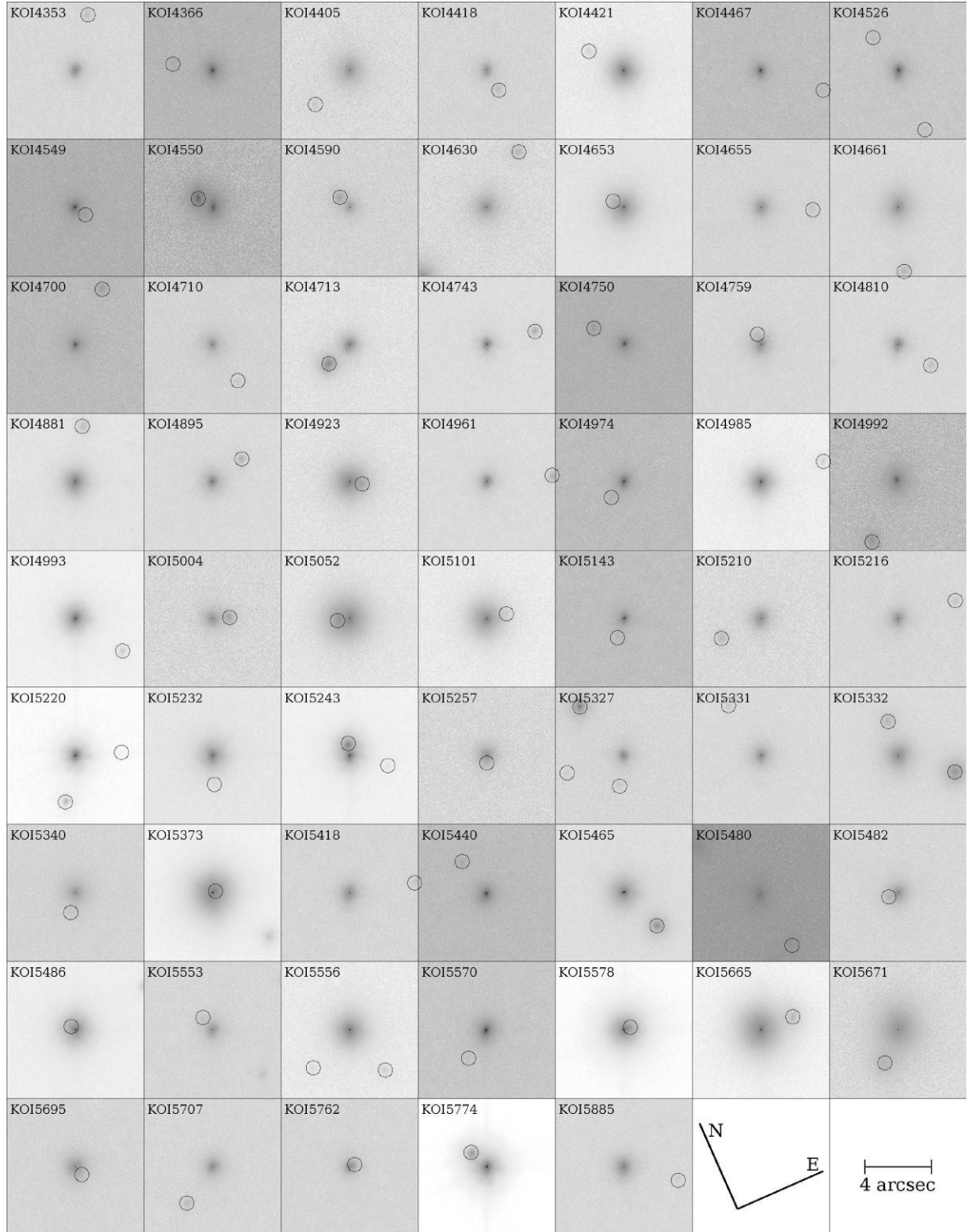


Figure F.7: Color inverted, normalized log-scale cutouts of 61 multiple KOI systems [KOI-4418 to KOI-6311] with separations $<4''$ resolved with Robo-AO in Ziegler et al. (2017a). The angular scale and orientation is similar for each cutout. The smaller circles are centered on the detected nearby star, and the larger circle is the limit of the survey's $4''$ separation range.

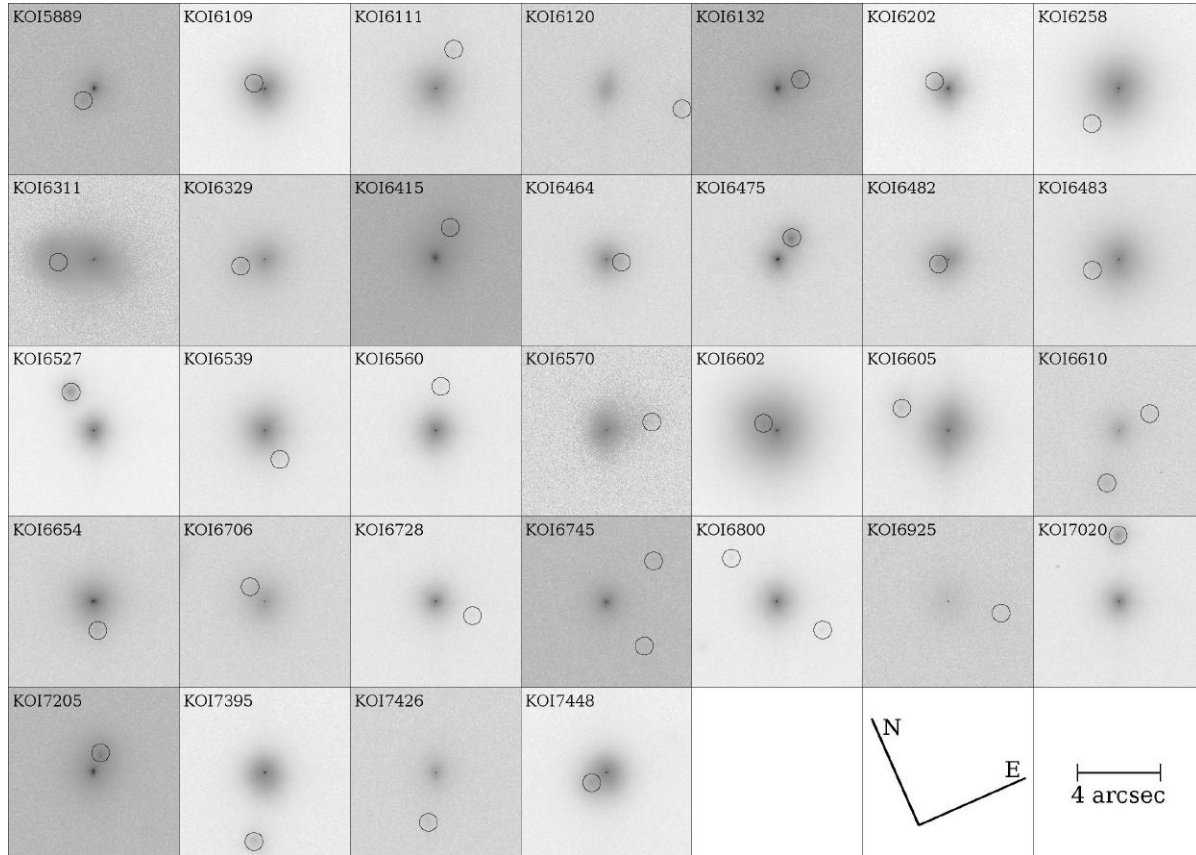


Figure F.8: Color inverted, normalized log-scale cutouts of 23 multiple KOI systems [KOI-6329 to KOI-7448] with separations $<4''$ resolved with Robo-AO in Ziegler et al. (2017a). The angular scale and orientation is similar for each cutout. The smaller circles are centered on the detected nearby star, and the larger circle is the limit of the survey's $4''$ separation range.

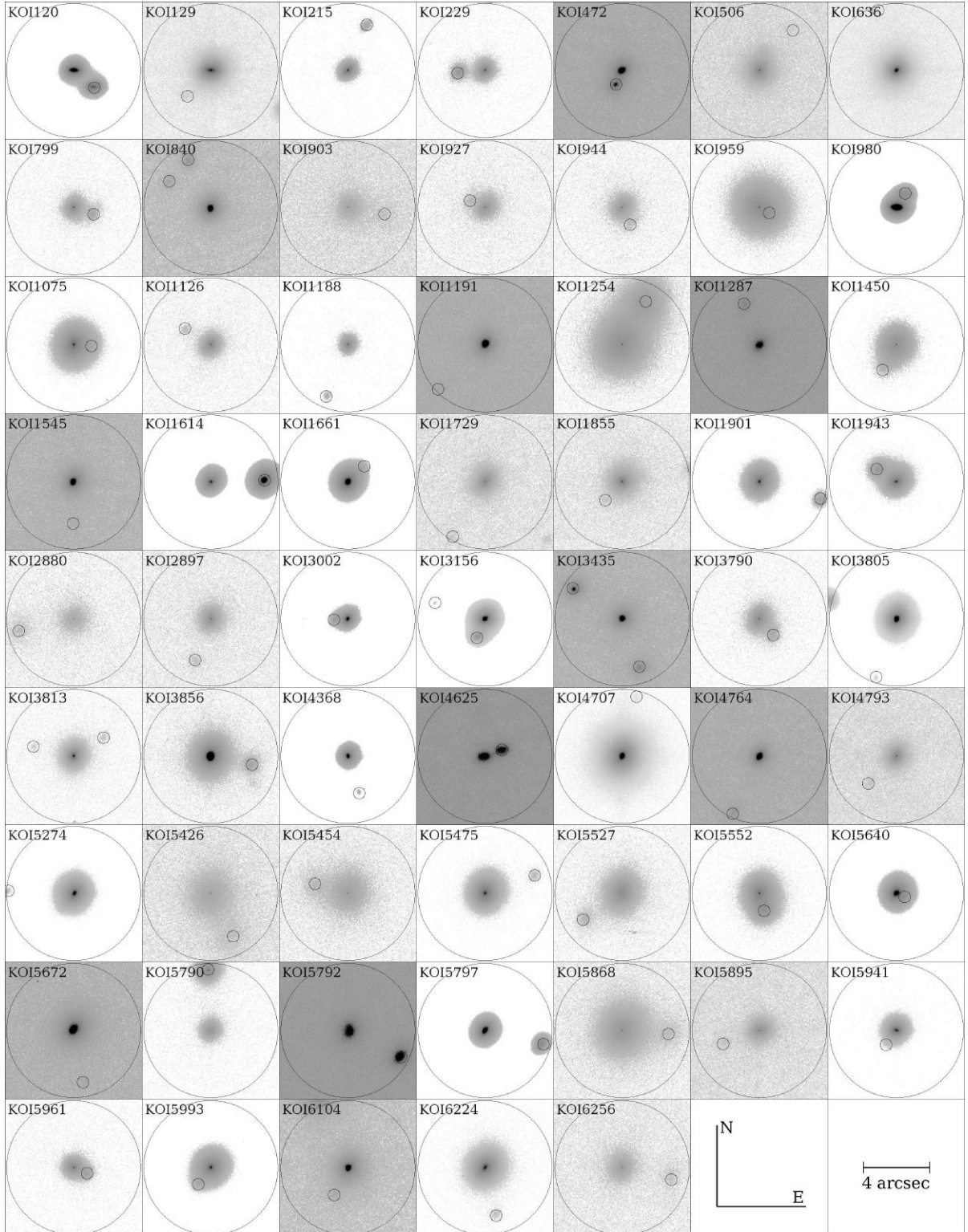


Figure F.9: Color inverted, normalized log-scale cutouts of 61 multiple KOI systems [KOI-120 to KOI-6256] resolved with Robo-AO from Kitt Peak (Ziegler et al., 2017b). The angular scale and orientation are similar for each cutout. The smaller circles are centered on the detected nearby star, and the larger circle is the limit of the survey's 4'' separation range.

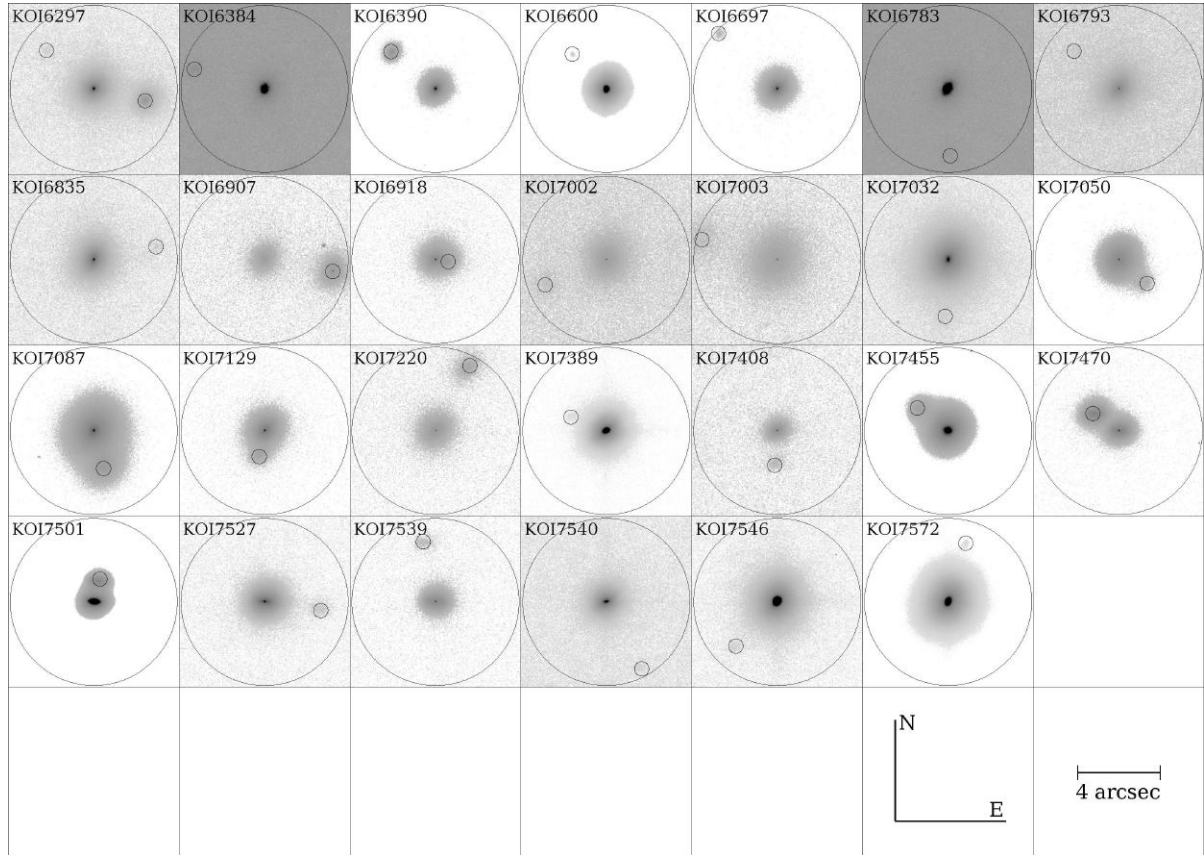


Figure F.10: Color inverted, normalized log-scale cutouts of 27 multiple KOI systems [KOI-6297 to KOI-7572] resolved with Robo-AO from Kitt Peak (Ziegler et al., 2017b). The angular scale and orientation are similar for each cutout. The smaller circles are centered on the detected nearby star, and the larger circle is the limit of the survey's 4" separation range.

BIBLIOGRAPHY

- Aarseth, S. J., & Hills, J. G. 1972, A&A, 21, 255
- Abadi, M. G., Navarro, J. F., & Steinmetz, M. 2006, MNRAS, 365, 747
- Abdul-Masih, M., Prša, A., Conroy, K., et al. 2016, AJ, 151, 101
- Abell, G. O. 1959, Leaflet of the Astronomical Society of the Pacific, 8, 121
- Abt, H. A. 2008, AJ, 135, 722
- Abt, H. A., & Willmarth, D. W. 1987, ApJ, 318, 786
- Adams, E. R., Ciardi, D. R., Dupree, A. K., et al. 2012, AJ, 144, 42
- Adams, E. R., Dupree, A. K., Kulesa, C., & McCarthy, D. 2013, AJ, 146, 9
- Adams, E. R., Jackson, B., Endl, M., et al. 2017, AJ, 153, 82
- Adams, W. S. 1915, ApJ, 42, doi:10.1086/142197
- Angerhausen, D., DeLarme, E., & Morse, J. A. 2015, PASP, 127, 1113
- Anglada-Escudé, G., Amado, P. J., Barnes, J., et al. 2016, Nature, 536, 437
- Atkinson, D., Baranec, C., Ziegler, C., et al. 2017, AJ, 153, 25
- Auvergne, M., Bodin, P., Boisnard, L., et al. 2009, A&A, 506, 411
- Bakos, G. Á., Noyes, R. W., Kovács, G., et al. 2007, ApJ, 656, 552
- Baranec, C., Ziegler, C., Law, N. M., et al. 2016, AJ, 152, 18
- Baranec, C., Riddle, R., Law, N. M., et al. 2013, Journal of Visualized Experiments, 72, e50021
- . 2014a, ApJL, 790, L8
- Baranec, C., Riddle, R., Law, N. M., et al. 2014b, in Proc. SPIE Conf. Ser., Vol. 9148, Adaptive Optics Systems IV, 914812
- Barge, P., Baglin, A., Auvergne, M., & CoRoT Team. 2008, in IAU Symposium, Vol. 249, Exoplanets: Detection, Formation and Dynamics, ed. Y.-S. Sun, S. Ferraz-Mello, & J.-L. Zhou, 3–16
- Basu, S., & Vorobyov, E. I. 2012, ApJ, 750, 30
- Batalha, N. M., Borucki, W. J., Koch, D. G., et al. 2010, ApJL, 713, L109
- Batalha, N. M., Rowe, J. F., Bryson, S. T., et al. 2013, ApJS, 204, 24

- Batten, A. H. 1973, Binary and multiple systems of stars
- Batygin, K. 2012, Nature, 491, 418
- Benedict, G. F., McArthur, B. E., Forveille, T., et al. 2002, ApJL, 581, L115
- Bond, I. A., Udalski, A., Jaroszyński, M., et al. 2004, ApJL, 606, L155
- Bordé, P. J., & Traub, W. A. 2006, ApJ, 638, 488
- Borucki, W. J., Koch, D. G., Brown, T. M., et al. 2010, ApJL, 713, L126
- Borucki, W. J., Koch, D. G., Basri, G., et al. 2011a, ApJ, 728, 117
- . 2011b, ApJ, 736, 19
- . 2011c, ApJ, 736, 19
- Borucki, W. J., Agol, E., Fressin, F., et al. 2013, Science, 340, 587
- Bourke, T. L., Myers, P. C., Evans, II, N. J., et al. 2006, ApJL, 649, L37
- Bovy, J., Rix, H.-W., & Hogg, D. W. 2012, ApJ, 751, 131
- Bowler, B. P. 2016, PASP, 128, 102001
- Brown, T. M. 2003, ApJL, 593, L125
- Bryson, S. T., Tenenbaum, P., Jenkins, J. M., et al. 2010, ApJL, 713, L97
- Burgasser, A. J., Kirkpatrick, J. D., Reid, I. N., et al. 2003, ApJ, 586, 512
- Burke, C. J., Bryson, S. T., Mullally, F., et al. 2014, ApJS, 210, 19
- Burke, C. J., Christiansen, J. L., Mullally, F., et al. 2015, ApJ, 809, 8
- Caldwell, D. A., van Cleve, J. E., Jenkins, J. M., et al. 2010, in Proc. SPIE Conf. Ser., Vol. 7731, Space Telescopes and Instrumentation 2010: Optical, Infrared, and Millimeter Wave, 773117
- Cardelli, J. A., Clayton, G. C., & Mathis, J. S. 1989, ApJ, 345, 245
- Carney, B. W., Laird, J. B., Latham, D. W., & Kurucz, R. L. 1987, AJ, 94, 1066
- Carney, B. W., Latham, D. W., Laird, J. B., & Aguilar, L. A. 1994, AJ, 107, 2240
- Chabrier, G., Baraffe, I., Allard, F., & Hauschildt, P. 2000, ApJ, 542, 464
- Chabrier, G., Baraffe, I., Leconte, J., Gallardo, J., & Barman, T. 2009, in American Institute of Physics Conference Series, Vol. 1094, 15th Cambridge Workshop on Cool Stars, Stellar Systems, and the Sun, ed. E. Stempels, 102–111
- Chambers, K. C., Magnier, E. A., Metcalfe, N., et al. 2016, ArXiv e-prints, arXiv:1612.05560

- Chanamé, J., & Gould, A. 2004, *ApJ*, 601, 289
- Charbonneau, D., Brown, T. M., Latham, D. W., & Mayor, M. 2000, *ApJL*, 529, L45
- Chauvin, G., Lagrange, A.-M., Dumas, C., et al. 2004, *A&A*, 425, L29
- Chew, T. Y., Clare, R. M., & Lane, R. G. 2006, *Optics Communications*, 268, 189
- Chiba, M., & Beers, T. C. 2000, *AJ*, 119, 2843
- Christiansen, J. L., Jenkins, J. M., Caldwell, D. A., et al. 2012, *PASP*, 124, 1279
- Chwolson, O. 1924, *Astronomische Nachrichten*, 221, 329
- Ciardi, D. R., Beichman, C. A., Horch, E. P., & Howell, S. B. 2015, *ApJ*, 805, 16
- Clemens, J. C., Crain, J. A., & Anderson, R. 2004, in Proc. SPIE Conf. Ser., Vol. 5492, Ground-based Instrumentation for Astronomy, ed. A. F. M. Moorwood & M. Iye, 331–340
- Close, L. M., Males, J. R., Follette, K. B., et al. 2014, in Proc. SPIE Conf. Ser., Vol. 9148, Adaptive Optics Systems IV, 91481M
- Collier Cameron, A., Bouchy, F., Hébrard, G., et al. 2007, *MNRAS*, 375, 951
- Coughlin, J. L., Thompson, S. E., Bryson, S. T., et al. 2014, *AJ*, 147, 119
- Coughlin, J. L., Mullally, F., Thompson, S. E., et al. 2016, *ApJS*, 224, 12
- Crepp, J. R., Pueyo, L., Brenner, D., et al. 2011, *ApJ*, 729, 132
- Crossfield, I. J. M., Ciardi, D. R., Petigura, E. A., et al. 2016, *ApJS*, 226, 7
- David, T. J., Stauffer, J., Hillenbrand, L. A., et al. 2015, *ApJ*, 814, 62
- de Bruijne, J. H. J., Rygl, K. L. J., & Antoja, T. 2014, in EAS Publications Series, Vol. 67, EAS Publications Series, 23–29
- Désert, J.-M., Charbonneau, D., Torres, G., et al. 2015, *ApJ*, 804, 59
- Dotter, A., Chaboyer, B., Jevremović, D., et al. 2008, *ApJS*, 178, 89
- Doyle, L. R., Carter, J. A., Fabrycky, D. C., et al. 2011, *Science*, 333, 1602
- Dressing, C. D., Adams, E. R., Dupree, A. K., Kulesa, C., & McCarthy, D. 2014, *AJ*, 148, 78
- Ducati, J. R., Bevilacqua, C. M., Rembold, S. B., & Ribeiro, D. 2001, *ApJ*, 558, 309
- Duchêne, G., & Kraus, A. 2013, *ARA&A*, 51, 269
- Duquennoy, A., & Mayor, M. 1991, *A&A*, 248, 485
- Einstein, A. 1936, *Science*, 84, 506

- Ellerbroek, B., & Andersen, D. 2008, in Proc. SPIE Conf. Ser., Vol. 7015, Adaptive Optics Systems, 70155W
- Esposito, S., Riccardi, A., Pinna, E., et al. 2011, in Proc. SPIE Conf. Ser., Vol. 8149, Astronomical Adaptive Optics Systems and Applications IV, 814902
- Evans, D. F., Southworth, J., Maxted, P. F. L., et al. 2016, *A&A*, 589, A58
- Everett, M. E., Barclay, T., Ciardi, D. R., et al. 2015, *AJ*, 149, 55
- Fabrycky, D., & Tremaine, S. 2007, *ApJ*, 669, 1298
- Fauvarque, O., Neichel, B., Fusco, T., & Sauvage, J.-F. 2015, *Optics Letters*, 40, 3528
- Fischer, D. A., & Marcy, G. W. 1992, *ApJ*, 396, 178
- Fischer, D. A., & Valenti, J. 2005, *ApJ*, 622, 1102
- Fragner, M. M., Nelson, R. P., & Kley, W. 2011, *A&A*, 528, A40
- Fressin, F., Torres, G., Charbonneau, D., et al. 2013, *ApJ*, 766, 81
- Fried, D. L. 1967, in Proc. IEEE, Volume 55, p. 57-67, Vol. 55, 57–67
- Fruchter, A. S., & Hook, R. N. 2002, *PASP*, 114, 144
- Fulton, B. J., Collins, K. A., Gaudi, B. S., et al. 2015, *ApJ*, 810, 30
- Fulton, B. J., Petigura, E. A., Howard, A. W., et al. 2017, ArXiv e-prints, arXiv:1703.10375
- Furlan, E., Ciardi, D. R., Everett, M. E., et al. 2017, *AJ*, 153, 71
- Fhring, D., Wilson, R., Osborn, J., & Dhillon, V. 2015, *Journal of Physics: Conference Series*, 595, 012010
- Gaudi, B. S. 2012, *ARA&A*, 50, 411
- Ghigo, M., Diolaiti, E., Perennes, F., & Ragazzoni, R. 2003, in Proc. SPIE Conf. Ser., Vol. 5169, Astronomical Adaptive Optics Systems and Applications, ed. R. K. Tyson & M. Lloyd-Hart, 55–61
- Gilliland, R. L., Cartier, K. M. S., Adams, E. R., et al. 2015, *AJ*, 149, 24
- Girardi, L., Groenewegen, M. A. T., Hatziminaoglou, E., & da Costa, L. 2005, *A&A*, 436, 895
- Gizis, J. E. 1997, *AJ*, 113, 806
- Gizis, J. E., & Reid, I. N. 2000, *PASP*, 112, 610
- Goodwin, S. P., Kroupa, P., Goodman, A., & Burkert, A. 2007, *Protostars and Planets V*, 133

- Goodwin, S. P., & Whitworth, A. 2007, A&A, 466, 943
- Gould, A. 2003, ApJ, 583, 765
- Gould, A., & Salim, S. 2003, ApJ, 582, 1001
- Greene, T. P., Line, M. R., Montero, C., et al. 2016, ApJ, 817, 17
- Grether, D., & Lineweaver, C. H. 2007, ApJ, 669, 1220
- Gross, E., & Vitells, O. 2010, European Physical Journal C, 70, 525
- Guyon, O., Martinache, F., Cady, E. J., et al. 2012, in Proc. SPIE Conf. Ser., Vol. 8447, Adaptive Optics Systems III, 84471X
- Haas, M. R., Batalha, N. M., Bryson, S. T., et al. 2010, ApJL, 713, L115
- Halverson, S., Terrien, R., Mahadevan, S., et al. 2016, in Proc. SPIE Conf. Ser., Vol. 9908, Ground-based and Airborne Instrumentation for Astronomy VI, 99086P
- Heber, U. 2009, ARA&A, 47, 211
- Hillenbrand, L. A., Zhang, C., Riddle, R. L., et al. 2018, AJ, 155, 51
- Hirsch, L. A., Ciardi, D. R., Howard, A. W., et al. 2017, AJ, 153, 117
- Hodapp, K. W., Jensen, J. B., Irwin, E. M., et al. 2003, PASP, 115, 1388
- Horch, E. P., Howell, S. B., Everett, M. E., & Ciardi, D. R. 2012, AJ, 144, 165
- . 2014, ApJ, 795, 60
- Howard, A. W., Marcy, G. W., Bryson, S. T., et al. 2012, ApJS, 201, 15
- Howard, W. S., Law, N. M., Ziegler, C. A., Baranec, C., & Riddle, R. 2018, AJ, 155, 59
- Howell, S. B., Everett, M. E., Sherry, W., Horch, E., & Ciardi, D. R. 2011, AJ, 142, 19
- Ishigaki, M. N., Chiba, M., & Aoki, W. 2012, ApJ, 753, 64
- Janson, M., Hormuth, F., Bergfors, C., et al. 2012, ApJ, 754, 44
- Janson, M., Bergfors, C., Brandner, W., et al. 2014, ApJS, 214, 17
- Jao, W.-C., Mason, B. D., Hartkopf, W. I., Henry, T. J., & Ramos, S. N. 2009, AJ, 137, 3800
- Jaschek, C., & Jaschek, M. 1959, Zeitschrift fr Astrophysik, 48, 263
- Jenkins, J. M., Caldwell, D. A., Chandrasekaran, H., et al. 2010, ApJL, 713, L120
- Jensen-Clem, R., Duev, D. A., Riddle, R., et al. 2017, ArXiv e-prints, arXiv:1703.08867

- Jiang, Y.-F., & Tremaine, S. 2010, MNRAS, 401, 977
- Johnson, J. A., Petigura, E. A., Fulton, B. J., et al. 2017, ArXiv e-prints, arXiv:1703.10402
- Jovanovic, N., Martinache, F., Guyon, O., et al. 2015, PASP, 127, 890
- Kaib, N. A., Raymond, S. N., & Duncan, M. 2013, Nature, 493, 381
- Kaltenegger, L., & Traub, W. A. 2009, ApJ, 698, 519
- Kasper, M., Looze, D. P., Hippler, S., et al. 2000, Experimental Astronomy, 10, 49
- Kasting, J. F., Whitmire, D. P., & Reynolds, R. T. 1993, Icarus, 101, 108
- Katz, B., Dong, S., & Malhotra, R. 2011, Physical Review Letters, 107, 181101
- Kepler Mission Team. 2009, VizieR Online Data Catalog, 5133, 0
- Koch, D., Borucki, W., Basri, G., et al. 2007, in IAU Symposium, Vol. 240, Binary Stars as Critical Tools Tests in Contemporary Astrophysics, ed. W. I. Hartkopf, P. Harmanec, & E. F. Guinan, 236–243
- Köhler, R., Petr-Gotzens, M. G., McCaughrean, M. J., et al. 2006, A&A, 458, 461
- Kolbl, R., Marcy, G. W., Isaacson, H., & Howard, A. W. 2015, AJ, 149, 18
- Kopal, Z. 1959, Leaflet of the Astronomical Society of the Pacific, 8, 81
- Kraus, A. L., & Hillenbrand, L. A. 2007, AJ, 134, 2340
- Kraus, A. L., Ireland, M. J., Huber, D., Mann, A. W., & Dupuy, T. J. 2016, AJ, 152, 8
- Kreidberg, L. 2015, PASP, 127, 1161
- Kroupa, P. 1995, MNRAS, 277, astro-ph/9508117
- Kuiper, G. P. 1939, ApJ, 89, 548
- Labeyrie, A. 1995, A&A, 298, 544
- Lafrenière, D., Marois, C., Doyon, R., Nadeau, D., & Artigau, É. 2007, ApJ, 660, 770
- Lammer, H., Bredehoft, J. H., Coustenis, A., et al. 2009, The Astronomy and Astrophysics Review, 17, 181
- Latham, D. W. 2004, in Astronomical Society of the Pacific Conference Series, Vol. 318, Spectroscopically and Spatially Resolving the Components of the Close Binary Stars, ed. R. W. Hilditch, H. Hensberge, & K. Pavlovski, 276–282
- Latham, D. W., Stefanik, R. P., Torres, G., et al. 2002, AJ, 124, 1144
- Latham, D. W., Bakos, G. Á., Torres, G., et al. 2009, ApJ, 704, 1107

- Law, N. M., Hodgkin, S. T., & Mackay, C. D. 2006, MNRAS, 368, 1917
- Law, N. M., Ziegler, C., & Tokovinin, A. 2016, in Proc. SPIE Conf. Ser., Vol. 9907, Optical and Infrared Interferometry and Imaging V, 99070K
- Law, N. M., Mackay, C. D., Dekany, R. G., et al. 2009, ApJ, 692, 924
- Law, N. M., Morton, T., Baranec, C., et al. 2014, ApJ, 791, 35
- Law, N. M., Fors, O., Ratzloff, J., et al. 2015, PASP, 127, 234
- Lawrence, A., Warren, S. J., Almaini, O., et al. 2007, MNRAS, 379, 1599
- Léger, A., Rouan, D., Schneider, J., et al. 2009, A&A, 506, 287
- Lépine, S., Rich, R. M., & Shara, M. M. 2007, ApJ, 669, 1235
- Lépine, S., & Shara, M. M. 2005, AJ, 129, 1483
- Lillo-Box, J., Barrado, D., & Bouy, H. 2012, A&A, 546, A10
- . 2014, A&A, 566, A103
- Lissauer, J. J., Marcy, G. W., Rowe, J. F., et al. 2012, ApJ, 750, 112
- Lodieu, N., Zapatero Osorio, M. R., & Martín, E. L. 2009, A&A, 499, 729
- Lopez, C., Calandra, F., Chalela, M., et al. 2012, Journal of Double Star Observations, 8, 73
- Lutz, T. E., & Kelker, D. H. 1973, PASP, 85, 573
- Luyten, W. J. 1979, New Luyten catalogue of stars with proper motions larger than two tenths of an arcsecond; and first supplement; NLTT. (Minneapolis (1979)); Label 12 = short description; Label 13 = documentation by Warren; Label 14 = catalogue
- Luyten, W. J., & Hughes, H. S. 1980, Proper Motion Survey, University of Minnesota, 55
- Macintosh, B., Graham, J., Palmer, D., et al. 2006, in Proc. SPIE Conf. Ser., Vol. 6272, Society of Photo-Optical Instrumentation Engineers (SPIE) Conference Series, 62720L
- Macintosh, B., Graham, J. R., Ingraham, P., et al. 2014, Proceedings of the National Academy of Science, 111, 12661
- Macintosh, B., Graham, J. R., Barman, T., et al. 2015, Science, 350, 64
- Marcy, G. W., Isaacson, H., Howard, A. W., et al. 2014, ApJS, 210, 20
- Marois, C., Zuckerman, B., Konopacky, Q. M., Macintosh, B., & Barman, T. 2010, Nature, 468, 1080
- Marshall, J. L. 2007, AJ, 134, 778

- . 2008, AJ, 135, 1000
- Mathur, S., Huber, D., Batalha, N. M., et al. 2017, ApJS, 229, 30
- Matsakis, D. N., Taylor, J. H., & Eubanks, T. M. 1997, A&A, 326, 924
- Mayor, M., & Queloz, D. 1995, Nature, 378, 355
- Mazeh, T., Nachmani, G., Holczer, T., et al. 2013, ApJS, 208, 16
- Meza, A., Navarro, J. F., Abadi, M. G., & Steinmetz, M. 2005, MNRAS, 359, 93
- Monteiro, H., Jao, W.-C., Henry, T., Subasavage, J., & Beaulieu, T. 2006, ApJ, 638, 446
- Morton, T. D. 2015, isochrones: Stellar model grid package, Astrophysics Source Code Library, , , ascl:1503.010
- Morton, T. D., Bryson, S. T., Coughlin, J. L., et al. 2016, The Astrophysical Journal, 822, 86
- Morton, T. D., & Johnson, J. A. 2011, ApJ, 738, 170
- Mullally, F., Coughlin, J. L., Thompson, S. E., et al. 2015, ApJS, 217, 31
- Müller, T. W. A., & Kley, W. 2012, A&A, 539, A18
- Murphy, S. J., Bedding, T. R., & Shibahashi, H. 2016, ApJL, 827, L17
- Naoz, S., Farr, W. M., & Rasio, F. A. 2012, ApJL, 754, L36
- Ngo, H., Knutson, H. A., Hinkley, S., et al. 2015, ApJ, 800, 138
- . 2016, ApJ, 827, 8
- Pacini, F. 1967, Nature, 216, 567
- Pepe, F., Lovis, C., Ségransan, D., et al. 2011, A&A, 534, A58
- Perryman, M., Hartman, J., Bakos, G. Á., & Lindegren, L. 2014, ApJ, 797, 14
- Peter, D., Feldt, M., Henning, T., & Hormuth, F. 2012, A&A, 538, A74
- Petrovich, C. 2015, ApJ, 799, 27
- Picogna, G., & Marzari, F. 2015, A&A, 583, A133
- Pourbaix, D., Tokovinin, A. A., Batten, A. H., et al. 2004, A&A, 424, 727
- Ragazzoni, R. 1996, Journal of Modern Optics, 43, 289
- Raghavan, D., McAlister, H. A., Henry, T. J., et al. 2010, ApJS, 190, 1
- Rasio, F. A., & Ford, E. B. 1996, Science, 274, 954

- Rauer, H., Catala, C., Aerts, C., et al. 2014, *Experimental Astronomy*, 38, 249
- Reid, I. N., & Hawley, S. L. 2005, New light on dark stars : red dwarfs, low-mass stars, brown dwarfs, doi:10.1007/3-540-27610-6
- Reid, I. N., Brewer, C., Brucato, R. J., et al. 1991, *PASP*, 103, 661
- Riaz, B., Gizis, J. E., & Samaddar, D. 2008, *ApJ*, 672, 1153
- Riccardi, A., Bindi, N., Ragazzoni, R., Esposito, S., & Stefanini, P. 1998, in SPIE proceedings, Vol. 3353, Adaptive Optical System Technologies, ed. D. Bonaccini & R. K. Tyson, 941–951
- Ricker, G. R., Winn, J. N., Vanderspek, R., et al. 2014, in Proc. SPIE Conf. Ser., Vol. 9143, Space Telescopes and Instrumentation 2014: Optical, Infrared, and Millimeter Wave, 914320
- Riddle, R. L., Burse, M. P., Law, N. M., et al. 2012, in Society of Photo-Optical Instrumentation Engineers (SPIE) Conference Series, Vol. 8447, Society of Photo-Optical Instrumentation Engineers (SPIE) Conference Series, 2
- Riddle, R. L., Tokovinin, A., Mason, B. D., et al. 2015, *ApJ*, 799, 4
- Roberts, Jr., L. C., Tokovinin, A., Mason, B. D., et al. 2015, *AJ*, 149, 118
- Roell, T., Neuhäuser, R., Seifahrt, A., & Mugrauer, M. 2012, *A&A*, 542, A92
- Rogers, L. A. 2015, *ApJ*, 801, 41
- Rowe, J. F., Bryson, S. T., Marcy, G. W., et al. 2014, *ApJ*, 784, 45
- Salim, S., & Gould, A. 2002, *ApJL*, 575, L83
- Sandage, A. R., & Eggen, O. J. 1959, *MNRAS*, 119, 278
- Santerne, A., Fressin, F., Díaz, R. F., et al. 2013, *A&A*, 557, A139
- Santerne, A., Díaz, R. F., Moutou, C., et al. 2012, *A&A*, 545, A76
- Santerne, A., Moutou, C., Tsantaki, M., et al. 2015, ArXiv e-prints, arXiv:1511.00643
- Schlieder, J. E., Crossfield, I. J. M., Petigura, E. A., et al. 2016, *ApJ*, 818, 87
- Schonhut-Stasik, J. S., Baranec, C., Huber, D., et al. 2017, *ApJ*, 847, 97
- Schulze-Makuch, D., Méndez, A., Fairén, A. G., et al. 2011, *Astrobiology*, 11, 1041
- Schwamb, M. E., Orosz, J. A., Carter, J. A., et al. 2013, *ApJ*, 768, 127
- Seager, S. 2013, *Science*, 340, 577
- Selsis, F., Kasting, J. F., Levrard, B., et al. 2007, *A&A*, 476, 1373

- Siegel, M. H., Majewski, S. R., Reid, I. N., & Thompson, I. B. 2002, ApJ, 578, 151
- Silvotti, R., Schuh, S., Janulis, R., et al. 2007, Nature, 449, 189
- Skrutskie, M. F., Cutri, R. M., Stiening, R., et al. 2006a, AJ, 131, 1163
- . 2006b, AJ, 131, 1163
- Sparks, W. B., & Ford, H. C. 2002, ApJ, 578, 543
- Spergel, D., Gehrels, N., Breckinridge, J., et al. 2013, ArXiv e-prints, arXiv:1305.5425
- Spiegel, D. S., Fortney, J. J., & Sotin, C. 2014, Proceedings of the National Academy of Science, 111, 12622
- Sterzik, M. F., & Durisen, R. H. 1998, A&A, 339, 95
- Sullivan, P. W., Winn, J. N., Berta-Thompson, Z. K., et al. 2015, ApJ, 809, 77
- Sumi, T., Bennett, D. P., Bond, I. A., et al. 2010, ApJ, 710, 1641
- Terziev, E., Law, N. M., Arcavi, I., et al. 2013, ApJS, 206, 18
- Thies, I., & Kroupa, P. 2007, ApJ, 671, 767
- Torres, G., Kipping, D. M., Fressin, F., et al. 2015, ApJ, 800, 99
- Tozzi, A., Stefanini, P., Pinna, E., & Esposito, S. 2008, in SPIE proceedings, Vol. 7015, Adaptive Optics Systems, 701558
- Tyson, J. A. 2002, in Proc. SPIE Conf. Ser., Vol. 4836, Survey and Other Telescope Technologies and Discoveries, ed. J. A. Tyson & S. Wolff, 10–20
- Udalski, A. 2003, Acta Astronomica, 53, 291
- van Dam, M. A., Bouchez, A. H., Le Mignant, D., et al. 2006a, PASP, 118, 310
- . 2006b, PASP, 118, 310
- Wang, J., Fischer, D. A., Horch, E. P., & Xie, J.-W. 2015a, ApJ, 806, 248
- Wang, J., Fischer, D. A., Xie, J.-W., & Ciardi, D. R. 2014, ApJ, 791, 111
- . 2015b, ArXiv e-prints, arXiv:1510.01964
- Weiss, L. M., & Marcy, G. W. 2014, ApJL, 783, L6
- Weiss, L. M., Marcy, G. W., Petigura, E. A., et al. 2018, AJ, 155, 48
- Wizinowich, P., Acton, D. S., Shelton, C., et al. 2000, PASP, 112, 315
- Wizinowich, P. L., Le Mignant, D., Bouchez, A. H., et al. 2006, PASP, 118, 297

- Wolszczan, A., & Frail, D. A. 1992, *Nature*, 355, 145
- Xie, J.-W., Wu, Y., & Lithwick, Y. 2014, *ApJ*, 789, 165
- Yelda, S., Lu, J. R., Ghez, A. M., et al. 2010, *ApJ*, 725, 331
- York, D. G., Adelman, J., Anderson, Jr., J. E., et al. 2000, *AJ*, 120, 1579
- Zeng, L., Sasselov, D. D., & Jacobsen, S. B. 2016, *ApJ*, 819, 127
- Zhang, Z. H., Pinfield, D. J., Burningham, B., et al. 2013, *MNRAS*, 434, 1005
- Ziegler, C., Law, N. M., Baranec, C., Riddle, R. L., & Fuchs, J. T. 2015, *ApJ*, 804, 30
- Ziegler, C., Law, N. M., & Tokovinin, A. 2016, *Proc. SPIE*, 9909, 99093Z
- Ziegler, C., Law, N. M., Morton, T., et al. 2017a, *AJ*, 153, 66
- Ziegler, C., Law, N. M., Baranec, C., et al. 2017b, *ArXiv e-prints*, arXiv:1712.04454
- Zsom, A., Seager, S., de Wit, J., & Stamenković, V. 2013, *ApJ*, 778, 109